Finite Volume Methods for the Multilayer Shallow Water Equations with Applications to Storm Surges

Kyle T. Mandli

A dissertation submitted in partial fulfillment
of the requirements for the degree of

Doctor of Philosophy

University of Washington

2011

Program Authorized to Offer Degree: Applied Mathematics

University of Washington
Graduate School

This is to certify that I have examined this copy of a doctoral dissertation by

Kyle T. Mandli

and have found that it is complete and satisfactory in all respects,
and that any and all revisions required by the final
examining committee have been made.

Chair of the Supervisory Committee:

_____

Randall J. LeVeque

Reading Committee:

_____

Randall J. LeVeque

_____

Christopher S. Bretherton

_____

James J. Riley

Date: _____

In presenting this dissertation in partial fulfillment of the requirements for the doctoral degree at the University of Washington, I agree that the Library shall make its copies freely available for inspection. I further agree that extensive copying of this dissertation is allowable only for scholarly purposes, consistent with "fair use" as prescribed in the U.S. Copyright Law. Requests for copying or reproduction of this dissertation may be referred to Proquest Information and Learning, 300 North Zeeb Road, Ann Arbor, MI 48106-1346, 1-800-521-0600, to whom the author has granted "the right to reproduce and sell (a) copies of the manuscript in microform and/or (b) printed copies of the manuscript made from microform."

Signature_____

Date_____

University of Washington

Abstract

Finite Volume Methods for the Multilayer Shallow Water Equations with Applications to Storm Surges

Kyle T. Mandli

Chair of the Supervisory Committee:
Professor Randall J. LeVeque
Applied Mathematics

Coastal hazards related to strong storms such as hurricanes and typhoons are one of the most frequently recurring and wide spread hazards to coastal communities. Storm surges are among the most devastating effects of these storms, and their prediction and mitigation is of great interest to coastal communities that need to plan for the subsequent rise in sea level during these storms. Past efforts to model storm surge have usually focused on the single-layer shallow water equations, due to the ease of computing a simulation on the relevant scales and domains relative to three-dimensional modeling. The drawback to this approach is that the primary generating mechanism for storm surge is the wind-momentum transfer to the ocean. This boundary layer phenomenon is not well-represented by the shallow water equations, especially in the deep ocean. An alternative is to use the two-layer shallow water equations, with a shallow upper layer driven by the wind and an abyssal layer representing the rest of the water column.

The focus of this thesis is on the development of a finite volume method for the multi-layer shallow water equations that is appropriate for application to storm surges. This has been done in the context of the GeoClaw framework, a code designed to handle the single-layer shallow water equations with adaptive mesh refinement algorithms, and uses many of the capabilities available to GeoClaw that are pertinent to storm surges. Approximations to the system are also discussed and tested along with methods for handling dry-states and inundation. Finally, idealized storm surge test cases comparing the single-layer and two-layer shallow water equations are explored.

TABLE OF CONTENTS

LIST OF FIGURES

ACKNOWLEDGMENTS

I would fist like to thank my advisor, Randall J. LeVeque, for his constant encouragement, helpful suggestions, and patience. This work would not have been possible without his constant support and push for making this a better body of work. His seemingly unending generous support to attend conferences and pursue collaboration with a wide variety of researchers has broadened the field of opportunities and collaborations that have been made available to me and is greatly appreciated.

My thesis committee, Chistopher Bretherton, James Riley, and Peter Mackenzie, have also provided indelible advice and comments. James Riley has been of particular help and I thank him for the many discussions we have had over the years that have often caused me to rethink how I was approaching a problem. Marsha Berger at the Courant Institute at NYU was also generous in her time and patience while working on multiple projects together. I would also like to thank the scientists at the U.S.G.S. Cascades Volcano Observatory, in particular Roger Denlinger, for their continued support, feedback and knowledge that was invaluable.

I am also grateful for the current and former students of Professor LeVeque who have provided a template for success and guidance throughout the years. David L. George has been of particular help and without his previous work and collaboration this work would not have been completed. The rest of the students and faculty of the Applied Mathematics department have also all been immensely helpful and I would like to thank them for their input and collaboration.

Finally, I would like to thank my friends and family that have been ever patient and encouraging through my years in graduate school. I am also forever indebted to Kristen Thyng whose constant patience and encouragement have been essential.

Chapter 1

INTRODUCTION

1.1 Background and Motivation

As computer technology advances, scientists continually attempt to use numerical modeling to better predict a growing number of high-impact geophysical events. In particular, coastal hazards have become an increasing concern as the world's population continues to grow and move towards the coastline, in fact 44% of the world's population lives within 150 km of the coast and 8 of the 10 largest cities in the world lie in that range [2]. As a consequence, loss of life and property is becoming a larger concern than before. One of the most recurring and wide spread hazards to many coastal communities is the inundation of coastlines that is caused by strong storms, one part of which is known as storm surges (see figure 1.1). A storm surge is a rise in the sea accompanying extratropical or tropical cyclones, the strongest examples of which are hurricanes and typhoons. Storm surges can cause massive amounts of damage, as was demonstrated by Hurricane Katrina, where an estimated $81 billion of damage was caused [10]. With the mounting evidence that severe storms, not only tropical cyclones such as Katrina but also extratropical cyclones in the mid-latitudes, may be increasingly common [1], the task of modeling these events becomes even more important to communities along the coasts.

Modeling of storm surges was first carried out by local empirical observations. Unfortunately, for more severe storms such as Katrina, these types of predictions can grossly under-predict storm surge size and effect. By the 1960's, scientists started using computer simulations to predict storm surge but, because these simulations were limited in resolution and size, these models also fell victim to the same shortcomings the empirically-based models had. It was not until more recent observational evidence, effort on the underlying physics and faster computers that progress on large-scale storm surge prediction was capable of making predictions that were within the realm of possible use in hazard planning.

Today, the state-of-the-art numerical models rely on single-layer depth-averaged equations for the ocean and make assumptions on the response the ocean has to a storm passing over it. The National Weather Service utilizes a storm surge model called the "Sea, Lake and Overland Surges from Hurricanes", or SLOSH, which uses local grids defined for many regions on the United States coastline to make predictions [30]. These simulations are efficient enough that ensembles of runs can be made quickly and for multiple different hurricane paths and intensities. Another currently

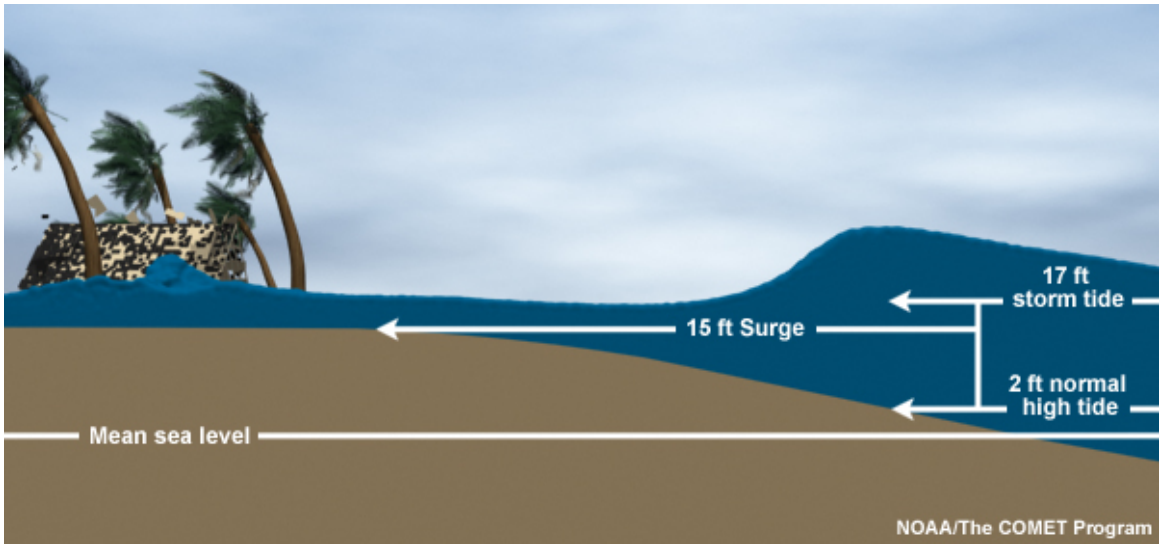

Figure 1.1: Diagram of storm surge and other phenomenon leading to inundation [36].

used model is the Advanced Circulation Model (ADCIRC) developed by Westerink et al who applied it to southern Louisiana in [45]. The effects currently modeled by these numerical models include momentum transfer due to wind stress on the surface of the water, pressure forcing due to the low pressure system associated with large storms, wave momentum transfer, and friction effects at the bottom of the water column, the largest effect being the wind stress transfer. As was suggested by previous researchers, one of the primary sources of error in storm surge modeling is due to vertical structure not being taken into account by single-layer depth averaged models [39]. This loss of accuracy is primarily due to the assumption that the water column acts almost completely as a single entity and no vertical variation in the momentum occurs (see figure 1.2a for an illustration). In reality the wind forces a boundary layer that has a limited depth in the vertical. This results in a faster top layer of water and a reduction in the overall transfer of momentum from the air to the sea. Conversely, the bottom-layer return currents yield a shoreward stress that can greatly increase the resulting surge. Parametric studies have suggested that the net result of these effects could lead to an increase in surge of up to 25%. Instead of representing the water velocity as a constant value through the depth, a more appropriate idealization might be to include multiple layers representing the boundary layers involved, as depicted in figure 1.2b for the two-layer case.

Simple test cases also suggest that much of the dynamics of storm surges in the deeper parts of the ocean may be neglected in single-layer simulations. Figure 1.4 represents a series of snapshots of a single-layer simulation with a hurricane traveling across a shallow sea as described by figure 1.3. The shallow sea is an idealized way

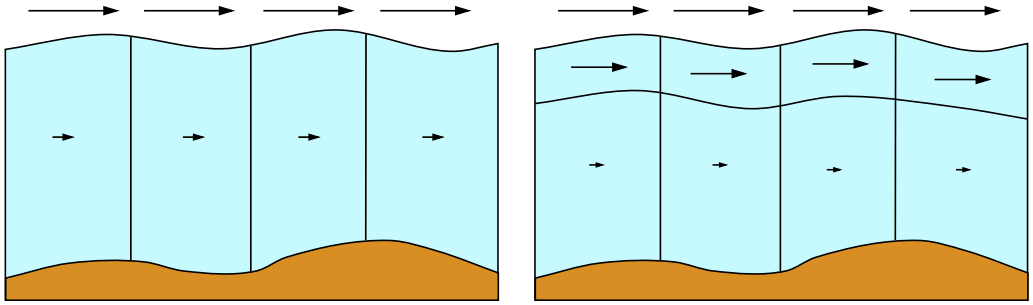

Figure 1.2: Illustration representing resulting velocities from a wind stress on the top of a water column. Figure 1.2a represents a single-layer model with wind forcing where the entire column of water is forced. Figure 1.2b represents a two-layer model where most of the energy from the wind forcing is put into the upper layer.

to represent the possible effect adding a layer at the top of the ocean might have on surge. Multiple structures exist in these simulations that could have significant impact on the surge strength and impact. When a similar simulation is done but with realistic depths, none of these structures exist, as seen in figure 1.5a.

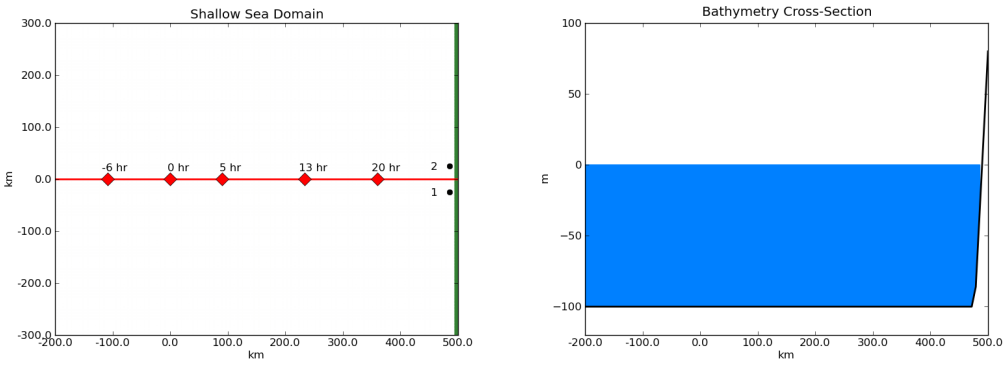

Figure 1.3: Setup for the shallow sea storm surge calculation shown in figure 1.4.

1.2 Objectives

The central goal of this thesis is to study the viability of using a two-layer depth averaged model for storm surge prediction in lieu of a full three dimensional model

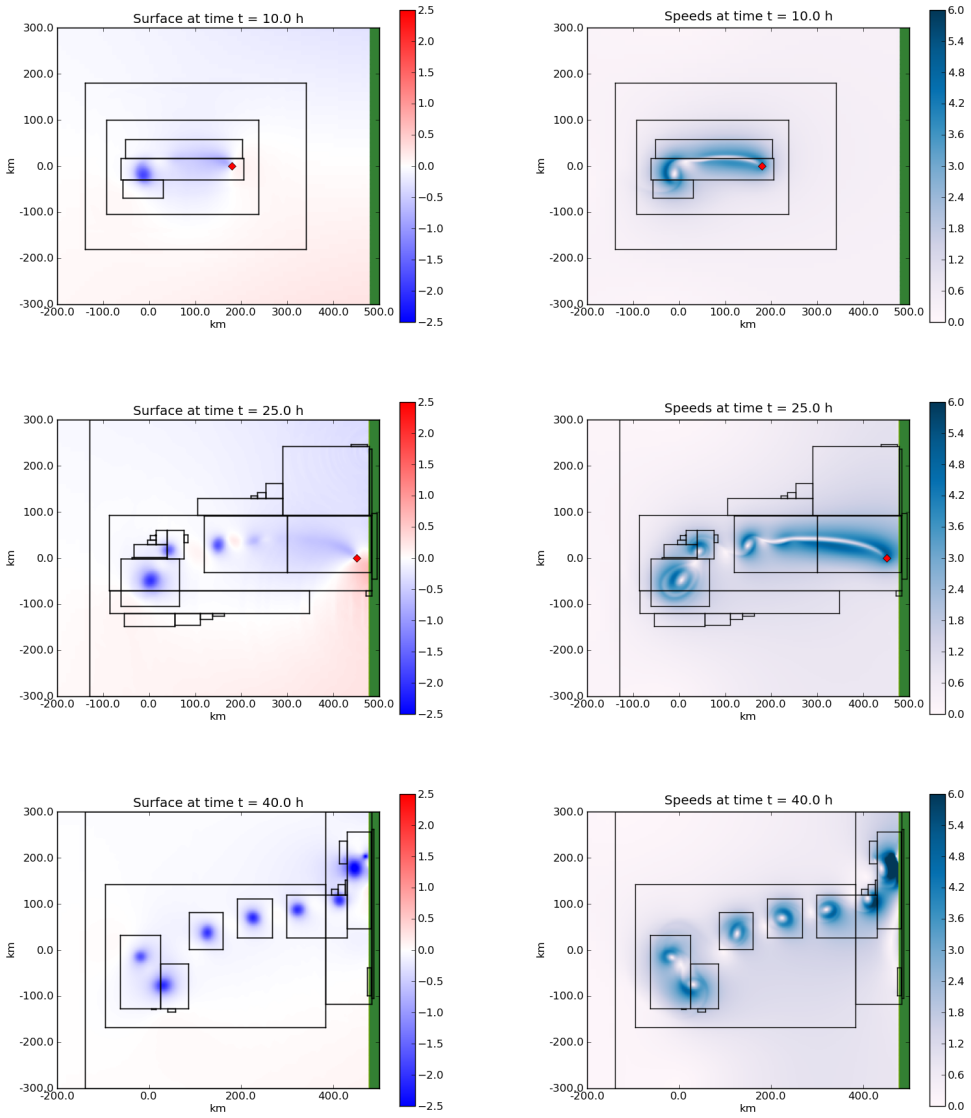

Figure 1.4: Simulation of a hurricane moving over a shallow sea. The figures on the left show the surface deviation from sea level. The figures on the right represent the magnitudes of the speed of the water. The boxes are adaptive mesh refinement grids that have been used to refine areas of interest in the simulation. The red diamond indicates the eye of the storm.

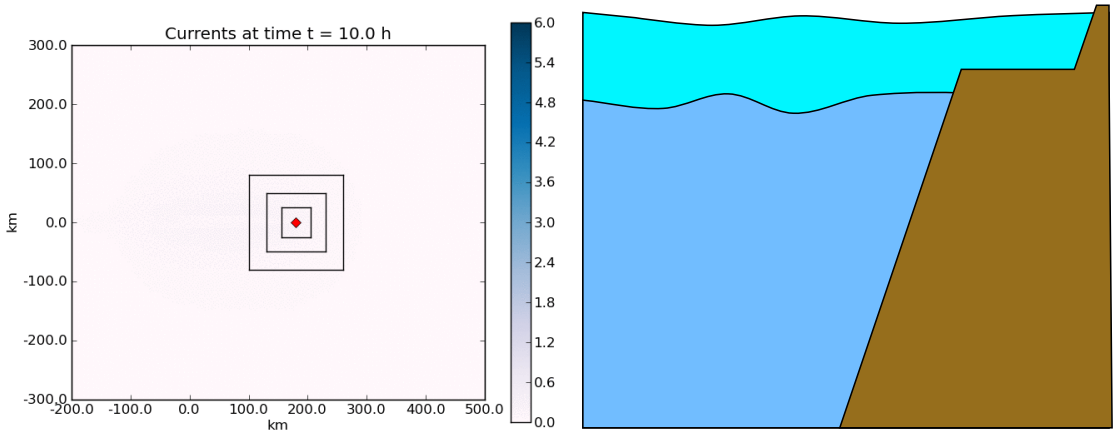

(a) (b)

Figure 1.5: In figure 1.5a a simulation identical to the one shown in figure 1.4 is shown except that the sea it is traveling over is now 3000 meters deep, a typical ocean basin depth in areas of interest, such as the Gulf of Mexico. Figure 1.5b shows an idealized setup for a two-layer storm surge simulation with the abyssal layer depth going to zero at the continental shelf rather than near the shore line.

or the commonly used single-layer model. The two-layer approach has advantages over the single-layer models for reasons explained in section 1.1 and could be the most computationally tractable way to account for the depth varying effects. A three dimensional model could also accomplish this to greater precision, but the main drawback to using a three dimensional model is the time needed to compute at relevant temporal and spatial scales as operational prediction relies on ensemble predictions to mitigate uncertainties in storm track and intensity.

Multi-layer depth averaged models have been of recent interest for many different applications. The reason why multi-layer models have not been more widely used however is due to the difficulty in computing numerical solutions to these equations. One of these difficulties is the complexity of the underlying Riemann problems and more specifically the wave speeds needed to compute these solutions. Approximations exist to overcome this problem such as more diffusive solvers [22], relaxation approaches [3], and decoupling schemes that still obey entropy laws [11]. Another difficulty is the loss of hyperbolicity commonly associated with the physical mechanism of Kelvin-Helmholtz instabilities that appear in the equations. Work has also been done to mitigate this effect by applying physically motivated momentum transfer to stabilize the system [15].

Fortunately, when applying the multi-layer equations to storm surges, many of the challenges that exist in general for these equations are either not applicable or

are only seen in extreme cases. In terms of the solution of the system, since most of the ocean is assumed to be at a steady state, linearization is an effective way to compute the otherwise difficult Riemann problems associated with the system. Another difficulty arises when considering dry states of the system. In constructing the two-layer problem for storm surges, requiring the bottom layer to become dry away from the top layer, and therefore the coast, simplifies this problem and the number of dry state cases that must be handled. In figure 1.5b for instance, the bottom layer has zero depth somewhere along the continental slope. The last difficulty mentioned above is loss of hyperbolicity. For storm surges, as will be shown, the loss of hyperbolicity does not generally occur, although the mechanisms described in [15] may be useful in providing a more accurate portrayal of the mixed layer under a storm.

The objective of this work is to provide a numerical scheme for the multi-layer depth-averaged equations in the context of storm surges. This scheme must be able to handle the complex Riemann problems associated with the multi-layer equations and still be efficient enough to use in an ensemble predictive capacity. The scheme must also handle dry states as is pertinent in the case of storm surges. Lastly, the conclusion of whether a multi-layer approach to storm surge modeling is worthwhile will be discussed via comparison to similar single-layer numerical models.

1.3 Overview

The first part of this thesis provides a general overview of hyperbolic partial differential equation theory, of which both the single and multi-layer depth-averaged equations are a part. In chapter 2 the theory of hyperbolic partial differential equations, including the basic approach to solving Riemann problems and classification of the solution and equations, is reviewed. Chapter 3 introduces finite volume methods and a related approach called wave-propagation algorithms that will be used to solve the systems in question.

The theory of depth-averaged equations for both single and multi-layer equations is presented in the second part of this thesis. In chapter 4 the single-layer equations are derived with details regarding what assumptions go into the derivation, what possible extensions are available, and a framework to adapt existing single-layer numerical methods for storm surges. This chapter also contains the basic Riemann solvers for the single-layer equations, a discussion of how dry states are handled, and other pertinent theoretical aspects of the single-layer equations. Chapter 5 contains derivations of the multi-layer equations and a discussion of the question of how to solve the Riemann problem and in particular, how to find a method for finding the wave speeds for the Riemann problem that respects dry states. Finally, in chapter 6 numerical methods are presented for the multi-layer depth-averaged equations including some test cases for the method used to determine the eigenspace and convergence tests in one and two dimensions.

The last part of this thesis illustrates how the methods developed apply to storm surges. In chapter 7, the numerical approach used for the forcing terms as well as the idealized model for the storm are discussed and implemented. Results are then given and compared for single-layer and two-layer simulations of an idealized historical hurricane approaching an idealized bathymetry and coastline at multiple different angles. Finally, chapter 8 contains a summary of the findings of this thesis, a discussion of whether the multi-layer depth averaged equations are a fruitful avenue of research for storm surge modeling, and possible future directions of research.

Chapter 2

HYPERBOLIC CONSERVATION AND BALANCE LAWS

Conservation and balance laws comprise a large class of fundamental governing equations in the physical world. This chapter contains brief introductions to many of the relevant concepts that will be used in analyzing depth-averaged fluid flow. First, a review of the general theory of hyperbolic conservation laws and the fundamental solutions to Riemann problems is given. Second, extensions of this basic theory to balance laws is considered. Finally, the shallow water equations will be used to demonstrate and explore many of the definitions, properties, and solution techniques laid out in this chapter. Later chapters will extend the shallow water equations and use the analysis here as a basis.

It should be noted that this chapter is primarily meant as an overview and intended as a means of establishing notation for later chapters. If the reader would like further information about all of the topics discussed here, refer to [32, 42, 20] and other references contained there.

2.1 Hyperbolic Conservation Laws

Consider the class of partial differential equations (PDEs) represented by

$$\frac{\partial}{\partial t}q(x,t) + \sum_{j=1}^{n} \frac{\partial}{\partial x_j} f_j(q) = 0, \quad x = (x_1, \ldots, x_n)^T \in \mathbb{R}^n \tag{2.1}$$

where $q \in \mathbb{R}^n$ represent a set of m conserved quantities and $f_j(q) \in \mathbb{R}^m$ the fluxes of these quantities. The reason why (2.1) is called a conservation law is that given an arbitrary domain $\Omega \in \mathbb{R}^n$ and an outward unit normal $\omega = (\omega_1, \ldots, \omega_n)$ to the boundary $\partial\Omega$ of Ω, from (2.1) and the divergence theorem, we can derive the relation

$$\frac{\mathrm{d}}{\mathrm{d}t}\int_{\Omega} q dx + \sum_{j=1}^{n} \int_{\partial\Omega} f_j(q)\omega_j dS = 0. \tag{2.2}$$

This equation states that the time variation of the conserved quantities q only varies due to the value of the flux functions f_j at the boundary $\partial\Omega$.

An important subset of the systems described by (2.1) are called hyperbolic if the flux functions f_j satisfy certain properties.

Definition 2.1.1 (Hyperbolicity)**.** *For $j = 1, \ldots, n$, let*

$$[A_j(q)]_{ip} = \frac{\partial (f_j)_i}{\partial q_p} \tag{2.3}$$

be the ipth entry of the Jacobian matrix of $f_j(q)$. the system (2.1) is called hyperbolic if for any $q \in \Omega$ and $\omega = (\omega_q, \ldots, \omega_n)^T \in \mathbb{R}^n$, $|\omega| = 1$, the matrix

$$A(q, \omega) = \sum_{j=1}^{n} \omega_j A_j(q) \tag{2.4}$$

has m real eigenvalues $\lambda^1(q, \omega) \leq \lambda^2(q, \omega) \leq \ldots \leq \lambda^m(q, \omega)$ and m linearly independent corresponding eigenvectors $r^1(q, \omega), \ldots, r^m(q, \omega)$, that is

$$A(q, \omega) r^p(q, \omega) = \lambda^p(q, \omega) r^p(q, \omega), \qquad 1 \leq p \leq m. \tag{2.5}$$

If, in addition, the eigenvalues $\lambda^p(q, \omega)$ are all distinct, then the system (2.1) is called strictly hyperbolic.

Since the direction ω is arbitrary, the hyperbolicity of the system in question is independent of direction. Note that if the system (2.1) is hyperbolic then by definition the integral form (2.2) is also hyperbolic. It is important to also note that although we have defined hyperbolicity of the PDE, often the more fundamental governing relation is the integral form of the hyperbolic conservation law (2.2), which has important consequences that are laid out in the next section.

2.1.1 Weak Solutions

Conservation laws written in the form of (2.1) are known as the *strong form* of the PDE where as conservation laws written in the form of (2.2) are known as *weak forms* of the PDE. This naming convention belies a deeper connection to the type of solution each form of the PDE can exhibit. Both the strong and weak form of the equations will admit differentiable solutions to the PDE. The weak form of the equations can also admit solutions that contain discontinuities which can be interpreted as weak solutions to the PDE in the distribution sense (see [23] for more on this connection and distribution theory in general). It is also important to note that non-linear hyperbolic conservation laws can develop discontinuous solutions in finite time even for smooth initial conditions.

If we now consider a function q that is piece-wise continuous that satisfies the strong form of the PDE (2.1) within the smooth regions and the weak form of the PDE (2.2) near the discontinuities. If we apply the weak form (2.2) in a region around the jump discontinuity, we can derive the *Rankine-Hugoniot* jump conditions which

in one dimension take the form

$$s(q_+ - q_-) = (f(q_+) - f(q_-)) \tag{2.6}$$

where s represents the speed of the traveling discontinuity and q_+ and q_- the limiting value of the conserved quantities to either side of the jump.

2.2 Riemann Problems

The *Riemann problem* consists of the hyperbolic equations along with piece-wise constant initial data

$$q_0(x) = \begin{cases} q_\ell & \text{if} \quad x < 0, \\ q_r & \text{if} \quad x > 0, \end{cases} \tag{2.7}$$

on $-\infty < x < \infty$. The solution to these problems are similarity solutions, *i.e.* $q(x,t) = \tilde{q}(x/t)$, and are composed of set of waves connecting constant states determined by the initial condition $q_0(x)$. Our goal then is to determine how these constant states are connected and how these connections behave.

2.2.1 Linear Hyperbolic Equations

The linear, one-dimensional, hyperbolic conservation law takes the general form

$$q_t + Aq_x = 0 \tag{2.8}$$

where A is a constant matrix and we have used the notation $\frac{\partial f}{\partial x} \equiv f_x$. Due to the definition of hyperbolicity, A is diagonalizable and can be decomposed as $A = R\Lambda R^{-1}$ where R is the right eigenvector matrix and Λ is the matrix with the eigenvalues on the diagonal. By replacing A with the decomposition in the hyperbolic equation and multiplying by R^{-1}, we can rewrite (2.8) as

$$w_t + \Lambda w_x = 0 \tag{2.9}$$

where w are now the characteristic variables defined by $w = R^{-1}q$. Since this transformation decouples the system into a set of scalar advection equations, the solution to the system is then a series of discontinuities determined by the representation of the initial condition in characteristic variables and propagating at the corresponding speed determined by the eigenvalue. In the $x-t$ plane the path of the discontinuities are constant slope characteristics. Each of these discontinuities obeys the principle of superposition and the solution can be written as

$$q(x,t) = \sum_{p=1}^{m} w_0^p(x - \lambda^p t) \tag{2.10}$$

where $w_0(x)$ is the initial condition transformed into characteristic variables.

For the Riemann problem we can write the solution in a particularly useful way by decomposing the discontinuity as

$$q_\ell = \sum_{p=1}^{m} w_\ell^p r^p \quad \text{and} \quad q_r = \sum_{p=1}^{m} w_r^p r^p. \tag{2.11}$$

The initial condition can then be transformed into the characteristic variables of the problem directly and the solution can be written as

$$q(x,t) = \sum_{p:\lambda^p<x/t} w_r^p r^p + \sum_{p:\lambda^p>x/t} w_\ell^p r^p. \tag{2.12}$$

We can also interpret the discontinuities themselves as waves traveling through the domain. If we project the jump in $q_r - q_\ell$ onto the eigenvectors

$$q_r - q_\ell = \sum_{p=1}^{m} \alpha^p r^p \tag{2.13}$$

and define

$$\mathcal{W}^p = \alpha^p r^p \tag{2.14}$$

as the p^{th} wave traveling at λ^p, the solution then becomes

$$q(x,t) = q_\ell + \sum_{p:\lambda^p<x/t} \mathcal{W}^p = q_r - \sum_{p:\lambda>x/t} \mathcal{W}^p. \tag{2.15}$$

Note that each wave satisfies the Rankine-Hugoniot conditions (2.6) with $s \equiv \lambda^p$.

2.2.2 Nonlinear Hyperbolic Equations

The general one-dimensional hyperbolic conservation law

$$q_t + f(q)_x = 0. \tag{2.16}$$

and the associated Riemann problem is much more difficult to solve as the waves in each characteristic family are non-constant and may interact. For that reason it is useful to study the individual waves in isolation and piece together the full solution once each of the waves have been determined. The first step in classifying waves is to determine whether the field it is a part of is *genuinely nonlinear*.

Definition 2.2.1. *The p^{th} characteristic field is genuinely nonlinear if*

$$\nabla\lambda^p(q) \cdot r^p(q) \neq 0 \quad \forall q \in \Omega. \tag{2.17}$$

Alternatively, the p^{th} characteristic field is linearly degenerate if

$$\nabla\lambda^p(q) \cdot r^p(q) \equiv 0 \qquad \forall q \in \Omega. \tag{2.18}$$

Examples of waves in genuinely nonlinear fields are shocks and rarefactions. Linearly degenerate fields contain waves that act similar to waves in a constant-coefficient problem and cannot develop shocks by themselves. In the rest of this section we will discuss the salient features of each of these types of waves and discuss how to determine which type of wave is appropriate for each family based on a set of physically motivated conditions.

Shock Waves

A shock is a wave in a genuinely nonlinear characteristic field representing a collision of characteristics in the appropriate family. This is represented as a traveling discontinuity in the solution q and consequently is governed by the Rankine-Hugoniot condition (2.6) for that family. An important property of shock waves unlike the other waves we will discuss is that the characteristic speeds on either side of the discontinuity are not equal, in other words $\lambda^p(q_\ell) \neq \lambda^p(q_r)$ and the resulting shock speed s cannot be determined from these values alone but must be obtained from the Rankine-Hugoniot condition. For a scalar conservation law this may not be difficult if all the quantities are well defined but for systems of conservation laws this may involve simultaneously solving a system of nonlinear equations assuming that the states connecting either side of the shock are known. If this is not the case the problem becomes more complicated and the analytical solution may be unobtainable by direct means.

It is important to recognize that for nonlinear conservation laws, even though a discontinuity is not present in the initial conditions, one may form in finite time. A simple example of this is the solution to Burger's equation

$$u_t + \left(\frac{1}{2}u^2\right)_x = 0$$

whose initial condition may be smooth but lead to a shock in finite time.

Centered Rarefactions

The second type of wave that can be present in a genuinely nonlinear characteristic field is a rarefaction, a smooth, differentiable variation in the function q connecting two states. In a Riemann problem these waves are called *centered rarefactions* since they are similarity solutions to the equations. Rarefactions in general are characterized by integral curves associated with the particular characteristic family. Since we expect the solution to the Riemann problem in this case to be a similarity solution $\tilde{q}(x/t)$,

and if we parameterize the integral curve with χ, then for an integral curve associated with the p^{th} characteristic family, we know

$$\tilde{q}'(\chi) = \alpha(\chi) r^p(\chi), \tag{2.19}$$

where α is a factor dependent on the parameterization χ chosen. As we connect the left and right states, we must travel on one integral curve associated with the particular characteristic field. This fact can then be leveraged by calculating the *Riemann invariant*, a constant common to any state on a given integral curve, and finding the admissible states connecting to the original state.

Contact Discontinuities

This is the final type of wave we expect to have to deal with when the wave is isolated to a single characteristic field. In Riemann problems these waves act as linear traveling discontinuities whose speed obeys the Rankine-Hugoniot condition but whose characteristic speeds are continuous: $s = \lambda^p(q_\ell) = \lambda^p(q_r)$. These waves often appear with advected quantities and transverse momenta in multi-dimensional conservation laws.

Entropy Conditions

For nonlinear problems with genuinely nonlinear characteristic fields a non-uniqueness now presents itself. Up until now we have found multiple weak solutions to the conservation law involving combinations of shocks and rarefactions in each genuinely nonlinear field but not all of these solutions may be permissible. We therefore must enforce another condition on the solution in order to pick out the correct physical solution from among the weak solutions. One such condition is the *Lax Entropy Condition* which can be shown to be correct for strictly hyperbolic conservation laws in which each field is genuinely nonlinear.

Definition 2.2.2 (Lax Entropy Condition)**.** *A discontinuity separating states q_ℓ and q_r, propagating at speed s, satisfies the Lax entropy condition if there is an index p such that*

$$\lambda^p(q_\ell) > s > \lambda^p(q_r) \tag{2.20}$$

so that p-characteristics are impinging on the discontinuity, while the other characteristics are crossing the discontinuity,

$$\lambda^j(q_\ell) < s \qquad \text{and} \qquad \lambda^j(q_r) < s \qquad \text{for } j < p, \tag{2.21}$$

$$\lambda^j(q_\ell) > s \qquad \text{and} \qquad \lambda^j(q_r) > s \qquad \text{for } j > p, \tag{2.22}$$

where, in this definition, the eigenvalues are ordered so that $\lambda^1 < \lambda^2 < \ldots < \lambda^m$ in each state.

Another method for establishing the correct solution is to use an entropy function $\eta(x,t)$ of the accompanying physical system and enforce the condition that entropy is conserved when q is smooth and must decrease (or increase depending on the form of the entropy function) across shocks. This form of entropy conditions often requires the evaluation of η and the entropy conservation equation

$$\eta(q)_t + \phi(q)_x = 0,$$

where $\phi(q)$ represents the entropy flux, must hold for smooth solutions. Once the appropriate entropy condition is established, we can then check which weak solution obeys the entropy conditions and identify it as the physically admissible solution.

2.3 Balance Laws and Source Terms

The systems we have previously considered are sometimes called *homogeneous conservation laws* in order to differentiate them from equations with a right hand side forcing function, often called a *source term*. These related systems are called either *inhomogenous conservation laws* or *balance laws*. In general, balance laws take the form

$$\frac{\partial}{\partial t}q(x,t) + \sum_{j=1}^{n}\frac{\partial}{\partial x_j}f_j(q) = \psi(q,x), \tag{2.23}$$

where $\psi(q,x)$ may include derivatives of q or other functions. Source terms physically represent sources or sinks of the state variables q. Physically, balance laws behave differently than homogenous conservation laws in the way the evolution of q occurs. For a conservation law, given a domain Ω, the time evolution of q is based solely on the flux through the boundary $\partial\Omega$. For balance laws, the time evolution of q is also determined by the sources or sinks of the quantity q located in the interior of Ω.

2.3.1 Riemann Problems With Source Terms

Unlike the previous solutions we found to the Riemann problem, balance laws may not admit a similarity solution, even in the linear case, as the characteristic families no longer depend only on the flux functions. Take for example the linear hyperbolic PDE

$$q_t + Aq_x = \psi \tag{2.24}$$

and diagonalize and transform the equation into characteristic variables

$$w_t + \Lambda w_x = R^{-1}\psi. \tag{2.25}$$

The equations are no longer fully decoupled as the source term may still depend on combinations of the characteristic variables. In general, defining the characteristic

path with $X(t) = x_0 + \lambda^p t$, we must solve a system of ordinary differential equations (ODEs) defined by

$$\frac{\mathrm{d}}{\mathrm{d}t}(w^p(X(t),t)) = (R^{-1}\psi)^p. \tag{2.26}$$

In the case of a nonlinear system, the source term's effect on the system can be considerably more complicated. One way to leverage our previous knowledge of homogeneous conservation laws is to idealize the source term as being applied at a single point, $\psi(q,x) = \Psi\delta(\hat{x})$ where Ψ is an appropriately chosen constant and δ is the delta function. It can be shown that in a vanishingly small neighborhood around the point source, the flux must satisfy [32]

$$f(q(\hat{x}^+,t)) - f(q(\hat{x}^-,t)) = \Psi. \tag{2.27}$$

Since the source term is only applied at the jump location $\hat{x}$, everywhere else the equations are homogeneous and what we have developed above applies. It should be noted that the exact definition of Ψ above is not straight forward as we need to evaluate ψ at a discontinuity in q where ψ may not be well-defined.

2.4 Example System: The Shallow Water Equations

We will now analyze many of the concepts introduced in this chapter in the context of the one dimensional shallow water equations. The one dimensional equations can be written as

$$\begin{aligned} &h_t + (hu)_x = 0 \quad \text{and} \\ &(hu)_t + \left(hu^2 + \frac{1}{2}gh^2\right)_x = 0 \end{aligned} \tag{2.28}$$

where h represents the depth of the fluid and u the velocity. This system can be written in terms of the vector q and flux function $f(q)$ as

$$q = [h, hu]^T \qquad \text{and} \qquad f(q) = [q^2, (q^2)^2/q^1 + 1/2g(q^1)^2]^T.$$

Calculating the flux Jacobian (2.28) leads to

$$f'(q) = \begin{bmatrix} 0 & 1 \\ gh^2 - u^2 & 2u \end{bmatrix}$$

whose eigenvalues are $\lambda^p = u \pm \sqrt{gh}$ with accompanying eigenvectors $[1, \lambda^p]$ for each characteristic field.

In two dimensions the system becomes

$$\begin{aligned} &h_t + (hu)_x + (hv)_y = 0, \\ &(hu)_t + (hu^2 + 1/2gh^2)_x + (huv)_y = 0, \quad \text{and} \\ &(hv)_t + (huv)_x + (hv^2 + 1/2gh^2)_y = 0. \end{aligned}$$

$$q = \begin{bmatrix} h \\ hu \\ hv \end{bmatrix}, \qquad f_1(q) = \begin{bmatrix} hu \\ hu^2 + \frac{1}{2}gh^2 \\ huv \end{bmatrix}, \qquad f_2(q) = \begin{bmatrix} hv \\ huv \\ hv^2 + \frac{1}{2}gh^2 \end{bmatrix}, \qquad \text{and}$$

Calculating the Jacobians of both fluxes

$$f_1'(q) = \begin{bmatrix} 0 & 1 & 0 \\ gh - u^2 & 2u & 0 \\ -uv & v & u \end{bmatrix} \qquad \text{and} \qquad f_2'(q) = \begin{bmatrix} 0 & 0 & 1 \\ -uv & v & u \\ gh - v^2 & 0 & 2v \end{bmatrix}$$

leads us to the eigenpairs

$$\begin{aligned} \lambda^1(q) &= u - \sqrt{gh} && \text{with} && r^1(q) = [1, \lambda^1, v]^T, \\ \lambda^2(q) &= u && \text{with} && r^2(q) = [0, 0, 1]^T, \qquad \text{and} \\ \lambda^3(q) &= u + \sqrt{gh} && \text{with} && r^3(q) = [1, \lambda^3, v]^T \end{aligned}$$

for f_1 and

$$\begin{aligned} \lambda^1(q) &= v - \sqrt{gh} && \text{with} && r^1(q) = [1, u, \lambda^1]^T, \\ \lambda^2(q) &= v && \text{with} && r^2(q) = [0, 1, 0]^T, \qquad \text{and} \\ \lambda^3(q) &= v + \sqrt{gh} && \text{with} && r^3(q) = [1, u, \lambda^3]^T \end{aligned}$$

for f_2.

Hyperbolicity

Checking the hyperbolicity of (2.28) we can see that the eigenvalues remain distinct if $h > 0$ which is also the expected physically relevant region in phase space. This is also true for the two dimensional equations. The case where $h = 0$ is a special case and will be discussed in greater detail in chapter 4.

Riemann Solution

The Riemann problem for the shallow water equations is in general nonlinear and the characteristic fields in the one dimensional case are both genuinely nonlinear. Our

goal is to connect states q_ℓ to q_* to q_r (see figure 2.1a). For each wave we can connect q_ℓ and q_r to q_* with either a rarefaction or a shock. Each type of wave has a different set of conditions and these give curves in the phase plane representing valid middle state q_* that can be connected over that wave. For shocks, these conditions are the Rankine-Hugoniot conditions

$$\lambda(h_+ - h_-) = h_+u_+ - h_-u_-, \quad \text{and}$$
$$\lambda(h_+u_+ - h_-u_-) = h_+u_+^2 - h_-u_-^2 + 1/2g(h_+^2 - h_-^2),$$

where h_+ and u_+ should be replaced by the appropriate right state and h_- and u_- with the appropriate left state. These conditions trace out a curve of valid connecting states in the phase plane satisfying

$$u_\pm = u_* \pm \sqrt{\frac{g}{2}\left(\frac{h_*}{h_\pm} - \frac{h_\pm}{h_*}\right)(h_* - h_\pm)},$$

often referred to as *Hugoniot loci* for two states $q_\pm$ and q_* which are both constant. An all shock solution to a shallow water Riemann problem is shown in figure 2.2 where the left state and right state are connected through the middle state q_*. If the Lax entropy conditions are evaluated in this case, if q_ℓ is connected over a 1-shock to q_* then $h_\ell < h_*$. Similarly the right state q_r can only be connected through a 2-shock if $h_r < h_*$. Since the second of these conditions does not hold, we know that the state depicted cannot be the correct entropy satisfying solution for the Riemann problem.

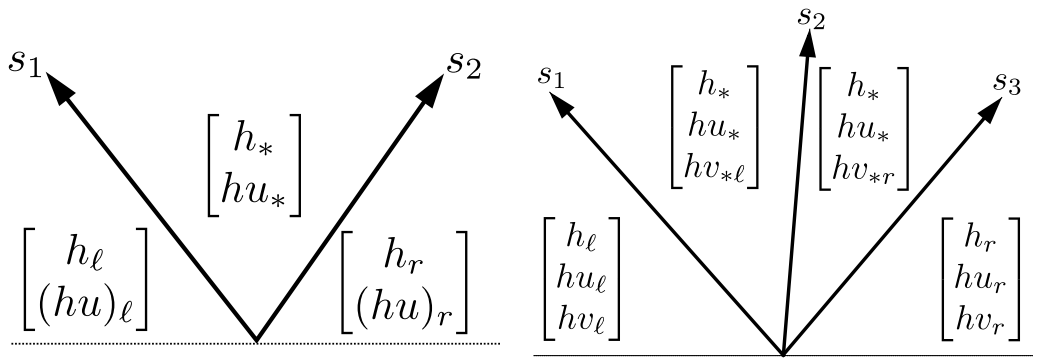

(a) One dimensional case (b) Two dimensional case

Figure 2.1: Representative diagrams of the $x - t$ plane with states in a Riemann problem. The arrows represent either shocks, rarefactions, or contact discontinuities in the two dimensional case.

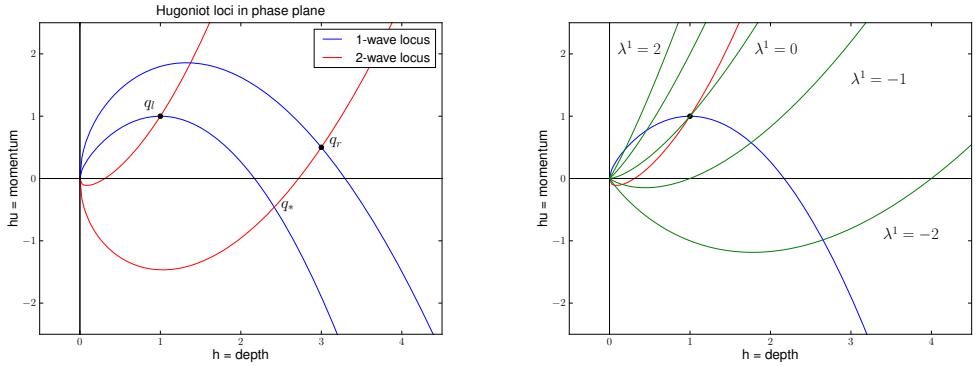

Figure 2.2: In the left figure the Hugoniot loci are shown through the states q_ℓ and q_r with possible middle state q_*. On the right are integral curves for the 1-wave family with one passing through the q_ℓ state representing which states could be connected over a rarefaction in the 1-wave family.

Rarefactions can be connected to any other state on the same integral curve. We can then use the Riemann invariants of the known state to find the correct integral curve and look for the correct state on that integral curve. For the shallow water equations, the Riemann invariants are

$$w^1(q) = u + 2\sqrt{gh} \qquad \text{and} \qquad w^2(q) = u - 2\sqrt{gh}$$

for the first and second characteristic families respectively. Figure 2.2 shows a set of integral curves for the 1-wave family with the state q_ℓ from earlier marked. The integral curve passing through this point denotes the states q_* which can connect to q_ℓ through a 1-wave rarefaction.

Finally, we must look for the intersections of the Hugoniot loci and integral curves for each wave and determine the possible connecting middle states. The non-uniqueness of this process is a representation of the task of picking out the physically relevant or entropy satisfying solution via either the Lax entropy condition (2.2.2) or the entropy function for the shallow water equations. In either case, we find that portions of our Hugoniot loci are not entropy satisfying or our integral curves would allow a multi-valued solution and only one valid intersection exists between the four different possibilities.

In the case of the two dimensional shallow water equations, there is an additional characteristic family that is linearly degenerate and will produce contact discontinuities. As these waves behave essentially linearly, it is important to note what quantity will jump across the discontinuity. In the case of the shallow water equations, the jump will be proportional to the corresponding eigenvector, which is either $[0, 0, 1]^T$

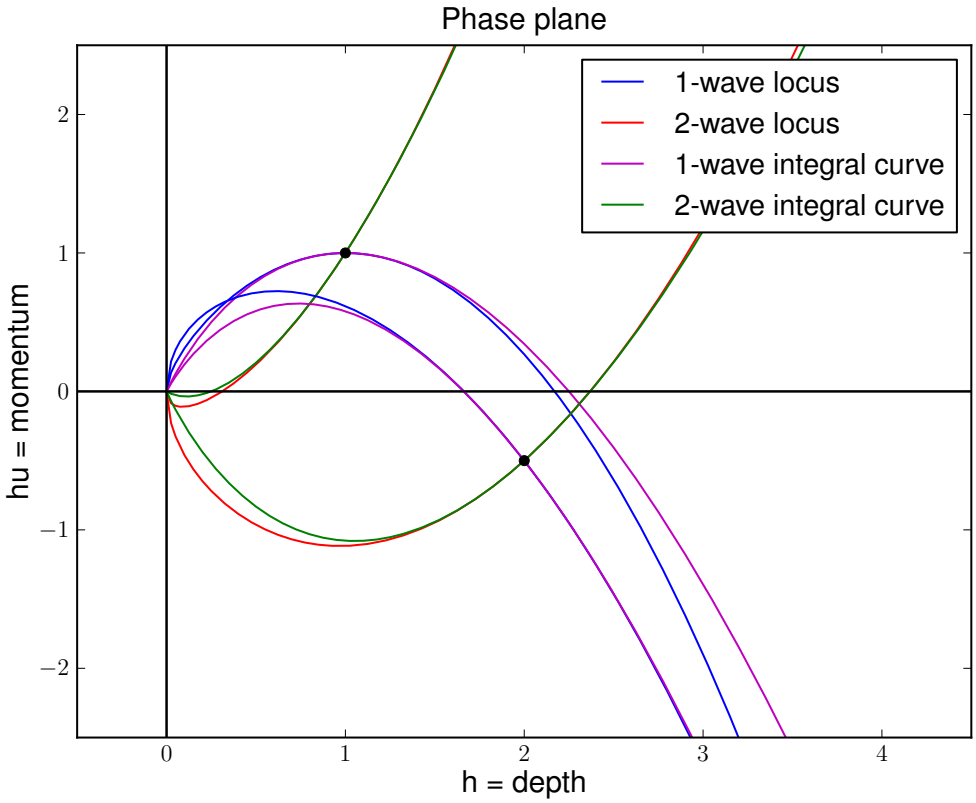

Figure 2.3: The full solution of the Riemann problem where two possible middle states have been marked with all integral curves and Hugoniot loci drawn. The final choice of middle state will be chosen by the entropy condition and single-valued requirement.

or $[0, 1, 0]^T$ depending on which dimension we are considering. Figure 2.1b contains an example Riemann solution for $f_1(q)$ containing a contact discontinuity and the other two genuinely nonlinear waves.

Bathymetry Source Term

An important aspect of the shallow water equations for real world applications is the inclusion of the bottom boundary source term as in

$$\begin{aligned} &h_t + (hu)_x = 0 \quad \text{and} \\ &(hu)_t + \left(hu^2 + \frac{1}{2} g h^2 \right)_x = -ghb_x. \end{aligned}$$

For the shallow water equations, this term can be handled in multiple ways but it is important to recognize that it contains a derivative of a function that is not one of the conserved quantities. Because of this, a lot of different approaches can be used to include the source term into the Riemann solution directly.

One such approach is to treat the function b as one of the conserved quantities (satisfying $b_t = 0$, when the bathymetry is stationary) where the equations now can only be written in a quasilinear form

$$q_t + \begin{bmatrix} 0 & 1 & 0 \\ gh - u^2 & 2u & gh \\ 0 & 0 & 0 \end{bmatrix} q_x = 0$$

where $q = [h, hu, b]^T$. Note that we have effectively added a third equation where $b_t = 0$. The Riemann solution of this new system has a stationary contact discontinuity representing the jump in b and possibly the depth h. For more discussion on how to handle this source term see for instance [24] and for a similar approach see section 3.5.2.

Chapter 3

FINITE VOLUME METHODS

This chapter introduces the basics of a class of methods for hyperbolic conservation laws known as finite volume methods. These methods center around an approach that discretizes space into finite-sized cells and evolves the average value of the quantities of interest in time. This is in contrast to finite difference approximations which take a point-wise approach to approximating the unknown quantities in space and time. In this chapter the mathematical framework underlying finite volume methods will be introduced and extensions to more general algorithms and applications will be explored.

3.1 Derivation of a Flux-Differencing Scheme

The central idea of a finite volume scheme is the partitioning of the domain $\Omega \in \mathbb{R}^n$ into grid cells $\mathcal{C}$ and evolving the average value of $q(x,t)$ in each grid cell. In one dimension[1], grid cells are intervals of the real line such that $\mathcal{C}_i = [x_{i-1/2}, x_{i+1/2}]$ and are each of length $\Delta x_i = x_{i+1/2} - x_{i-1/2}$. The centers of each grid cell are defined as $x_i = x_0 + i\Delta x_i$ and therefore the grid cell boundaries as $x_{i\pm1/2} = x_i \pm 1/2\Delta x_i$. We can then integrate the function $q(x,t)$ over each grid cell $\mathcal{C}_i$ to find the average value of $q(x,t)$ defined as

$$Q_i^n \equiv \frac{1}{\Delta x_i} \int_{\mathcal{C}_i} q(x, t^n) dx. \tag{3.1}$$

Often it is advantageous to map the physical grid with varying grid cell size to a computational grid with a uniform distribution of grid cells through a mapping function. For the rest of this discussion we will have assumed that we are working on a uniform grid or that we have already used a suitable mapping function and are working on the computational grid.

Turning now to the time evolution of the cell averages, we look back at the homogeneous conservation law (2.16) we considered earlier. Integrating in space over a

[1]We only consider one dimension here for clarity and address multiple dimensions in section 3.6.

grid cell and using the fundamental theorem of calculus leads to

$$\int_{\mathcal{C}_i} q(x,t)_t dx + \int_{\mathcal{C}_i} f(q(x,t))_x dx = 0 \Rightarrow \tag{3.2}$$

$$\int_{\mathcal{C}_i} q(x,t)_t dx + f(q(x_{i+1/2},t)) - f(q(x_{i-1/2},t)) = 0. \tag{3.3}$$

Moving the flux terms to the right hand side of the equation, moving the time derivative on q outside the integral, integrating in time from t^n to t^{n+1} and multiplying by $1/\Delta x$ allows us to write the equations as

$$\frac{1}{\Delta x}\int_{\mathcal{C}_i} q(x,t^{n+1})dx - \frac{1}{\Delta x}\int_{\mathcal{C}_i} q(x,t^n)dx = -\frac{1}{\Delta x}\int_{t^n}^{t^{n+1}} \left[f(q(x_{i+1/2},t)) - f(q(x_{i-1/2},t))\right] dt. \tag{3.4}$$

Replacing the averages of q over the grid cell $\mathcal{C}_i$ we can then write

$$Q_i^{n+1} = Q_i^n - \frac{1}{\Delta x}\int_{t^n}^{t^{n+1}} \left[f(q(x_{i+1/2},t)) - f(q(x_{i-1/2},t))\right] dt. \tag{3.5}$$

Now defining

$$F^n_{i\pm 1/2} \equiv \frac{1}{\Delta t}\int_{t^n}^{t^{n+1}} f(q(x_{i\pm 1/2},t))dt \tag{3.6}$$

we can write the original conservation law as an explicit *flux-differencing scheme*

$$Q_i^{n+1} = Q_i^n - \frac{\Delta t}{\Delta x}[F^n_{i+1/2} - F^n_{i-1/2}]. \tag{3.7}$$

Since we have not made any approximations so far when deriving (3.7), the update to Q_i^{n+1} is exact. It is only when we use numerical approximations to $F^n_{i\pm 1/2}$ that a numerical error may become important. The crux of a finite volume scheme then is the determination of the approximate evaluation of $F^n_{i\pm 1/2}$ such that a convergent scheme is obtained. It is also important to note that in this form, if the grid cell $\mathcal{C}_i$ and $\mathcal{C}_{i+1}$ use the same approximation to $F^n_{i+1/2}$, conservation is maintained modulo the boundaries of the domain.

3.2 Godunov-Type Methods

One way to approximate the flux integral $F^n_{i\pm 1/2}$ was introduced by Godunov [27]. It is a first-order upwind-type scheme that uses Riemann solutions as the primary building block of the numerical scheme. The algorithm is often referred to as an *REA algorithm* due to the three primary steps involved:

1. **Reconstruction** - The reconstruction step's goal is to reconstruct a piece-wise

defined function $\tilde{q}^n(x,t^n)$ in each grid cell based on the current grid cell average Q_i^n. In the case of Godunov's method, these are piece-wise constant functions based on the cell averages such that

$$\tilde{q}^n(x,t^n) = Q_i^n \qquad \text{for all } x \in \mathcal{C}_i. \tag{3.8}$$

For higher order schemes one can imagine reconstructing higher order polynomials to approximate the true solution inside of the grid cell. In fact, in section 3.3, we will construct higher order approximations this way.

2. **Evolution** - The evolution step requires the update of the reconstructed function $\tilde{q}^n(x,t^n)$ to the next time $\tilde{q}^n(x,t^{n+1})$ at time Δt in the future. This construction naturally leads to a Riemann problem defined by the difference at each grid cell interface $x_{i+1/2}$ between subsequent reconstruction in each grid cell. This also leads to an ideal restriction on the size of time step to limit the interaction of the waves coming from each Riemann problem solution.

3. **Averaging** - The averaging step takes the evolved solution $\tilde{q}^{n+1}(x,t^{n+1})$ and averages the new solution back into cell averages as in

$$Q_i^{n+1} = \frac{1}{\Delta x}\int_{\mathcal{C}_i} \tilde{q}^n(x,t^{n+1})dx. \tag{3.9}$$

The effective numerical flux function $F^n_{i\pm1/2}$ for Godunov's method is found by replacing the exact function $q(x,t)$ in the definition for $F^n_{i\pm1/2}$ (3.6) with the piece-wise constant evolved function $\tilde{q}^n(x,t^{n+1})$. Since this function is constant over the time step Δt, we can easily integrate along the edge of the cell boundary. Denoting the value along the grid cell edge in time as $q'(Q_i^n, Q_{i-1}^n)$ we can write

$$F^n_{i-1/2} = \frac{1}{\Delta t}\int_{t^n}^{t^{n+1}} f(q'(Q_i^n, Q_{i-1}^n))dt = f(q'(Q_i^n, Q_{i-1}^n)). \tag{3.10}$$

3.2.1 Wave-Propagation Form of Godunov's Method

We can also extend Godunov's method to the wave-propagation forms introduced in section 2.2.1. If we again consider projecting the jump in q at each grid cell and project this jump onto the eigenspace of the hyperbolic equations

$$Q_i - Q_{i-1} = \sum_{p=1}^{m} \alpha^p_{i-1/2} r^p \equiv \sum_{p=1}^{m} \mathcal{W}_{i-1/2}, \tag{3.11}$$

we can form the solution to the Riemann problem in terms of waves. The final task is to average the effect of each wave on the grid cell into which they have traveled. Take for instance the situation in figure 3.1 where there are three waves in the Riemann solution. The fraction of the grid cell length that the waves have traveled through in time Δt is $s^p_{i-1/2}\Delta t/\Delta x$ for the $i-1/2$th grid cell boundary. The effect that the pth wave $\mathcal{W}^p_{i-1/2}$ will have on the ith grid cell is then

$$-\frac{s^p_{i-1/2}\Delta t}{\Delta x}\mathcal{W}^p_{i-1/2}. \tag{3.12}$$

This assumes that $s^p_{i-1/2} > 0$, otherwise the wave would be entering the C_{i-1} grid cell and it should be averaged there. We can then add up all the effects of the waves to produce an update to the average in the ith cell as

$$Q^{n+1}_i = Q^n_i - \frac{\Delta t}{\Delta x}\left[\sum_{p=1}^{m}(s^p_{i-1/2})^+\mathcal{W}^p_{i-1/2} - \sum_{p=1}^{m}(s^p_{i+1/2})^-\mathcal{W}^p_{i+1/2}\right] \tag{3.13}$$

where the $(s^p)^+ \equiv \max(0, s^p)$ and $(s^p)^- \equiv \min(0, s^p)$. Following the notation in [32] we can write the total fluctuations entering the ith grid cell from the right as $\mathcal{A}^+\Delta Q_{i-1/2}$ and from the left as $\mathcal{A}^-\Delta Q_{i+1/2}$ which allows us to write the update in the ith grid cell as simply

$$Q^{n+1}_i = Q^n_i - \frac{\Delta t}{\Delta x}\left[\mathcal{A}^+\Delta Q_{i-1/2} + \mathcal{A}^-\Delta Q_{i+1/2}\right]. \tag{3.14}$$

3.3 High-Resolution Methods

Hyperbolic PDE solutions, as we have seen, can exhibit both solutions that have smooth regions (such as through rarefactions) and shocks. Godunov's method was constructed with the purpose of handling discontinuous solutions to hyperbolic PDEs, but in the case of linear constant-coefficient problems is only first-order accurate. The Lax-Wendroff method is a second-order accurate method derived via a Taylor-series approximation to terms up to second-order, but can be numerically dispersive near steep gradients and discontinuities. We would like to construct a hybrid of both Godunov's method and the Lax-Wendroff method that will be sensitive to the solution's local behavior and apply the correction terms from Lax-Wendroff only in smooth regions of the solution and use Godunov's method near steep gradients in the solution. Methods that exhibit this type of behavior are commonly known as *high-resolution methods*.

In general, high-resolution methods can be formulated as corrections to the stan-

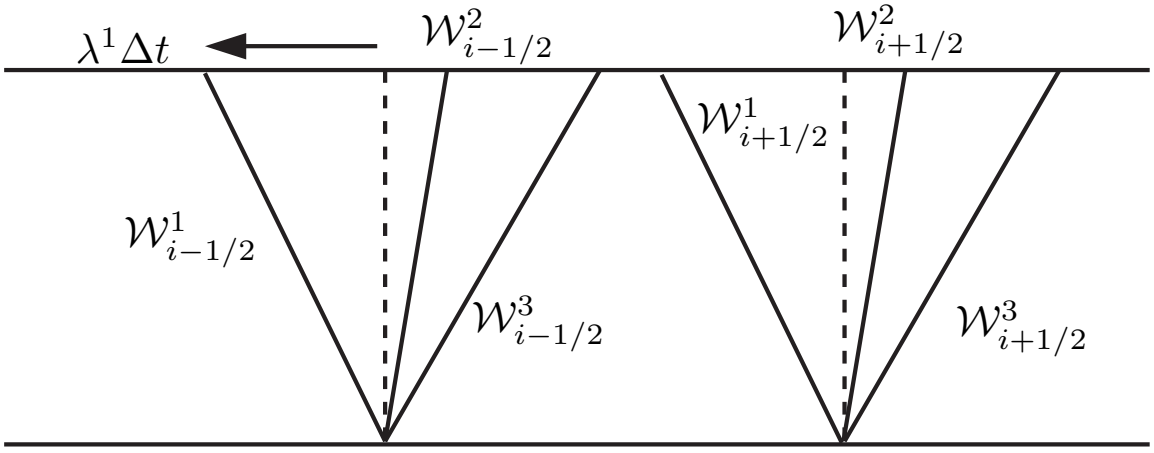

Figure 3.1: Diagram of the resulting waves from the boundaries of the ith grid cell. In this case, the Riemann problem resulted in three wave families with speeds denoted by λ^p. The waves that will be averaged in the the ith grid cell here would be $\mathcal{W}^2_{i-1/2}$, $\mathcal{W}^3_{i-1/2}$, and $\mathcal{W}^1_{i+1/2}$.

dard flux-differencing scheme (3.7)

$$Q_i^{n+1} = Q_i^n - \frac{\Delta t}{\Delta x}\left[\mathcal{A}^+ \Delta Q_{i-1/2} + \mathcal{A}^- \Delta Q_{i+1/2}\right] + \frac{\Delta t}{\Delta x}\left[\tilde{F}_{i+1/2} - \tilde{F}_{i-1/2}\right] \tag{3.15}$$

where $\tilde{F}_{i\pm 1/2}$ are limited second-order *correction fluxes* defined as

$$\tilde{F}_{i-1/2} = \frac{1}{2}\sum_{p=1}^{m} \left|s^p_{i-1/2}\right| \left(1 - \frac{\Delta t}{\Delta x}\left|s^p_{i-1/2}\right|\right) \tilde{\mathcal{W}}^p_{i-1/2}$$

where $\tilde{\mathcal{W}}^p_{i-1/2} = \mathcal{W}^p_{i-1/2}\phi(\theta^p_{i-1/2})$, a limited version of the original wave $\mathcal{W}^p_{i-1/2}$. Since we already calculate $\mathcal{W}^p_{i-1/2}$ and $s^p_{i-1/2}$ in the Riemann problem, the corrections can be applied without any additional work besides the calculation of the limited waves. In order to calculate the limited wave, a limiter function must be applied to two quantities. We then only need to prescribe the *limiter* $\phi(\theta^p_{i-1/2})$ to complete the high-resolution scheme.

3.3.1 Limiters

The purpose of a limiter in a high-resolution scheme is to provide a means to switch on the correction terms that give second order accuracy if applied in a smooth region of the solution and to switch the correction terms off when in a region where the solution

contains a steep gradient or a discontinuity. A limiter does this by comparing the local variations in the solution, such as the ratio of the jumps in Q_i^n. For scalar hyperbolic problems, defining I such that it represents the interface on the upwind side of $x_{i-1/2}$

$$I = \begin{cases} i-1 & \text{if } \ s_{i-1/2} > 0, \quad \text{or} \\ i+1 & \text{if } \ s_{i-1/2} < 0 \end{cases} \tag{3.16}$$

we can define a measure of the smoothness of the local solution with

$$\theta_{i-1/2}^n = \frac{\Delta Q_{I-1/2}^n}{\Delta Q_{i-1/2}^n}. \tag{3.17}$$

With this definition, if $\theta_{i-1/2}^n \approx 1$, the solution is relatively smooth (except at extrema) and if $\theta_{i-1/2}^n \approx 0$ that the solution contains a steep gradient or discontinuity. Therefore, if we would like to switch on the high-order correction terms in smooth parts of the solution, our limiter function $\phi(\theta)$ should work as

$$\phi(\theta) = \begin{cases} 1 & \text{if } \theta \approx 1 \quad \text{and} \\ 0 & \text{if } \theta \approx 0. \end{cases} \tag{3.18}$$

Another approach to understanding the role of limiters in a high-resolution method is to consider the main failing of the Lax-Wendroff method, production of oscillatory solutions. One way to measure oscillations in a method is to define the *total variation* of a grid functions as

$$\text{TV}(Q) = \sum_{i=-\infty}^{\infty} |Q_i - Q_{i-1}|$$

and require that for subsequent time steps the method should require

$$\text{TV}(Q^{n+1}) < \text{TV}(Q^n),$$

also known as the *total variation diminishing* (TVD) property. A consequence of this is a theorem due to Harten that provides conditions on limiters for the resulting method to be TVD,

Theorem 3.3.1. *Consider a general method of the form*

$$Q_i^{n+1} = Q_i^n - C_{i-1}^n (Q_i^n - Q_{i-1}^n) + D_i^n (Q_{i+1}^n - Q_i^n)$$

over one time step, where the coefficients C_{i-1}^n and D_i^n are arbitrary values (which may depend on Q_i^n leading to a nonlinear limiter). Then

$$TV(Q^{n+1}) \leq TV(Q^n)$$

provided the following conditions are met:

$$C_{i-1}^n \geq 0 \quad \forall i, \qquad D_i^n \geq 0 \quad \forall i, \qquad \textit{and} \qquad C_i^n + D_i^n \leq 1 \quad \forall i.$$

Applying this theorem to the flux-limiter method introduced in (3.15) to the advection problem $q_t + uq_x = 0$ the Harten TVD theorem reduces to the condition

$$0 \leq \phi(\theta) \leq \text{minmod}(2, 2\theta)$$

where the minmod limiter is defined as

$$\text{minmod}(a,b) = \begin{cases} a & \text{if } |a| < |b| \quad \text{and } ab > 0, \\ b & \text{if } |a| > |b| \quad \text{and } ab > 0, \quad \text{and .} \\ 0 & \text{if } ab \leq 0. \end{cases} \tag{3.19}$$

From here multiple limiters can be derived that obey this condition and some are summarized in table 3.1.

Limiter Method		$\phi(\theta)$
Linear	upwind	0
	Lax-Wendroff	1
	Beam-Warming	θ
	Fromm	$\frac{1}{2}(1+\theta)$
Nonlinear	minmod	$\text{minmod}(1,\theta)$
	superbee	$\max(0, \min(1, 2\theta), \min(2, \theta))$
	MC	$\max(0, \min(1/2(1+\theta)), 2, 2\theta)$
	van Leer	$\frac{\theta+\lvert\theta\rvert}{1+\lvert\theta\rvert}$

Table 3.1: List of some common limiters. The minmod function is defined by equation (3.19).

Since we would like to solve nonlinear systems of hyperbolic equations, we must define a suitable measure beyond the one given in (3.17). One suitable choice involves comparing the length of the projection of the upwind wave in the appropriate family $\mathcal{W}_{I-1/2}^p$ onto the wave being limited $\mathcal{W}_{i-1/2}^p$ to the length of that same wave,

$$\theta_{i-1/2}^p = \frac{\mathcal{W}_{I-1/2}^p \cdot \mathcal{W}_{i-1/2}^p}{|\mathcal{W}_{i-1/2}^p|^2} \tag{3.20}$$

where we can redefine the upwind index as

$$I = \begin{cases} i-1 & \text{if } s^p_{i-1/2} > 0, \quad \text{or} \\ i+1 & \text{if } s^p_{i-1/2} < 0. \end{cases} \tag{3.21}$$

3.4 Approximate Riemann Solvers

In general, finding the full solution to a Riemann problem can be quite expensive. This is particularly true for nonlinear problems where a set of nonlinear equations needs to be solved to find the correct entropy satisfying waves connecting the different states. We would like to develop fast approximate Riemann solvers that still maintain many of the properties that the true solution to the Riemann problem would have provided.

One straight forward way to build an approximate Riemann solver is to define a locally defined, linearized version of the nonlinear equation,

$$\hat{q}_t + \hat{A}_{i-1/2}\hat{q}_x = 0, \tag{3.22}$$

where $\hat{A}_{i-1/2}$ and $\hat{q}$ are locally valid approximations to $f'(q)$ and q respectively. In order for this approximation to be useful, we need to require that $\hat{A}_{i-1/2}$ is diagonalizable with real eigenvalues and that the resulting approximation is consistent with the original problem in the following sense

$$\hat{A}_{i-1/2} \to f'(\overline{q}) \qquad \text{as } Q_i, Q_{i-1} \to \overline{q}. \tag{3.23}$$

By calculating the eigenvectors $\hat{r}^p_{i-1/2}$ and eigenspeeds $\hat{\lambda}^p_{i-1/2}$ of the matrix $\hat{A}_{i-1/2}$ we can construct a wave-propagation method with

$$Q_i - Q_{i-1} = \sum_{p=1}^{m} \hat{\alpha}^p_{i-1/2}\hat{r}^p_{i-1/2} = \sum_{p=1}^{m} \mathcal{W}^p_{i-1/2} \tag{3.24}$$

and proceed as we would for a linear problem.

A simple way to define the matrix $\hat{A}_{i-1/2}$ is to evaluate the flux Jacobian at an average $\hat{Q}_{i-1/2}$ that is determined by local grid cell averages Q_i and Q_{i-1}. Another obvious way to linearize is to let

$$\hat{A}_{i-1/2} = \frac{1}{2}[f'(Q_i) + f'(Q_{i-1})]. \tag{3.25}$$

Note that these averages do not guarantee any of the properties that we have required of $\hat{A}_{i-1/2}$. In particular, if we would also like the resulting numerical scheme to

continue to preserve conservation, we also must require that

$$f(Q_i) - f(Q_{i-1}) = \sum_{p=1}^{m} \hat{\lambda}^p_{i-1/2} \mathcal{W}^p_{i-1/2}. \tag{3.26}$$

3.4.1 Failure of Linearized Solvers

Linearized Riemann solvers are often very successful in representing the nonlinear Riemann problem with much less effort, however there are times when they can fail and it is important to realize when this may occur. The linearized solvers essentially assume that all of the waves in the Riemann solution are discontinuities and that the jumps across these waves are proportional to the approximate eigenvectors $\hat{r}^p_{i-1/2}$. This view is nearly correct if the jump $||Q_i - Q_{i-1}|| = \mathcal{O}(\Delta x)$, since the flux Jacobian matrix is nearly constant, $f'(Q_i) \approx f'(Q_{i-1})$. This happens in relatively smooth sections of the solution.

Near discontinuities in the solution we do not expect that $||Q_i - Q_{i-1}||$ will be small and from section 2.2.2 we know that for a genuinely nonlinear characteristic family that $\lambda^p(Q_i) \neq \lambda^p(Q_{i-1})$. This can lead to unphysical solutions such as negative depth or densities in many common linearized solvers.

The other failure that can occur in linearized Riemann solvers involves the assumption of the basic structure of the solution. As was mentioned in section 2.2.2, a physical solution to the weak form of the hyperbolic equations must obey an entropy condition. If the structure of the Riemann solution is always assumed to be comprised of discontinuities, violation of entropy conditions can happen. In general this is only a problem when the true solution contains a *transonic rarefaction* in which $f'(Q_{i-1}) < 0 < f'(Q_i)$. For some solvers, it can easily be checked if a transonic rarefaction exists in the solution and appropriate steps to can be taken to avoid generating an entropy violating solution.

3.4.2 Examples of Approximate Riemann Solvers

Roe Linearization

The Roe linearization adds additional requirements to the matrix $\hat{A}_{i-1/2}$ based on the observation that even where $||Q_i - Q_{i-1}|| \neq \mathcal{O}(\Delta x)$, this is usually only the case in one of the wave families. We can then require that if Q_i and Q_{i-1} are connected by a single wave $\mathcal{W}^p = Q_i - Q_{i-1}$ in the true Riemann solution, then $\mathcal{W}^p$ should also be an eigenvector of $\hat{A}_{i-1/2}$. This condition comes down to requiring that the linearization satisfies

$$\hat{A}_{i-1/2}(Q_i - Q_{i-1}) = f(Q_i) - f(Q_{i-1}), \tag{3.27}$$

which is identical to the condition for conservation (3.26). The goal of the linearization is then to find a path through phase space such that (3.27) holds.

In 1981, Roe found a method to construct a path through state space such that (3.27) holds for the Euler equations effectively calculating the correct averaging functions $\hat{Q}_{i-1/2}$ [40]. This can also be done for the shallow water equations whose Roe averages are

$$\overline{h} = \frac{1}{2}(h_i + h_{i-1}) \tag{3.28}$$

$$\hat{u} = \frac{\sqrt{h_i}u_i + \sqrt{h_{i-1}}u_{i-1}}{\sqrt{h_i} + \sqrt{h_{i-1}}} \tag{3.29}$$

resulting in the linearized matrix

$$\hat{A}_{i-1/2} = \begin{bmatrix} 0 & 1 \\ -\hat{u}^2 + g\overline{h} & 2\hat{u} \end{bmatrix}. \tag{3.30}$$

HLLE Solvers

Another approach to finding an approximate Riemann solver that does not use a linearization approach was introduced by Harten, Lax, and van Leer [28] and extended by Einfeldt [21]. The solver uses only two waves to represent the Riemann solution regardless of the true number of waves. This assumption implies that there is one unknown state $\hat{Q}_{i-1/2}$ connecting Q_i and Q_{i-1} and adding to this the assumption that these states are connected via discontinuities implies

$$\mathcal{W}^1_{i-1/2} = \hat{Q}_{i-1/2} - Q_{i-1} \qquad \text{and} \qquad \mathcal{W}^2_{i-1/2} = Q_i - \hat{Q}_{i-1/2}. \tag{3.31}$$

If we also require that the approximate solution be conservative, which by (3.26) requires

$$s^1_{i-1/2}(\hat{Q}_{i-1/2} - Q_{i-1}) + s^2_{i-1/2}(Q_i - \hat{Q}_{i-1/2}) = f(Q_i) - f(Q_{i-1}), \tag{3.32}$$

we can solve for the middle state $\hat{Q}_{i-1/2}$ as

$$\hat{Q}_{i-1/2} = \frac{f(Q_i) - f(Q_{i-1}) - s^2_{i-1/2}Q_i + s^1_{i-1/2}Q_{i-1}}{s^1_{i-1/2} - s^2_{i-1/2}}. \tag{3.33}$$

The final specification is of the wave speeds $s^p_{i-1/2}$ which in can be taken to be

$$s^1_{i-1/2} = \min_p(\min(\lambda^p_i, \hat{\lambda}^p_{i-1/2})) \qquad \text{and} \tag{3.34}$$

$$s^2_{i-1/2} = \max_p(\max(\lambda^p_{i+1}, \hat{\lambda}^p_{i-1/2})), \tag{3.35}$$

where $\hat{\lambda}^p_{i-1/2}$ are the eigenvalues associated with the Roe averaging approximation. This particular set of speeds picks out the leading edge of any rarefaction wave and reduces to the Roe approximation of the shock speeds if the wave is a shock.

3.4.3 F-Wave Propagation Methods

There is an alternative way to specify an approximate Riemann solver that utilizes a different type of wave-propagation. Instead of the jumps in q being split into waves, we split the jump in $f(q)$ into *f-waves* via

$$f(Q_i) - f(Q_{i-1}) = \sum_{p=1}^{m} \mathcal{Z}^p_{i-1/2}$$

which move at the same speeds $s^p_{i-1/2}$. In section 3.5 the advantages of this approach will be discussed in the context of handling source terms. There are also a number of other advantages to using f-waves, including relaxation solvers [33]. Here we will concentrate on their usefulness in creating approximate Riemann solvers and how they change the wave-propagation methods we have already developed.

If we use a linearized Riemann solver, we can project $f(Q_i) - f(Q_{i-1})$ onto the eigenspace of $\hat{A}_{i-1/2}$ such that

$$f(Q_i) - f(Q_{i-1}) = \sum_{p=1}^{m} \beta^p_{i-1/2} \hat{r}^p_{i-1/2} \tag{3.36}$$

therefore identifying the f-waves as

$$\mathcal{Z}^p_{i-1/2} \equiv \beta^p_{i-1/2} \hat{r}^p_{i-1/2}. \tag{3.37}$$

We can also identify the relationship between $\mathcal{W}^p_{i-1/2}$ and $\mathcal{Z}^p_{i-1/2}$ in the linear case or under special conditions where $s^p_{i-1/2} \neq 0$, as

$$\mathcal{W}^p_{i-1/2} = \frac{\mathcal{Z}^p_{i-1/2}}{s^p_{i-1/2}}. \tag{3.38}$$

Using this splitting approach guarantees that we will arrive at a conservative scheme as the condition (3.26) is satisfied regardless of the average state $\hat{Q}_{i-1/2}$ that is used.

Wave-propagation methods can also be written in terms of f-waves by equating

$$\mathcal{A}^- \Delta Q_{i-1/2} = \sum_{p: s^p_{i-1/2} < 0} \mathcal{Z}^p_{i-1/2} \qquad \text{and} \qquad \mathcal{A}^+ \Delta Q_{i-1/2} = \sum_{p: s^p_{i-1/2} > 0} \mathcal{Z}^p_{i-1/2}.$$

Furthermore, second order corrections can be written in terms of f-waves where now

the correction flux is

$$\tilde{F}_{i-1/2} = \frac{1}{2}\sum_{p=1}^{m} \text{sign}(s^p_{i-1/2}) \left(1 - \frac{\Delta t}{\Delta x}|s^p_{i-1/2}|\right) \mathcal{Z}^p_{i-1/2}.$$

3.5 Handling Source Terms

The methods that have been discussed so far treat homogeneous conservation laws only. In order to extend them to more general inhomogenous conservation laws approaches have been developed that allow the application of the methods already presented along side methods for solving the inhomogenous forcing terms. We will discuss the most common method for solving source terms and which we will use later for storm surge source terms, and a method which incorporates the source terms directly into the Riemann solver which has advantages when the source terms and flux may be nearly in balance.

3.5.1 Fractional Step Methods

Fractional step methods utilize a splitting of the solution operators in order to update the solution in two separate steps. In the case of inhomogenous conservation laws this splitting entails separately solving

$$q_t + f(q)_x = 0$$

and

$$q_t = \psi(q).$$

and applying the updates to the solution q in alternating steps. The order of these steps determines the accuracy of the splitting method and is based on the commutator of the solution operators being applied. In practice the first order method, known as Godunov splitting, is sufficient. The main difficulty with these methods is the prescription of mid-step boundary conditions. For a discussion of these issues and their derivation please refer to [32].

The popularity of this approach is due to the ease at which they can be applied and their relative success in many cases. The error due to the splitting approach is often smaller than what is predicted and can be advantageous for equations that have terms that are different in character and therefore require different solution methods.

In the case of the bathymetry source term in the shallow water equations introduced in section 2.4, fractional step approaches generally do not work since the update due to the bathymetry source term nearly negates the update from the homogeneous conservation law. The splitting error in this case can cause spurious waves to form near bathymetry jumps and can quickly dominate the solution in practical problems.

An alternative approach that incorporates the update from the bathymetry directly into the solver for homogenous conservation law is advantageous and is discussed in section 3.5.2.

3.5.2 F-Wave Methods and Source Terms

F-wave methods were introduced in section 3.4.3 as an alternative to wave-propagation methods that split the jump in the flux rather than the jump in the conserved quantities. This approach has an added advantage that we can incorporate source terms directly into the Riemann solver by including the source term into the projection onto the eigenspace by extending (3.36) to

$$f(Q_i) - f(Q_{i-1}) - \Delta x \Psi_{i-1/2} = \sum_{p=1}^{m} \beta_{i-1/2}^p \hat{r}_{i-1/2}^p$$

where

$$\Delta x \Psi_{i-1/2} \approx \int \psi(q, x) dx. \tag{3.39}$$

In the case of the shallow water equations with a bathymetry source term, the projection becomes

$$\begin{bmatrix} [hu] \\ [hu^2 + g/2h^2] - g\overline{h}[b] \end{bmatrix} = \sum_{p=1}^{m} \beta_{i-1/2}^p \hat{r}_{i-1/2}^p$$

where the form of Ψ is motivated by path-conservative jump conditions. This causes the flux and the source term to cancel one another out directly rather than through a source term splitting method. In general if a suitable approximation to (3.39) can be found, it is often advantageous to use this method over fractional step approaches for cases where the source term and fluxes are expected to be nearly in steady state, in other words cancel each other.

3.6 Multiple Dimensions

Wave propagation methods can be extended to multidimensional hyperbolic problems in one of two ways. The first involves a technique similar to fractional stepping that was introduced in section 3.5.1 but now for each dimension. The second involves solving an extra set of transverse Riemann problems representing the direction waves travel parallel (or transverse) to the cell interfaces. For clarity, we will only consider two dimensional hyperbolic equations of the form

$$q_t + f(q)_x + g(q)_y = 0 \tag{3.40}$$

but this can easily be extended to three and higher dimensions.

3.6.1 Dimensional Splitting

In dimensional splitting we use the same tactic as in section 3.5.1 where now we alternately solve

$$q_t + f(q)_x = 0$$

and

$$q_t + g(q)_y = 0.$$

This amounts to sweeping over a grid in alternating directions solving the Riemann problems at the grid cell interfaces in each direction. The accuracy of this approach follows what would be expected of a fractionally split approach in general. This is again a popular approach as a one dimensional method can easily be extended to more dimensions with this approach and in practice can be sufficient for many problems.

3.6.2 Un-Split Methods

The alternative to dimensional splitting is to solve the Riemann problem taking into account the multi-dimensional nature of the problem. In an un-split method, sweeps in each direction are still performed across the grid except that for each single Riemann problem that was solved in the dimensionally split approach, an additional transverse Riemann problem is solved. This is motivated by the corner-transport method which for advection in two dimensions allows an advected quantity moving at an angle to the grid to flow into a corner grid cell as in figure 3.2.

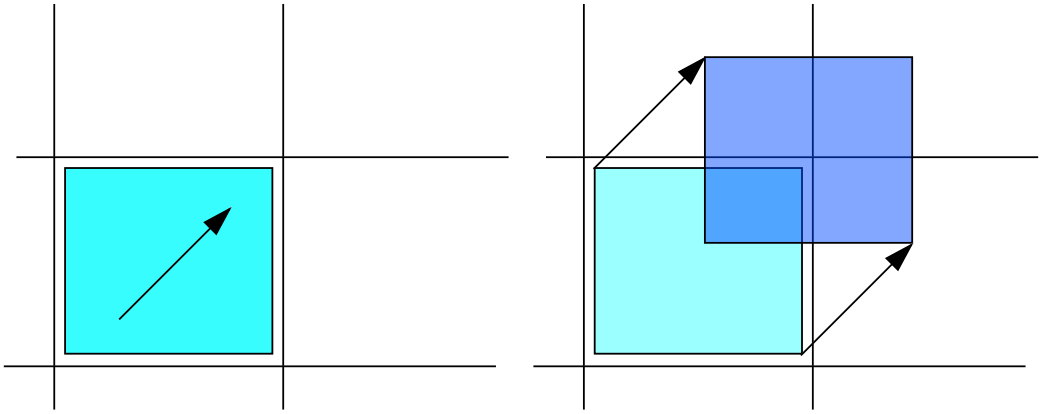

Figure 3.2: Example of an advection problem where the direction of flow is 45° to the grid. The corner transport method allows the quantity to correctly flow into the corner cell as well as the cell adjacent to the grid cell.

The method for a single grid cell proceeds as follows for a grid cell edge at $x_{i-1/2}$:

1. Solve a Riemann problem normal to the grid cell interface and find the fluctuations $\mathcal{A}^{\pm}\Delta Q$ (left figure in 3.3).

2. Solve a Riemann problem transverse to the normal direction breaking up the fluctuations $\mathcal{A}^{\pm}\Delta Q$ into components $\mathcal{B}^{\pm}\mathcal{A}^{\pm}\Delta Q$ (middle figure in 3.3).

3. Use the fluctuations found to update the appropriate cells. In particular, the grid cells directly bordering the grid cell interface under consideration are updated by $\mathcal{A}^{\pm}\Delta Q$ and then the grid cells in the transverse direction are updated by $\mathcal{B}^{\pm}\mathcal{A}^{\pm}\Delta Q$ along with a correction to the grid cells directly bordering the grid cell boundary (right figure in 3.3).

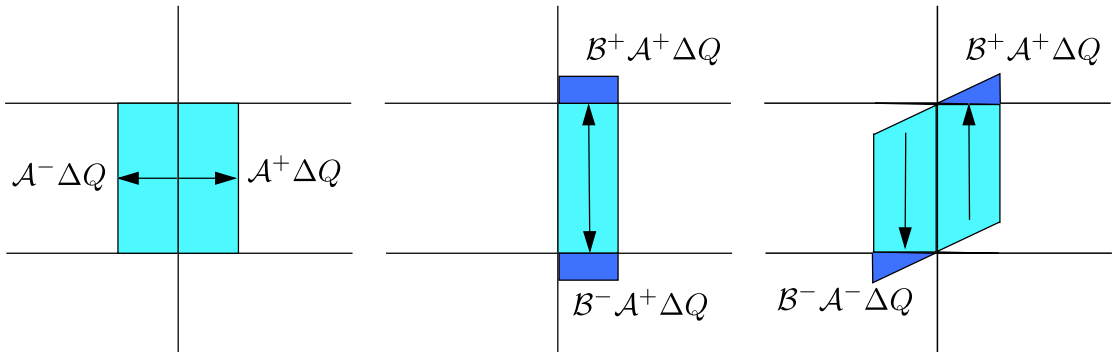

Figure 3.3: Diagram of the steps in an un-split method. First a normal Riemann problem is solved and the fluctuations $\mathcal{A}^{\pm}\Delta Q$ are found (left figure). Next a transverse solver finds the fluctuations that would be going transverse to the grid cell edge that is under consideration (middle figure). Last the fluctuations are used to effectively allow a wave to move at across multiple grid cells (right figure).

These methods in practice can be very successful and are dependent on formulating a transverse Riemann problem. These methods are also more expensive than the dimensionally split approach and for the same accuracy can be more efficient.

Chapter 4

SINGLE-LAYER DEPTH AVERAGED EQUATIONS

Many relevant flows in geophysical contexts cover a vast number of spatial and temporal scales that a direct numerical simulation cannot resolve with the computing technology we have available today. In order to address pertinent problems in geophysics we must rely on approximations that can reduce the complexity or dimensionality of the flows of interest. One of these techniques is averaging through the depth of the flow, thereby reducing the dimensionality of the overall flow. In this chapter we will study how depth averaged equations are obtained largely following [43] and describe one method of numerical solving the equations in geophysical contexts.

4.1 Derivation of Depth Averaged Models

We start our discussion with the construction of a depth averaged model using the three dimensional, inviscid Navier-Stokes equations,

$$\begin{cases} \rho_t + \nabla \cdot \underline{u}\rho = 0 \\ (\rho \underline{u})_t + \nabla \cdot (\rho \underline{u} u) = -\nabla P + \nabla \cdot \underline{\underline{\tau}} - \rho g \hat{z} \end{cases} \tag{4.1}$$

where $\underline{u} \equiv (u, v, w)$ are the velocities in the x, y, and z direction respectively, P is the pressure, g is the acceleration due to gravity, and $\underline{\underline{\tau}}$ is the stress tensor. The boundary conditions we will consider are

$$\begin{aligned}
&w = \eta_t + u\eta_x + v\eta_y \quad \text{and} \quad P = P_A(x,y,t) && \text{at} \quad z = \eta, \\
&\tau_{sx} = -\tau_{xx}\eta_x - \tau_{xy}\eta_y + \tau_{xz} && \text{at} \quad z = \eta, \\
&\tau_{sy} = -\tau_{yx}\eta_x - \tau_{yy}\eta_y + \tau_{yz} && \text{at} \quad z = \eta, \\
&\tau_{bx} = \tau_{xx}b_x + \tau_{xy}b_y - \tau_{xz} && \text{at} \quad z = \eta, \\
&\tau_{by} = \tau_{xy}b_x + \tau_{yy}b_y - \tau_{yz} && \text{at} \quad z = \eta, \\
&w = ub_x + vb_y && \text{at} \quad z = b
\end{aligned}$$

representing a wide range of permissible geophysical flows with a top free surface η subject to stresses τ_{s*} and an impermeable bottom boundary whose elevation is determined from a given function $b(x, y, t)$ and subject to stresses τ_{b*}. In addition to the stresses at the top surface, we also will assume that an atmospheric pressure at the top surface $P_A(x, y, t)$ is also given. If we make also make the simplifying assumption

that ρ is constant the advection of density in (4.1) simplifies to

$$\nabla \cdot \underline{u} = 0. \tag{4.2}$$

This also allows us rewrite the momentum conservation equations as

$$\underline{u}_t + \nabla \cdot (\underline{u}u) = \frac{1}{\rho}\left[-\nabla P + \nabla \cdot \underline{\underline{\tau}}\right] - g\hat{z}.$$

In this section we will make various assumptions about the pressure field and variations of the fluid velocities through the depth which are not necessarily accurate but lead to the shallow water equations. For a more complete discussion and derivation where these issues are further developed, see appendix A.

4.1.1 Integration

Integrating the continuity equation through the depth leads to

$$\begin{aligned}\int_b^\eta (u_x + v_y + w_z)dz &= \frac{\partial}{\partial x}\int_b^\eta u dz + \frac{\partial}{\partial y}\int_b^\eta v dz + (w - u\eta_x - v\eta_y)|_{z=\eta} \\ &\qquad - (w - ub_x - vb_y)|_{z=b} \\ &= (h\overline{u})_x + (h\overline{v})_y + \eta_t \Rightarrow \\ &= h_t + (h\overline{u})_x + (h\overline{v})_y.\end{aligned}$$

where we have defined

$$\overline{f} \equiv \frac{1}{h}\int_b^\eta f dz$$

representing the average of the quantity f through the depth. For the momentum equations, the advective terms in the x-direction are

$$\begin{aligned}\int_b^\eta [u_t + (u^2)_x + (uv)_y + (uw)_z]dz = \\ \frac{\partial}{\partial t}\int_b^\eta u dz + \frac{\partial}{\partial x}\int_b^\eta u^2 dz + \frac{\partial}{\partial y}\int_b^\eta uv dz \\ + \left[u(w - u\eta_x - v\eta_y - \eta_t)\right]_{z=\eta} - \left[u(w - ub_x - vb_y)\right]_{z=b} \\ = (h\overline{u})_t + (h\overline{u^2})_x + (h\overline{uv})_y,\end{aligned}$$

for the y-direction

$$\begin{aligned}\int_b^\eta [v_t + (uv)_x + (v^2)_y + (vw)_z]dz \\ &= \frac{\partial}{\partial t}\int_b^\eta v dz + \frac{\partial}{\partial x}\int_b^\eta uv dz + \frac{\partial}{\partial y}\int_b^\eta v^2 dz \\ &\qquad + [v(w - u\eta_x - v\eta_y - \eta_t)]_{z=\eta} - [v(w - ub_x - vb_y)]_{z=b} \\ &= (h\overline{v})_t + (h\overline{uv})_x + (h\overline{v^2})_y.\end{aligned}$$

and finally for the z-momentum advective terms

$$\begin{aligned}\int_b^\eta [w_t + (uw)_x + (vw)_y + (w^2)_z]dz \\ &= \frac{\partial}{\partial t}\int_b^\eta w dz + \frac{\partial}{\partial x}\int_b^\eta uw dz + \frac{\partial}{\partial y}\int_b^\eta vw dz \\ &\qquad + [w(w - u\eta_x - v\eta_y - \eta_t)]_{z=\eta} - [w(w - ub_x - vb_y)]_{z=b} \\ &= (h\overline{w})_t + (h\overline{uw})_x + (h\overline{vw})_y.\end{aligned}$$

Turning to the right side of the momentum conservation equations,

$$\frac{1}{\rho}\left[-\nabla P + \nabla \cdot \underline{\underline{\tau}}\right].$$

let us first consider the pressure term P. Assume that P is of the form

$$P(x, y, z, t) = P_A(x, y, t) + \rho g(\eta - z) + p(x, y, z, t),$$

where again P_A is the pressure at the surface of the flow, the second term is due to the hydrostatic pressure, and p is the deviation from hydrostatic pressure. Inserting these into the gradient leads to

$$\nabla P = \begin{bmatrix}(P_A)_x + \rho g \eta_x \\ (P_A)_y + \rho g \eta_y \\ -\rho g\end{bmatrix} + \nabla p.$$

Integrating ∇P through the depth then gives

$$\int_b^\eta \nabla P dz = h\begin{bmatrix}(P_A)_x + \rho g \eta_x \\ (P_A)_y + \rho g \eta_y \\ -\rho g\end{bmatrix} + \int_b^\eta \nabla p dz.$$

The stress tensor $\underline{\underline{\tau}}$ can also be integrated in each direction where in the x-direction

we have

$$\int_b^\eta \left(\frac{\partial \tau_{xx}}{\partial x} + \frac{\partial \tau_{xy}}{\partial y} + \frac{\partial \tau_{xz}}{\partial z}\right) dz$$
$$= \frac{\partial}{\partial x}\int_b^\eta \tau_{xx} dz + \frac{\partial}{\partial y}\int_b^\eta \tau_{xy} dz - (\eta_x \tau_{xx} + \eta_y \tau_{xy} - \tau_{xz})$$
$$+ (b_x \tau_{xx} + b_y \tau_{xy} - \tau_{xz})$$
$$= \frac{\partial}{\partial x}\int_b^\eta \tau_{xx} dz + \frac{\partial}{\partial y}\int_b^\eta \tau_{xy} dz + \tau_{sx} + \tau_{bx},$$

and in the y-direction we have

$$\int_b^\eta \left(\frac{\partial \tau_{yx}}{\partial x} + \frac{\partial \tau_{yy}}{\partial y} + \frac{\partial \tau_{yz}}{\partial z}\right) dz$$
$$= \frac{\partial}{\partial x}\int_b^\eta \tau_{yx} dz + \frac{\partial}{\partial y}\int_b^\eta \tau_{yy} dz - (\eta_x \tau_{yx} + \eta_y \tau_{yy} - \tau_{yz})$$
$$+ (b_x \tau_{yx} + b_y \tau_{yy} - \tau_{yz})$$
$$= \frac{\partial}{\partial x}\int_b^\eta \tau_{yx} dz + \frac{\partial}{\partial y}\int_b^\eta \tau_{yy} dz + \tau_{sy} + \tau_{by}, \quad \text{and}$$

in the z-direction we have

$$\int_b^\eta \left(\frac{\partial \tau_{zx}}{\partial x} + \frac{\partial \tau_{zy}}{\partial y} + \frac{\partial \tau_{zz}}{\partial z}\right) dz$$
$$= \frac{\partial}{\partial x}\int_b^\eta \tau_{zx} dz + \frac{\partial}{\partial y}\int_b^\eta \tau_{zy} dz - (\eta_x \tau_{zx} + \eta_y \tau_{zy} - \tau_{zz})_{z=\eta}$$
$$+ (b_x \tau_{zx} + b_y \tau_{zy} - \tau_{zz})_{z=b}$$
$$= (h\overline{\tau_{zx}})_x + (h\overline{\tau_{zy}})_y - (\eta_x \tau_{zx} + \eta_y \tau_{zy} - \tau_{zz})_{z=\eta}$$
$$+ (b_x \tau_{zx} + b_y \tau_{zy} - \tau_{zz})_{z=b}$$

where τ_{sx},τ_{sy},τ_{bx}, and τ_{by} are the stress boundary conditions.

Taking all of these expressions together we can write the integrated momentum equations as

$$(h\overline{u})_t + \left(h\overline{u^2} + \frac{1}{2}gh^2 - \frac{h}{\rho}\overline{\tau_{xx}}\right)_x + \left(h\overline{uv} - \frac{h}{\rho}\overline{\tau_{xy}}\right)_y$$
$$= -ghb_x - \frac{h}{\rho}(P_A)_x - \frac{1}{\rho}\int_b^\eta p_x dz + \frac{1}{\rho}\left[\tau_{sx} + \tau_{bx}\right],$$

$$(h\overline{u})_t + \left(h\overline{uv} - \frac{h}{\rho}\overline{\tau_{yx}}\right)_x + \left(h\overline{v^2} + \frac{1}{2}gh^2 - \frac{h}{\rho}\overline{\tau_{yy}}\right)_y = -ghb_y - \frac{h}{\rho}(P_A)_y - \frac{1}{\rho}\int_b^\eta p_y dz + \frac{1}{\rho}[\tau_{sy} + \tau_{by}],$$

and

$$\begin{aligned}(h\overline{w})_t + (h\overline{uw})_x + (h\overline{vw})_y \\ = -\frac{1}{\rho}p|_{z=b} + \frac{1}{\rho}\left[(h\overline{\tau_{zx}})_x + (h\overline{\tau_{zy}})_y - (\eta_x\tau_{zx} + \eta_y\tau_{zy} - \tau_{zz})_{z=\eta}\right. \\ \left. +(b_x\tau_{zx} + b_y\tau_{zy} - \tau_{zz})_{z=b}\right].\end{aligned}$$

Assuming that p is insignificant compared to the other terms and assuming that the lateral stress averages $\overline{\tau_{xx}}$, $\overline{\tau_{xy}}$, and $\overline{\tau_{yy}}$ are small simplifies the momentum equations and allows us to ignore the vertical momentum equation. The pertinent equations are then

$$\begin{aligned}&h_t + (h\overline{u})_x + (h\overline{v})_y = 0 \\ &(h\overline{u})_t + \left(h\overline{u^2} + \frac{1}{2}gh^2\right)_x + (h\overline{uv})_y = -ghb_x - \frac{h}{\rho}(P_A)_x + \frac{1}{\rho}\left[\tau_{sx} + \tau_{bx}\right] \text{ and} \\ &(h\overline{u})_t + (h\overline{uv})_x + \left(h\overline{v^2} + \frac{1}{2}gh^2\right)_y = -ghb_y - \frac{h}{\rho}(P_A)_y + \frac{1}{\rho}[\tau_{sy} + \tau_{by}].\end{aligned} \tag{4.3}$$

The system is then closed by appropriate specifications of the terms P_A, b, τ_{sx}, τ_{sy}, τ_{bx}, and τ_{by} dependent on the problem in question. For further discussion about alternatives to the hydrostatic assumption see appendix A.

4.2 Numerical Methods for the Single-Layer Shallow Water Equations

In this section we will review the numerical methods employed to solve the single-layer shallow water equations including appropriate approximate Riemann solvers, dry state solvers, and a description of the adaptive mesh refinement framework. These are all implemented in the GeoClaw framework which will also be described.

4.2.1 Approximate Riemann Solvers

The general approach uses the f-wave algorithm described in section 3.4.3 and a solver with more waves than equations. This approach is described in [33] and in the case

of the homogenous shallow water equations takes the form

$$\begin{bmatrix} h_i - h_{i-1} \\ (hu)_i - (hu)_i - 1 \\ \varphi_i - \varphi_{i-1} \end{bmatrix} = \sum_{p=1}^{3} \alpha^p_{i-1/2} \begin{bmatrix} r^P_{i-1/2} \\ z^p_{i-1/2} \end{bmatrix}$$

where φ is the flux function of the momentum and the waves are defined as $\alpha^p_{i-1/2} r^p_{i-1/2} = \mathcal{W}^p_{i-1/2}$ and $\alpha^p_{i-1/2} z^p_{i-1/2} = \mathcal{Z}^p_{i-1/2}$. Note that the reason there is only 3 elements of the vector is due to the redundancy of the momentum equation. This formulation now includes an additional wave over the Roe shallow water solver which can be used to provide an entropy correction as described in [25]. Additionally, with appropriate choices of wave speeds and strengths, it can shown that this approach can preserve positivity of the depth and steady states with non-trivial bathymetry.

4.2.2 Dry State Handling

The primary difficulty in the single-layer shallow water equations is the positivity of the depth and the strong rarefactions that can be present at the shoreline. The solver in GeoClaw first distinguishes two different dry states, a wall dry state in which the adjacent cell will not become wet and an inundation problem where the adjacent cell will become wet. After this is determined, appropriate ghost cell values are set in the dry cell in the case of the wall dry state or speeds are directly calculated for the inundation problem related to the inundation front speed. The solver above is then applied directly.

4.2.3 Adaptive Mesh Refinement

Adaptive mesh refinement (AMR) algorithms are designed to solve hyperbolic systems on a hierarchical set of logically rectangular grids. A single coarse grid covers the entire domain and contains multiple nested grids that are of higher resolution. These patches are determined dynamically based on the state of the solution. GeoClaw implements these algorithms following [8, 7] and described in detail in [34] for tsunami modeling. The primary difference between using AMR for tsunami modeling and storm surge is the use of the flagging routine. This routine marks which cells should be collected into a finer nested grid in the regridding algorithm. In the case of tsunamis this flagging routine primarily uses the gradient of the surface η. In single-layer storm surge AMR, the momentum is used as the primary flagging criterion. A set of nested grids also surrounds the storm in order to provide adequate resolution of the storm eye.

4.2.4 GeoClaw

GeoClaw is a software package that was originally developed to model tsunamis but has been expanded to include debris flow, dam breaks, and now storm surges. It

utilizes the algorithms described here and includes functionality to include multiple complex bathymetry specifications, tools for region refinement, and simulated tide gauges. GeoClaw can be downloaded at `http://www.clawpack.org/geoclaw`.

Chapter 5

MULTILAYER DEPTH AVERAGED EQUATIONS

In this chapter a multi-layer version of the shallow water equations is derived and analyzed. The motivation for some of the approximations are due to storm surge modeling which is discussed in chapter 7.

5.1 Derivation

The multi-layer shallow water equations are derived from the integration of the same equations as the single-layer shallow water equations, the inviscid Navier-Stokes equations, which consist of equations for

$$\begin{aligned}
&\text{incompressibility } u_x + w_z = 0,\\
&\text{mass conservation } \rho_t + (u\rho)_x + (w\rho)_z = 0,\\
&\text{x-momentum conservation } (\rho u)_t + (\rho u^2)_x + (\rho uw)_z = -P_x, \text{ and}\\
&\text{z-momentum conservation } (\rho w)_t + (\rho uw)_x + (\rho w^2)_z = -P_z - \rho g
\end{aligned}$$

in one-dimension. In the multi-layer case the velocity u and density ρ are allowed to be piece-wise defined through the depth where η defines the interface between each layer (see figure 5.1 for a two-layer example). We now proceed to integrate through each layer.

Integration of the incompressibility condition gives the familiar equation for the depth dynamics,

$$\begin{aligned}
\int_{\eta_2}^{\eta_1} (u_x + w_z)dz &= \frac{\partial}{\partial x}\int_{\eta_2}^{\eta_1} udz - (\eta_1)_x u|_{\eta_1} + (\eta_2)_x u|_{\eta_2} + w|_{\eta_1} - w|_{\eta_2}\\
&= (h_1u_1)_x + (\eta_1 - \eta_2)_t\\
&= (h_1)_t + (h_1u_1)_x = 0.
\end{aligned}$$

Integration of the mass conservation can be done using the conservative form $\rho_t + (u\rho)_x + (w\rho)_z = 0$ or via the equation above. Whichever version is used, the integration yields

$$(\rho_1 h_1)_t + (\rho_1 h_1 u_1)_x = 0$$

which can be used instead of the continuity equation above. This can also be modified

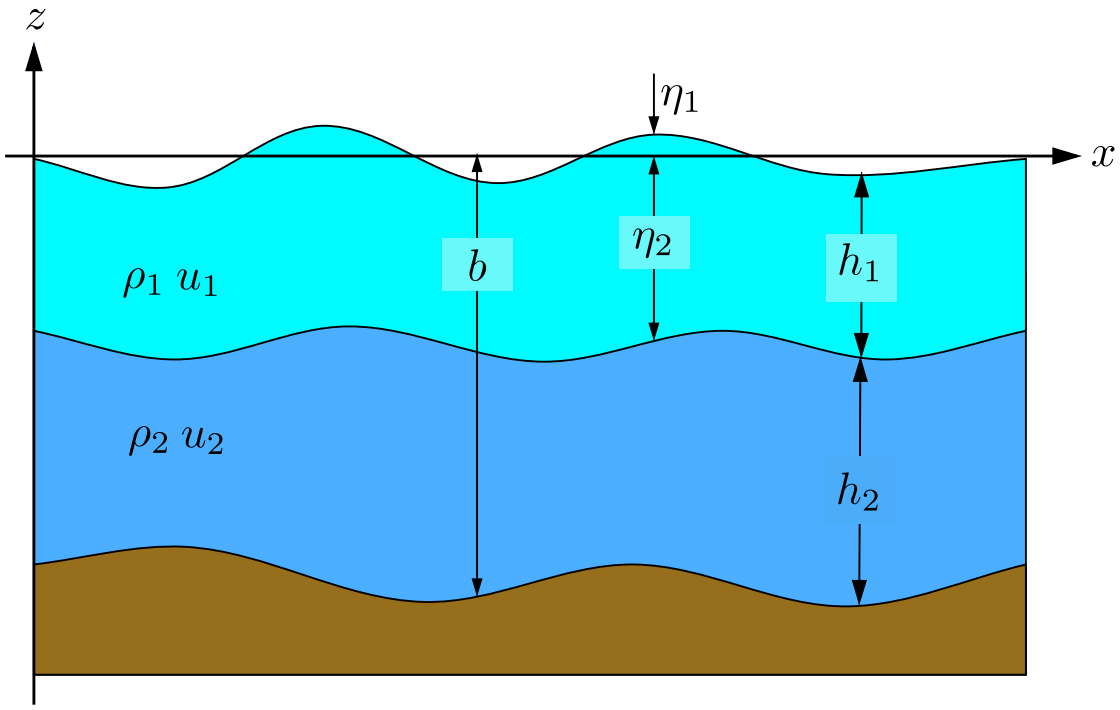

Figure 5.1: Coordinates for a one-dimensional system with two-layers and varying bathymetry.

such that the derivatives only exist on ρ_1 as in

$$(\rho_1)_t + u_1(\rho_1)_x = 0.$$

Integration through the bottom layer gives

$$\begin{aligned}\int_b^{\eta_2}(u_x + w_z)dz &= \frac{\partial}{\partial x}\int_b^{\eta_2} u dz - (\eta_2)_x u|_{\eta_2} + b_x u|_b + w|_{\eta_2} - w|_b \\ &= (h_2u_2)_x + (\eta_2)_t \\ &= (h_2)_t + (h_2u_2)_x = 0.\end{aligned}$$

and as before

$$\begin{aligned}&(\rho_2 h_2)_t + (\rho_2 h_2 u_2)_x = 0 \text{ and} \\ &(\rho_2)_t + u_2(\rho_2)_x = 0.\end{aligned}$$

In order to integrate the horizontal-momentum equations, we first need to find

the pressure as a function of depth. Looking at the vertical-momentum equation, integrating in depth from the top surface η_1 to a intermediate surface coordinate ξ and making the assumption that the advective terms for w are negligible we have

$$\int_{\xi}^{\eta_1} P_z dz = \int_{\xi}^{\eta_1} \rho g dz. \tag{5.1}$$

Integrating the left hand side we have

$$\int_{\xi}^{\eta_1} P_z dz = P(x,\eta_1,t) - P(x,\xi,t) = P_A(x,t) - P(x,\xi,t),$$

where $P_A(x,t)$ is the surface pressure at η_1. The right hand side of (5.1) gives a different result depending on where ξ is in relation to the internal surface η_2.

$$\int_{\xi}^{\eta_1} \rho g dz = \begin{cases} \rho_1(x,t) g(\eta_1 - \xi) & \eta_2 < \xi < \eta_1 \\ \rho_1(x,t) g h_1(x,t) + \rho_2(x,t) g(\eta_2 - \xi) & b < \xi < \eta_2 \end{cases}$$

Integrating the horizontal-momentum equation through the top layer leads to

$$\begin{aligned} \int_{\eta_2}^{\eta_1} \left[(\rho u)_t + (\rho u^2)_x + (\rho u w)_z\right] dz &= \frac{\partial}{\partial t}\int_{\eta_2}^{\eta_1} \rho u dz - (\eta_1)_t \rho u|_{\eta_1} + (\eta_2)_t \rho u|_{\eta_2} \\ &\quad + \frac{\partial}{\partial x}\int_{\eta_2}^{\eta_1} \rho u^2 dz - (\eta_1)_x \rho u^2|_{\eta_1} + (\eta_2)_x \rho u^2|_{\eta_2} \\ &\quad + \rho u w|_{\eta_1} + \rho u w|_{\eta_2} \\ &= (\rho_1 u_1)_t + (\rho_1 h_1 u_1^2)_x \end{aligned}$$

for the left hand side. Integration of the pressure gradient leads to

$$\begin{aligned} -\int_{\eta_2}^{\eta_1} P_x dz &= -\frac{\partial}{\partial x}\int_{\eta_2}^{\eta_1} P dz + (\eta_1)_x P|_{\eta_1} - (\eta_2)_x P|_{\eta_2} \\ &= -\frac{\partial}{\partial x}\left(\frac{1}{2} g \rho_1 (\eta_1 - \eta_2)^2\right) - (h_2 + b)_x \rho_1 g (\eta_1 - \eta_2) \\ &= -\left(\frac{1}{2}\rho_1 g h_1^2\right)_x - \rho_1 g h_1 (h_2 + b)_x \end{aligned}$$

where we have used one sided evaluations of the density in the top layer where necessary. This leads to the integrated x-momentum equation for the top layer of

$$(\rho_1 h_1 u_1)_t + \left(\rho_1 h_1 u_1^2 + \frac{1}{2}\rho_1 g h_1^2\right) = -\rho_1 g h_1 (h_2 + b)_x.$$

For the second layer, the integration of the left hand side is identical but the pressure integration is more complicated as we have contributions from the layer on top which also may be varying. Integrating the pressure leads to

$$-\int_b^{\eta_2} P_x dz = -\frac{\partial}{\partial x}\int_b^{\eta_2} P dz + (\eta_2)_x P|_{\eta_2} - b_x P|_b \tag{5.2}$$

whose terms we must now evaluated. First the pressure integrated through the depth gives

$$\begin{aligned}
-\frac{\partial}{\partial x}\int_b^{\eta_2} P dz &= -\frac{\partial}{\partial x}\int_b^{\eta_2} (g\rho_1 h_1 + g\rho_2(\eta_2 - z))dz \\
&= -\frac{\partial}{\partial x}\left(g\rho_1 h_1 h_2 + \frac{1}{2}g\rho_2(\eta_2 - b)^2\right) \\
&= -\frac{\partial}{\partial x}\left(g\rho_1 h_1 h_2 + \frac{1}{2}g\rho_2 h_2^2\right).
\end{aligned}$$

Evaluating the pressure gives

$$(\eta_2)_x P|_{\eta_2} = \rho_1 g h_1 (h_2 + b)_x$$

and

$$b_x P|_b = (\rho_1 g h_1 + \rho_2 g h_2) b_x$$

which gives us the following form for the pressure integral through the second layer:

$$-\int_b^{\eta_2} P_x dz = -\frac{\partial}{\partial x}\left(g\rho_1 h_1 h_2 + \frac{1}{2}g\rho_2 h_2^2\right) + \rho_1 g h_1 (h_2 + b)_x - (\rho_1 g h_1 + \rho_2 g h_2) b_x.$$

Finally putting this integration with the left hand side integration for the bottom layer we have the following depth integrated conservation law for the bottom layer,

$$(\rho_2 h_2 u_2)_t + (\rho_2 h_2 u_2^2 + 1/2\rho_2 g h_2^2)_x = -g h_2 (\rho_1 h_1)_x - g\rho_2 h_2 b_x. \tag{5.3}$$

The new system of equations for one dimensional, two-layer, depth-integrated flow with variable horizontal density is

$$\begin{cases}
(h_1)_t + (h_1 u_1)_x = 0 & \text{for continuity} \\
(\rho_1 h_1)_t + (h_1 u_1 \rho_1)_x = 0 & \text{for mass conservation, and} \\
(\rho_1 h_1 u_1)_t + \left(\rho_1 h_1 u_1^2 + \frac{1}{2}\rho_1 g h_1^2\right)_x = -\rho_1 g h_1 (h_2 + b)_x & \text{for momentum conservation}
\end{cases}$$

in the top layer and

$$\begin{cases} (h_2)_t + (h_2u_2)_x = 0 & \text{for continuity} \\ (\rho_2 h_2)_t + (h_2u_2\rho_2)_x = 0 & \text{for mass conservation, and} \\ (\rho_2 h_2 u_2)_t + \left(\rho_2 h_2 u_2^2 + \frac{1}{2}\rho_2 g h_2^2\right)_x = -g h_2(\rho_1 h_1)_x - g\rho_2 h_2 b_x & \text{for momentum conservation} \end{cases}$$

in the bottom layer.

A common approximation used for the multi-layer shallow water equations is to assume that the density is constant inside of each of the layers. This leads to a system of four equations in one dimension that are commonly written as

$$\begin{aligned} &(h_1)_t + (h_1u_1)_x = 0, \\ &(h_1u_1)_t + (h_1u_1^2 + 1/2gh_1^2)_x = -gh_1(h_2+b)_x, \\ &(h_2)_t + (h_2u_2)_x = 0, \quad \text{and} \\ &(h_2u_2)_t + (h_2u_2^2 + 1/2gh_2^2)_x = -rgh_2(h_1)_x - gh_2b_x \end{aligned} \tag{5.4}$$

where $r = \rho_1/\rho_2 < 1$ and $r \approx 1$. Another equivalent way to write these same equations involves integrating the momentum transfer terms on the right hand side of the momentum equations to cause them to become symmetric which we will see has advantages. Using this form, the equations can be rewritten as

$$\begin{aligned} &(\rho_1 h_1)_t + (\rho_1 h_1 u_1)_x = 0, \\ &(\rho_1 h_1 u_1)_t + \left(\rho_1 h_1 u_1^2 + \frac{1}{2}g\rho_1 h_1^2\right)_x = -g\rho_1 h_1(h_2)_x - g\rho_1 h_1 b_x, \\ &(\rho_2 h_2)_t + (\rho_2 h_2 u_2)_x = 0, \quad \text{and} \\ &(\rho_2 h_2 u_2)_t + \left(\rho_2 h_2 u_2^2 + \frac{1}{2}g\rho_2 h_2^2 + g\rho_1 h_2 h_1\right)_x = \rho_1 g h_1(h_2)_x - \rho_2 g h_2 b_x. \end{aligned} \tag{5.5}$$

5.1.1 Quasi-Linear Coefficient Matrices

We can write the equations (5.4) in a quasi-linear coefficient matrix by first defining

$$q = \begin{bmatrix} h_1 \\ h_1u_1 \\ h_2 \\ h_2u_2 \end{bmatrix}, \quad f(q) = \begin{bmatrix} q^2 \\ \frac{(q^2)^2}{q^1} + \frac{1}{2}g(q^1)^2 \\ q^4 \\ \frac{(q^4)^2}{q_3} + \frac{1}{2}g(q^3)^2 \end{bmatrix}, \quad \text{and} \quad S(q) = \begin{bmatrix} 0 \\ -gh_1(h_2+b)_x \\ 0 \\ -rgh_2(h_1)_x - gh_2b_x \end{bmatrix}$$

which allow us to write the original equations as

$$q_t + f(q)_x = S(q). \tag{5.6}$$

If we write the source term $S(q)$ as

$$S(q) = \begin{bmatrix} 0 & 0 & 0 & 0 \\ 0 & 0 & -gh_1 & 0 \\ 0 & 0 & 0 & 0 \\ -rgh_2 & 0 & 0 & 0 \end{bmatrix} q_x + \begin{bmatrix} 0 \\ -g\rho_1 h_1 b_x \\ 0 \\ -g\rho_2 h_2 b_x \end{bmatrix}$$

and calculating the flux Jacobian

$$f'(q) = \begin{bmatrix} 0 & 1 & 0 & 0 \\ -u_1^2 + gh_1 & 2u_1 & 0 & 0 \\ 0 & 0 & 0 & 1 \\ 0 & 0 & -u_2^2 + gh_2 & 2u_2 \end{bmatrix}$$

we can rewrite the original equation form (5.6) as

$$q_t + A(q)q_x = \tilde{S}(q). \tag{5.7}$$

where

$$A(q) = \begin{bmatrix} 0 & 1 & 0 & 0 \\ gh_1 - u_1^2 & 2u_1 & gh_1 & 0 \\ 0 & 0 & 0 & 1 \\ rgh_2 & 0 & gh_2 - u_2^2 & 2u_2 \end{bmatrix} \quad \text{and} \quad \tilde{S}(q) = \begin{bmatrix} 0 \\ -gh_1 b_x \\ 0 \\ -gh_2 b_x \end{bmatrix}$$

We can also do this for the modified equations (5.5), with the same result but now with

$$q = [\rho_1 h_1, \rho_1 h_1 u_1, \rho_2 h_2, \rho_2 h_2 u_2]^T$$

and

$$A(q) = \begin{bmatrix} 0 & 1 & 0 & 0 \\ gh_1 - u_1^2 & 2u_1 & rgh_1 & 0 \\ 0 & 0 & 0 & 1 \\ gh_2 & 0 & gh_2 - u_2^2 & 2u_2 \end{bmatrix} \quad \text{and} \quad \tilde{S}(q) = \begin{bmatrix} 0 \\ -g\rho_1 h_1 b_x \\ 0 \\ -g\rho_2 h_2 b_x \end{bmatrix}.$$

With this form of the equations we can incorporate the momentum transfer between layers directly into the eigenspace calculation. This is an important step since without this, the eigenspace would reduce to that of two decoupled single-layer fluids. This becomes important to stability of the numerical method and will be discussed in chapter 6.

5.1.2 Two Dimensional Multi-Layer Shallow Water Equations

We can also derive the two dimensional multi-layer shallow water equations from the three dimensional inviscid Navier-Stokes equations as a straight forward extension of the derivation above. Assuming that density is again constant and writing the equations in a similar form to equations (5.5) leads to

$$
\begin{aligned}
&(\rho_1 h_1)_t + (\rho_1 h_1 u_1)_x + (\rho_1 h_1 v_1)_y = 0,\\
&(\rho_1 h_1 u_1)_t + \left(\rho_1 h_1 u_1^2 + \frac{1}{2} g \rho_1 h_1^2\right)_x + (\rho_1 h_1 u_1 v_1)_y = -g\rho_1 h_1 (h_2)_x - g\rho_1 h_1 b_x,\\
&(\rho_1 h_1 v_1)_t + (\rho_1 h_1 u_1 v_1)_x + \left(\rho_1 h_1 v_1^2 + \frac{1}{2} g \rho_1 h_1^2\right)_y = -g\rho_1 h_1 (h_2)_y - g\rho_1 h_1 b_y,\\
&(\rho_2 h_2)_t + (\rho_2 h_2 u_2)_x + (\rho_2 h_2 v_2)_y = 0,\\
&(\rho_2 h_2 u_2)_t + \left(\rho_2 h_2 u_2^2 + \frac{1}{2} g \rho_2 h_2^2 + g\rho_1 h_2 h_1\right)_x + (\rho_2 h_2 u_2 v_2)_y = \rho_1 g h_1 (h_2)_x - \rho_2 g h_2 b_x,\\
&(\rho_2 h_2 u_2)_t + (\rho_2 h_2 u_2 v_2)_x + \left(\rho_2 h_2 v_2^2 + \frac{1}{2} g \rho_2 h_2^2 + g\rho_1 h_2 h_1\right)_y = \rho_1 g h_1 (h_2)_y - \rho_2 g h_2 b_y
\end{aligned}
\tag{5.8}
$$

where we have jumped directly to a form similar to the modified equations in one dimension (5.5).

The corresponding quasi-linear coefficient matrices of the two dimensional equations can be found in a similar manner as in section 5.1.1. First, defining the quantities

$$
q = \begin{bmatrix} \rho_1 h_1 \\ \rho_1 h_1 u_1 \\ \rho_1 h_1 v_1 \\ \rho_2 h_2 \\ \rho_2 h_2 u_2 \\ \rho_2 h_2 v_2 \end{bmatrix}, \qquad S(q) = \begin{bmatrix} 0 \\ -\rho_1 g h_1 (h_2)_x - g\rho_1 h_1 b_x \\ -\rho_1 g h_1 (h_2)_y - g\rho_1 h_1 b_y \\ 0 \\ \rho_1 g h_1 (h_2)_x - g\rho_2 h_2 b_x \\ \rho_1 g h_1 (h_2)_y - g\rho_2 h_2 b_y \end{bmatrix},
$$

$$
f(q) = \begin{bmatrix} \rho_1 h_1 u_1 \\ \rho_1 h_1 u_1^2 + \frac{1}{2} g \rho_1 h_1^2 \\ \rho_1 h_1 u_1 v_1 \\ \rho_2 h_2 u_2 \\ \rho_2 h_2 u_2^2 + \frac{1}{2} g \rho_2 h_2^2 + g\rho_1 h_2 h_1 \\ \rho_2 h_2 u_2 v_2 \end{bmatrix} = \begin{bmatrix} q^2 \\ (q^2)^2/q^1 + \frac{1}{2} g (q^1)^2/\rho_1 \\ q^2 q^3/q^1 \\ q^5 \\ (q^5)^2/q^4 + \frac{1}{2} g (q^4)^2/\rho_2 + g q^1 q^4/\rho_2 \\ q^5 q^6/q^4 \end{bmatrix}, \quad \text{and}
$$

$$g(q) = \begin{bmatrix} \rho_1 h_1 v_1 \\ \rho_1 h_1 u_1 v_1 \\ \rho_1 h_1 v_1^2 + \frac{1}{2} g \rho_1 h_1^2 \\ \rho_2 h_2 v_2 \\ \rho_2 h_2 u_2 v_2 \\ \rho_2 h_2 v_2^2 + \frac{1}{2} g \rho_2 h_2^2 + g \rho_1 h_2 h_1 \end{bmatrix} = \begin{bmatrix} q^3 \\ q^2 q^3 / q^1 \\ (q^3)^2 / q^1 + \frac{1}{2} g (q^1)^2 / \rho_1 \\ q^6 \\ q^5 q^6 / q^4 \\ (q^6)^2 / q^4 + \frac{1}{2} g (q^4)^2 / \rho_2 + g q^1 q^4 / \rho_2 \end{bmatrix},$$

we can calculate the flux Jacobians of $f(q)$ as

$$f'(q) = \begin{bmatrix} 0 & 1 & 0 & 0 & 0 & 0 \\ -\left(\frac{q^2}{q^1}\right)^2 + g q^1 / \rho_1 & 2\frac{q^2}{q^1} & 0 & 0 & 0 & 0 \\ -\frac{q^2 q^3}{(q^1)^2} & q^3/q^1 & q^2/q^1 & 0 & 0 & 0 \\ 0 & 0 & 0 & 0 & 1 & 0 \\ g q^4 / \rho_2 & 0 & 0 & -\left(\frac{q^5}{q^1}\right)^2 + g q^4/\rho_2 + g q^1/\rho_2 & 2q^5/q^4 & 0 \\ 0 & 0 & 0 & -q^5 q^6/(q^4)^2 & q^6/q^4 & q^5/q^4 \end{bmatrix}$$

$$= \begin{bmatrix} 0 & 1 & 0 & 0 & 0 & 0 \\ -u_1^2 + g h_1 & 2u_1 & 0 & 0 & 0 & 0 \\ -u_1 v_1 & v_1 & u_1 & 0 & 0 & 0 \\ 0 & 0 & 0 & 0 & 1 & 0 \\ g h_2 & 0 & 0 & -u_2^2 + g h_2 + g r h_1 & 2u_2 & 0 \\ 0 & 0 & 0 & -u_2 v_2 & v_2 & u_2 \end{bmatrix}$$

and $g(q)$ as

$$g'(q) = \begin{bmatrix} 0 & 0 & 1 & 0 & 0 & 0 \\ -\frac{q^2 q^3}{(q^1)^2} & q^3/q^1 & q^2/q^1 & 0 & 0 & 0 \\ -\left(\frac{q^3}{q^1}\right)^2 + g q^1/\rho_1 & 0 & 2q^3/q^1 & 0 & 0 & 0 \\ 0 & 0 & 0 & 0 & 0 & 1 \\ 0 & 0 & 0 & -\frac{q^5 q^6}{(q^4)^2} & q^6/q^4 & q^5/q^4 \\ g q^4/\rho_2 & 0 & 0 & -\left(\frac{q^6}{q^4}\right)^2 + g q^4/\rho_2 + g q^1/\rho_2 & 0 & 2q^6/q^4 \end{bmatrix}$$

$$= \begin{bmatrix} 0 & 0 & 1 & 0 & 0 & 0 \\ -u_1 v_1 & v_1 & u_1 & 0 & 0 & 0 \\ -v_1^2 + g h_1 & 0 & 2v_1 & 0 & 0 & 0 \\ 0 & 0 & 0 & 0 & 0 & 1 \\ 0 & 0 & 0 & -u_2 v_2 & v_2 & u_2 \\ g h_2 & 0 & 0 & -v_2^2 + g h_2 + g r h_1 & 0 & 2v_2 \end{bmatrix}.$$

Again, writing the source term as

$$S(q) = \begin{bmatrix} 0 & 0 & 0 & 0 & 0 & 0 \\ 0 & 0 & 0 & -rgh_1 & 0 & 0 \\ 0 & 0 & 0 & 0 & 0 & 0 \\ 0 & 0 & 0 & 0 & 0 & 0 \\ 0 & 0 & 0 & rgh_1 & 0 & 0 \\ 0 & 0 & 0 & 0 & 0 & 0 \end{bmatrix} \frac{\partial q}{\partial x} + \begin{bmatrix} 0 & 0 & 0 & 0 & 0 & 0 \\ 0 & 0 & 0 & 0 & 0 & 0 \\ 0 & 0 & 0 & -rgh_1 & 0 & 0 \\ 0 & 0 & 0 & 0 & 0 & 0 \\ 0 & 0 & 0 & 0 & 0 & 0 \\ 0 & 0 & 0 & rgh_1 & 0 & 0 \end{bmatrix} \frac{\partial q}{\partial y} + \begin{bmatrix} 0 \\ -gq^1 b_x \\ -gq^1 b_y \\ 0 \\ -gq^2 b_x \\ -gq^2 b_y \end{bmatrix},$$

we can write the quasi-linear coefficient matrices of the original equations (5.8) as

$$q_t + A(q)q_x + B(q)q_y = \tilde{S}(q) \tag{5.9}$$

where

$$A(q) = \begin{bmatrix} 0 & 1 & 0 & 0 & 0 & 0 \\ -u_1^2 + gh_1 & 2u_1 & 0 & rgh_1 & 0 & 0 \\ -u_1 v_1 & v_1 & u_1 & 0 & 0 & 0 \\ 0 & 0 & 0 & 0 & 1 & 0 \\ gh_2 & 0 & 0 & -u_2^2 + gh_2 & 2u_2 & 0 \\ 0 & 0 & 0 & -u_2 v_2 & v_2 & u_2 \end{bmatrix}, \tag{5.10}$$

$$B(q) = \begin{bmatrix} 0 & 0 & 1 & 0 & 0 & 0 \\ -u_1 v_1 & v_1 & u_1 & 0 & 0 & 0 \\ -v_1^2 + gh_1 & 0 & 2v_1 & rgh_1 & 0 & 0 \\ 0 & 0 & 0 & 0 & 0 & 1 \\ 0 & 0 & 0 & -u_2 v_2 & v_2 & u_2 \\ gh_2 & 0 & 0 & -v_2^2 + gh_2 & 0 & 2v_2 \end{bmatrix}, \tag{5.11}$$

and

$$\tilde{S}(q) = [0, -g\rho_1 h_1 b_x, -g\rho_1 h_1 b_y, 0, -g\rho_2 h_2 b_x, -g\rho_2 h_2 b_y]^T.$$

5.2 Calculating the Eigenspace

One of the primary building blocks to solving the multi-layer shallow water equations is the calculation of the systems' eigenspace. In general the system has two sets of eigenvalues and eigenvectors, those corresponding to slightly perturbed classical shallow water gravity waves and those corresponding to an internal wave traveling at a much lower speed. The speeds of these waves, depending on the ratio of the densities of the layers $r = \rho_1/\rho_2$, determines how different these speeds are. For realistic situations in the ocean, this ratio is nearly one and the external waves corresponding to the shallow water gravity wave are nearly the same as shallow water and internal waves are much slower.

The characteristic polynomial of the quasi-linear coefficient matrix (5.7) in one dimension is

$$((\lambda - u_1)^2 - gh_1)((\lambda - u_2)^2 - gh_2) - rg^2h_1h_2 = 0 \tag{5.12}$$

and in two dimensions is a sixth degree polynomial. Since the additional eigenvalues in two dimensions are simple to factor out and therefore to determine, we will concentrate on solving the fourth degree characteristic polynomial. Since we know that there is an expression for the roots of a fourth degree polynomial, it is conceivable that we could evaluate the eigenvalues of the system directly. This is prohibitively expensive and numerically difficult to do with precision in practice. Instead, approximations are commonly used to represent the key aspects of the system in question. In this section we will explore a number of different approximations and discuss their limitations with both analytical results and numerical experiments, often compared to a simulation where the eigenvalues are calculated using a numerical eigensolver package such as LAPACK [4].

5.2.1 Velocity Difference Expansions

One general approach to calculating the eigenspeeds is to expand about differences in the layer speeds $u_1 - u_2$. Using this approximation to first order we can calculate the external eigenspeeds to be

$$\lambda^{\pm}_{\text{ext}} \approx \frac{h_1u_1 + h_2u_2}{h_1 + h_2} \pm \sqrt{g(h_1 + h_2)}$$

and the internal wave speeds as

$$\lambda^{\pm}_{\text{int}} \approx \frac{h_1u_2 + h_2u_1}{h_1 + h_2} \pm \sqrt{g'\frac{h_1h_2}{h_1 + h_2}\left[1 - \frac{(u_1 - u_2)^2}{g'(h_1 + h_2)}\right]}$$

where $g' \equiv (1 - r)g$. This approximation has the nice property that it has a similar form to the eigenvalues of the single-layer equations for the external speeds and the clear result that the internal wave speeds are small compared to the external speeds when $1 - r \ll 1$, i.e. when $\rho_1 \approx \rho_2$.

Assuming that we have accurately calculated the eigenvalues λ^p, we can then solve for the eigenvectors by solving

$$\begin{bmatrix} 0 & 1 & 0 & 0 \\ gh_1 - u_1^2 & 2u_1 & rgh_1 & 0 \\ 0 & 0 & 0 & 1 \\ gh_2 & 0 & gh_2 - u_2^2 & 2u_2 \end{bmatrix} \cdot \begin{bmatrix} 1 \\ \alpha_1 \\ \alpha_2 \\ \alpha_3 \end{bmatrix} = \begin{bmatrix} \lambda \\ \alpha_1\lambda \\ \alpha_2\lambda \\ \alpha_3\lambda \end{bmatrix}$$

which immediately implies that $\alpha_1 = \lambda$ and $\alpha_3 = \lambda\alpha_2$. We then have two equations

for one unknown α_2 which should satisfy both equations simultaneously. Solving each of the equations separately we have

$$\alpha_{2,p} = \begin{cases} \dfrac{(\lambda_p - u_1)^2 - gh_1}{gh_1}, \text{ and} \\ \dfrac{rgh_2}{(\lambda_p - u_2)^2 - gh_2}. \end{cases} \tag{5.13}$$

Setting these two equations equal to one another we obtain the characteristic polynomial of the system (5.12). We therefore can use either form of $\alpha_{2,p}$ in (5.13) for the eigenvectors. The final form of the eigenvectors using one of the expressions from (5.13) is

$$[1, \lambda_p, \alpha_p, \lambda_p \alpha_p]^T \tag{5.14}$$

where we have simplified the notation of $\alpha_{2,p}$ to α_p.

5.2.2 Linearized Eigenspace

Another useful approximation for calculating the eigenspeeds of (5.7) is to linearize the original equations. Since we will eventually want to consider an ocean primarily at rest, we will linearize about a steady state where $\hat{u}_1$ and $\hat{u}_2$ are zero and the sea surface $\hat{\eta}_1$ and internal surface $\hat{\eta}_2$ are constant. We then define the perturbation from the steady state as $\tilde{\eta}_1$, $\tilde{\eta}_2$, $\tilde{u}_1$, and $\tilde{u}_2$ (see figure 5.2). We can then define the following conservative variables

$$\begin{aligned} h_1 &= \hat{\eta}_1 - \hat{\eta}_2 + \tilde{\eta}_1(x,t) - \tilde{\eta}_2(x,t) = \hat{h}_1 + \tilde{h}_1(x,t) \\ h_2 &= \hat{\eta}_2 - b(x) + \tilde{\eta}_2(x,t) = \hat{h}_2(x) + \tilde{h}_2(x,t) \\ \mu_1 &= h_1 u_1 = (\hat{\eta}_1 - \hat{\eta}_2 + \tilde{\eta}_1 - \tilde{\eta}_2)\tilde{u}_1 = \hat{h}_1 \tilde{u}_1(x,t) + \tilde{h}_1(x,t)\tilde{u}_1(x,t) \\ \mu_2 &= h_2 u_2 = (\hat{\eta}_2 - b + \tilde{\eta}_2)\tilde{u}_2 = \hat{h}_2(x)\tilde{u}_2(x,t) + \tilde{h}_2(x,t)\tilde{u}_2(x,t) \end{aligned}$$

where we have defined $\hat{h}_1 = \hat{\eta}_1 - \hat{\eta}_2$ and $\tilde{h}_1 = \tilde{\eta}_1 - \tilde{\eta}_2$ for convenience. Putting these expressions into the constant density layered equations (5.4) we arrive at

$$\begin{aligned} (h_1)_t + (\mu_1)_x &= 0 \\ (\tilde{h}_1)_t + (\tilde{\mu}_1)_x &= 0 \end{aligned}$$

for the upper layer continuity equation,

$$\begin{aligned} &(\mu_1)_t + (\mu_1^2/h_1 + 1/2gh_1^2)_x + gh_1(h_2 + b)_x = 0 \\ &(\tilde{\mu}_1)_t + (\tilde{\mu_1}^2/(\hat{h}_1 + \tilde{h}_1) + 1/2g(\hat{h}_1 + \tilde{h}_1)^2)_x + g(\hat{h}_1 + \tilde{h}_1)(\hat{\eta_2} + \tilde{\eta}_2)_x = 0 \\ &(\tilde{\mu}_1)_t + g\hat{h}_1(\tilde{h}_1 + \tilde{h}_2)_x = 0 \end{aligned}$$

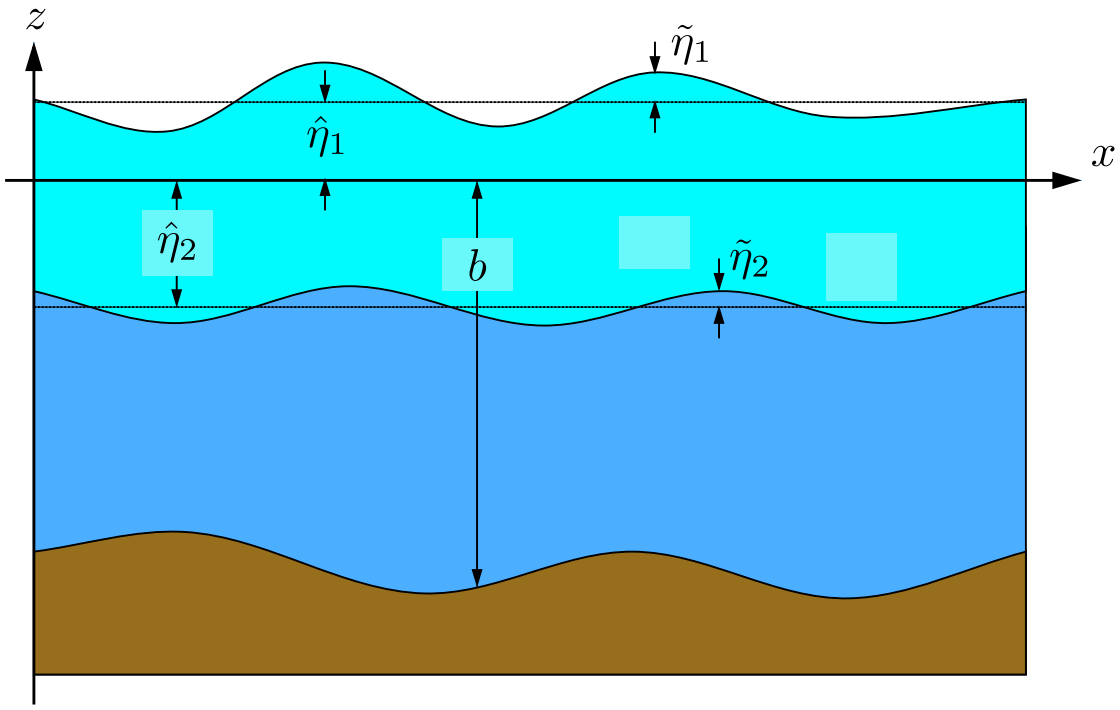

Figure 5.2: Coordinate system for linearized equations with $b(x) \neq 0$.

for the upper layer momentum equation,

$$(h_2)_t + (\mu_2)_x = 0$$
$$(\tilde{h_2})_t + (\tilde{\mu}_2)_x = 0$$

for the lower layer continuity equation, and

$$\begin{aligned}
&(\mu_2)_t + (\mu_2^2/h_2 + 1/2gh_2^2)_x + gh_2(rh_1 + b)_x = 0\\
&(\tilde{\mu}_2)_t + (\tilde{\mu}_2^2/(\hat{h}_2 + \tilde{h}_2) + 1/2g(\hat{h}_2 + \tilde{h}_2)^2)_x + g(\hat{h}_2 + \tilde{h}_2)(r(\hat{h}_1 + \tilde{h}_1) + b)_x = 0\\
&(\tilde{\mu}_2)_t + g(\hat{h}_2 + \tilde{h}_2)(\hat{h}_2 + \tilde{h}_2)_x + g(\hat{h}_2 + \tilde{h}_2)(r(\tilde{h}_1)_x + b_x) = 0\\
&(\tilde{\mu}_2)_t + g(\hat{h}_2 + \tilde{h}_2)(\tilde{h}_2 - b)_x + gr\hat{h}_2(\tilde{h}_1)_x + g\hat{h}_2 b_x + g\tilde{h}_2 b_x = 0\\
&(\tilde{\mu}_2)_t + g\left[\hat{h}_2(\tilde{h}_2)_x - \hat{h}_2 b_x - \tilde{h}_2 b_x + r\hat{h}_2(\tilde{h}_1)_x + \hat{h}_2 b_x + \tilde{h}_2 b_x\right] = 0\\
&(\tilde{\mu}_2)_t + g\hat{h}_2\left[(\tilde{h}_2)_x + r(\tilde{h}_1)_x\right] = 0
\end{aligned}$$

for the lower layer momentum equation. Here we have redefined $\tilde{\mu}_n = \hat{h}_n\tilde{u}_n$ as the second term is of higher order. The final system becomes

$$\begin{aligned}
&(\tilde{h}_1)_t + (\tilde{\mu}_1)_x = 0,\\
&(\tilde{\mu}_1)_t + g\hat{h}_1(\tilde{h}_1 + \tilde{h}_2)_x = 0,\\
&(\tilde{h_2})_t + (\tilde{\mu}_2)_x = 0, \quad \text{and}\\
&(\tilde{\mu}_2)_t + g\hat{h}_2\left[(\tilde{h}_2)_x + r(\tilde{h}_1)_x\right] = 0.
\end{aligned} \tag{5.15}$$

With these equations, we can also write the system in the form $\tilde{q}_t + A(\hat{q})\tilde{q}_x = 0$ where

$$\hat{q} = \begin{bmatrix}\hat{h}_1\\0\\\hat{h}_2\\0\end{bmatrix}, \quad \tilde{q} = \begin{bmatrix}\tilde{h}_1\\\hat{h}_1\tilde{u}_1\\\tilde{h}_2\\\hat{h}_2\tilde{u}_2\end{bmatrix}, \quad \text{and} \quad A(\hat{q}) = \begin{bmatrix}0 & 1 & 0 & 0\\ g\hat{h}_1 & 0 & g\hat{h}_1 & 0\\ 0 & 0 & 0 & 1\\ rg\hat{h}_2 & 0 & g\hat{h}_2 & 0\end{bmatrix}.$$

Turning to the eigenspace of the linearized system, the characteristic polynomial is now

$$(\lambda^2 - g\hat{h}_1)(\lambda^2 - g\hat{h}_2) - rg^2\hat{h}_1\hat{h}_2 = 0$$

and if we assume that the eigenvectors have the form $v = [1, \lambda, \alpha, \alpha\lambda]^T$, the relevant

equations for the unknowns α and λ from $Av - \lambda v = 0$ are

$$g\hat{h}_1 + g\hat{h}_1\alpha = \lambda^2 \quad \text{and}$$
$$rg\hat{h}_2 + g\hat{h}_2\alpha = \lambda^2\alpha.$$

We can eliminate λ from both equations and find that α must satisfy

$$\frac{r\hat{h}_2 + \hat{h}_2\alpha}{\hat{h}_1 + \hat{h}_1\alpha} = \alpha.$$

Dropping the hat notation, we find a quadratic equation for α,

$$\alpha^2 + \alpha\left(1 - \frac{h_2}{h_1}\right) - r\frac{h_2}{h_1} = 0$$

leading to

$$2\alpha = -(1-\gamma) \pm \sqrt{(1-\gamma)^2 + 4r\gamma}$$

where $\gamma = h_2/h_1$. As γ approaches 0, or as the bottom layer depth goes to 0,

$$\alpha = \{-1, 0\}$$

depending on the wave family in question. In another pertinent case, if $\gamma = 1$, or that the top and bottom layer steady states have equal depth, $\alpha = \pm\sqrt{r}$.

As for the form for λ, we can find λ in terms of either the top layer or bottom layer,

$$\lambda = \begin{cases} \pm\sqrt{gh_1}\sqrt{1+\alpha} & \text{and} \\ \pm\sqrt{gh_2}\sqrt{\alpha(r+\alpha)}. \end{cases}$$

Since α also takes on two values, these are the correct number of eigenvalues and do satisfy the characteristic polynomial. To find which values correspond to which wave-family, consider the dry-state case where the bottom layer goes to zero and take the eigenvalues dependent on the top layer only. Taking the + value of α with γ leads to the eigenvalues $\pm\sqrt{gh_1}$ which are what we expect the external waves to correspond to in the limiting case implying that taking the + value for α leads to the external eigenvalues in both directions. For the case when $\gamma = 1$, or when both layers are the same depth, $\alpha = \pm\sqrt{r}$ and $\lambda = \pm\sqrt{gh_1(1 \pm r)}$ where the case where $r > 1$ is eliminated as this represents a situation where the top layer has a higher density then

the bottom. In summary, we have

$$\begin{aligned}\lambda_{1,\text{ext}} &= -\sqrt{gh_1(1+\alpha_+)} \\ \lambda_{2,\text{int}} &= -\sqrt{gh_1(1+\alpha_-)} \\ \lambda_{3,\text{int}} &= \sqrt{gh_1(1+\alpha_-)} \\ \lambda_{4,\text{ext}} &= \sqrt{gh_1(1+\alpha_+)}\end{aligned} \tag{5.16}$$

where

$$\alpha_\pm = \frac{1}{2}\left[\gamma - 1 \pm \sqrt{(\gamma-1)^2 + 4r\gamma}\right].$$

These values then lead to the following eigenvectors

$$R = \begin{bmatrix} 1 & 1 & 1 & 1 \\ -\sqrt{gh_1(1+\alpha_+)} & -\sqrt{gh_1(1+\alpha_-)} & \sqrt{gh_1(1+\alpha_-)} & \sqrt{gh_1(1+\alpha_+)} \\ \alpha_+ & \alpha_- & \alpha_- & \alpha_+ \\ -\alpha_+\sqrt{gh_1(1+\alpha_+)} & -\alpha_-\sqrt{gh_1(1+\alpha_-)} & \alpha_-\sqrt{gh_1(1+\alpha_-)} & \alpha_+\sqrt{gh_1(1+\alpha_+)} \end{bmatrix}.$$

Note that the eigenspace that we have calculated is valid for both the original system we derived (5.4) and the modified system (5.5).

5.2.3 Loss of Hyperbolicity

An interesting consequence of the form of the approximate eigenvalues given by the velocity difference expansion from section 5.2.1 is that we can observe that if

$$\kappa \equiv \frac{(u_1 - u_2)^2}{g(1-r)(h_1+h_2)} \leq 1, \tag{5.17}$$

the approximate eigenvalues will be real. The condition is nearly the inverse to the definition of the Richardson number in stratified flow, defined as

$$\text{Ri} \equiv \frac{\rho_2 g(1-r)(h_1+h_2)}{\rho_0(u_1-u_2)^2},$$

where an additional background density ρ_0 is defined, and indicates the presence of Kelvin-Helmholtz instabilities in realistic flow conditions usually for $\text{Ri} < 1/4$ [18]. In work done by Le Sommer et al [31] it was shown that by assuming a rigid lid approximation, the shear instability corresponding to complex eigenvalues is in fact Kelvin-Helmholtz instability. For the free surface case, Chumakova et al [16] showed that the shear instability corresponding to complex eigenvalues is indicative of a Miles-Howard type of instability. Further work identifying if the elliptic region is analytically attainable has been done by Milewski et al [35] who showed that the

elliptic domain of the PDE is attainable given non-smooth initial data. Unfortunately, as shown by Abgrall and Karni [3], this condition is neither sufficient nor necessary to ensure hyperbolicity as was defined in section 2.1.

We can also plot the expected region of hyperbolicity via the κ approximation to find, given a particular r, the region we expect to remain hyperbolic, an example of which is plotted in figure 5.3.

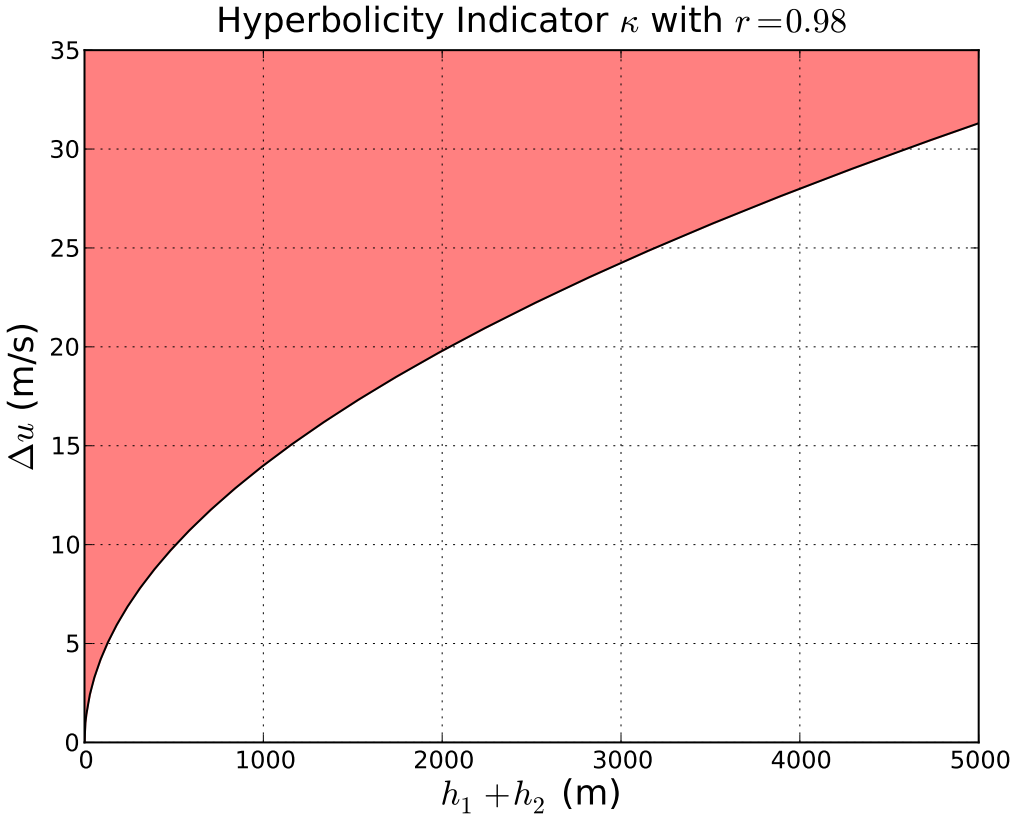

Figure 5.3: Plot of the predicted hyperbolic region from (5.17) for $r = 0.98$. For the storm surge application we expect that the total depth will be greater than 100 meters as the bottom layer will become dry away from the top layer going dry. The velocities present also will be on the order of about 5 m/s. This implies that we should not have to worry about the approximate hyperbolicity condition κ except possibly near the dry state of the bottom layer.

As an example of a situation where hyperbolicity is lost, consider the following situation. A two-layer system contained with wall boundary conditions is forced via an oscillatory wind field. The initial condition at rest with $\rho_1 = 1025$ and $\rho_2 = 1045$

for each of the layers leading to an effective $r = 0.98$ and $\rho_{\text{air}} = 1.15$. The wind field, shown at $t = 2$ in figure 5.4, forces the top layer and is prescribed by

$$W(t) = A \sin\left(\frac{n\pi x}{L}\right) \cdot \sin\left(\frac{2\pi\omega}{T}t\right)$$

where $A = 5$, $n = 2$, $\omega = 2$, $L = 1$ and $T = 10$. The momentum imparted into the layer is discussed in section 7.2. It should be noted that shocks similar to the one observed in figure 5.5 that form on the internal surface have been observed in nature at the Straight of Gibraltar [14].

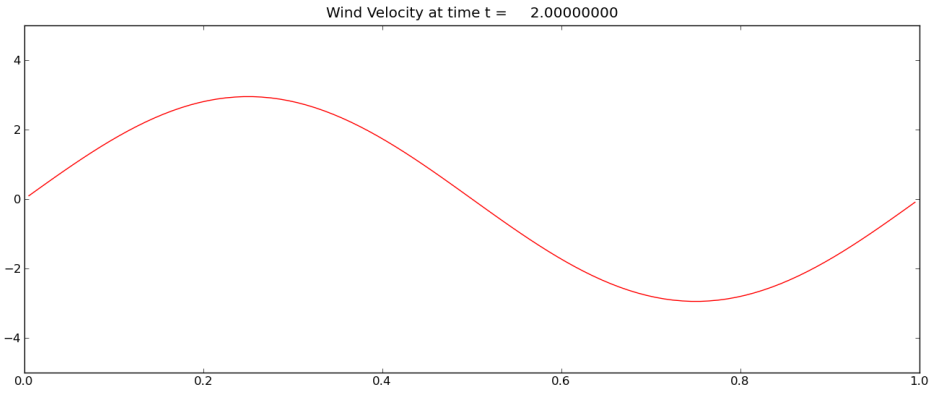

Figure 5.4: The prescribed wind field in the middle of the test.

5.2.4 Eigenspace in Two Dimensions

The calculation of the two dimensional eigenspace is a straightforward extension of the one dimensional space. If we first consider the quasi-linear coefficient matrix in the x-direction (5.10), we can factor the characteristic polynomial of the quasi-linear coefficient matrix as

$$(\lambda - u_1)(\lambda - u_2)[((\lambda - u_1)^2 - gh_1)((\lambda - u_2)^2 - gh_2) - rg^2h_1h_2] = 0.$$

This polynomial contains the same roots as the one dimensional characteristic polynomial (5.12) with the addition of $\lambda = u_1$ and u_2. We can therefore apply the approximations we have developed for the one dimensional case to the two dimensional case. We will subsequently use the notational convention that eigenvalues λ^1, λ^2,λ^3, and λ^4 refer to the eigenvalues solving the one-dimensional eigenvalues as before and $\lambda^5 = u_1$ and $\lambda^6 = u_2$ refer to the eigenvalues due to the transverse momentum.

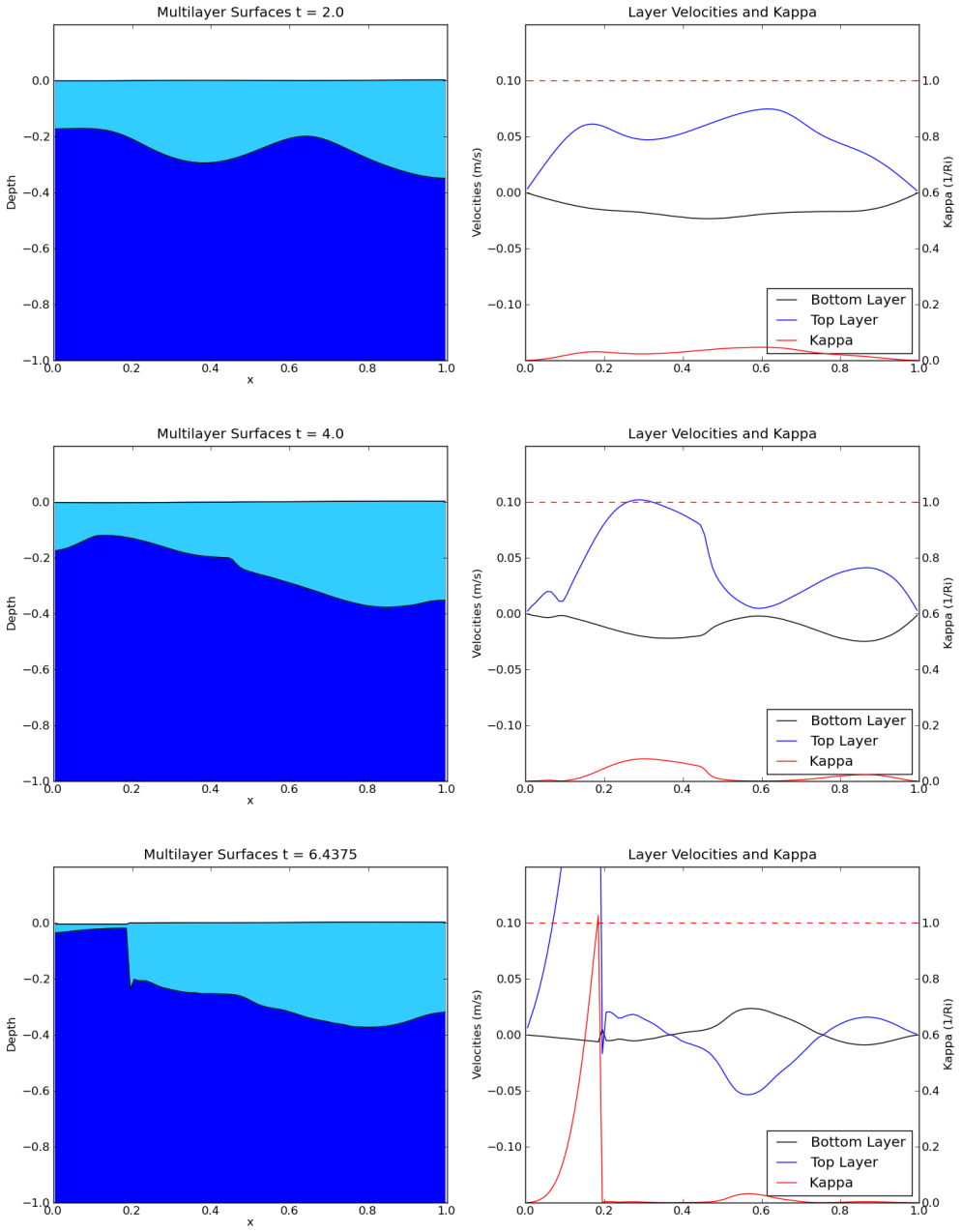

Figure 5.5: Snapshots of the solution computed by the LAPACK eigensolver for the oscillatory wind field problem. The last time shown is approximately where the method produced complex eigenvalues.

In a similar way, the eigenvectors of the two dimensional case include two extra vectors corresponding to the transverse momenta in each direction. The vectors are dependent on the eigenvalues and a value α that can be determined as described above again. The eigenvectors are then

$$\begin{bmatrix} 1 & 1 & 0 & 0 & 1 & 1 \\ \lambda^1 & \lambda^2 & 0 & 0 & \lambda^3 & \lambda^4 \\ v_1 & v_1 & 1 & 0 & v_1 & v_1 \\ \alpha_1 & \alpha_2 & 0 & 0 & \alpha_3 & \alpha_4 \\ \alpha_1\lambda_1 & \alpha_2\lambda_2 & 0 & 0 & \alpha_3\lambda_3 & \alpha_4\lambda_4 \\ \alpha_1 v_2 & \alpha_2 v_2 & 0 & 1 & \alpha_3 v_2 & \alpha_4 v_2 \end{bmatrix}$$

where we have kept the same definition of the eigenvalues as before.

The y-direction eigenspace calculated from the quasi-linear coefficient matrix (5.11) is nearly identical to the x-direction. The eigenvalues corresponding to the one dimensional equations are λ^1, λ^2, λ^3, and λ^4 and obey

$$((\lambda - v_1)^2 - gh_1)((\lambda - v_2)^2 - gh_2) - rg^2h_1h_2 = 0$$

while $\lambda^5 = v_1$ and $\lambda^6 = v_2$. The eigenvectors are

$$\begin{bmatrix} 1 & 1 & 0 & 0 & 1 & 1 \\ u_1 & u_1 & 1 & 0 & u_1 & u_1 \\ \lambda^1 & \lambda^2 & 0 & 0 & \lambda^3 & \lambda^4 \\ \alpha_1 & \alpha_2 & 0 & 0 & \alpha_3 & \alpha_4 \\ \alpha_1 u_2 & \alpha_2 u_2 & 0 & 1 & \alpha_3 u_2 & \alpha_4 u_2 \\ \alpha_1\lambda^1 & \alpha_2\lambda^2 & 0 & 0 & \alpha_3\lambda^3 & \alpha_4\lambda^4 \end{bmatrix}$$

5.3 Solving the Riemann Problem

In general we would like to solve the Riemann problem defined by the quasi-linear coefficient matrix (5.7) in conjunction with the bathymetry source terms. In order to treat the bathymetry terms, we can add an additional conserved quantity b and rewrite the system again with the addition of $q^5 = b$, $[f(q)]^5 = 0$, and $[S(q)]^5 = 0$ and rewriting quasi-linear coefficient matrix as

$$A(q) = \begin{bmatrix} 0 & 1 & 0 & 0 & 0 \\ gh_1 - u_1^2 & 2u_1 & -gh_1 & 0 & -gh_1 \\ 0 & 0 & 0 & 1 & 0 \\ -rgh_2 & 0 & gh_2 - u_2^2 & 2u_2 & -gh_2 \\ 0 & 0 & 0 & 0 & 0 \end{bmatrix}.$$

This allows us to treat the basic problem analytically in its entirety in the Riemann solver. To identify the type of behavior we expect, first we must identify the genuinely non-linear fields as was defined in definition (2.2.1). As we do not have explicit forms for the eigenvalues, this is rather difficult although the approximations we have indicate that all of the fields are genuinely nonlinear. This implies that in order to solve the Riemann problem, we must find the appropriate jump conditions for these equations, either the Riemann invariants or integral curves for the rarefactions, and a suitable entropy condition to choose between the two. We will also address the practical consideration of what to do if the bottom layer reaches a dry state.

5.3.1 Path Conservative Jump Conditions

In order to derive a set of shock or jump conditions for the system it is useful to consider the more general conditions of a path conservative scheme, which dictates that

$$s(q_r - q_\ell) = \int_0^1 \tilde{A}(q(s))q'(s)ds \tag{5.18}$$

where $\tilde{A}(q)$ is the quasi-linear coefficient matrix and can be related to the original flux jacobian A by

$$\tilde{A} = A + \hat{A}.$$

In the case of a homogenous system, this condition simplifies to the Rankine-Hugoniot conditions (2.6). For a particular wave then we can define the jump in the conserved quantities using this equation. We will use this later to find jump conditions across all of the waves in the system but first we will evaluate the integral here so that we can later use it as an approximation as in

$$\int_0^1 \tilde{A}(q(s))q'(s)ds \approx f(q_r) - f(q_\ell) + \psi. \tag{5.19}$$

We can begin by expanding the integral out into its components as

$$\begin{aligned}\int_0^1 \tilde{A}(q(s))q'(s)ds &= \int_0^1 A(q(s))q'(s)ds + \int_0^1 \hat{A}(q(s))q'(s)ds \\ &= \int_0^1 f'(q(s))ds + \int_0^1 \hat{A}(q(s))q'(s)ds = f(q_r) - f(q_\ell) + \int_0^1 \hat{A}(q(s))q'(s)ds.\end{aligned}$$

Assuming a linearly parameterized path through state space defined by

$$q(s) = \begin{bmatrix} (h_{1r} - h_{1\ell})s + h_{1\ell} \\ ((hu)_{1r} - (hu)_{1\ell})s + (hu)_{1\ell} \\ (h_{2r} - h_{2\ell})s + h_{2\ell} \\ ((hu)_{2r} - (hu)_{2\ell})s + (hu)_{2\ell} \\ (b_r - b_\ell)s + b_\ell \end{bmatrix},$$

and its derivative

$$q'(s) = \begin{bmatrix} h_{1r} - h_{1\ell} \\ hu_{1r} - hu_{1\ell} \\ h_{2r} - h_{2\ell} \\ hu_{2r} - hu_{2\ell} \\ b_r - b_\ell \end{bmatrix} = \begin{bmatrix} [h_1] \\ [h_1 u_1] \\ [h_2] \\ [h_2 u_2] \\ [b] \end{bmatrix},$$

the integral can be calculated as

$$\int_0^1 \hat{A}(q(s))q'(s)ds = \int_0^1 \begin{bmatrix} 0 & 0 & 0 & 0 & 0 \\ 0 & 0 & -gh_1(s) & 0 & -gh_1(s) \\ 0 & 0 & 0 & 0 & 0 \\ -rgh_2(s) & 0 & 0 & 0 & -gh_2(s) \\ 0 & 0 & 0 & 0 & 0 \end{bmatrix} \cdot \begin{bmatrix} [h_1] \\ [h_1 u_1] \\ [h_2] \\ [h_2 u_2] \\ [b] \end{bmatrix} ds$$

$$= \begin{bmatrix} 0 \\ \int_0^1 (-gh_1(s)[h_2] - gh_1(s)[b])ds \\ 0 \\ \int_0^1 (-rgh_2(s)[h_1] - gh_2(s)[b])ds \\ 0 \end{bmatrix} = \begin{bmatrix} 0 \\ -g([h_2] + [b]) \int_0^1 h_1(s)ds \\ 0 \\ -g(r[h_1] + [b]) \int_0^1 h_2(s)ds \\ 0 \end{bmatrix}.$$

The integrals left to evaluate are simply

$$\int_0^1 h_1(s)ds = \int_0^1 ((h_{1r} - h_{1\ell})s + h_{1\ell})ds = \frac{h_{1r} - h_{1\ell}}{2} + h_{1\ell} = \frac{h_{1r} + h_{1\ell}}{2} = \overline{h_1} \quad \text{and}$$
$$\int_0^1 h_2(s)ds = \int_0^1 ((h_{2r} - h_{2\ell})s + h_{2\ell})ds = \frac{h_{2r} - h_{2\ell}}{2} + h_{2\ell} = \frac{h_{2r} + h_{2\ell}}{2} = \overline{h_2}$$

and the final integrals are

$$\int_0^1 \hat{A}(q(s))q'(s)ds = \begin{bmatrix} 0 \\ -g([h_2] + [b])\overline{h_1} \\ 0 \\ -g(r[h_1] + [b])\overline{h_2} \\ 0 \end{bmatrix}. \tag{5.20}$$

The jump conditions resulting from the choice of a linear path through state space is then

$$s(q_r - q_\ell) = f(q_r) - f(q_\ell) - g \begin{bmatrix} 0 \\ ([h_2] + [b])\overline{h_1} \\ 0 \\ (r[h_1] + [b])\overline{h_2} \\ 0 \end{bmatrix}. \tag{5.21}$$

This defines a set of four non-linear equations for connecting across a single shock moving at speed s with left and right states q_ℓ and q_r respectively.

5.3.2 Rarefaction Solutions

Due to the complexity of the system, deriving the Riemann invariants directly for the multi-layer equations is intractable currently. A set of approximate Riemann invariants may be possible based on the Riemann invariants found in the single-layer shallow water equations (which is in fact what we will do when evaluating dry state problems for the bottom layer).

5.3.3 Entropy Condition

As with the shallow water equations, the multi-layer shallow water equations admit a global convex entropy motivated by physics, the energy. According to Bouchut and Morales de Luna [11], admissible weak solutions of the equations should then satisfy the inequality

$$E(q)_t + G(q)_x \leq 0 \tag{5.22}$$

where the energy can be written as

$$E(q) = \rho_1 \left(h_1 \frac{u_1^2}{2} + g\frac{h_1^2}{2} \right) + \rho_2 \left(h_2 \frac{u_2^2}{2} + g\frac{h_2^2}{2} \right) + \rho_1 g h_1 h_2 + \rho_1 g h_1 b + \rho_2 g h_2 b$$

and the energy flux

$$G(q) = \rho_1 \left(h_1 \frac{u_1^2}{2} + g h_1^2 \right) u_1 + \rho_2 \left(h_2 \frac{u_2^2}{2} + g h_2^2 \right) u_2 + \rho_1 g h_1 h_2 (u_1 + u_2) + \rho_1 g h_1 u_1 b + \rho_2 g h_2 u_2 b.$$

In the context of numerically computing solutions to the multi-layer equations, Bouchut and Morales de Luna discuss using a splitting method that inherently obeys the discrete version of the entropy conditions.

In principle, we could use these to ensure that we choose the correct entropy satisfying solutions. However, since we do not have explicit relationships for the simple wave case as discussed in section 5.3.2, these equations only provide an estimate as to whether we have found a valid physical solution to the problem.

5.3.4 Wall Dry States

The focus of this section is to solve the Riemann problem when a dry state exists for the bottom layer. Consider the Riemann problem illustrated in figure 5.6a where $h_{2\ell} > 0$, $h_{2r} = 0$, and $h_{2\ell} + b_\ell < b_r$. We would expect that a wave on the internal interface to reflect off of the bathymetry and the associated Riemann solution to have a structure similar to figure 5.6b. The assumption will also be made that the momentum $h_{2\ell}u_{2\ell}$ is not large enough to overcome the bathymetry jump. The states for this Riemann problem are

$$q_r = \begin{bmatrix} h_{1r} \\ (hu)_{1r} \\ 0 \\ 0 \end{bmatrix}, \quad q_r^* = \begin{bmatrix} h_{1r}^* \\ (hu)_{1r}^* \\ 0 \\ 0 \end{bmatrix}, \quad \text{and} \quad q_\ell^{**} = \begin{bmatrix} h_{1\ell}^{**} \\ (hu)_{1\ell}^{**} \\ h_{2\ell}^{**} \\ 0 \end{bmatrix}. \tag{5.23}$$

We can then connect the right state q_r to q_r^* over the 4th wave family, which gives the relation

$$\lambda^4 \begin{bmatrix} h_{1r} - h_{1r}^* \\ (hu)_{1r} - (hu)_{1r}^* \\ 0 \\ 0 \end{bmatrix} = \begin{bmatrix} (hu)_{1r} - (hu)_{1r}^* \\ \varphi_{1r} - \varphi_{1r}^* \\ 0 \\ 0 \end{bmatrix}. \tag{5.24}$$

This is the usual Rankine-Hugoniot condition $s(q_r - q_\ell) = f(q_r) - f(q_\ell)$, but only for the top surface, revealing that this wave should act just as the rightward going wave of single layer shallow water would. Using the above equations gives us the following parameterized Hugoniot locus for the valid connecting states from q_r to q_r^*

$$(hu)_{1r}^* = (hu)_{1r} + \gamma \left[u_{1r} + \sqrt{g h_{1r} \left(1 + \frac{\gamma}{h_{1r}}\right) \left(1 + \frac{\gamma}{2h_{1r}}\right)} \right] \tag{5.25}$$

where γ acts to parameterize the movement along the Hugoniot locus via $h_{1r}^* = h_{1r} + \gamma$. Note that in general there is a choice of sign that would determine which wave this is. Since we are interested in what would be the 2-wave in shallow water, the positive sign is the correct choice corresponding to $\lambda^4 = u_{1r} + \sqrt{g h_{1r}}$.

We now turn to the formulation of a family of states that can connect one state to another, similar to what has been done for the single-layer shallow water equations. Consider a fixed state q_* and the set of states that lie on the same Hugoniot locus q. The Rankine-Hugoniot condition for the two-layer shallow water system (2.6) then

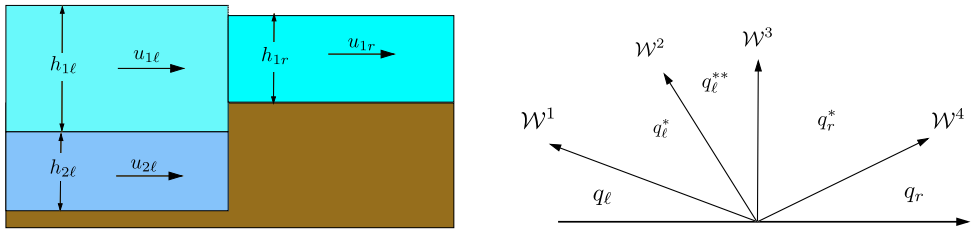

(a) Dry state problem setup.

(b) Riemann solution structure.

Figure 5.6: Sample dry state Riemann problem for the two-layer shallow water equations. In this case, the dry state exists for the right side and the states q_ℓ^{**} and q_r^* have specific values that will enforce the dry state.

prescribes a set of 4 equations for connecting q to q_*

$$\lambda(h_{1*} - h_1) = h_{1*}u_{1*} - h_1u_1 \tag{5.26}$$

$$\lambda(h_{1*}u_{1*} - h_1u_1) = h_{1*}u_{1*}^2 - h_1u_1^2 + \frac{1}{2}g(h_{1*}^2 - h_1^2 - (h_{2*} - h_2)(h_{1*} + h_1)) \tag{5.27}$$

$$\lambda(h_{2*} - h_2) = h_{2*}u_{2*} - h_2u_2 \tag{5.28}$$

$$\lambda(h_{2*}u_{2*} - h_2u_2) = h_{2*}u_{2*}^2 - h_2u_2^2 + \frac{1}{2}g(h_{2*}^2 - h_2^2 - gr(h_{1*} - h_1)(h_{2*} + h_2)) \tag{5.29}$$

Here we will ignore the jump in bathymetry for the time being until we connect across the 3-wave, which propagates with speed 0. Dividing equation (5.26) by equation (5.28) leads to a relationship between the jumps in depth and momentum between the layers

$$\frac{h_{1*} - h_1}{h_{2*} - h_2} = \frac{h_{1*}u_{1*} - h_1u_1}{h_{2*}u_{2*} - h_2u_2} \quad \text{or} \quad \frac{\Delta h_1}{\Delta h_2} = \frac{\Delta hu_1}{\Delta hu_2}.$$

Turning to the relationship for the momentum of the top-layer (5.27) we can perform the following manipulations

$$\begin{aligned}
&(h_{1*}u_{1*} - h_1u_1)^2 = (h_{1*} - h_1)\left[h_{1*}u_{1*}^2 - h_1u_1^2 + 1/2g(h_{1*}^2 - h_1^2 - (h_{2*} - h_2)(h_{1*} + h_1)\right], \\
&(h_{1*}u_{1*})^2 - 2h_{1*}u_{1*}h_1u_1 + (h_1u_1)^2 \\
&\quad = (h_{1*} - h_1)\left[h_{1*}u_{1*}^2 - h_1u_1^2 + 1/2g(h_{1*}^2 - h_1^2 - h_{2*}h_{1*} - h_{2*}h_1 + h_2h_{1*} + h_2h_1)\right], \\
&(h_{1*}u_{1*})^2 - 2h_{1*}u_{1*}h_1u_1 + (h_1u_1)^2 \\
&\quad = h_{1*}\left[h_{1*}u_{1*}^2 - h_1u_1^2 + 1/2g(h_{1*}^2 - h_1^2 - h_{2*}h_{1*} - h_{2*}h_1 + h_2h_{1*} + h_2h_1)\right] \\
&\quad - h_1\left[h_{1*}u_{1*}^2 - h_1u_1^2 + 1/2g(h_{1*}^2 - h_1^2 - h_{2*}h_{1*} - h_{2*}h_1 + h_2h_{1*} + h_2h_1)\right].
\end{aligned}$$

Unfortunately, there is no clear way to proceed in the analysis at this point. One would

have to solve a system of non-linear equations in order to find the valid connecting states.

Another approach is to use the linearized form of the equations found earlier in section 5.2.2. Again consider the dry state problem defined in figure 5.6b. In order to solve the Riemann problem in the linear case, we must project the initial condition

$$q(x,0) = q_0 + \epsilon r^p H(x) \tag{5.30}$$

where q_0 is a background state with a perturbation of size ϵ in one of the eigenfamilies p and $H(x)$ is the Heaviside function, onto the eigenspace. Note that we are assuming that the wave contains values from the left steady state but with appropriate directions. The α value for the steady state with a dry state on the left is

$$\alpha_{\pm\ell} = \frac{1}{2}\left[\gamma_\ell - 1 \pm \sqrt{(\gamma_\ell - 1)^2 + 4r\gamma_\ell}\right]$$

and for the right

$$\alpha_{\pm r} = \frac{1}{2}(-1 \pm 1)$$

since $\gamma = 0$ for the right state. The corresponding eigenvalues are then

$$\begin{aligned}
\lambda_1 &= -\sqrt{gh_{1\ell}(1+\alpha_1)},\\
\lambda_2 &= -\sqrt{gh_{1\ell}(1+\alpha_2)},\\
\lambda_3 &= \sqrt{gh_{1r}(1+1/2(-1-1))} = 0,\\
\lambda_4 &= \sqrt{gh_{1r}(1+1/2(-1+1))} = \sqrt{gh_{1r}}.
\end{aligned}$$

This leads to the eigenspace

$$R = \begin{bmatrix} 1 & 1 & 1 & 1 \\ \lambda_1 & \lambda_2 & 0 & \lambda_4 \\ \alpha_1 & \alpha_2 & -1 & 0 \\ \lambda_1\alpha_1 & \lambda_2\alpha_2 & 0 & 0 \end{bmatrix}. \tag{5.31}$$

Projecting $q(x,0)$ onto the eigenspace (5.31) leads to the following system of equations

$$\begin{aligned}
\beta_1 + \beta_2 + \beta_3 + \beta_4 &= \Delta_1,\\
\lambda_1\beta_1 + \lambda_2\beta_2 + \lambda_4\beta_4 &= \Delta_2,\\
\alpha_1\beta_1 + \alpha_2\beta_2 - \beta_3 &= \Delta,\\
\lambda_1\alpha_1\beta_1 + \lambda_2\alpha_2\beta_2 &= \Delta_4.
\end{aligned}$$

Solving these equations leads to expressions for

$$\begin{aligned}\beta_2 &= \frac{\Delta_4 - \lambda_1\alpha_1\beta_1}{\lambda_2\alpha_2},\\ \beta_3 &= \alpha_1\beta_1 + \alpha_2\beta_2 - \Delta_3,\\ \beta_4 &= \frac{\Delta_2 - \lambda_1\beta_1 - \lambda_2\beta_2}{\lambda_4}.\end{aligned}$$

Using a computational algebra system, β_1 can be found to be

$$\beta_1 = \frac{\lambda_4\left\{\Delta_4 + \alpha_2\left[\Delta_4 + \lambda_2(\Delta_1 + \Delta_3)\right]\right\} + \lambda_2(\Delta_2\alpha_2 - \Delta_4)}{\lambda_4\left\{\lambda_1\alpha_1 + \alpha_2\left[\alpha_1(\lambda_1 - \lambda_2) - \lambda_2\right]\right\} + \lambda_1\lambda_2(\alpha_2 - \alpha_1)}.$$

Looking at some simple cases, consider the case where γ_ℓ is also zero, reducing the equations to the single layer shallow water equations everywhere (including the initial condition). This leads to

$$R = \begin{bmatrix} 1 & 1 & 1 & 1 \\ -\sqrt{gh_{1\ell}} & 0 & 0 & \sqrt{gh_{1r}} \\ 0 & -1 & -1 & 0 \\ 0 & 0 & 0 & 0 \end{bmatrix}.$$

This is the linearized single layer shallow water eigenspace and our results agree with what is expected.

Now consider the case where $\gamma_\ell = 1$, in other words the two layers on the left have equal steady state depth. The eigenvectors then become

$$R = \begin{bmatrix} 1 & 1 & 1 & 1 \\ -\sqrt{gh_{1\ell}(1+\sqrt{r})} & -\sqrt{gh_{1\ell}(1-\sqrt{r})} & 0 & \sqrt{gh_{1r}} \\ \sqrt{r} & -\sqrt{r} & -1 & 0 \\ -\sqrt{rgh_{1\ell}(1+\sqrt{r})} & -\sqrt{rgh_{1\ell}(1-\sqrt{r})} & 0 & 0 \end{bmatrix}.$$

Solving this system leads to

$$\begin{aligned}\beta_3 &= (\beta_1 - \beta_2 - \epsilon)\sqrt{r}\\ \beta_4 &= \frac{(\epsilon + \beta_1)\sqrt{gh_{1\ell}(1+\sqrt{r})} + \sqrt{gh_{1\ell}(1-\sqrt{r})}\beta_2}{\sqrt{gh_{1r}}}\\ \beta_2 &= \frac{-\sqrt{gh_{1\ell}(1+\sqrt{r})}(\beta_1 + \epsilon)}{-\sqrt{gh_{1\ell}(1-\sqrt{r})}}\end{aligned}$$

Finally, using an approximate solver described in chapter 6, figures 5.7 shows an idealized simulation in the 3rd wave family with the initial conditions prescribed by

(5.30). Figures 5.8 and 5.9 shows a similar simulation in the 4th wave family. The initial condition used was based on calculating the eigenvector of the initial state at rest and adding it to the background steady state $\hat{q}(x,0) = [\rho_1 h_1, 0, \rho_2 h_2, 0]^T$ such that

$$q(x,0) = \begin{cases} r^p \epsilon + \hat{q}(x,0) & \text{if } x < x_0 \text{ and} \\ \hat{q}(x,0) & \text{if } x \geq x_0. \end{cases}.$$

5.3.5 Inundation

Inundation of the bottom layer occurs either if the momentum of the wet state is large enough to overcome the bathymetry jump or the wet state surface is greater than the bathymetry jump. For the single-layer equations methods have been reliably developed in order to solve the inundation of just the top surface but unfortunately the same methods do not apply reliably to the multi-layer equations due to interactions between the layers. Various approximations may be possible and Bouchut and Morales de Luna in [11] have proposed a method that does not require the use of explicitly treating this problem separately from the single layer case by satisfying a discrete form of the entropy condition (5.22).

For simplicity, consider the case when the left state is wet and inundation will occur due to $h_{2\ell} + b_\ell > b_r$ as in figure 5.10. We expect a rarefaction to wet the dry cells moving at high speed relative to the speeds of the local eigenvalue problem. For the cases of interest here, we will assume that $s^3 < s^4$. In general this is not guaranteed but it allows us to consider only one situation where the states in the Riemann problem sketched in figure 5.10 are defined as

$$\begin{aligned} q_\ell &= \begin{bmatrix} h_{1\ell} \\ \mu_{1\ell} \\ h_{2\ell} \\ \mu_{2\ell} \end{bmatrix}, \quad q_\ell^* = \begin{bmatrix} h_{1\ell}^* \\ \mu_{1\ell}^* \\ h_{2\ell}^* \\ \mu_{2\ell}^* \end{bmatrix}, \qquad q_\ell^{**} = \begin{bmatrix} h_{1\ell}^{**} \\ \mu_{1\ell}^{**} \\ h_{2\ell}^{**} \\ \mu_{2\ell}^{**} \end{bmatrix}, \\ q_r^{**} &= \begin{bmatrix} h_{1r}^{**} \\ \mu_{1r}^{**} \\ h_{2r}^* \\ \mu_{2r}^* \end{bmatrix}, \quad q_r^* = \begin{bmatrix} h_{1r}^* \\ \mu_{1r}^* \\ 0 \\ 0 \end{bmatrix}, \qquad \text{and} \quad q_r = \begin{bmatrix} h_{1r} \\ \mu_{1r} \\ 0 \\ 0 \end{bmatrix}. \end{aligned} \tag{5.32}$$

As is suggested, wave $\mathcal{Z}^4$ carries only a jump in the top layer and for the case when $h_{1r}^* > h_{1r}$ the states are connected via a shock. The states satisfy the relationship

$$u_{1r}^* - h_{1r}^* \sqrt{\frac{g}{2}\left(\frac{1}{h_{1r}^*} + \frac{1}{h_{1r}}\right)} = u_{1r} - h_{1r} \sqrt{\frac{g}{2}\left(\frac{1}{h_{1r}^*} + \frac{1}{h_{1r}}\right)}$$

which is derived from the Rankine-Hugoniot condtion (2.6) for the single-layer equa-

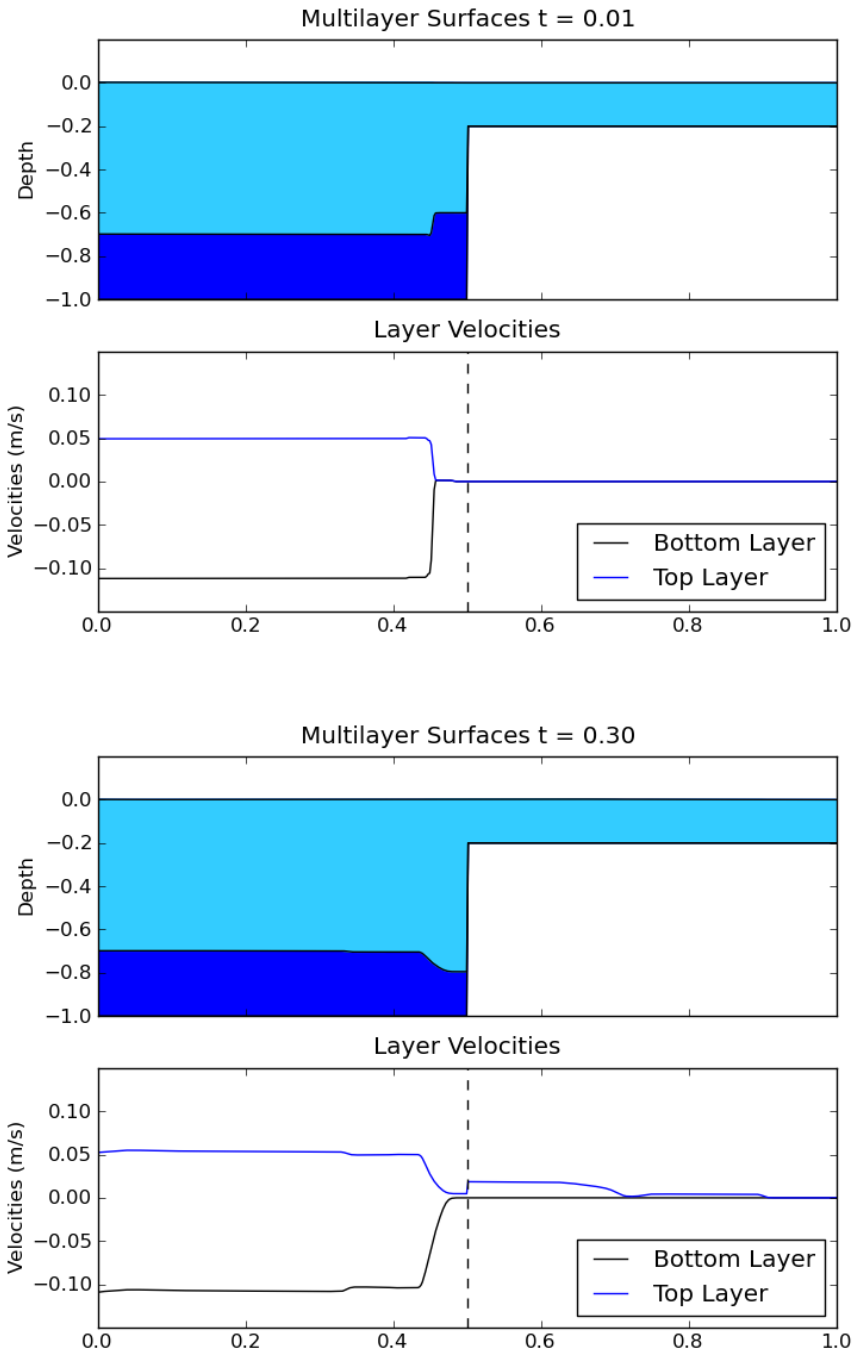

Figure 5.7: Simulation showing a wave in the 3rd wave-family at a wall dry state problem. The values used for the simulation were $r = 0.95$ and $\epsilon = 0.1$.

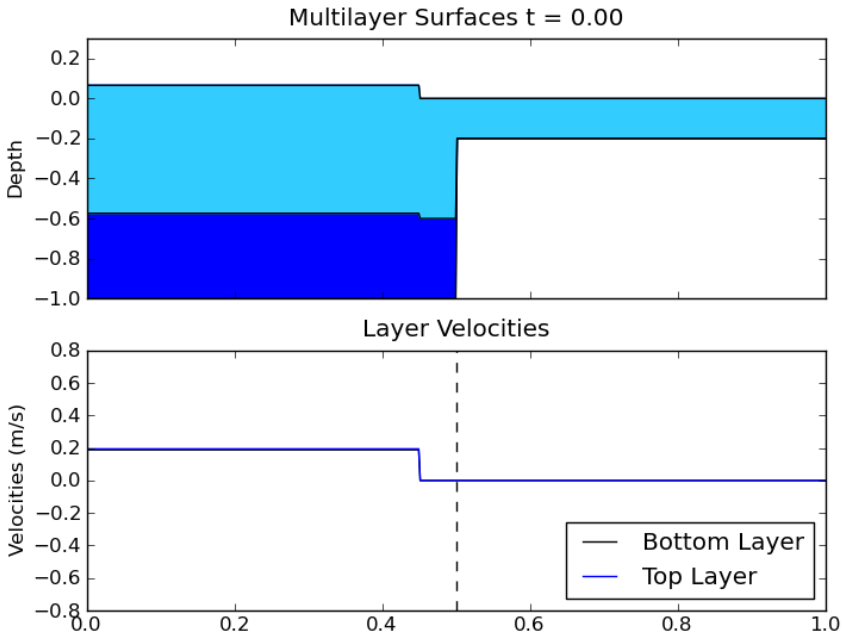

Figure 5.8: Initial perturbation on a steady state in the 4th wave-family.

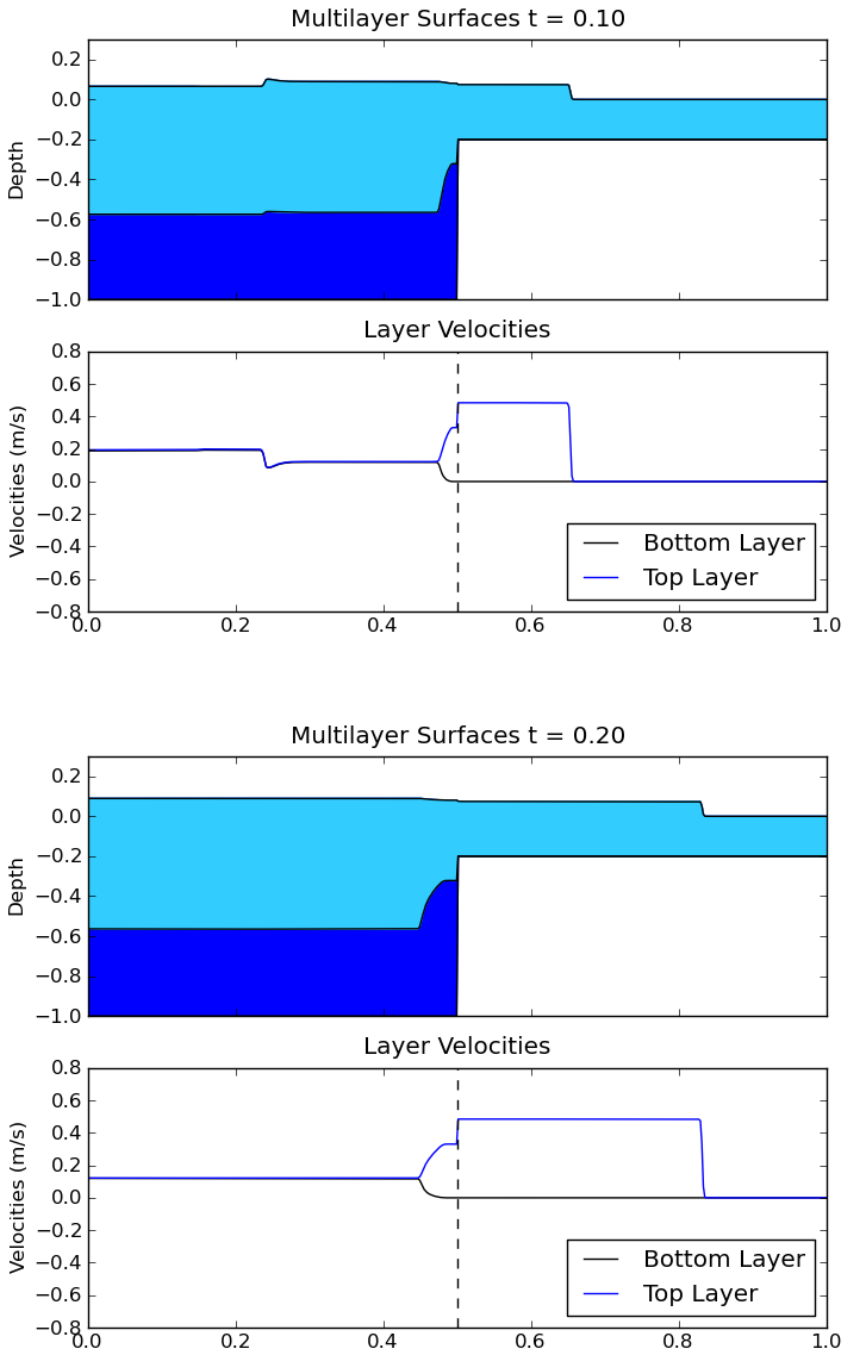

Figure 5.9: Simulation showing a wave in the 4th wave-family at a wall dry state problem. The values used for the simulation were $r = 0.95$ and $\epsilon = 0.04$

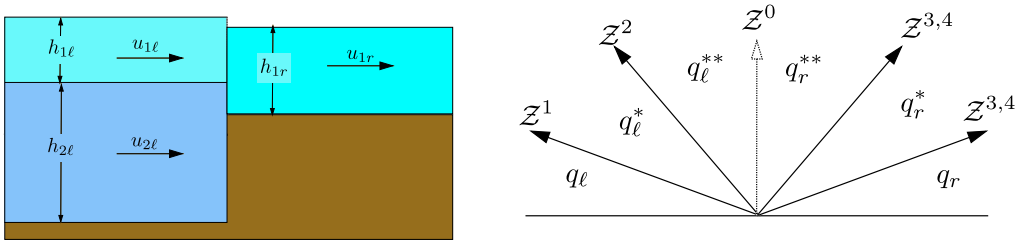

Figure 5.10: On the right is a representation of the states being considered in the inundation problem. In particular, $h_{2\ell} + b_\ell > b_r$ and so we expect the right cell to become wet in the bottom layer. On the right is a diagram of the Riemann solution waves and the labels of the states in between each state.

tions. If $h^*_{1r} < h_{1r}$ then a rarefaction connects the states, with the Riemann invariant

$$u^*_{1r} - 2\sqrt{gh^*_{1r}} = u_{1r} - 2\sqrt{gh_{1r}}.$$

The wave $\mathcal{Z}^3$ contains the jump from wet to dry in the bottom layer. In terms of the states in (5.32), $\mathcal{Z}^3$ can be written as

$$\mathcal{Z}^3 = \begin{bmatrix} h^*_{1r}u^*_{1r} - h^{**}_{1r}u^{**}_{1r} \\ h^*_{1r}(u^*_{1r})^2 - h^{**}_{1r}(u^{**}_{1r})^2 + \frac{1}{2}g\left((h^*_{1r})^2 - (h^{**}_{1r})^2\right) - \frac{1}{2}rg(h^*_{1r} + h^{**}_{1r})h^*_{2r} \\ -h^*_{2r}u^*_{2r} \\ -h^*_{2r}(u^*_{2r})^2 - \frac{1}{2}g\left(h^*_{2r}\right)^2 + \frac{1}{2}rg\left(h^*_{1r} - h^{**}_{1r}\right)h^*_{2r} \end{bmatrix}.$$

The jump conditions that were derived in section 5.3.1 also relate the speeds of the waves and the jump in conserved quantities to the waves such that

$$\mathcal{Z}^p = s^p(q_r - q_\ell) \tag{5.33}$$

for the appropriate connecting states q_r and q_ℓ. For the 3rd wave, this relationship implies

$$\begin{bmatrix} h^*_{1r}u^*_{1r} - h^{**}_{1r}u^{**}_{1r} \\ h^*_{1r}(u^*_{1r})^2 - h^{**}_{1r}(u^{**}_{1r})^2 + \frac{1}{2}g\left((h^*_{1r})^2 - (h^{**}_{1r})^2\right) - \frac{1}{2}rg(h^*_{1r} + h^{**}_{1r})h^*_{2r} \\ -h^*_{2r}u^*_{2r} \\ -h^*_{2r}(u^*_{2r})^2 - \frac{1}{2}g\left(h^*_{2r}\right)^2 + \frac{1}{2}rg\left(h^*_{1r} - h^{**}_{1r}\right)h^*_{2r} \end{bmatrix} = s^3 \begin{bmatrix} h^*_{1r} - h^{**}_{1r} \\ h^*_{1r}u^*_{1r} - h^{**}_{1r}u^{**}_{1r} \\ -h^*_{2r} \\ -h^*_{2r}u^*_{2r} \end{bmatrix}.$$

For the stationary wave $\mathcal{Z}^0$ at the jump in bathymetry, we assume that the fluxes are continuous over the wave, implying that $f(q^{**}_r) = f(q^{**}_\ell)$. This relation then

implies

$$\begin{aligned} h^{**}_{1r}u^{**}_{1r} &= h^{**}_{1\ell}u^{**}_{1\ell}, \\ h^{**}_{1r}(u^{**}_{1r})^2 + \frac{1}{2}g(h^{**}_{1r})^2 &= h^{**}_{1\ell}(u^{**}_{1\ell})^2 + \frac{1}{2}(h^{**}_{1\ell})^2, \\ h^{*}_{2r}u^{*}_{2r} &= h^{**}_{2\ell}u^{**}_{2\ell}, \quad \text{and} \\ h^{*}_{2r}(u^{*}_{2r})^2 + \frac{1}{2}g(h^{*}_{2r})^2 &= h^{**}_{2\ell}(u^{**}_{2\ell})^2 + \frac{1}{2}g(h^{**}_{2\ell})^2. \end{aligned} \tag{5.34}$$

Similarly we can write the expected waves $\mathcal{Z}^1$ and $\mathcal{Z}^2$ as

$$\mathcal{Z}^1 = \begin{bmatrix} h^{*}_{1\ell}u^{*}_{1\ell} - h_{1\ell}u_{1\ell} \\ h^{*}_{1\ell}(u^{*}_{1\ell})^2 - h_{1\ell}(u_{1\ell})^2 + \frac{1}{2}g\left((h^{*}_{1\ell})^2 - (h_{1\ell})^2\right) + \frac{1}{2}rg(h^{*}_{1\ell} + h_{1\ell})(h^{*}_{2\ell} - h_{2\ell}) \\ h^{*}_{2\ell}u^{*}_{2\ell} - h_{2\ell}u_{2\ell} \\ h^{*}_{2\ell}(u^{*}_{2\ell})^2 - h_{2\ell}(u_{2\ell})^2 + \frac{1}{2}g\left((h^{*}_{2\ell})^2 - (h_{2\ell})^2\right) \quad \hookleftarrow \\ \qquad + rg(h^{*}_{1\ell}h^{*}_{2\ell} - h_{1\ell}h_{2\ell}) - \frac{1}{2}rg(h^{*}_{1\ell} + h_{1\ell})(h^{*}_{2\ell} - h_{2\ell}) \end{bmatrix}$$

and

$$\mathcal{Z}^2 = \begin{bmatrix} h^{**}_{1\ell}u^{**}_{1\ell} - h^{*}_{1\ell}u^{*}_{1\ell} \\ h^{**}_{1\ell}(u^{**}_{1\ell})^2 - h^{*}_{1\ell}(u^{*}_{1\ell})^2 + \frac{1}{2}g\left((h^{**}_{1\ell})^2 - (h^{*}_{1\ell})^2\right) + \frac{1}{2}rg(h^{**}_{1\ell} + h^{*}_{1\ell})(h^{**}_{2\ell} - h^{*}_{2\ell}) \\ h^{**}_{2\ell}u^{**}_{2\ell} - h^{*}_{2\ell}u^{*}_{2\ell} \\ h^{**}_{2\ell}(u^{**}_{2\ell})^2 - h^{*}_{2\ell}(u^{*}_{2\ell})^2 + \frac{1}{2}g\left((h^{*}_{2\ell})^2 - (h^{*}_{2\ell})^2\right) \quad \hookleftarrow \\ \qquad + rg(h^{**}_{1\ell}h^{**}_{2\ell} - h^{*}_{1\ell}h^{*}_{2\ell}) - \frac{1}{2}rg(h^{**}_{1\ell} + h^{*}_{1\ell})(h^{**}_{2\ell} - h^{*}_{2\ell}) \end{bmatrix}.$$

With the relation (5.33) we in principle could solve for the connecting states q^{*}_{ℓ}, q^{**}_{ℓ}, q^{**}_{r}, and q^{*}_{r}. This would involve solving 12 nonlinear equations due to the Rankine-Hugoniot condition and 4 nonlinear equations due to the flux continuity requirement over the stationary wave $\mathcal{Z}^0$. Unfortunately this is again an intractable problem and an approximation method must be employed. One way to accomplish this would be to solve using a Newton solver. In the next chapter another way of approximating the solution to this problem is presented which is a fraction of the cost of computing a Newton iteration.

Chapter 6

FINITE VOLUME METHODS FOR MULTI-LAYER SHALLOW WATER EQUATIONS

The goal of this chapter is to establish a fast, accurate solver for the multi-layer shallow water equations in two dimensions (5.8) in an oceanic scale setting. The main assumption made is that dry states only exist in two cases, either at shore where the only layer present is the top, or away from the shore so that both will not become dry at the same time. The robust treatment of these dry states are one of the primary challenges in designing a robust solver. First the basic algorithm will be described for a one dimensional solver with the relevant cases described in detail. Then a description of the issues that appear in two dimensions will be described. Finally both solvers will be evaluated using idealized test cases designed to stress the handling of dry states and the disparate wave speeds present in the system.

6.1 One Dimensional Riemann Solvers

The goal here is to describe an algorithm for solving the one dimensional modified multilayer shallow water equations (5.5). The primary strategy of the solver uses an F-wave wave-propagation approach which necessitates the reconstruction of a locally approximate eigenspace with corresponding eigenvalues and the prescription of a way to evaluate the flux vector jump at the grid cell boundaries. The basic algorithm then has the following steps:

1. State evaluation - The states relevant to the Riemann problem must be extracted from the vectors Q_ℓ and Q_r handed to the routine. Also, the determination of the type of dry state problem, if one exists, is handled here.

2. Find the eigenvalues s^p and eigenvectors R.

3. Compute the jump in the fluxes $F(Q_r) - F(Q_\ell) - \Delta x \Psi = \delta$.

4. Project the jump in the fluxes onto the eigenspace solving $R\beta = \delta$.

5. Determine F-waves $\mathcal{Z}^p$ and the fluctuations $\mathcal{A}^\pm \Delta Q$.

The approach to some of these steps is also dependent on whether a bottom layer dry state exists and what kind of dry state it is. We will first describe the case

where no dry state exists and proceed with describing the algorithm and explain any modifications to the fully wet problem in the last part of this section.

6.1.1 State Evaluation

The states that are relevant to the multi-layer Riemann problem are the depths h of each layer, the momentum hu in each layer, and the speeds u of each layer. Since the depth and momentum are easily obtained from the state vectors Q_r and Q_ℓ these values do not pose a significant challenge. However the velocity of each layer needs to be handled carefully since it is obtained by dividing the momentum by the depth. A simple limiting procedure is therefore used with a dry tolerance C_{dry} to determine whether to treat the cell as wet or as dry, in which case the velocity is set to zero:

$$u_{1,2} = \begin{cases} \dfrac{hu_{1,2}}{h_{1,2}} & \text{if } h_{1,2} \geq C_{\text{dry}} \qquad \text{and} \\ 0 & \text{if } h_{1,2} < C_{\text{dry}}. \end{cases} . \tag{6.1}$$

It is important to note that this procedure does not modify the state vectors themselves but only the quantities that will be used to determine the Riemann problem's solution.

The other benefit of using the limiting procedure is that the dry states of each layer can be detected at the same time. With the addition of the bathymetry states b_r and b_ℓ the type of dry state can be detected and the rest of the steps in the algorithm can proceed accordingly. Since the methods used in this solver do not provide estimates for the middle states, the two cases are solely determined based on the initial states present. If a dry state exists for both sides of the grid cell interface, the problem is treated solely as a single-layer problem and an appropriate solver is used, including dry states for the single-layer if necessary as was discussed in section 6.2.2. Since the assumption is that the bottom layer will become dry before the top, the single-layer solver can handle all instances when the top layer becomes dry. If one side of the grid cell interface becomes dry, either a wall dry state exists or an inundation problem exists. Since the middle states are not being evaluated, the difference between these two problems is

$$h_{\text{wet}} + b_{\text{wet}} > b_{\text{dry}}. \tag{6.2}$$

If this occurs than the wet cell will flow into the dry cell causing the dry cell to become wet. If this is not true, a wall dry state problem must be solved. Ignoring the middle states is equivalent to ignoring the case where (6.2) is not true but the wet cell has enough momentum to overcome the jump in bathymetry. In this case the cell will have a jump in layer depth greater than the dry cell's bathymetry level and in the subsequent time step, an inundation problem will be solved.

6.1.2 Eigenspace Solvers

In section 5.2 two approximate eigenspace solvers were discussed, one based on the difference in velocities of the two layers and one based on a linearization of the equations. Numerically both of these solvers are straight forward to implement except for dry states.

In the case of the eigenvalues prescribed by the velocity difference, the states used to evaluate the eigenvalues are

$$\lambda^-_{\text{ext,int}} = \lambda^-_{\text{ext,int}}(Q_\ell) \quad \text{and}$$
$$\lambda^+_{\text{ext,int}} = \lambda^+_{\text{ext,int}}(Q_r).$$

This approach generally works for systems where the middle states are not expected to differ significantly from the right and left states. If this were not the case, the estimated speeds are greater than what would be obtained using the true middle states. This approach is similar to how Roe averages are taken except that in the case of F-waves, the Roe condition (3.27) is automatically satisfied. Once the eigenvalues are found, the eigenvectors can be evaluated using the same technique, evaluating the eigenvectors corresponding to the left going waves with the left states and similarly with the right states, with the forms found in (5.14), which are exact representations as far as the eigenvalues are concerned.

The linearized eigensolver uses the same state evaluation as above. With the linearization presented in section 5.2.2 the eigenspace is completely determined by the initial condition, however, and does not change in time since the states used are the steady state values $\hat{h}$ and $\hat{\mu}$. An alternative to this is to use the full values of the states $h = \hat{h} + \tilde{h}$ and $\mu = \hat{\mu} + \tilde{\mu}$ so that the computed eigenspace evolves in time and is sensitive to changes in the states. It is important to note that this eigensolver can handle a dry bottom layer but neither of the dry state situations are handled fully and care must be taken to account for this. The eigenvectors are evaluated as prescribed by the linearized eigenvectors at the appropriate states as before.

Another approach to solving for the eigenspace is to use a computational eigensolver such those provided by LAPACK. In order to do this, the quasi-linear coefficient matrix found in section 5.1.1 is evaluated at the arithmetic average of the states Q_r and Q_ℓ. This approach works only for Riemann problems without any dry states, so one of the approximate eigensolvers above must be used in these cases.

For ease of later reference, the eigensolvers presented here are summarized in table 6.1.

The final issue to resolve in calculating the eigenspace is how to handle dry states. For the wall dry state, the modified wall boundary condition state discussed in section 6.1.3 is used to evaluate the eigenspace for all of the approaches mentioned thus far. In the inundation case for the bottom layer, the eigenspace is evaluated via the true states in the problem with two possible approaches. In both cases, the expec-

Method	Solver	Description
1	Static Linearized	Eigenvalues are calculated by using the eigenvalues from the linearized system as in section 5.2.2. The initial steady state is used for all time so that the speeds do not change in time.
2	Dynamic Linearized	The same as the static linearized method except that we use the current local states in the evaluation of the linearized eigenvalue equations.
3	Velocity Difference	Eigenvalues are calculated via the expansion about the difference in the layer velocities $u_1 - u_2$ detailed in section 5.2.1.
4	LAPACK	The LAPACK eigensolver is used to find all eigenvalues and eigenvectors of the matrix $A(1/2(Q_\ell + Q_r))$.

Table 6.1: Summary of the eigensolvers used for the multi-layer equations.

tation is that the internal wave will carry the jump in depth in the bottom layer, the external wave moving in the same direction as the dry state is identical to a single-layer shallow water wave for which the eigenspace is known. The approaches for evaluating the wave carrying the wetting state differ in what value is used for the dry cell's depth. If the dry cell's bottom layer depth is set identically to zero, the eigensolver will compute a zero wave speed and the eigenvector will be incorrect. An estimate to the internal wave is then used based on a single-layer inundation wave, and

$$s^2 = u_{2r} - 2\sqrt{g(1-r)h_{2r}}$$

for the case where the left state is dry and

$$s^3 = u_{2\ell} + 2\sqrt{g(1-r)h_{2\ell}}$$

for the case where the right state is dry. The eigenvectors are then evaluated using the exact forms (5.14) while evaluating with the originally wet state. The second approach uses non-zero depth for the dry cell's depth to calculate the eigenspace. In this case it is assumed that the eigenspace is accurately portrayed by a fully wet problem with a small depth, in practice taken to be the dry state cutoff C_{dry} used earlier.

Currently both approaches to inundation appear to produce an entropy violating transonic rarefaction in the simple case illustrated in figure 6.1. A possible course would be to modify the the appropriate eigenvector that is near $x = 0$ by splitting it in to two waves.

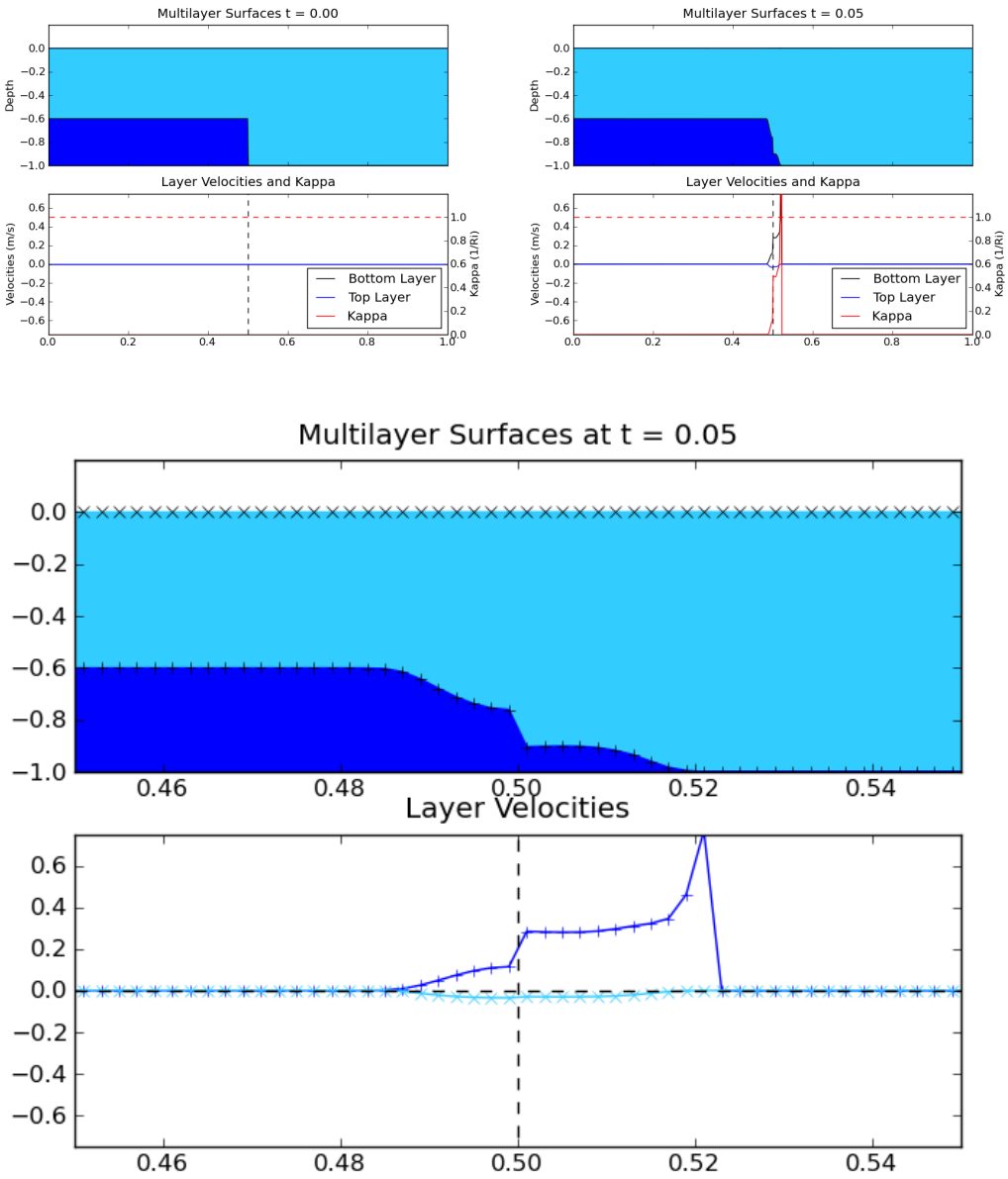

Figure 6.1: Inundation problem with a potentially entropy violating solution. The bottom figure is a zoomed in version of the top right figure where the grid cell averages have been marked. The entropy violation is occurring at $x = 0.5$.

6.1.3 Computation of the Jump in Fluxes

In the case that no dry states exist, the vector δ can be computed simply by evaluating

$$f(q_r) - f(q_\ell) - \Delta x \Psi^n_{i-1/2}$$

where in the case of the multi-layer shallow water equations, the resulting differences are

$$\delta = \begin{bmatrix} [\rho_1 h_1 u_1] \\ [\rho_1 h_1 u_1^2 + 1/2 g \rho_1 h_1^2] + g\rho_1 \overline{h}_1 [h_2 + b] \\ [\rho_2 h_2 u_2] \\ [\rho_2 h_2 u_2^2 + 1/2 g \rho_2 h_2^2 + \rho_1 h_1 h_2] - \rho_1 \overline{h}_1 [h_2] + g\rho_2 \overline{h}_2 [b] \end{bmatrix}. \tag{6.3}$$

Note that we have used averages for the depths as motivated by the path-conservative jump conditions we found in section (5.3.1). We expect that if the state presented to the Riemann solver should be in steady state, then by including the source terms directly into the flux difference the possibly small differences will be canceled out.

The wall dry state problem is an important case to compute correctly as it may be an important component of differences between the single-layer equations and the multi-layer equations for the targeted problem. Consider the case illustrated in figure 6.2, where from the discussion in section 5.3.4 we know some of the states and waves of the solution. The approximate eigenspace solvers described above take this into account and the primary concern now is evaluating the jump in the fluxes. It is also worth pointing out that the reason the Riemann solver described here has been developed using the modified equations (5.5) instead of the original equations (5.4) is to handle the wall dry state problem.

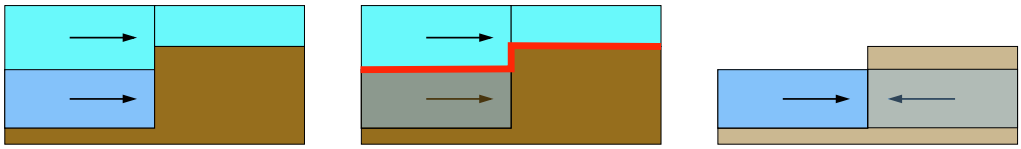

Figure 6.2: Illustrations of the dry state method presented. The left most figure represents the general state we are interested in solving. In the middle figure the red line is what the top layer "sees" when solving the dry state problem. The right most figure is the wall boundary problem solved for the bottom layer.

Handling the wall dry state problem is similar to solving the wall dry state problem for the single-layer with some care taken in what states are reflected across the dry state. Consider the dry-state case illustrated in figure 6.2, the goal is to calculate the vector δ from equation (6.3) such that the expected Riemann problem solution is achieved. In this case, the correct flux jump can be achieved by setting the dry cell's

state to one representing a wall boundary condition with

$$h_{2r} = h_{2\ell} \quad \text{and} \quad \mu_{2r} = -\mu_{2r}.$$

With this state, δ_2 becomes

$$\delta_2 = \rho_1[h_1 u_1^2] + 1/2 g\rho_1[h_1^2] + g\rho_1 \overline{h}_1(h_{2\ell} - h_{2\ell} + b_r - b_l)$$

which is an incorrect flux. Looking back at the original modified equations, the top layer is affected by the bottom layer through the momentum exchange term $-g\rho_1 h_1 (h_2)_x$ and combining this with the bathymetry source term $-g\rho_1 h_1 b_x$, the full source term can be rewritten as

$$-g\rho_1 h_1 (h_2 + b)_x = -g\rho_1 h_1 (\eta_2)_x.$$

This implies that the top layer responds to the surface η_2 only and is insensitive to whether that surface is the bathymetry or the bottom layer. This allows us to treat the source term by calculating η_2 with the understanding that if $h_2 = 0$ then $\eta_2 \equiv b$ as illustrated in figure 6.2. Instead of using the wall boundary condition value of h_{2r}, the value of η_2 is calculated since $h_2 + b = \eta_2$. For this case then the jump can be calculated as

$$[h_2 + b] = b_r - h_{2\ell} - b_\ell$$

and δ_2 is given by

$$\delta_2 = \rho_1[h_1 u_1^2] + 1/2 g\rho_1[h_1^2] + g\rho_1 \overline{h}_1(b_r - h_{2\ell} - b_l).$$

Turning to the momentum flux of the bottom layer, δ_4 becomes

$$\begin{aligned} \delta_4 &= \rho_2[h_2 u_2^2] + 1/2 g\rho_2[h_2^2] + \rho_1[h_1 h_2] - \rho_1 \overline{h}_1[h_2] + g\rho_2 \overline{h}_2[b] \\ &= g\rho_2 h_{2\ell}(b_r - b_\ell) \end{aligned}$$

Since the bathymetry's effect has been simulated by the wall boundary condition, $[b] = 0$ and $\delta_4 \equiv 0$. This is the expected result as there is no flux through the wall.

Insuring that in the wall dry state problem that no fluctuations are allowed to wet the bottom layer in the dry grid cell is extremely important. Small errors that may be well below the dry tolerance C_{dry} will accumulate and for long time simulations this may lead to unphysical wetting of dry states. It also may be necessary to control the high-order correction terms near large jumps in bathymetry as this can introduce small errors in the flux as well.

6.1.4 Projection of the Jump in Fluxes onto the Eigenspace

The projection of the flux difference onto the eigenspace can be obtained by $R\beta = \delta$ where R is the right eigenvector matrix, β the resulting projection coefficients, and δ the flux difference in each field. The primary difficulty in solving this linear system is ensuring that the solution exists and is unique. This may not be true numerically if the Riemann problem presented is nearly dry in the bottom layer. It is important then to identify dry states and treat them appropriately before performing the projection. Since each of the dry state problems is handled either by a different method all together, as is the case with the completely dry bottom layer, or by modified systems as in the case of the wall and inundation dry state problems, it is a numerical consequence that a solution cannot be found. Dry state limiting as described in section 6.1.1 can handle this but more robust systems may be necessary depending on the problem being solved.

6.1.5 Loss of Hyperbolicity

The question of hyperbolicity as raised in section 5.2.1 is important to monitor in many of these cases. If the solution should cause Kelvin-Helmholtz types of instabilities, the solver should either take steps to correct the situation or stop the calculation. Calculating the value of κ from 5.17 can provide at least warnings as to whether the simulation should be stopped. In practice, κ is only computed as an estimate of stability and is not used further than an indication that the computed solution may be suspect.

6.2 Two Dimensional Riemann Solvers

The two dimensional Riemann solver is based on the un-split method described in section 3.6. The normal and transverse solvers are based on the one dimensional Riemann solver explained in the previous section with the addition of a modified eigensolver and care in detecting and handling dry state problems.

6.2.1 Eigenspace Evaluation in Two Dimensions

The two dimensional modified equations (5.8) contain two additional waves carrying the transverse momentum as an advected quantity. The eigenvectors were given in section 5.2.4 and only require the evaluation of the transverse velocity at the appropriate left or right state depending on which wave is being evaluated. The wave speeds are taken to be the arithmetic average of the normal velocities in the appropriate layer. These additional waves do not need special treatment due to dry states.

The transverse Riemann solver projects the presented fluctuation $\mathcal{A}^*\Delta Q$ onto the transverse flux matrix's eigenspace. Since the state where this split is being done is not over a jump in states, the values of the appropriate cell are used to calculate the eigenspace. As the example in figure 6.3 shows, the states used would be those in the grid cell to the right of the original Riemann problem.

6.2.2 Dry State Handling

Adding an additional dimension requires attention to the additional dry states that may be important to the problem at hand. The normal Riemann solver can treat dry states as was done in the one dimensional case and in general no modification needs to be made. Since the transverse solver splits up the difference in $\mathcal{A}^*\Delta Q$ care must be taken to make sure that the transverse waves are not allowed to enter a dry cell if no inundation is expected. Figure 6.3 illustrates the normal solver case, in particular note that the cells that need to be checked for dry states are simply the cells to either side of the Riemann problem in question. If the bottom layer is determined to be dry, then the fluxes are modified accordingly. If both the sides of the Riemann problem have dry bottom layers then the solver reverts to an appropriate single-layer solver. Inundation is not handled in the case that it could occur in the transverse solver.

6.3 Results and Comparisons

6.3.1 One Dimensional Test Cases

Idealized Ocean Shelf

As a test of the solver in a context similar to what we will be doing for storm surges, we will look at a test originally proposed in [34] for the single-layer equations. It involves a large domain size with a step discontinuity representing an idealized continental shelf and a wall boundary condition at the left boundary representing a coast. An ocean at rest is used as the background initial condition with a perturbation approximately 0.4 m in amplitude and affects both the top and bottom layers. The densities of the layers are $\rho_1 = 1025$ kg/m^3 and $\rho_2 = 1028$ kg/m^3, similar to that found in the ocean.

An interesting feature of this solution are the high amplitude and short wave length internal waves being generated as the waves are coming off of the shelf. This is due to the bottom layer reacting to the additional water being loaded on top of it but because the internal wave speeds are much smaller than the shallow water gravity speeds from the shelf, the waves have much shorter wave lengths. Simulations were also performed at multiple grid resolutions and for multiple eigenspace solvers which all indicated that these high amplitude and short wave length internal waves are present and not a numerical instability.

Finally, a plot of showing the convergence rates of the method is shown in figures 6.8 and 6.9 for each field. A solution was computed at a resolution of $N = 51200$

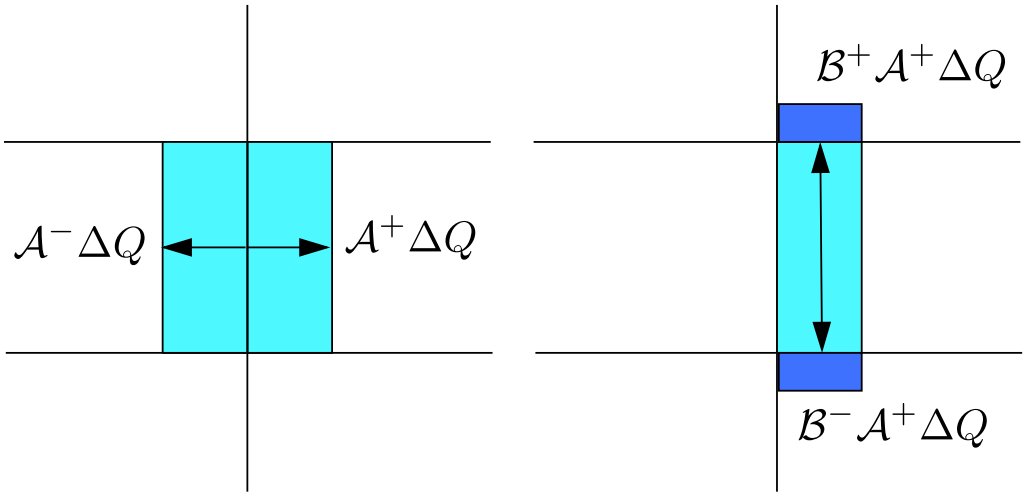

Figure 6.3: The left figure is an illustration of the normal Riemann solve in a x-direction sweep. The fluctuations $\mathcal{A}^{\pm}\Delta Q$ are calculated in this step and if a dry state exists in one direction, the appropriate fluctuation is checked to make sure an invalid flux is not going into a dry cell. The right figure is a fluctuation $\mathcal{A}^+\Delta Q$ being split into up and down going fluctuations. As in the normal Riemann solver case, the cells that the fluctuations are going into must be checked to see if a dry state exists and calculated accordingly.

in space and all lower resolutions compared to it. In figure 6.8 the solution was compared through time at a single spatial location 100 km from the wall boundary condition in two-layers of water. We see that for all the fields, convergence eventually drops off as at least a first order method. This convergence result is unsurprising given that the bathymetry is discontinuous. In figure 6.9 solutions are compared at a single instance of time and compared throughout the spatial domain. Here again we see at least first order convergence but the error increases in the depth fields for subsequently higher resolutions and only begins to converge after $N = 1200$. This may be due to the high amplitude waves that are generated on the internal interface which the lower resolutions cannot represent and may be due to the averaging method for comparing the error. For reference, figure 6.10 shows the convergence results for a single spatial location in time for the simulation shown in figure 5.7 where we see consistent first order convergence for a simpler case.

Ocean Shelf with Continental Slope

This test is nearly identical to the test above except that the continental slope is represented by a linear function rather than a jump in the bathymetry. This is

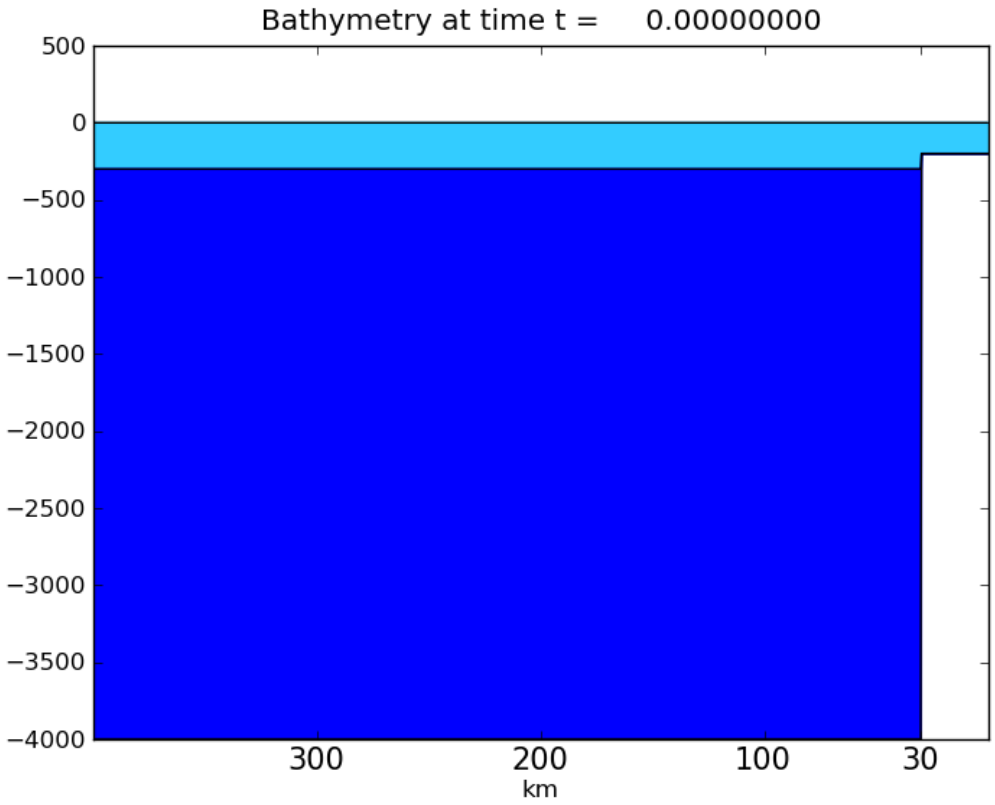

Figure 6.4: Problem setup for the idealized ocean shelf problem.

meant to demonstrate the solver's ability to handle inundation dry states like that which would be found in a storm surge simulation. The bathymetry used is shown in figure 6.11 and the results of the simulation are shown in figures 6.12 and 6.13. A contour plot of the top and internal surfaces is shown in figure 6.14.

In this test the high amplitude internal waves do not appear as the loading on the bottom layer is more gradual. We also see the effect that a linear change in bathymetry has on all the waves. This simulation also demonstrates the ability of the solver to handle the source terms of the equations correctly as well as the inundation version of the dry state of the bottom layer.

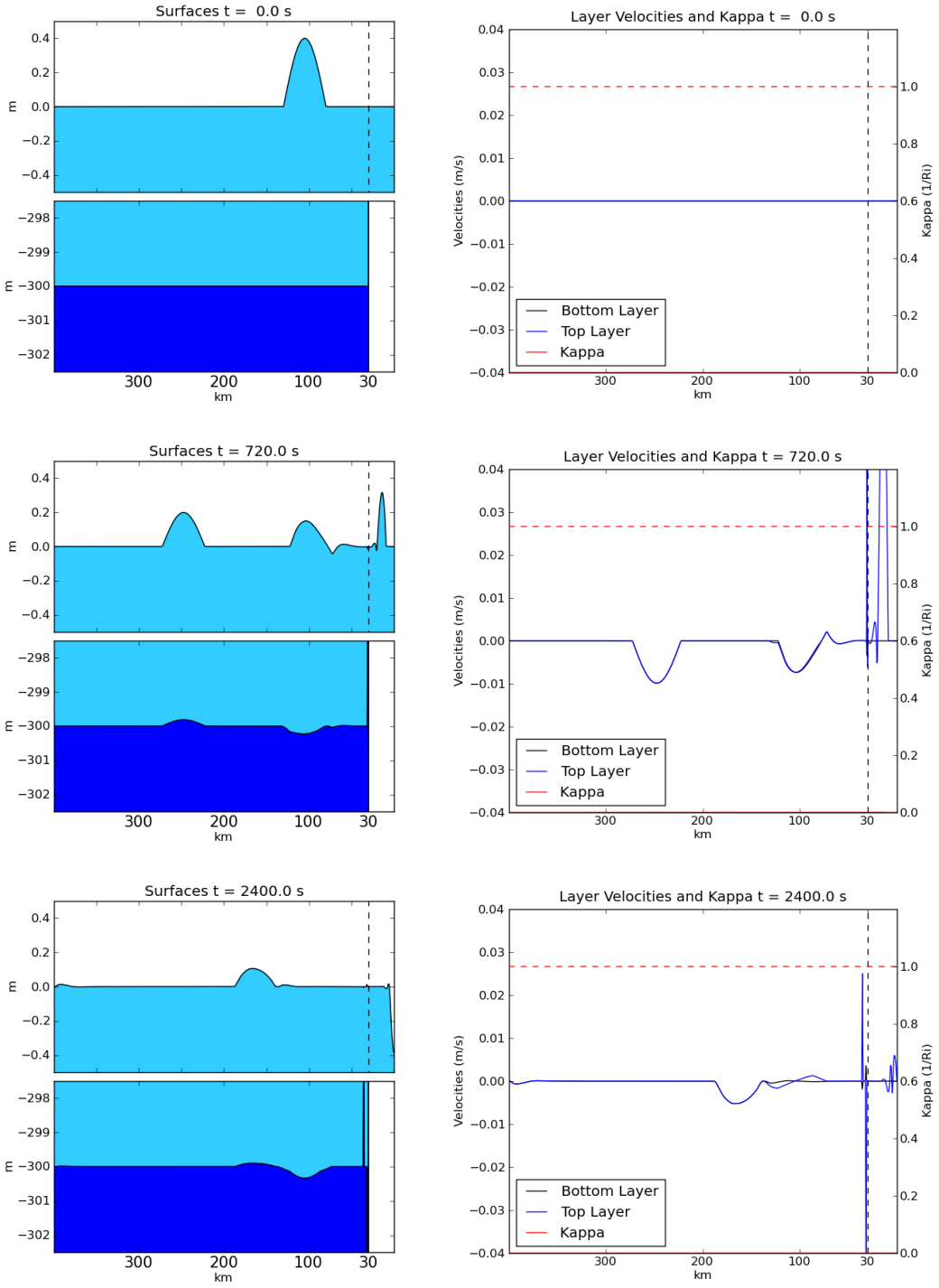

Figure 6.5: Time snapshots from an idealized ocean shelf test using the dynamic linearized eigensolver.

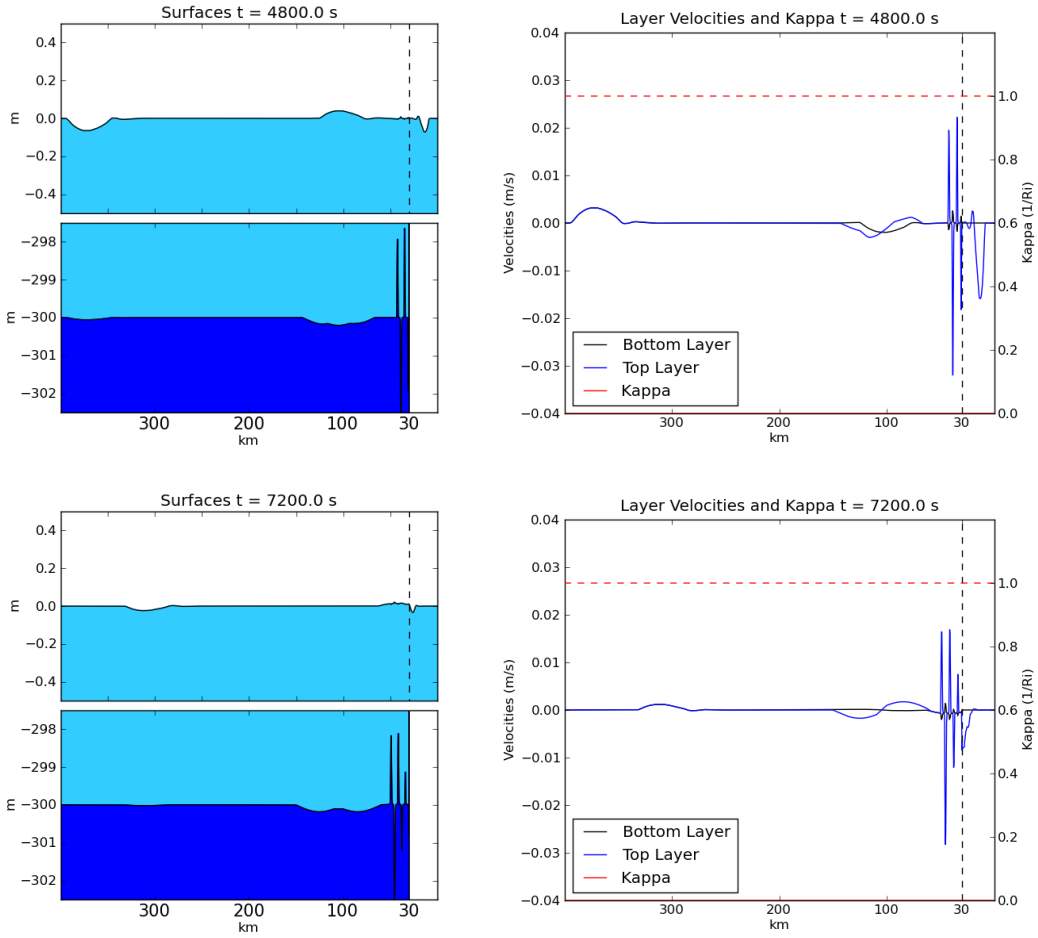

Figure 6.6: Time snapshots from an idealized ocean shelf test using the dynamic linearized eigensolver.

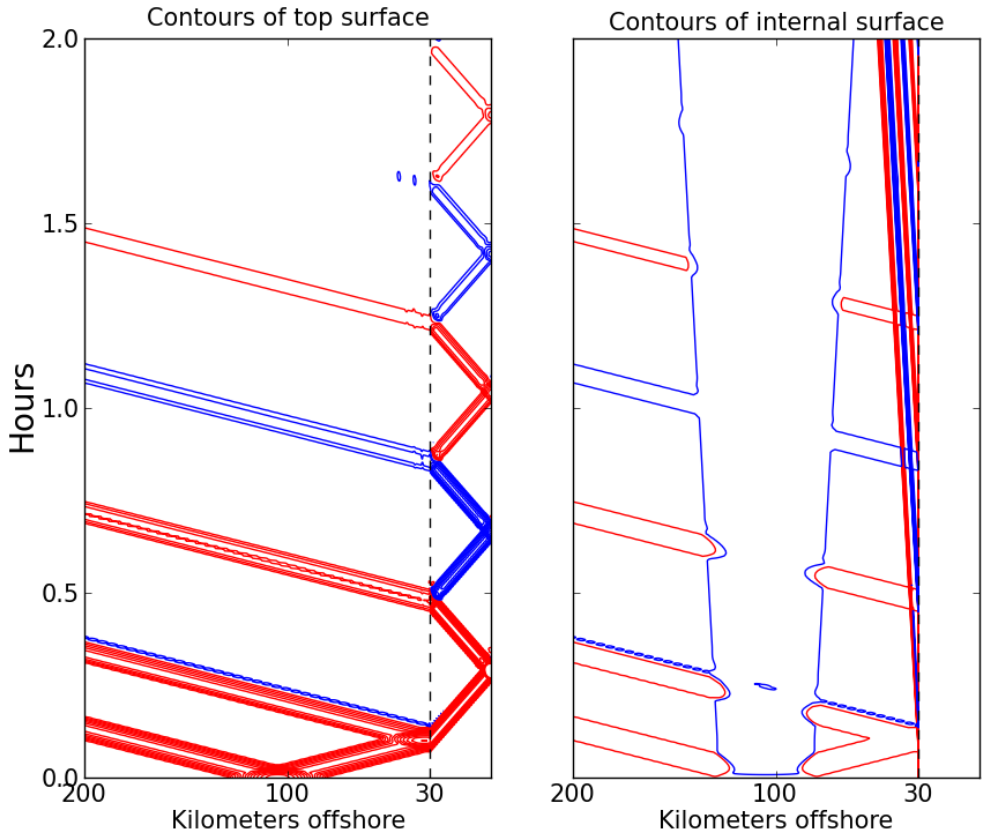

Figure 6.7: Contour plots of the top and internal surface height through time. The top surface has 30 contour levels from -0.4 to 0.4 and bottom surface has 30 contour levels from -0.5 to 0.5 where red contours indicate positive displacement and blue dashed lines negative displacement

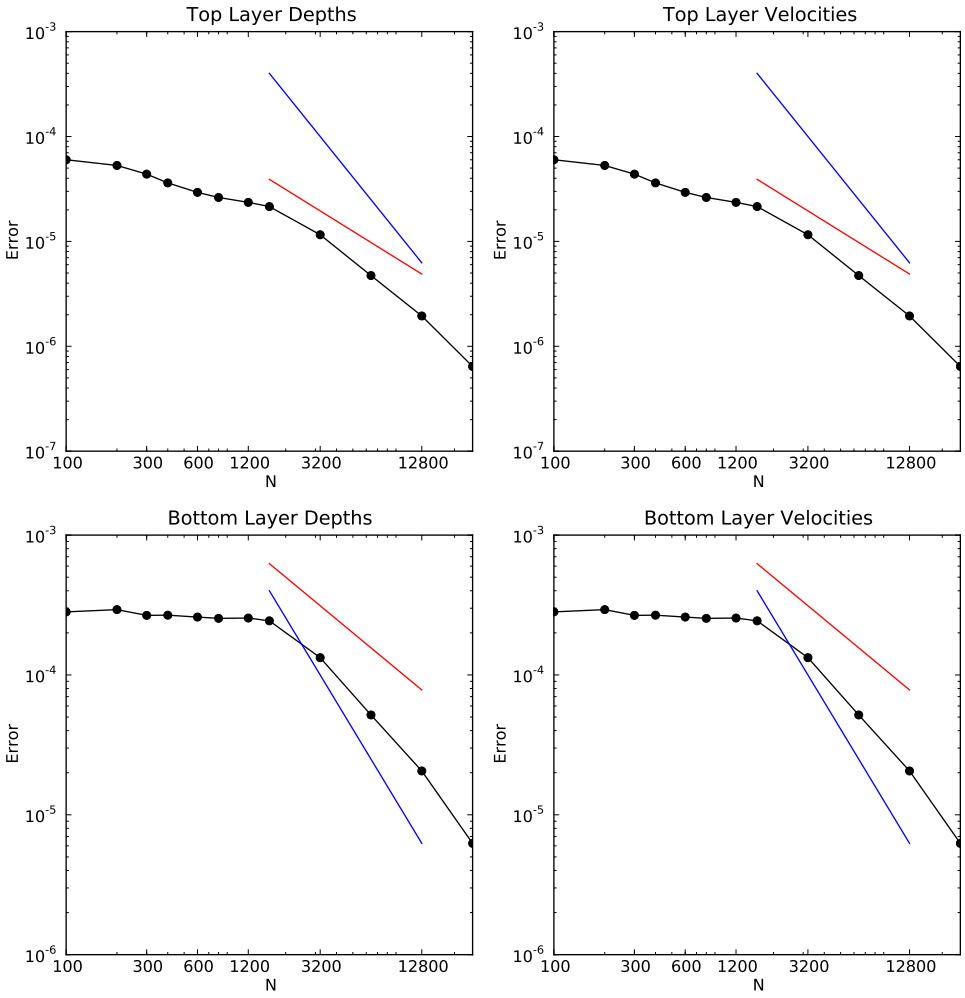

Figure 6.8: Convergence plots of the idealized ocean shelf simulations looking at a point at $x = 100$ km in time. Each resolution is compared with a fine resolution run $N = 51200$. The black line represents the L^2 norm of the error at each resolution compared, red first order convergence and blue second order convergence.

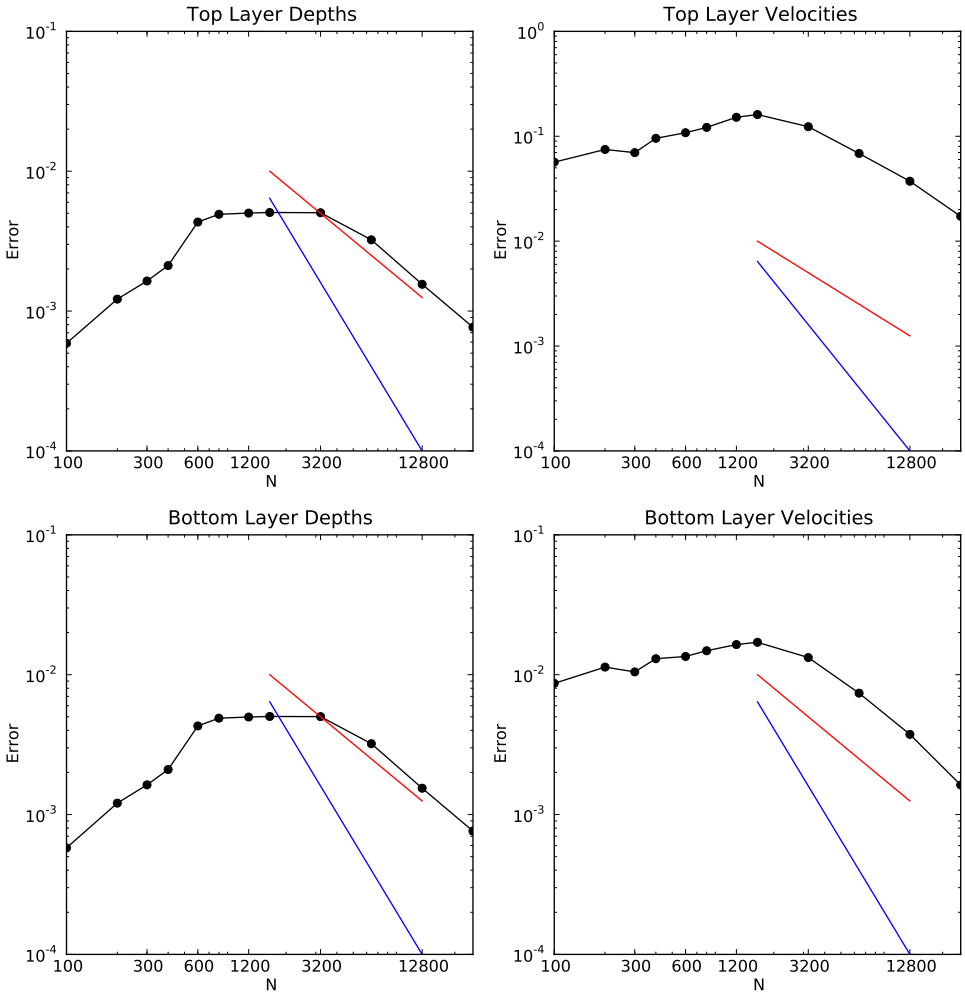

Figure 6.9: Convergence plots of the idealized ocean shelf simulations looking at a point at the entire domain at $t = 2832$ seconds. Each resolution is compared with a fine resolution run $N = 51200$. The black line represents the L^2 norm of the error at each resolution compared, red first order convergence and blue second order convergence.

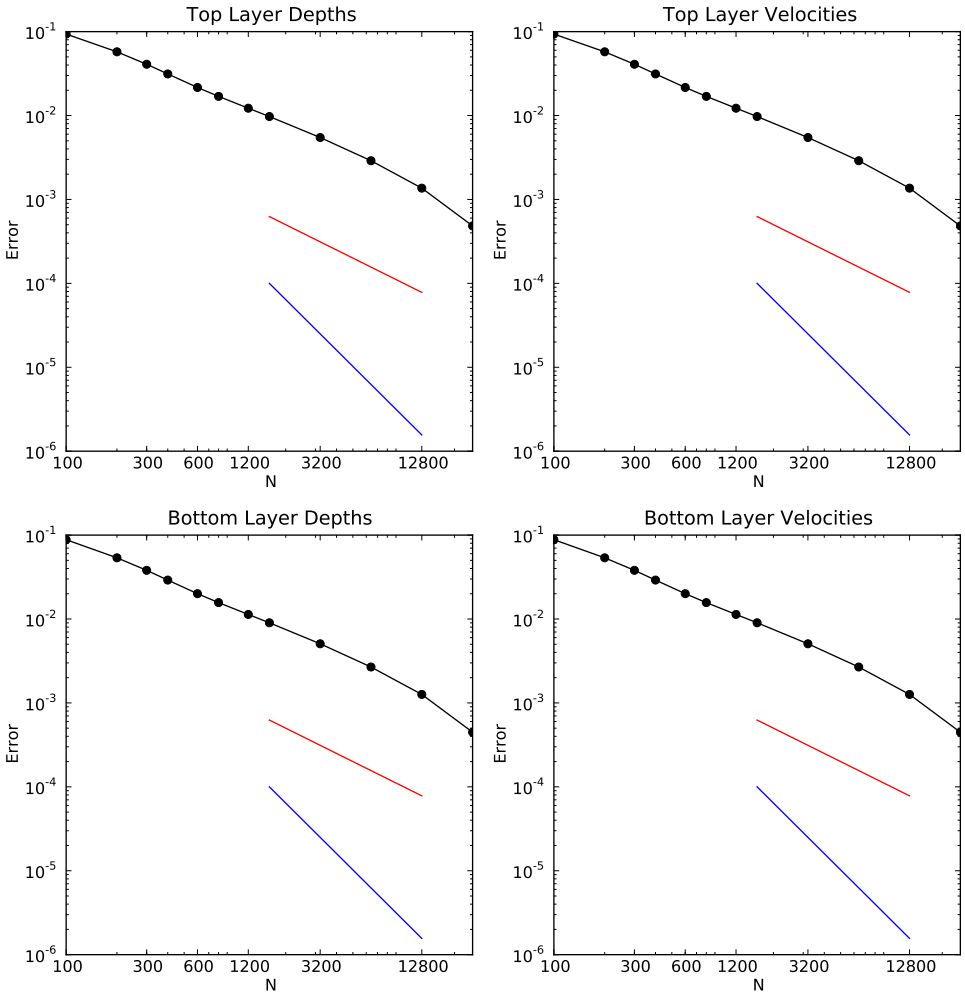

Figure 6.10: Convergence plots of the simulation of figure 5.7 looking at a point at $x = 0.4$ km in time. Each resolution is compared with a fine resolution run $N = 51200$. The black line represents the L^2 norm of the error at each resolution compared, red first order convergence and blue second order convergence.

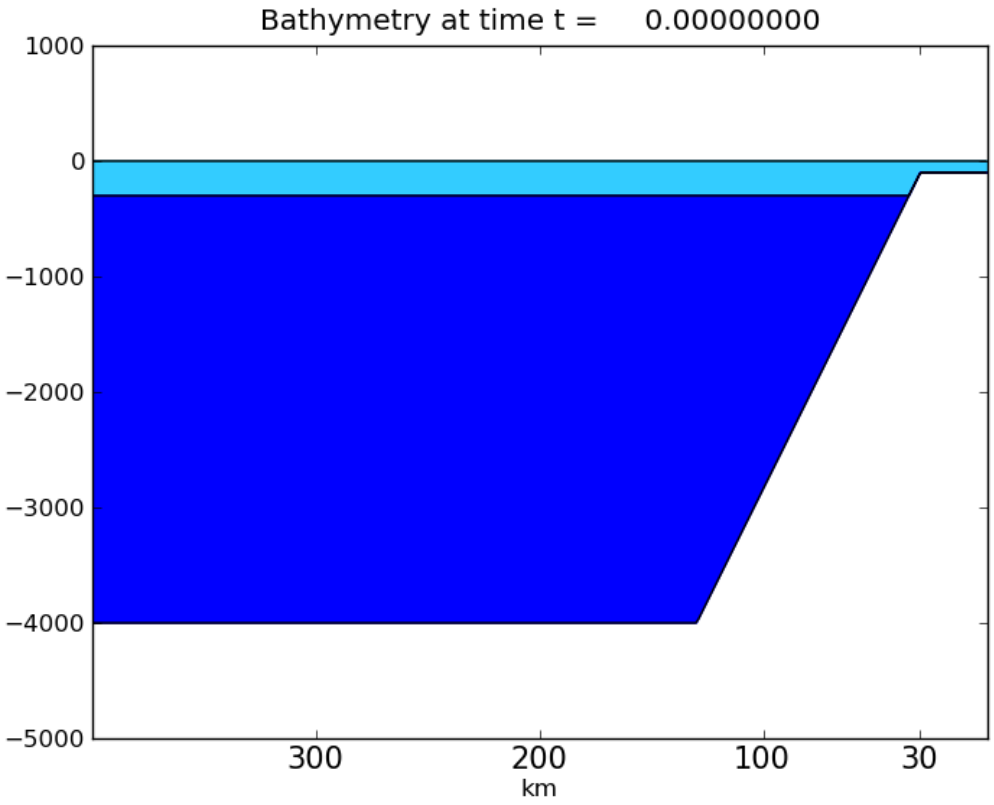

Figure 6.11: Bathymetry and steady state for the ocean shelf with a continental shelf test.

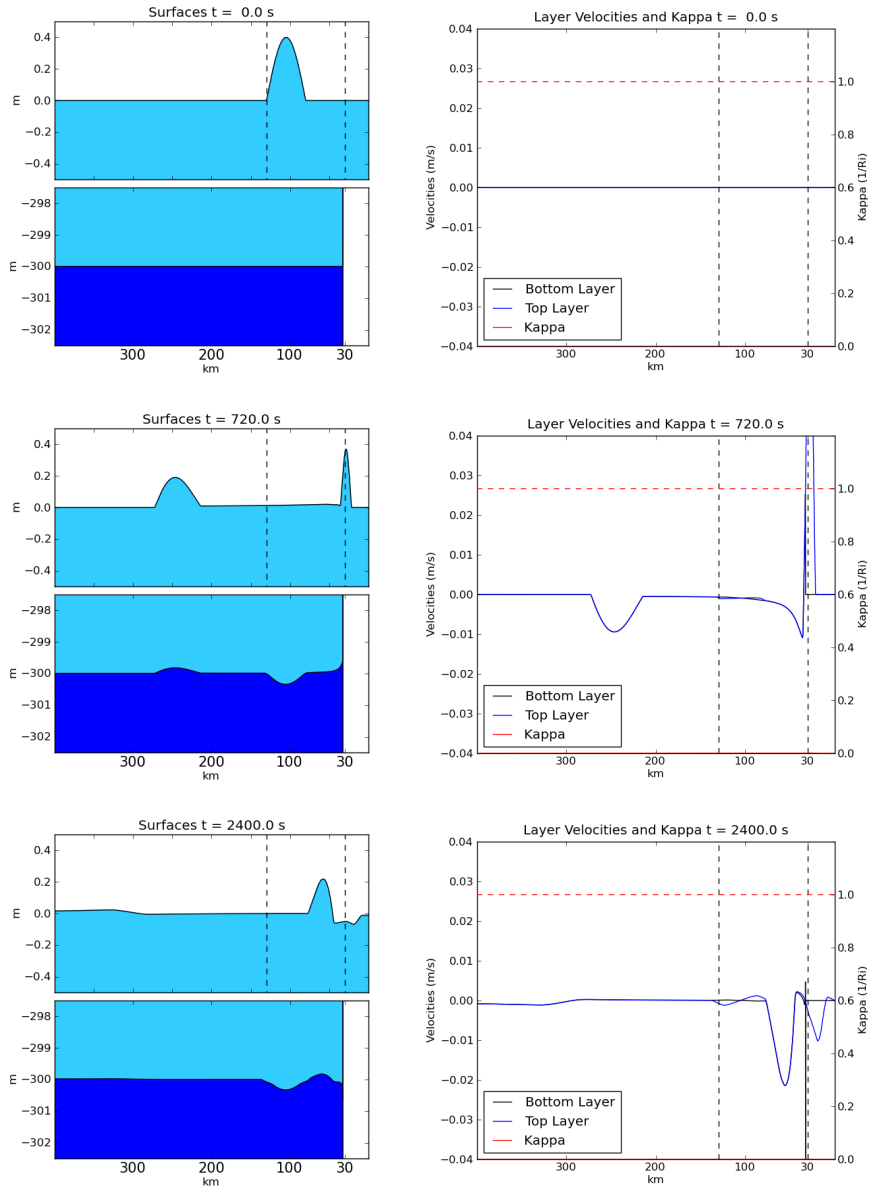

Figure 6.12: Time snapshots from an idealized ocean test with a continental slope using the dynamic linearized eigensolver. The left figures show surface profiles and right contain velocities and the hyperbolicity parameter κ. The dashed lines represent the limits of the continental slope.

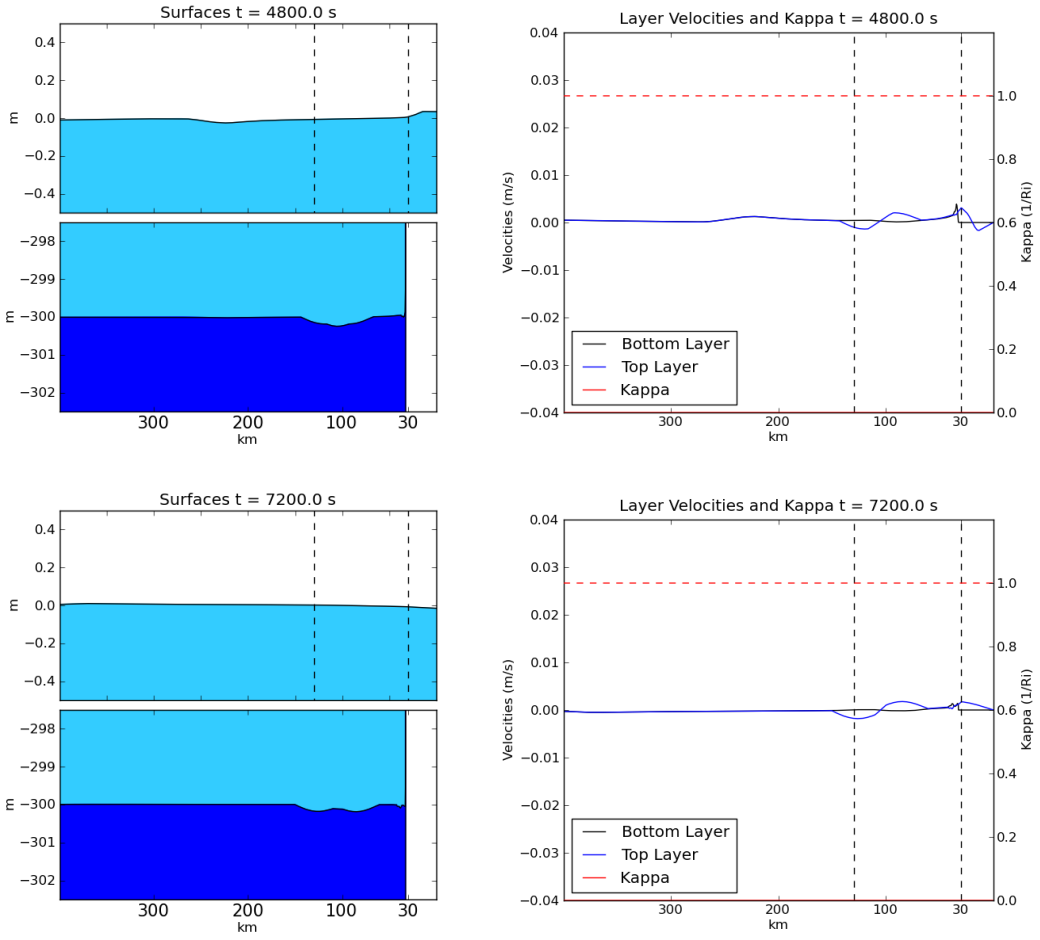

Figure 6.13: Time snapshots from an idealized ocean test with a continental slope using the dynamic linearized eigensolver. The left figures show surface profiles and right contain velocities and the hyperbolicity parameter κ. The dashed lines represent the limits of the continental slope.

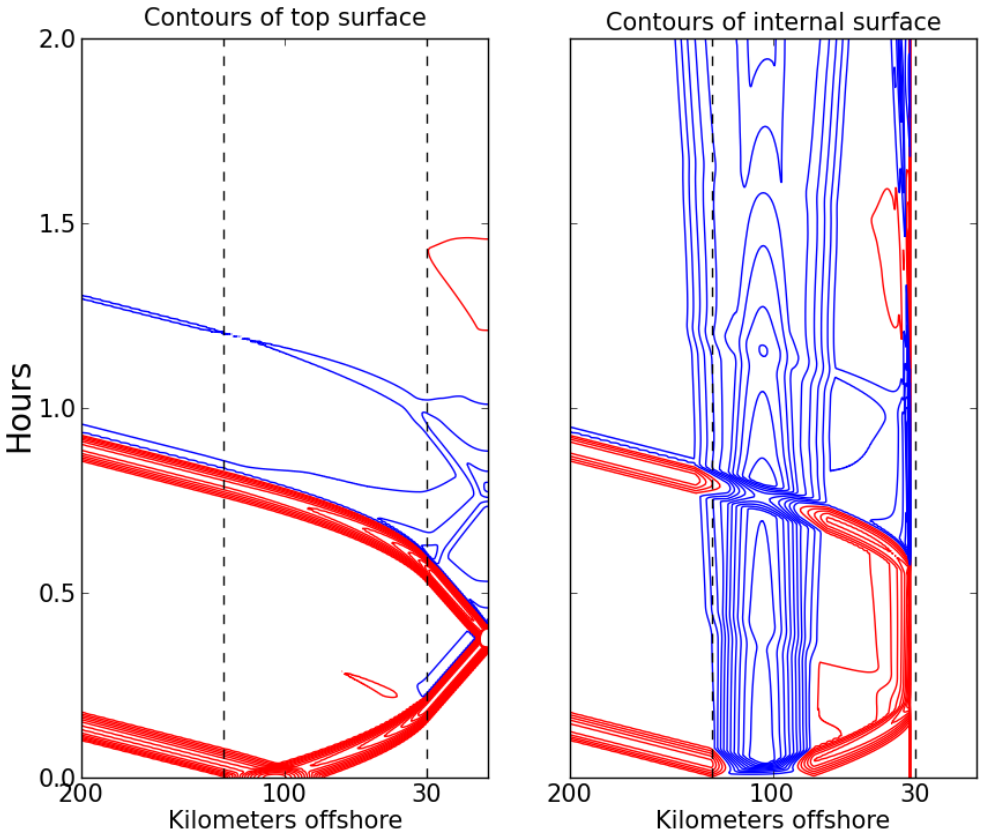

Figure 6.14: Contour plots of the top and internal surface height through time. The top surface has 30 contour levels from -0.4 to 0.4 and bottom surface has 30 contour levels from -0.5 to 0.5 where red contours indicate positive displacement and blue dashed lines negative displacement.

6.3.2 Two Dimensional Test Cases

Hump of Water

This test is meant to demonstrate both the ability of the solver to handle two dimensions robustly and symmetrically but also that waves can reflect off of a jump discontinuity in bathymetry in two dimensions as well. The initial condition involves a gaussian hump of water described by

$$h_1 = \epsilon e^{-(\frac{x-x_0}{\sigma})^2} e^{-(\frac{y-y_0}{\sigma})^2}$$

where $\epsilon = 0.4$, x_0 and y_0 describe the center of the hump, and $\sigma = 0.08$ the width as is shown in figure 6.15. As the wave moves out symmetrically it eventually runs into the jump discontinuity and the top layer continues to propagate a wave to the right and out of the domain while the internal layer wave is reflected and continues towards the right. We can see in this example also that the solver behaves stably and symmetrically in this test case.

Plane Wave Incident on a Bathymetry Jump

This simulation is designed to test whether the two dimensional code can handle waves and coastlines that are not aligned with the grid in a robust manner. A set of three simulations was performed where the wave and bathymetry jump are rotated relative to one another, one where the bathymetry is aligned with the grid, the other with the wave aligned with the grid. In order to minimize boundary effects, the simulation domain is $[-1.5, 1.5] \times [-1.5, 1.5]$ and the domain for comparison is taken as $[-0.5, 0.5] \times [-0.5, 0.5]$. Numerical tide gauges are placed at the same locations relative to the rotated coordinate systems.

These simulations are meant to demonstrate again the ability of the solver to handle changes in bathymetry. More importantly they also demonstrate the possible disadvantage of using a structured grid to represent complex coastlines. Each simulation is effectively run twice with different orientations to the grid and compared. Any discrepancies between each orientation is due to the aliasing of the initial condition and bathymetry onto the grid. Overall it is apparent that the solutions are very similar but the aliasing of the initial condition and bathymetry does have an impact.

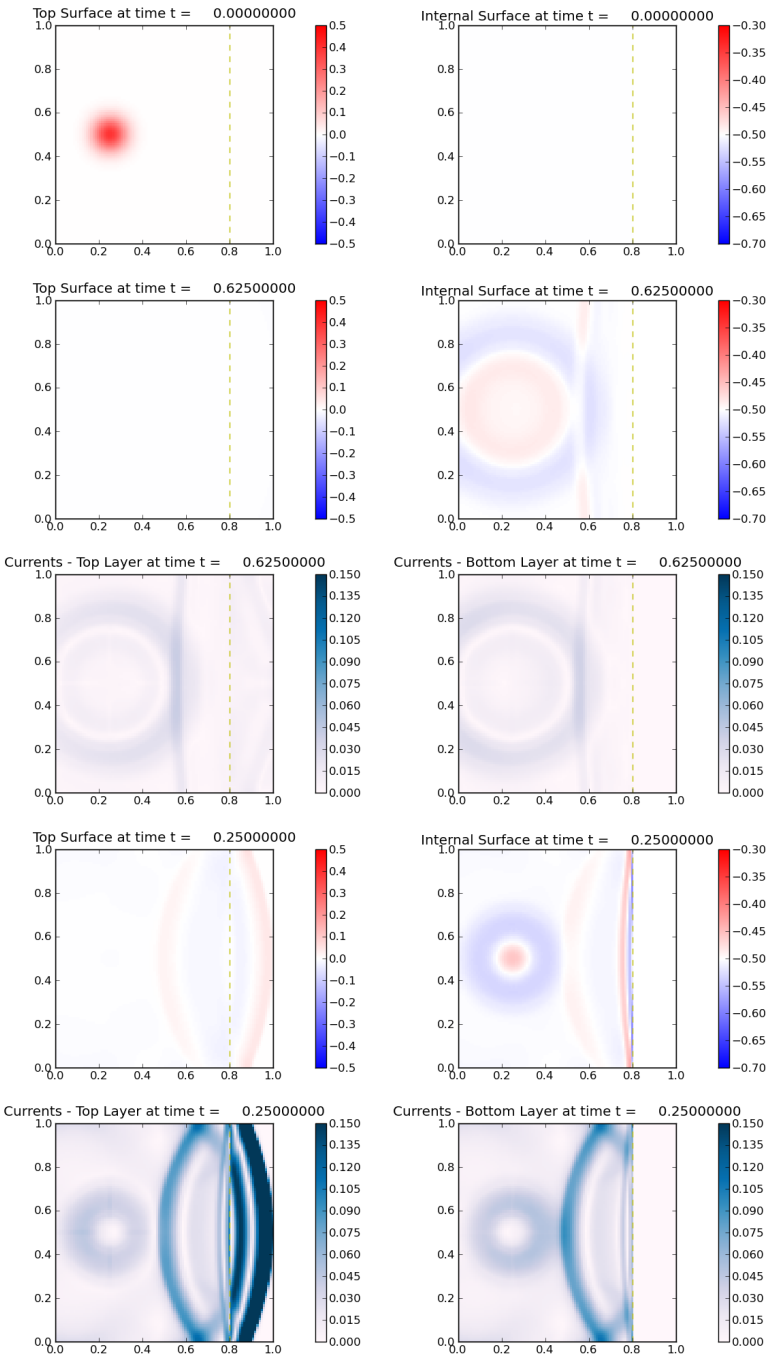

Figure 6.15: Time snap shots of the hump of water test case depicting the surfaces and velocities of each layer.

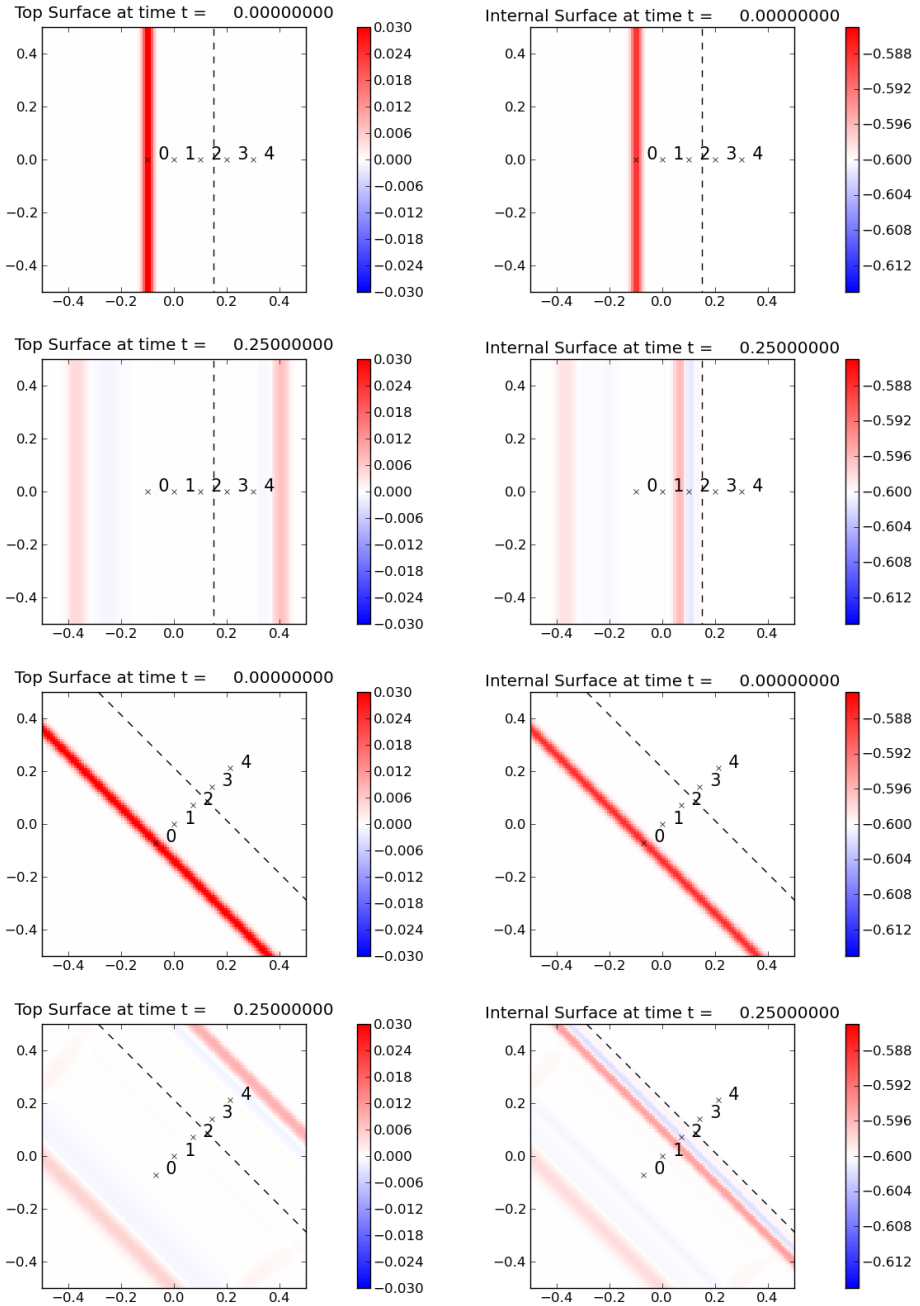

Figure 6.16: Time snapshots from a perpendicular incidence wave in the case where everything is aligned with the grid and off by 45°.

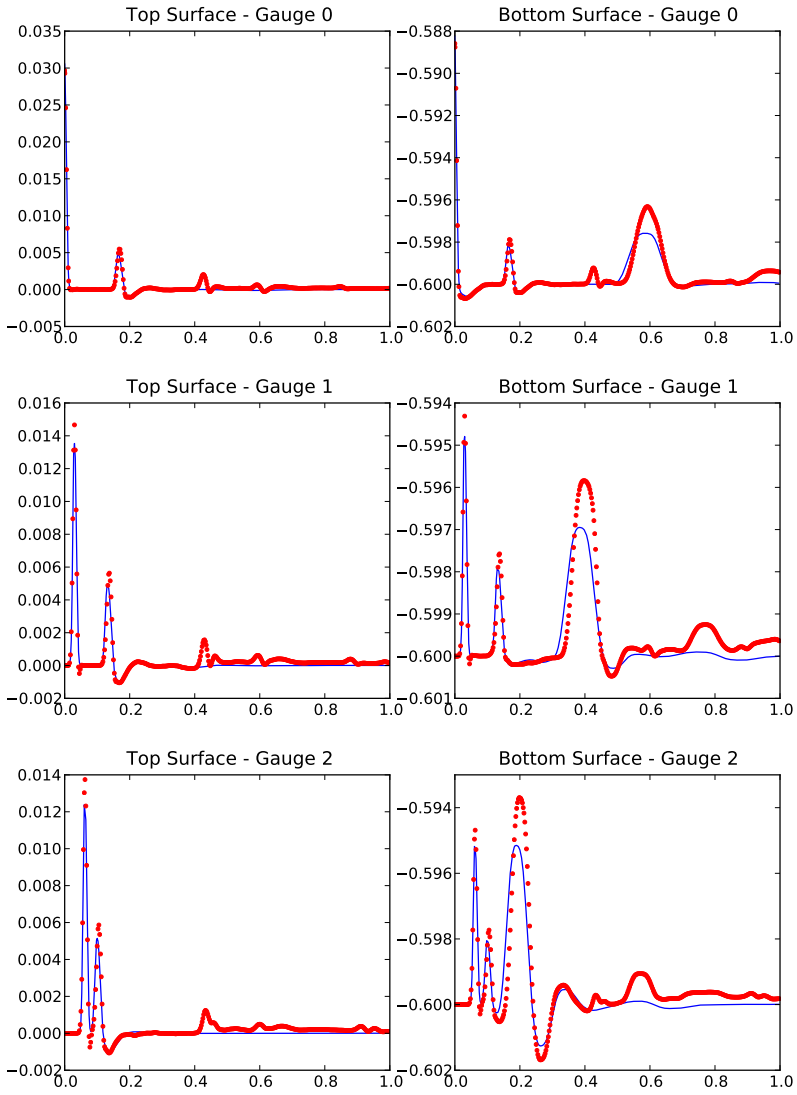

Figure 6.17: Simulated tidal gauges 0,1 and 2 comparing for each orientation for a perpendicular incident wave.

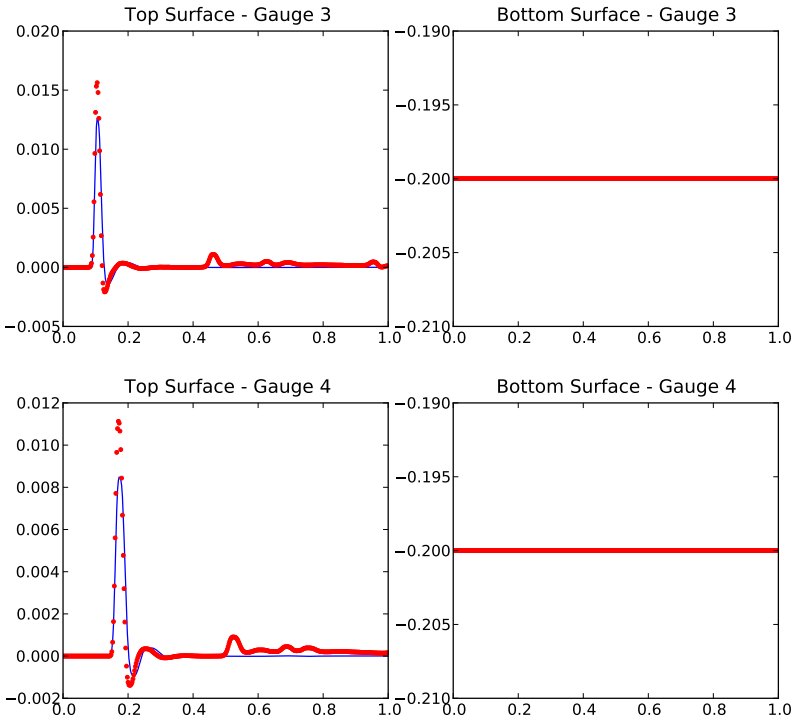

Figure 6.18: Simulated tidal gauges 3 and 4 comparing for each orientation for a perpendicular incident wave.

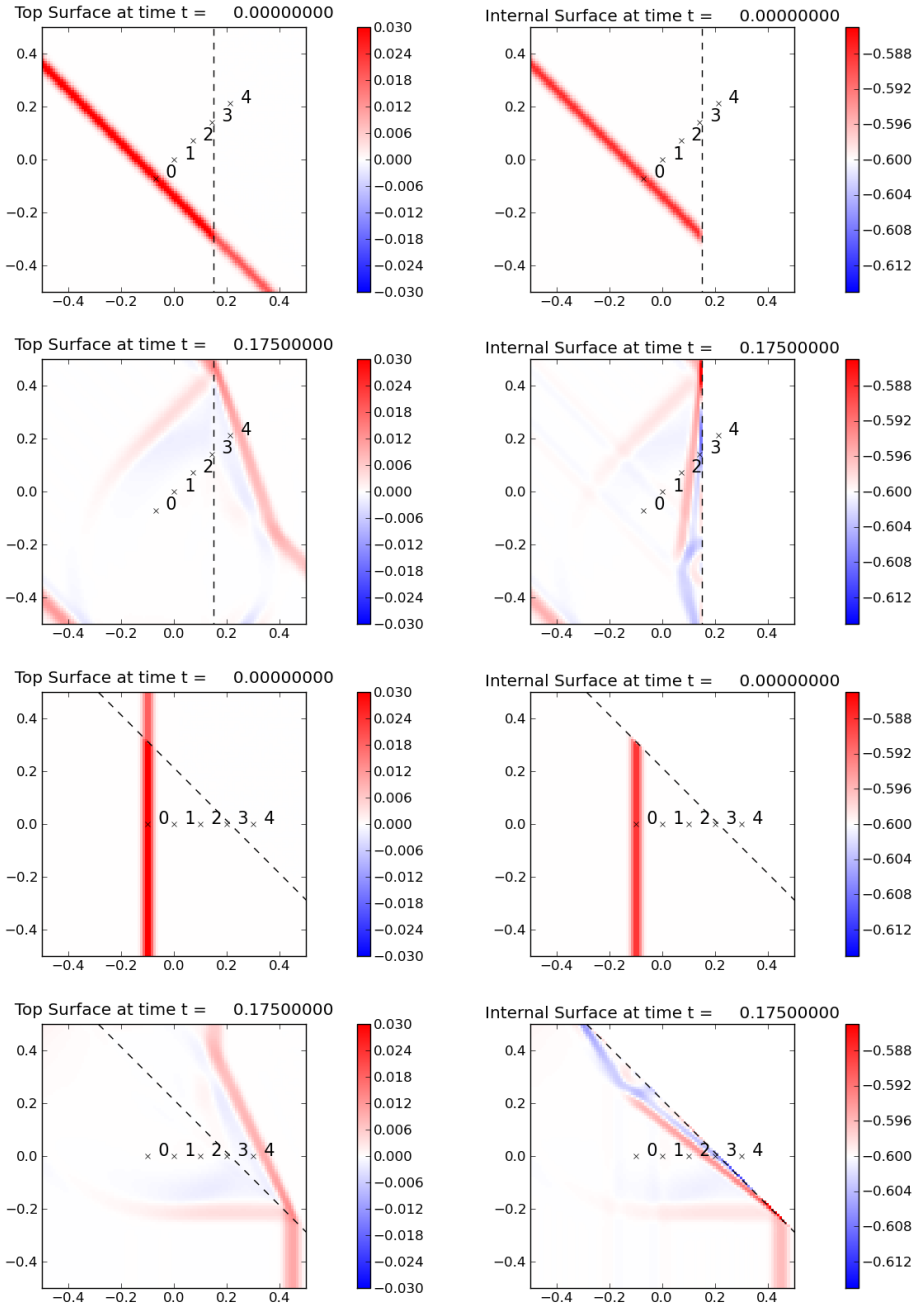

Figure 6.19: Time snapshots from an incidence wave at a 45° angle to the bathymetry jump.

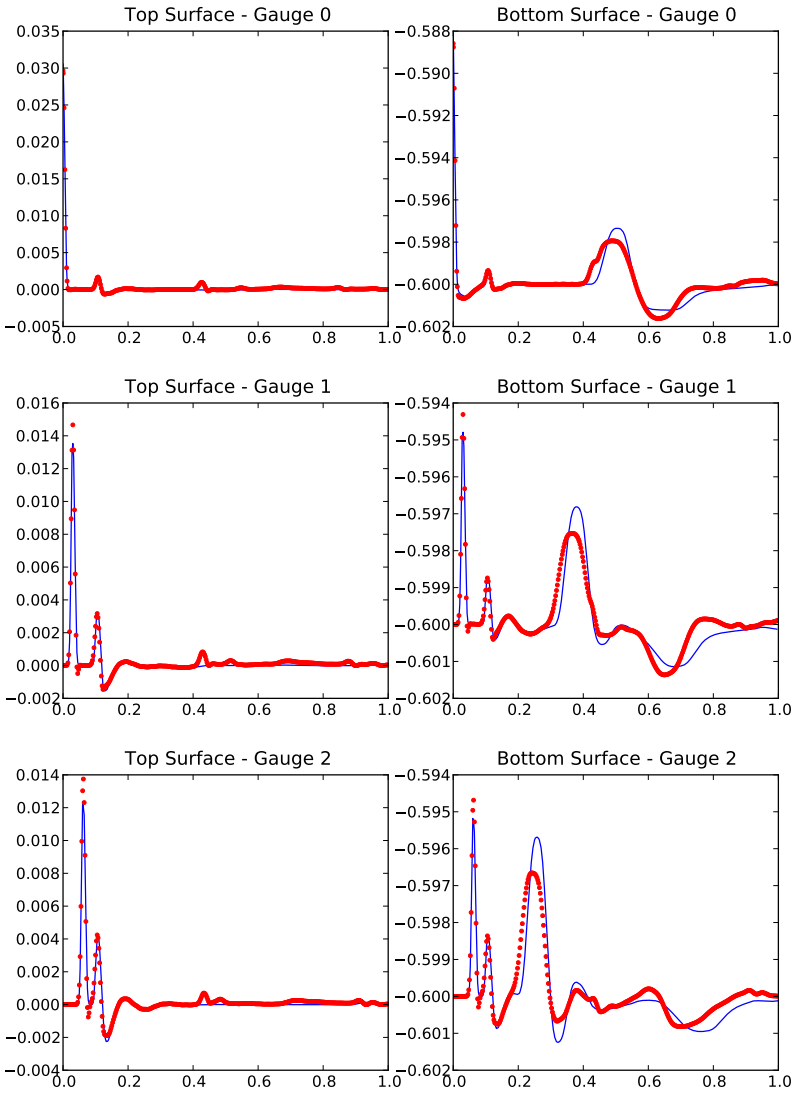

Figure 6.20: Simulated tidal gauges 0, 1 and 2 comparing each orientation for a wave at a 45° angle to the bathymetry jump.

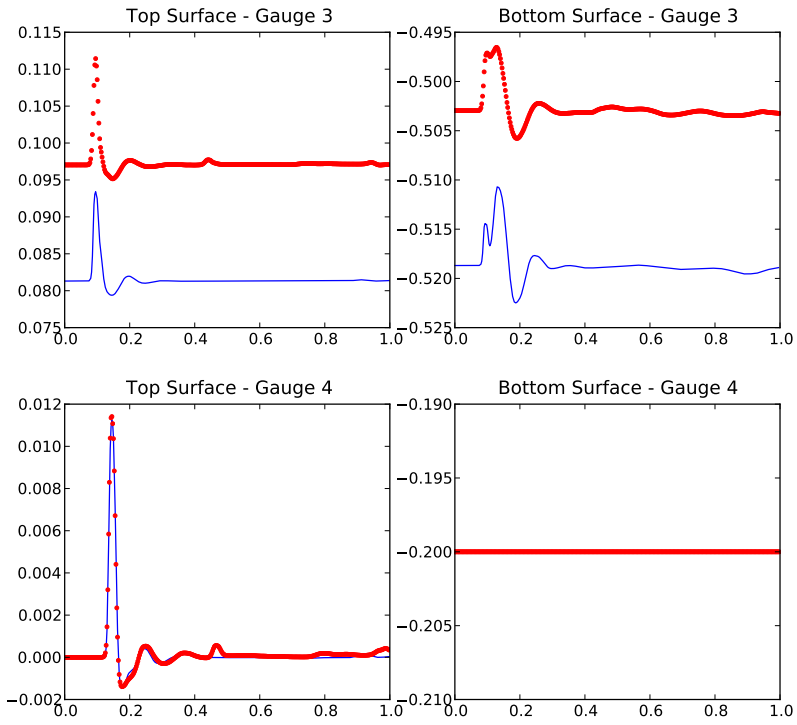

Figure 6.21: Simulated tidal gauges 3 and 4 comparing each orientation for a wave at a 45° angle to the bathymetry jump. Note that for gauge 3 the discrepancy in magnitude and not wave form is due to the representation of the bathymetry being aliased across the grid. This causes the depth of the 3rd gauge which is located very close to the jump to be represented differently in the two configurations.

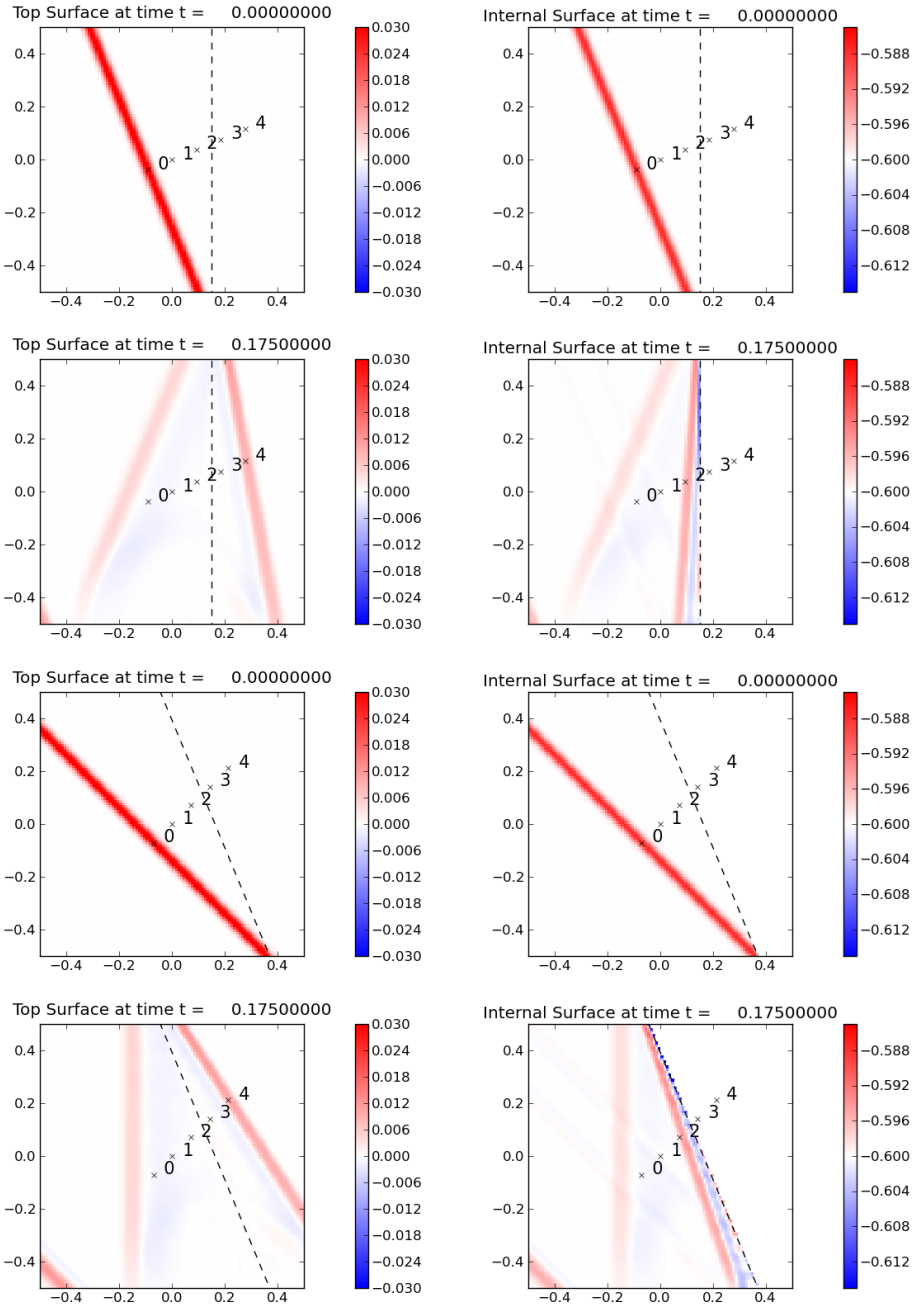

Figure 6.22: Time snapshots from an incidence wave at a 22.5° angle to the bathymetry jump.

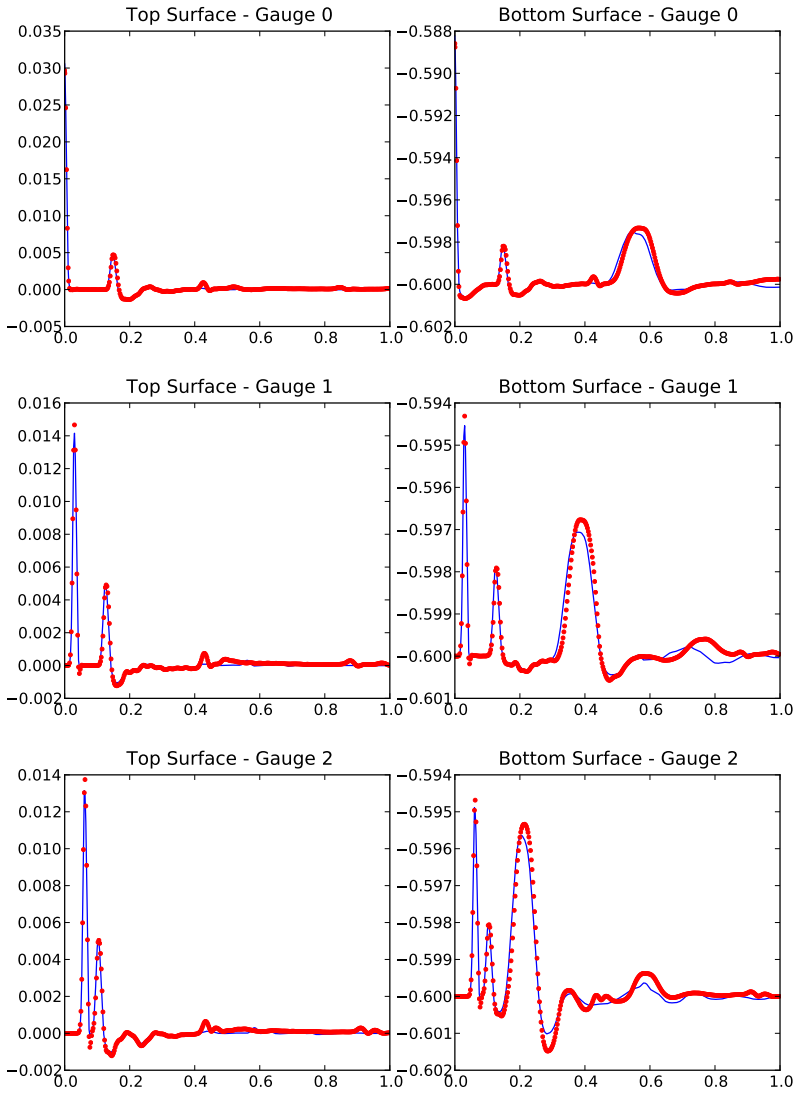

Figure 6.23: Simulated tidal gauges 0, 1 and 2 comparing each orientation for a wave at a 22.5° angle to the bathymetry jump.

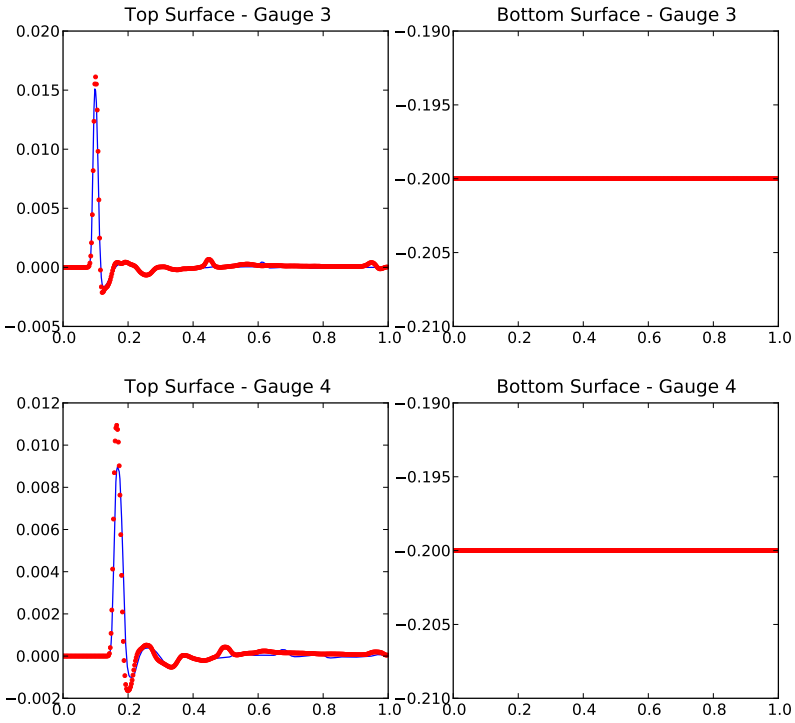

Figure 6.24: Simulated tidal gauges 3 and 4 comparing each orientation for a wave at a 22.5° angle to the bathymetry jump.

Chapter 7

STORM SURGE SIMULATION

This chapter is primarily concerned with the application of methods that have been presented and developed in the previous chapters to the numerical modeling of storm surges. First we will establish what the form of the model equations for both the single-layer and two-layer equations are that we will attempt to solve. This includes the specification of the source terms and the storm forcing to be used. Second, methods for including these source terms that were not addressed in earlier discussions are laid out. Finally simulations of storm surges in idealized cases will be carried out in both the single and two-layer cases.

7.1 Model Equations

The fundamental governing equations of the ocean involve the Navier-Stokes equations (4.1) from which both the single-layer and multi-layer equations were derived. With this as our base, we must now prescribe the forcing terms particular to storm surge calculations which include a specification of the storm including the wind and pressure fields, a Coriolis term, bottom friction stresses, top surface wind stresses, and atmospheric pressure forcing.

7.1.1 Source Terms

Bottom Friction

The forcing terms due to the bottom, τ_{bx}, τ_{by}, and b are all due to physics not directly taken into account via the physics already considered. The bathymetry b affects the momentum via a gradient and is assumed to be an input into the simulation and possibly time varying. Theoretically one could also use a time dependent bathymetry to model sediment transport. The bottom stresses τ_{bx} and τ_{by} are due to bottom friction and are a function of the flow. There are many different ways to calculate the friction but we will use a Manning's-n law

$$\tau_{bx} = hu\frac{gn^2}{h^{7/3}}\sqrt{u^2+v^2}$$
$$\tau_{by} = hv\frac{gn^2}{h^{7/3}}\sqrt{u^2+v^2}$$

where n is the Manning coefficient of roughness. For other similar flows, this friction often is small in comparison to the actual momentum and is often neglected except in shallow areas. For storm surge the friction is of the same order as the primary forcing functions and as such needs to be taken into account for all depths.

Storm Forcing

The forcing terms on the surface P_A, τ_{sx}, and τ_{sy} are due to the storm itself and are functions of the location and strength of the storm. The pressure field P_A is assumed to be given and its gradient is the important quantity. Note that this implies that it is only the deviation from the far field atmospheric pressure that is important in this case. The relevant source terms we have already seen derived and take the form

$$-h\nabla P_A(x, y, t).$$

The stresses at the top surface τ_{sx} and τ_{sy} are primarily due to wind stress from the storm. The wind stress is calculated by the empirical formula

$$\begin{aligned} \tau_{sx} &= \rho_{\text{air}} c_f(|W|)|W| W \cdot \hat{x} \quad \text{and} \\ \tau_{sy} &= \rho_{\text{air}} c_f(|W|)|W| W \cdot \hat{y} \end{aligned}$$

where $\hat{x}$ and $\hat{y}$ are the unit vectors in the x and y directions, that assumes a value for the wind W as being valid 10 meters above the surface of the ocean. The effective momentum transfer is determined by an empirically defined coefficient c_f calculated as

$$c_f = 10^{-3} \times \begin{cases} 1.2 & \text{if } |W| \leq 11, \\ 0.49 + 0.065\ |W| & \text{if } 11 < |W| \leq 25, \quad \text{and} \\ 0.49 + 0.065 \cdot 25 & \text{if } 25 < |W|. \end{cases}$$

taken from [44].

Coriolis Effect

The Coriolis effect is the apparent force or motion of an object on the Earth due to the Earth's rotation. For many geophysical flows the Coriolis effect can be important depending on the scales associated with the flow. The Rossby number, defined as

$$\text{Ro} \equiv \frac{U}{Lf}$$

[1] Another source of surface stress is due to wave stress from the wave action, but for this study these effects are ignored.

where U is a characteristic velocity, L is a characteristic length scale, and f the Coriolis parameter, compares the inertial terms in the equations to the Coriolis terms and can be a useful measure of how much impact we can expect the Coriolis terms to have on the solution. If we ignore all other forces on the ocean, the effective equations due to the Coriolis effect are

$$u_t = fv \quad \text{and} \quad v_t = -fu$$

where the Coriolis parameter is defined as

$$f = 2\Omega \sin \phi$$

where Ω is the angular speed of the earth and ϕ the given latitude.

For storm surges, if we assume a characteristic velocity $1 < U < 5$ m/s, a characteristic length scale in the range $10 \leq L \leq 250$ km and a Coriolis parameter at $\phi = 30°$, the Rossby number will be in the range $0.05 \leq \text{Ro} \leq 7.0$ (see figure 7.1) which indicates that Coriolis may be an important component of the dynamics of the flow. An alternative to this definition uses the fact that for much of the domain, the wave involved act nearly linearly. In this case, the Rossby number defined as

$$\text{Ro}_w = \frac{\omega}{f} \tag{7.1}$$

where ω is the wave frequency, may be more appropriate. For shallow water waves, taking

$$\omega = \sqrt{\frac{g}{h}}$$

implies that $\text{Ro}_w \approx 800$ assuming a $h = 3000$ m, $g = 9.8\text{m/s}^2$, and $\phi = 30°$. This is well outside the range where Coriolis should have an effect on the flow. This also holds true for internal waves with the assumption that $\omega = \sqrt{\frac{(1-r)g}{h}}$ with the same values as before and $r = 0.98$. These two conflicting results lead to the conclusion that for different aspects of the flow, Coriolis may or may not be important. Later in this chapter we will see that Coriolis effects appear to have little impact on the simulations which implied that the definition of the Rossby number in (7.1) may be the correct one to use here.

7.1.2 Idealized Storm Model

The storm is modeled via an empirical formula for the pressure and wind profiles derived by Holland in [29]. The profile for pressure is

$$P_A = P_c + (P_n - P_c)e^{-A/r^B}$$

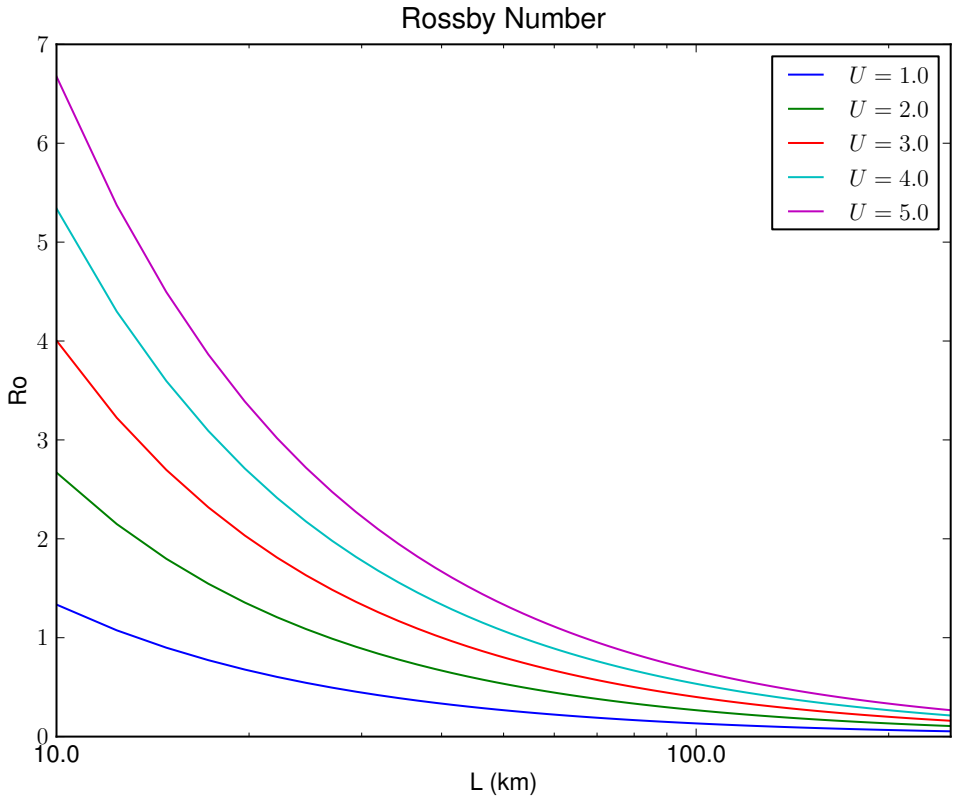

Figure 7.1: A plot of the Rossby number at different characteristic speeds versus different length scales characterizing the size of the storm to the size of the domain.

where P_c is the central pressure, P_n is the ambient pressure, and A and B are scaling parameters determined by the particular storm. The profile for the wind magnitude is

$$|W| = \sqrt{\frac{AB(P_n - P_c)e^{-A/r^B}}{\rho_{\text{air}} r^B} + \frac{r^2 f^2}{4}} - \frac{rf}{2}$$

where the same parameters are present as in the pressure profile with the addition of ρ_{air} which represents the density of air and the Coriolis parameter f. These profiles are the assumed to be angularly symmetric for the pressure and wind magnitude. The direction of the wind field is assumed to be along the $\hat{\theta}$ direction moving counter-clockwise so that

$$W = \frac{-|W|y}{r}\hat{x} + \frac{|W|x}{r}\hat{y}$$

where the coordinates x and y are distances from the eye of the storm in the appropriate directions and $r = \sqrt{x^2 + y^2}$. The storm is also assumed to move with constant speed such that at any point in time, the storm's location is given by

$$r_{\text{eye}} = V_{\text{storm}} t + r_{\text{eye},0}$$

where V_{storm} is a velocity vector, t is the time and $r_{\text{eye},0}$ is the position of the storm at $t = 0$.

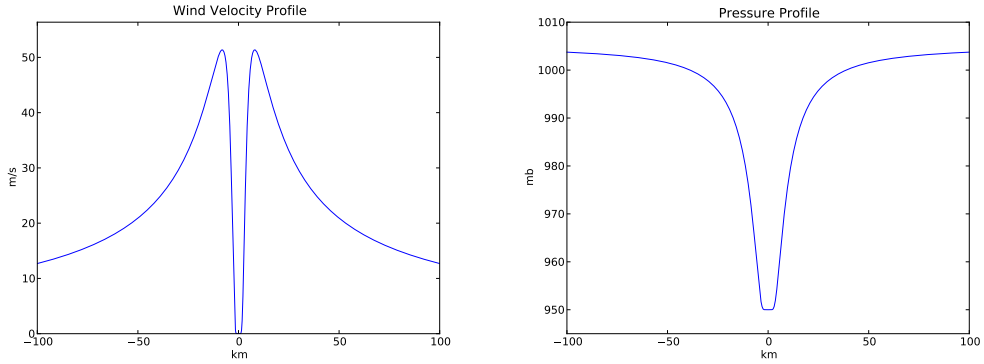

Figure 7.2: Wind and pressure profiles of a storm whose center is located at $x = 0$ with parameters $A = 23.0$, $B = 1.5$, $P_n = 1005$ mb and $P_c = 950$ mb which are fits for Hurricane Tracy from 1974.

7.1.3 Single-Layer Storm Surge Equations

From the single-layer equations we derived (4.3) and the addition of the Coriolis terms and specification of the boundary stresses, the equations we will use to model storm surges are

$$\begin{aligned}
&h_t + (hu)_x + (hv)_y = 0, \\
&(hu)_t + \left(hu^2 + \frac{1}{2}gh^2\right)_x + (huv)_y = fhv - ghb_x - \frac{h}{\rho}(P_A)_x + \frac{1}{\rho}\tau_{sx} - \frac{1}{\rho}\tau_{bx}, \quad \text{and} \\
&(hv)_t + (huv)_x + \left(hv^2 + \frac{1}{2}hv^2\right)_y = -fhu - ghb_y - \frac{h}{\rho}(P_A)_y + \frac{1}{\rho}\tau_{sy} - \frac{1}{\rho}\tau_{by}.
\end{aligned}$$

7.1.4 Two-Layer Storm Surge Equations

The two-layer equations we will use are based on (5.8) with the appropriate source terms added. The source terms affect the appropriate layer depending on the location

of the forcing source. For the wind stress, the top layer is only affected. The bottom friction only effects the bottom layer when it is wet and otherwise is applied to the top layer. The pressure gradient and Coriolis terms affect the entire water column and they are applied to both layers.

$$
\begin{aligned}
&(\rho_1 h_1)_t + (\rho_1 h_1 u_1)_x + (\rho_1 h_1 v_1)_y = 0,\\
&(\rho_1 h_1 u_1)_t + \left(\rho_1 h_1 u_1^2 + \frac{1}{2} g \rho_1 h_1^2\right)_x + (\rho_1 h_1 u_1 v_1)_y = -g\rho_1 h_1 (h_2 + b)_x + f\rho_1 h_1 v_1\\
&\qquad - h_1 (P_A)_x + \tau_{sx} + \tau_{bx},\\
&(\rho_1 h_1 v_1)_t + (\rho_1 h_1 u_1 v_1)_x + \left(\rho_1 h_1 v_1^2 + \frac{1}{2} g \rho_1 h_1^2\right)_y = -g\rho_1 h_1 (h_2 + b)_y\\
&\qquad - h_1 (P_A)_y - f\rho_1 h_1 u_1 + \tau_{wx} + \tau_{bx},\\
&(\rho_2 h_2)_t + (\rho_2 h_2 u_2)_x + (\rho_2 h_2 v_2)_x = 0,\\
&(\rho_2 h_2 u_2)_t + \left(\rho_2 h_2 u_2^2 + \frac{1}{2} g \rho_2 h_2^2 + g\rho_1 h_1 h_2\right)_x + (\rho_2 h_2 u_2 v_2)_y = g\rho_1 h_1 (h_2)_x - g\rho_2 h_2 b_x\\
&\qquad - h_2 (P_A)_x + f\rho_2 h_2 v_2 + \tau_{bx}, \quad \text{and}\\
&(\rho_2 h_2 v_2)_t + (\rho_2 h_2 u_2 v_2)_x + \left(\rho_2 h_2 v_2^2 + \frac{1}{2} g \rho_2 h_2^2 + g\rho_1 h_1 h_2\right)_y = g\rho_1 h_1 (h_2)_y - g\rho_2 h_2 b_y\\
&\qquad - h_2 (P_A)_y - f\rho_2 h_2 u_2 + \tau_{by}.
\end{aligned}
$$

7.2 Numerical Approaches

In order to include all of the source terms that were added beyond the original numerical methods discussed earlier, we will employ an operator splitting method. This allows us to separate out the pieces of the numerics that are being handled already in the Riemann solver from the terms above. In the case of the single-layer equations, the PDEs we need to solve for the source terms are

$$
\begin{aligned}
h_t &= 0\\
(hu)_t &= fhv - \frac{h}{\rho}(P_A)_x + \frac{1}{\rho}\tau_{sx} - \frac{1}{\rho}\tau_{bx} \quad \text{and}\\
(hv)_t &= -fhu - \frac{h}{\rho}(P_A)_y + \frac{1}{\rho}\tau_{sy} - \frac{1}{\rho}\tau_{by}.
\end{aligned}
$$

For the two-layer equations the PDEs are

$$\begin{aligned}
&(\rho_1 h_1)_t = 0,\\
&(\rho_1 h_1 u_1)_t = f\rho_1 h_1 v_1 - h_1 (P_A)_x + \tau_{sx} + \tau_{bx},\\
&(\rho_1 h_1 v_1)_t = -h_1 (P_A)_y - f\rho_1 h_1 u_1 + \tau_{wx} + \tau_{bx},\\
&(\rho_2 h_2)_t = 0,\\
&(\rho_2 h_2 u_2)_t = -h_2 (P_A)_x + f\rho_2 h_2 v_2 + \tau_{bx}, \quad \text{and}\\
&(\rho_2 h_2 v_2)_t = -h_2 (P_A)_y - f\rho_2 h_2 u_2 + \tau_{by}.
\end{aligned}$$

Another approach is to include all of the source terms in the Riemann solver as we have done for the bathymetry and the layer momentum transfer terms in the multi-layer case. This would allow a more direct numerical computation of some of the source terms and may be especially advantageous for the wind and bottom friction as these source terms are physically expected to be of the same order.

Bottom Friction

For the bottom friction terms, τ_{bx} and τ_{by} take the form

$$\tau_{bx} = Dhv \tau_{by} = Dhv$$

in the single-layer case and are multiplied by the appropriate density in the multi-layer case. The friction coefficient is defined as $D = \frac{gn^2}{h^{7/3}}\sqrt{u^2 + v^2}$. If we assume that D can be evaluated using the current time t_n's states, we can exactly integrate the equations and form the update

$$\begin{aligned}
(hu)_{ij}^{n+1} &= (hu)_{ij}^{n} e^{-D_{ij}^{n}\Delta t} \quad \text{and}\\
(hv)_{ij}^{n+1} &= (hv)_{ij}^{n} e^{-D_{ij}^{n}\Delta t}.
\end{aligned}$$

For the single-layer system, this update can be applied directly with

$$D_{ij}^{n} = n^2 g (h_{ij}^{n})^{-7/3} \sqrt{(u_{ij}^{n})^2 + (v_{ij}^{n})^2}.$$

In the case of the multi-layer system, the update is evaluated such that

$$\begin{aligned}
(h_2 u_2)_{ij}^{n+1} &= (h_2 u_2)_{ij}^{n} e^{-D_{ij}^{n}\Delta t} \quad \text{and}\\
(h_2 v_2)_{ij}^{n+1} &= (h_2 v_2)_{ij}^{n} e^{-D_{ij}^{n}\Delta t}
\end{aligned}$$

where now D is evaluated as

$$D_{ij}^n = n^2 g \left(\sum_{m=1}^{2} h_{m,ij}^n \right)^{-7/3} \sqrt{(u_{2,ij}^n)^2 + (v_{2,ij}^n)^2}.$$

If the bottom layer becomes dry, the source term reverts back to the single layer case source term.

Coriolis Effect

The first step in evaluating the Coriolis terms is to calculate the coefficient f. This can be done by either using a β-plane approach which uses a Taylor-expansion of the Coriolis term up to first order about a particular latitude, or evaluate the term directly if the grid is in latitude-longitude coordinates. The β-plane approach uses a tangent plane approximation to the earth so that a quadrilateral grid can be used by converting the coordinate representing the north-south direction into radians via

$$\theta = \frac{y\pi}{20\,000\text{km}}$$

assuming that the half circumference of the earth is roughly 20,000 km. We then evaluate

$$f = 2\omega(\sin\theta_0 + (\theta - \theta_0)\cos\theta_0)$$

for some ideal latitude θ_0 and the y location on the grid. The second step is to find the update to the conserved quantities. In the single layer case, this amounts to solving

$$w_t = Afw \tag{7.2}$$

where $w = [u, v]^t$ and

$$A = \begin{bmatrix} 0 & 1 \\ -1 & 0 \end{bmatrix}.$$

We can integrate this exactly and find the solution to the ODE (7.2) over a time interval of length Δt as

$$w = w_0 e^{fA\Delta t}$$

leaving us only to evaluate the matrix exponential. This can be done to any order one wishes but for practical purposes we will only evaluate it to fourth order. The two-layer equations use the exact same procedure to update each layer's momentum.

Storm Forcing

The wind stress terms do not depend on the solution at all in the form given above and are therefore straight forward to calculate. A more accurate wind friction coefficient

should take into account the velocity of the water it is moving over the common practice is to ignore that effect.

The pressure gradient terms are evaluated by taking the second order centered difference of the pressure field P_A such that

$$(P_A)_x = \frac{[P_A]_{i+1,j} - [P_A]_{i-1,j}}{2\Delta x} \quad \text{and} \quad (P_A)_y = \frac{[P_A]_{i,j+1} - [P_A]_{i,j-1}}{2\Delta y}.$$

In any number of layers, the source term PDEs state that the depth does not change in time during the source term evaluations which means that the pressure gradient source term does not depend on the unknown function and similar to the wind stress can be simply evaluated.

7.3 Storm Surge Simulation Results

A number of simulations using the numerical methods found in this and previous chapters were used to simulate a number of idealized storm surge events. Each of the simulations included wind, pressure, Coriolis, and friction source terms. For each simulation a number of simulated tide gauges were also used located as shown in figure 7.3. The bathymetry used has the cross section indicated in figure 7.3 where the initial surfaces have been indicated as well. Each simulation shown also has been run for 12 hours before $t = 0$ so that the hurricane forcing can be ramped up smoothly to the maximum value. It was demonstrated recently for Hurricane Ike that a storms direction relative to the continental shelf can have a large impact on surge height [19]. In order to address the potential differences in surge behavior depending on storm track, the storms in each of the simulations varied their direction and speed of travel. Table 7.1 has a summary of all the simulation results including which figures correspond to which event.

The single-layer test cases are using the AMR available in GeoClaw utilizing a momentum based criteria in addition to the surface gradient condition used in GeoClaw. The storm is also refined around the eye of the storm. The coarse grid cells have a resolution of $\Delta x = 10$ km with a refinement factor of two between each level (drawn as black rectangles in the single-layer figures). The two-layer cases are not using AMR and have a resolution $\Delta x = 31/3$ km.

It is clear from these simulations that there are significant differences between the single-layer and two-layer simulations. As is expected, the top layer velocities are much higher than in the single-layer case as the wind transfers the same amount of momentum to smaller parcel of water. One consequence of this is that the momentum imparted to the water is located in the upper part of the ocean and as the surge reaches the continental shelf, a small amount of momentum can cause a large surge to form and much of the momentum from the top-layer to be transmitted onto the continental shelf (similar to what figure 5.9 shows). Another consequence of this is that the loss

Velocity	Direction	Figures	Gauge Figures
5.0 m/s	0°	7.4,7.5,7.6, 7.7	7.8
5.0 m/s	45°	7.9,7.10,7.11,7.12	7.13
5.0 m/s	−45°	7.14,7.15,7.16,7.17	7.18
5.0 m/s	90°	7.19,7.20,7.21,7.22	7.23
5.0 m/s	−90°	7.24,7.25,7.26,7.27	7.28
25.0 m/s	0°	7.29,7.30,7.31,7.32	7.33

Table 7.1: Simulations of storm surge results with various hurricane directions and speeds.

of momentum due to friction, which in the single-layer case nearly negates the flux of momentum due to the wind in deep water, is largely decoupled and has much less of an effect on the velocities of the top layer. Finally, although we have neglected wave-stress as a source, current storm surge models include source terms to account for shorter wave-length waves. It is believed that these waves can have a significant impact on overall surge height and capturing them is important for forecast accuracy. As the two-layer model can better represent the two inputs to the wave-stress models currently available, momentum and wave height, the two-layer model should provide a better representation for the wave-stresses and consequently better storm surge predictions.

The hurricane tracks also have an impact on both the single and two-layer simulations. The direction of travel and the location of the simulated tidal gauges show that the variation in storm track can be an important aspect to consider. This again emphasizes the importance of a fast solver so that ensembles of hurricane tracks can be taken into account for storm surge forecasting. The hurricane speeds also appear to have a large impact on the form and severity of the storm surge. As was the case with the storm moving at 25 m/s, momentum was not transferred to the top layer as effectively and overall wave height and speed was reduced.

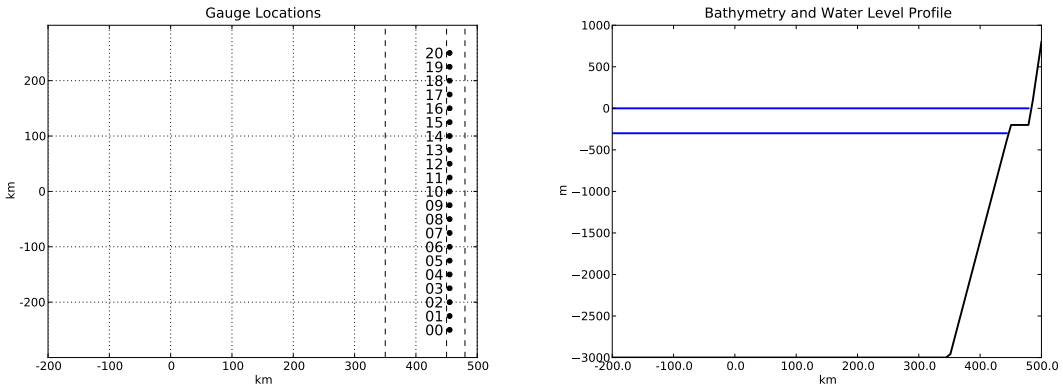

Figure 7.3: The left figure marks the location of the simulated tide gauges as well as the entirety of the domain. The right figure shows a cross section of the bathymetry in the x-direction with the initial sea surfaces shown in relation to the bathymetry.

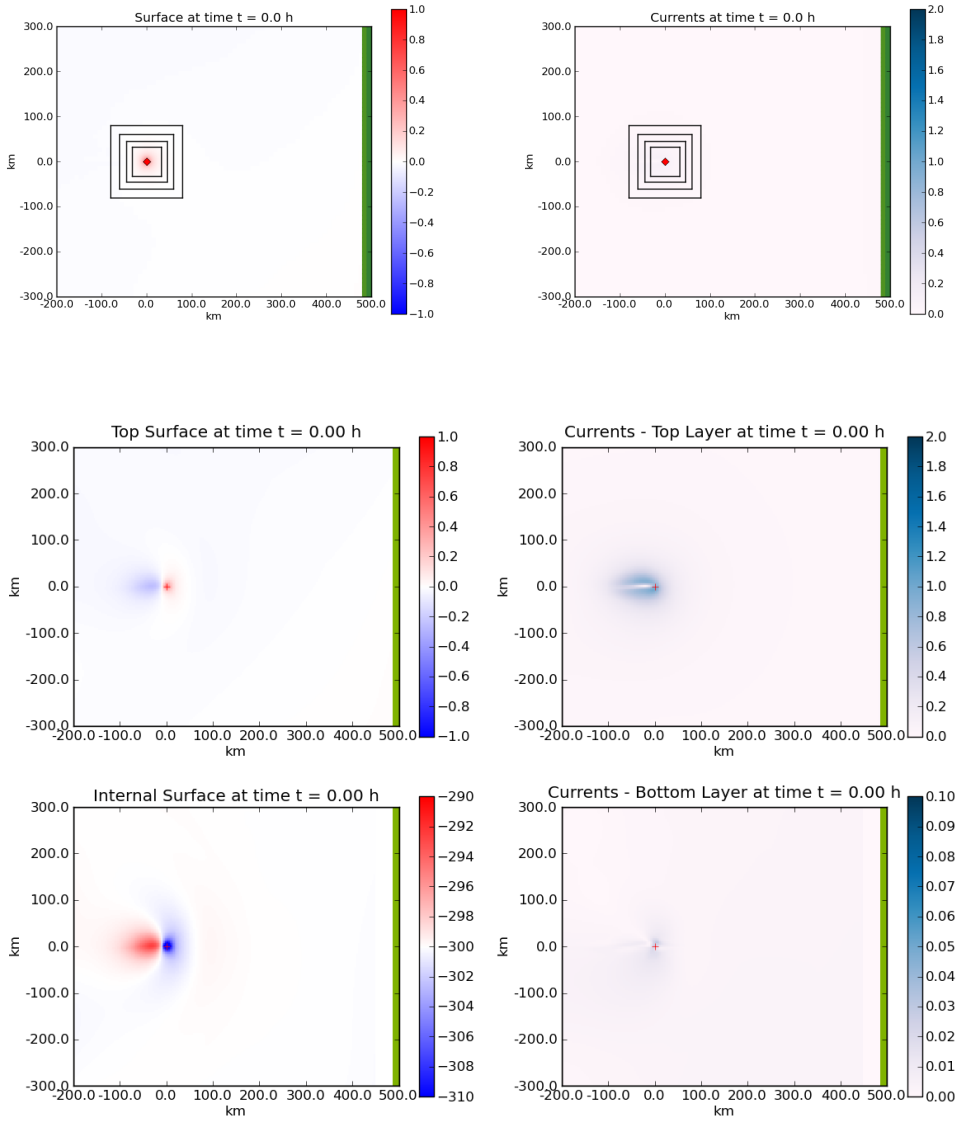

Figure 7.4: Comparison at $t = 0$ of single and two-layer simulations with a hurricane moving perpendicular to the shelf at 5 m/s. The top two figures show the single-layer results of the sea surface on the left and the currents on the right. The bottom two rows are from the two-layer simulation again with the values of the top and internal surfaces on the left and the currents in the top and bottom layers on the right.

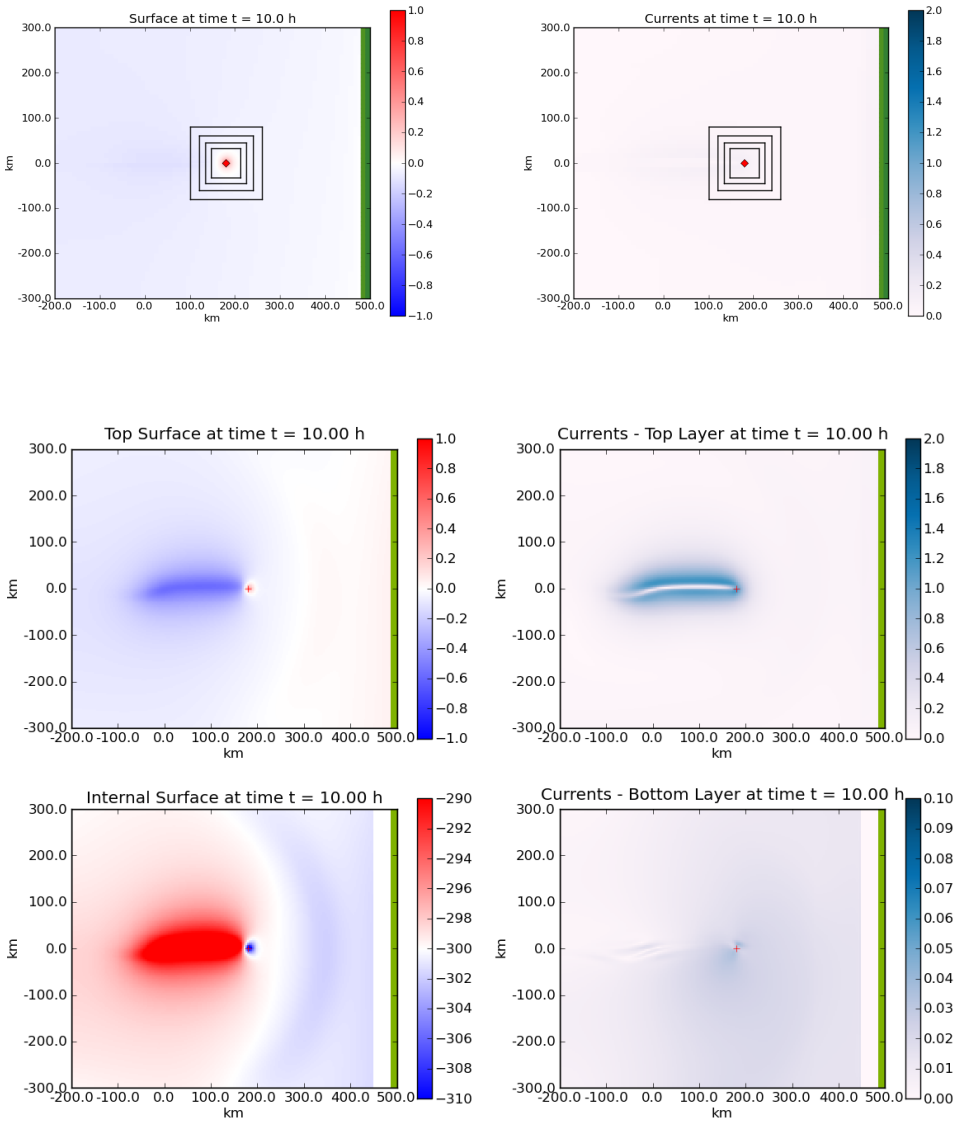

Figure 7.5: Comparison at $t = 10$ hours of single and two-layer simulations with a hurricane moving perpendicular to the shelf at 5 m/s. The top two figures show the single-layer results of the sea surface on the left and the currents on the right. The bottom two rows are from the two-layer simulation again with the values of the top and internal surfaces on the left and the currents in the top and bottom layers on the right.

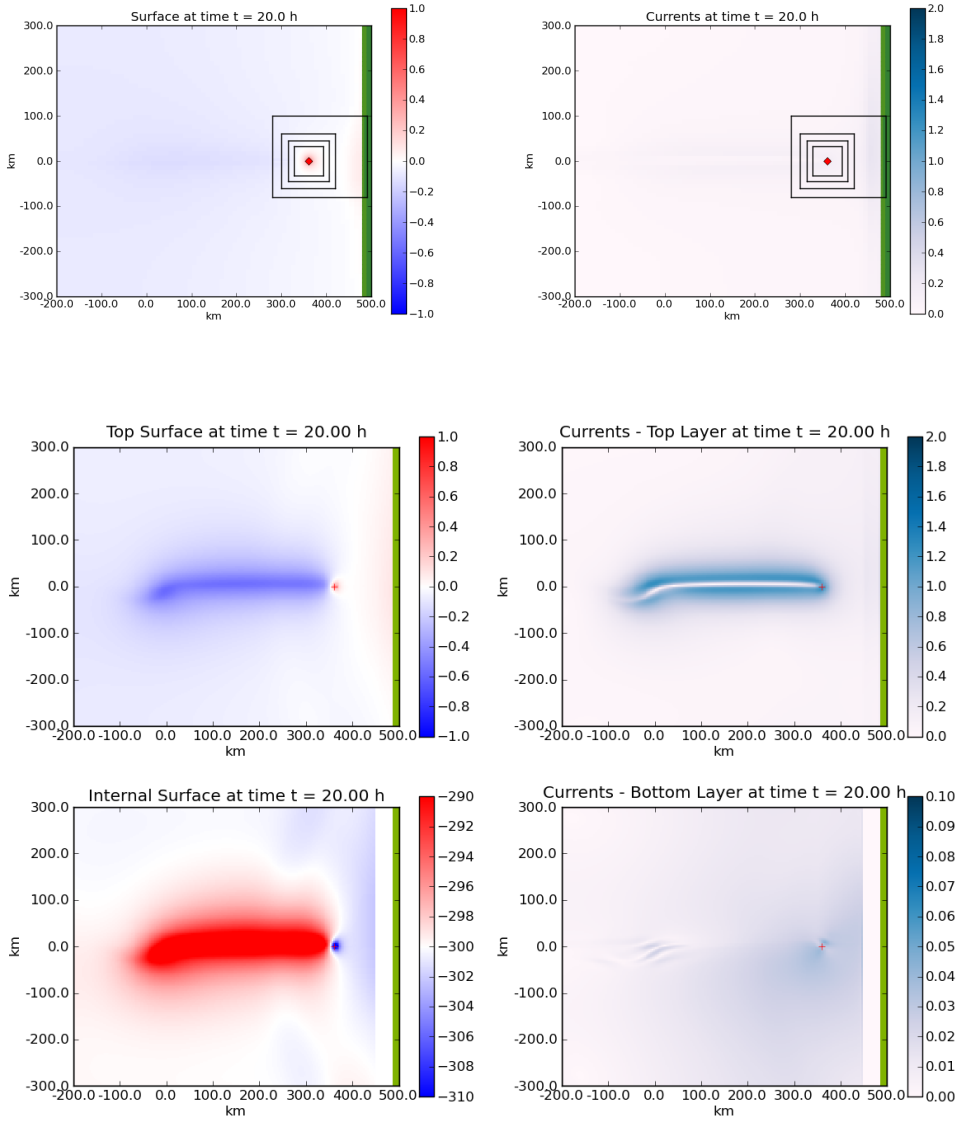

Figure 7.6: Comparison at $t = 20$ hours of single and two-layer simulations with a hurricane moving perpendicular to the shelf at 5 m/s. The top two figures show the single-layer results of the sea surface on the left and the currents on the right. The bottom two rows are from the two-layer simulation again with the values of the top and internal surfaces on the left and the currents in the top and bottom layers on the right.

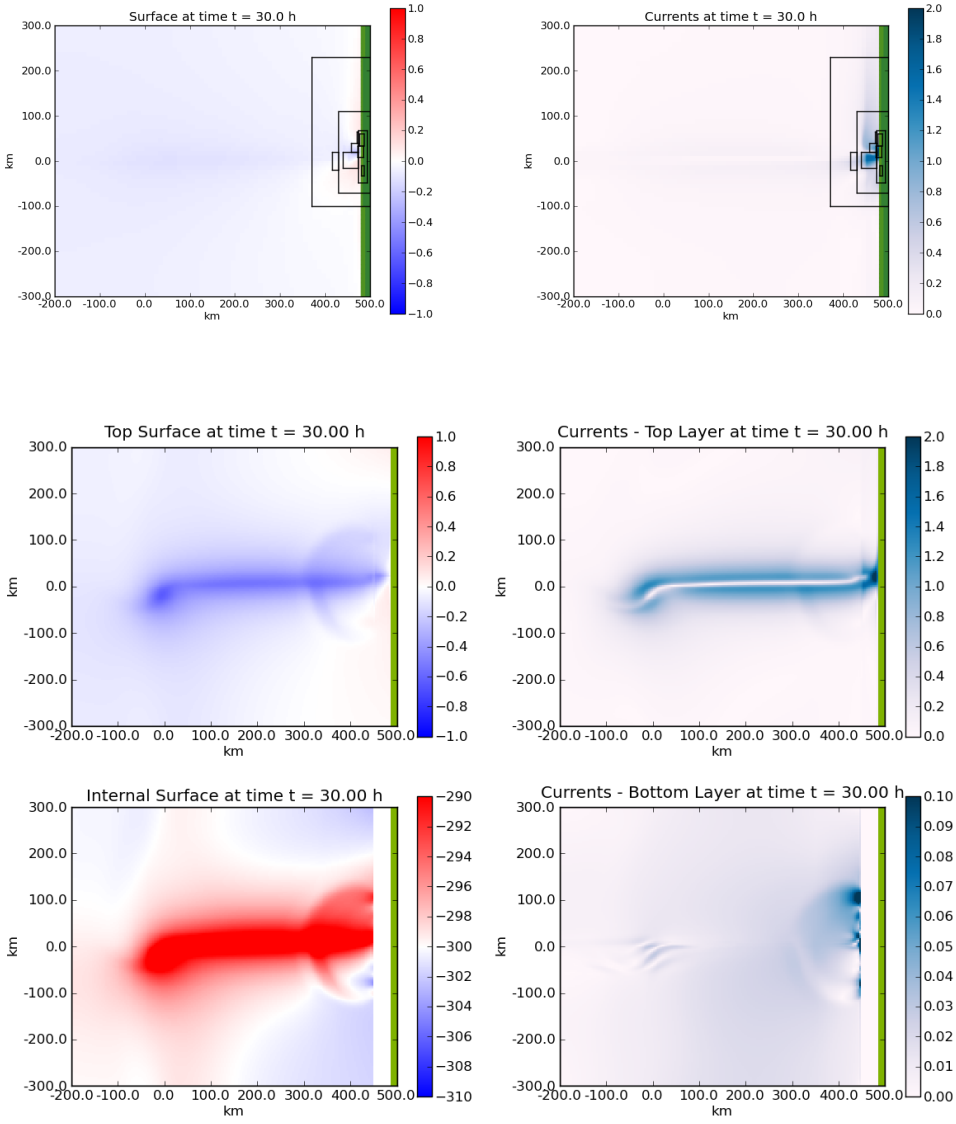

Figure 7.7: Comparison at $t = 30$ hours of single and two-layer simulations with a hurricane moving perpendicular to the shelf at 5 m/s. The top two figures show the single-layer results of the sea surface on the left and the currents on the right. The bottom two rows are from the two-layer simulation again with the values of the top and internal surfaces on the left and the currents in the top and bottom layers on the right.

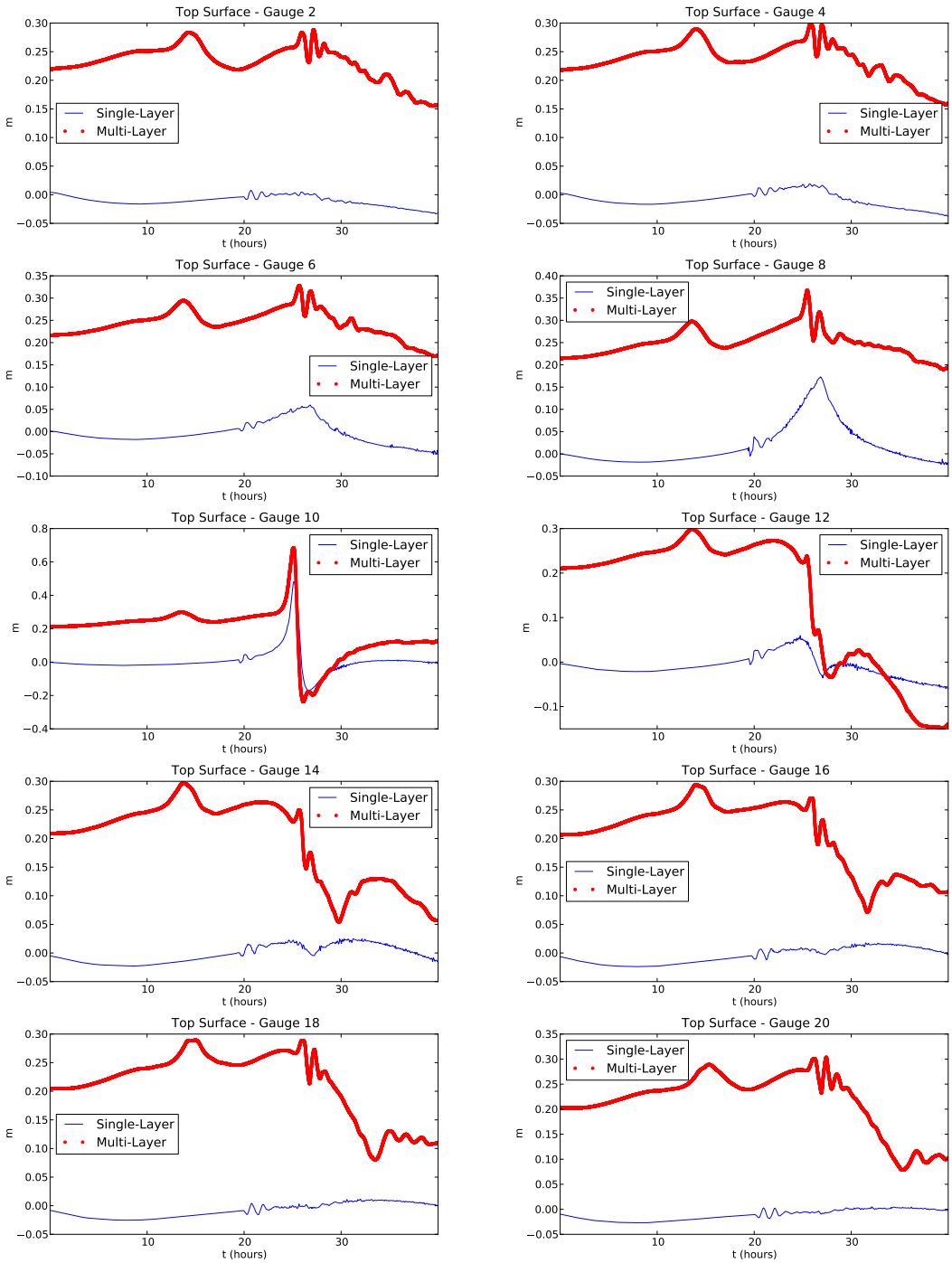

Figure 7.8: Simulated tide gauge data for both the single and two-layer simulations with a hurricane moving perpendicular to the shelf at 5 m/s. The blue line represents the single-layer and the red line the two-layer results.

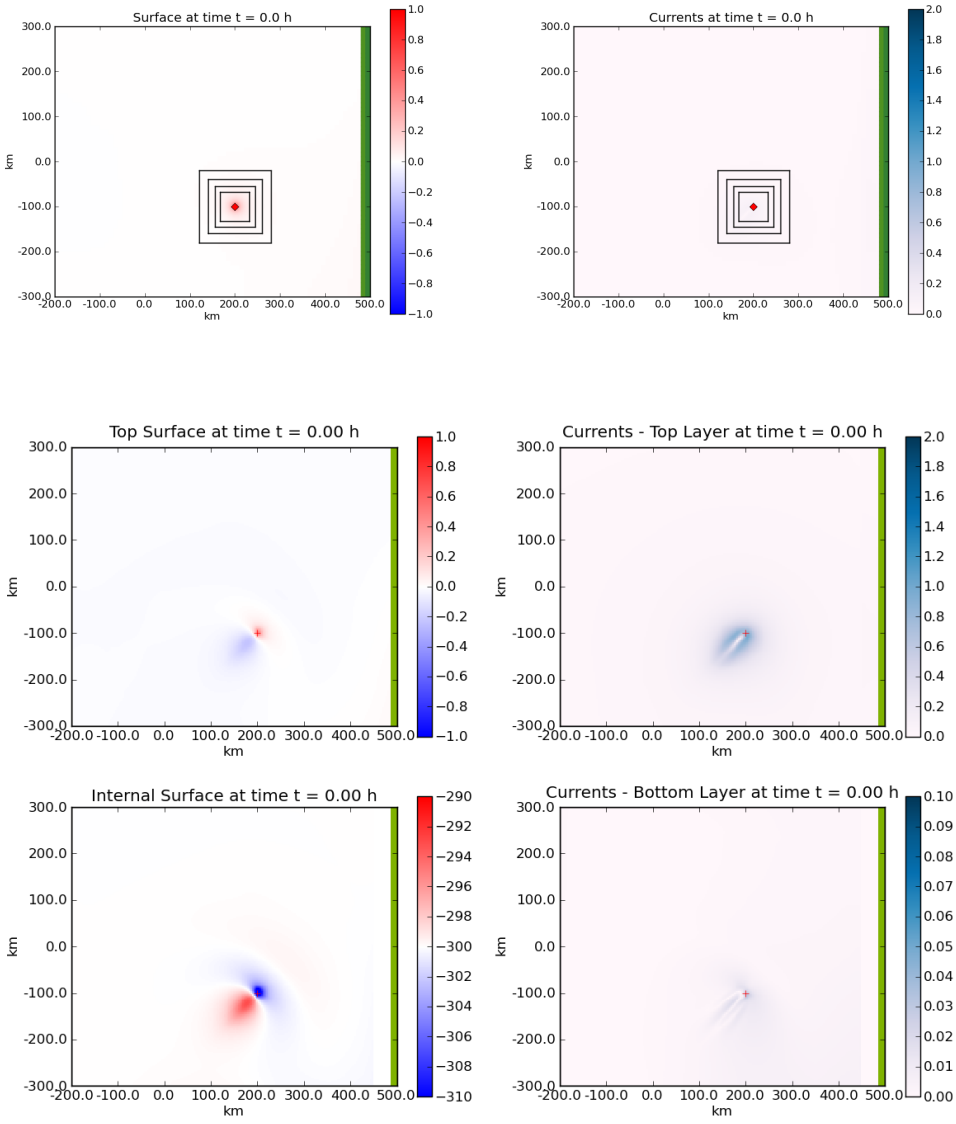

Figure 7.9: Comparison at $t = 0$ of single and two-layer simulations with a hurricane moving at a 45° angle to the shelf at 5 m/s. The top two figures show the single-layer results of the sea surface on the left and the currents on the right. The bottom two rows are from the two-layer simulation again with the values of the top and internal surfaces on the left and the currents in the top and bottom layers on the right.

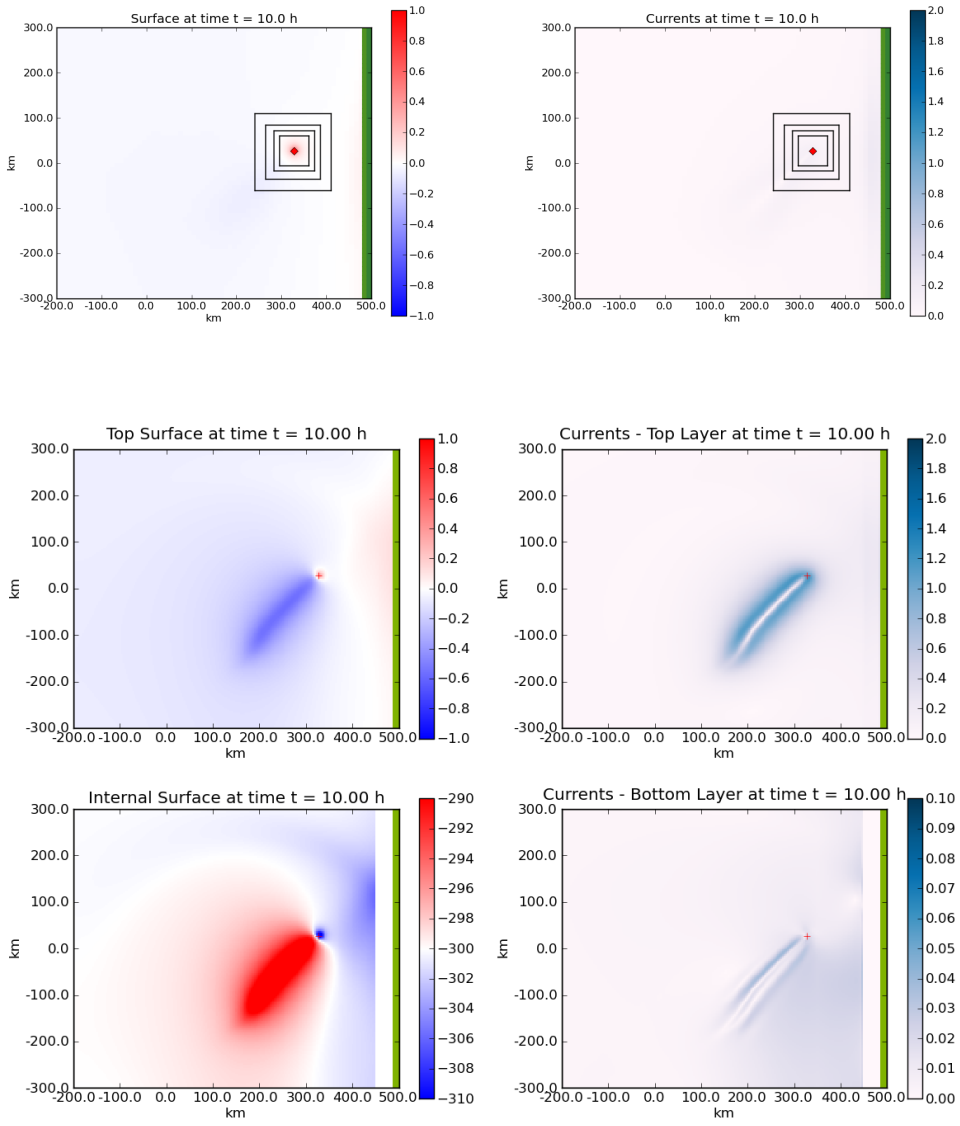

Figure 7.10: Comparison at $t = 10$ hours of single and two-layer simulations with a hurricane moving at a 45° angle to the shelf at 5 m/s. The top two figures show the single-layer results of the sea surface on the left and the currents on the right. The bottom two rows are from the two-layer simulation again with the values of the top and internal surfaces on the left and the currents in the top and bottom layers on the right.

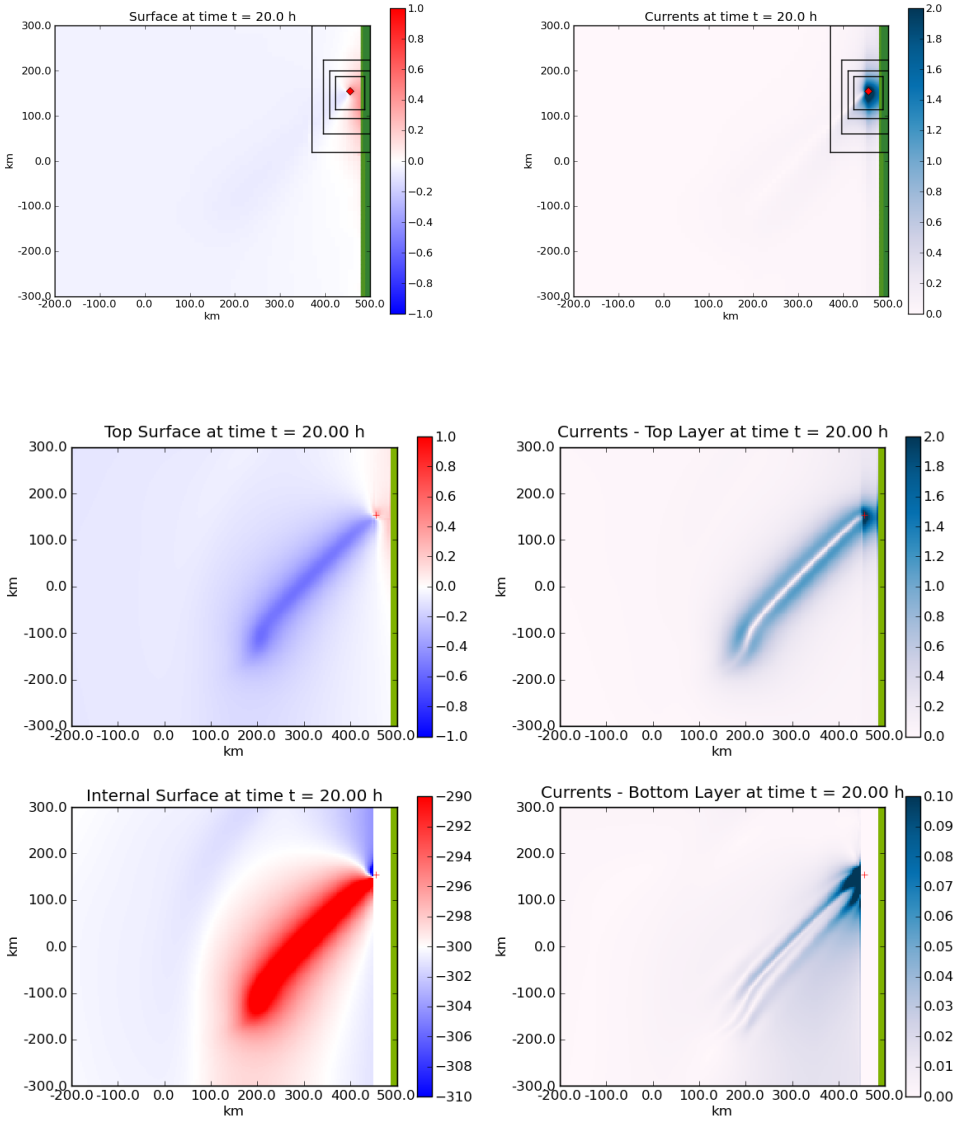

Figure 7.11: Comparison at $t = 20$ hours of single and two-layer simulations with a hurricane moving at a 45° angle to the shelf at 5 m/s. The top two figures show the single-layer results of the sea surface on the left and the currents on the right. The bottom two rows are from the two-layer simulation again with the values of the top and internal surfaces on the left and the currents in the top and bottom layers on the right.

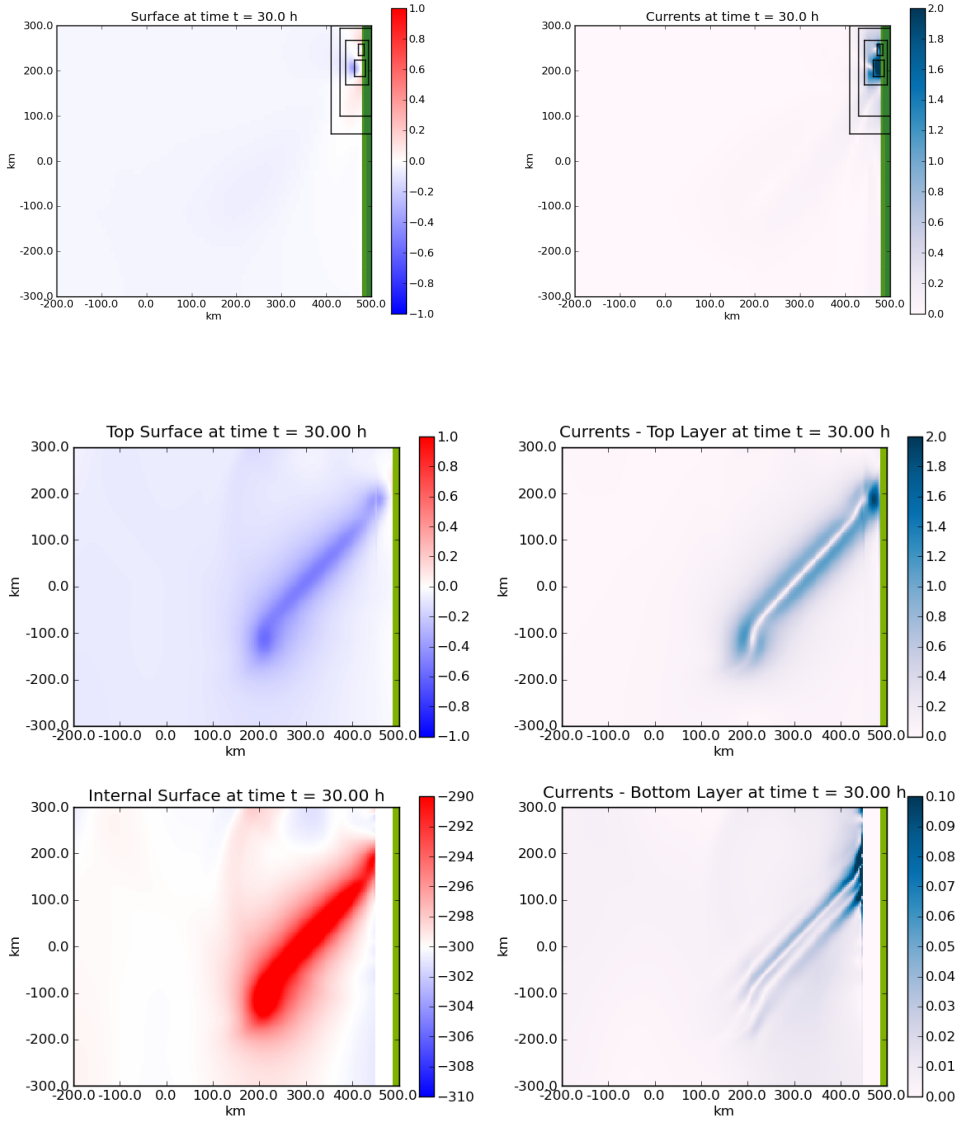

Figure 7.12: Comparison at $t = 30$ hours of single and two-layer simulations with a hurricane moving at a 45° angle to the shelf at 5 m/s. The top two figures show the single-layer results of the sea surface on the left and the currents on the right. The bottom two rows are from the two-layer simulation again with the values of the top and internal surfaces on the left and the currents in the top and bottom layers on the right.

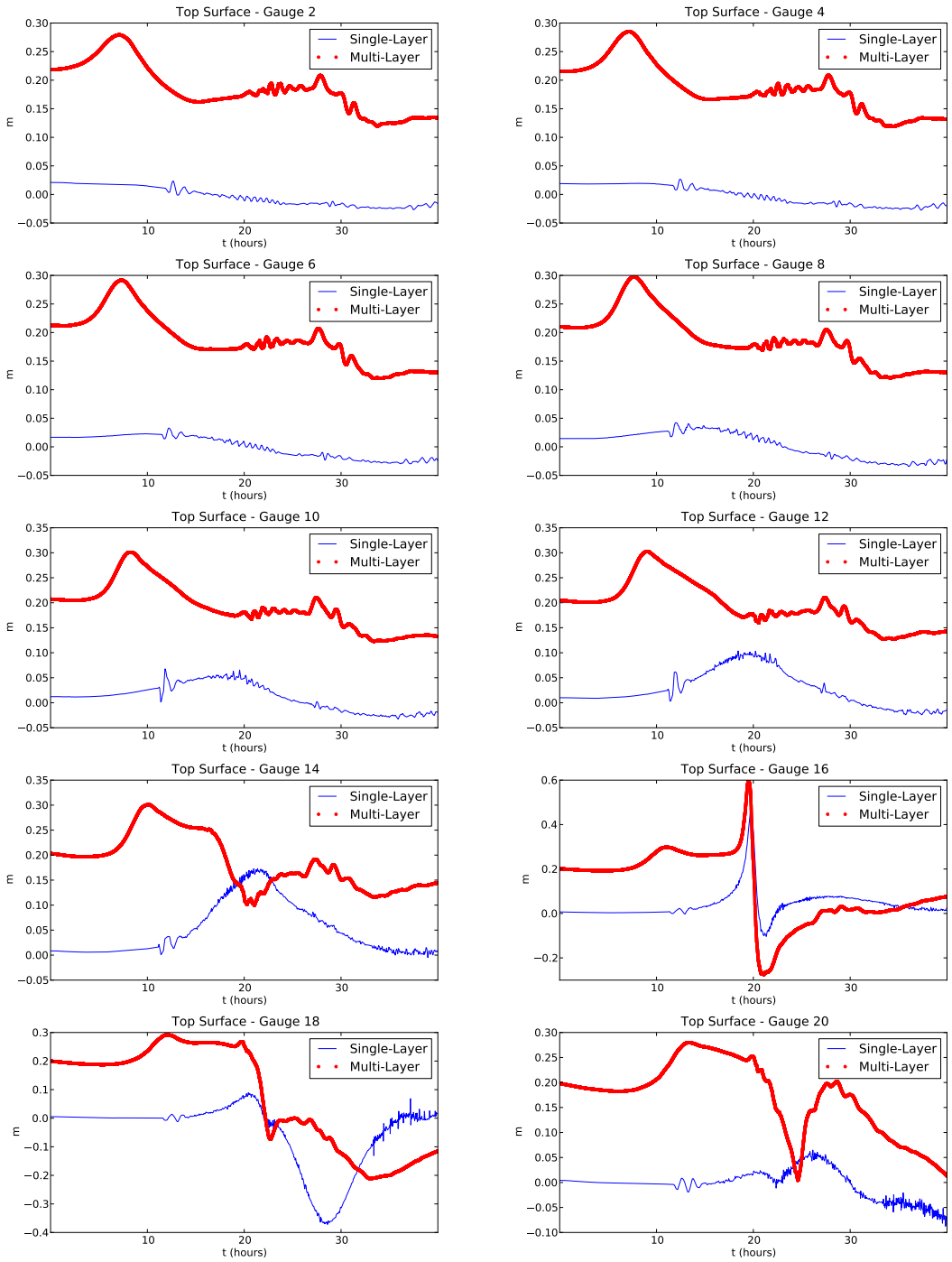

Figure 7.13: Simulated tide gauge data for both the single and two-layer simulations with a hurricane moving at a 45° angle to the shelf at 5 m/s. The blue line represents the single-layer and the red line the two-layer results.

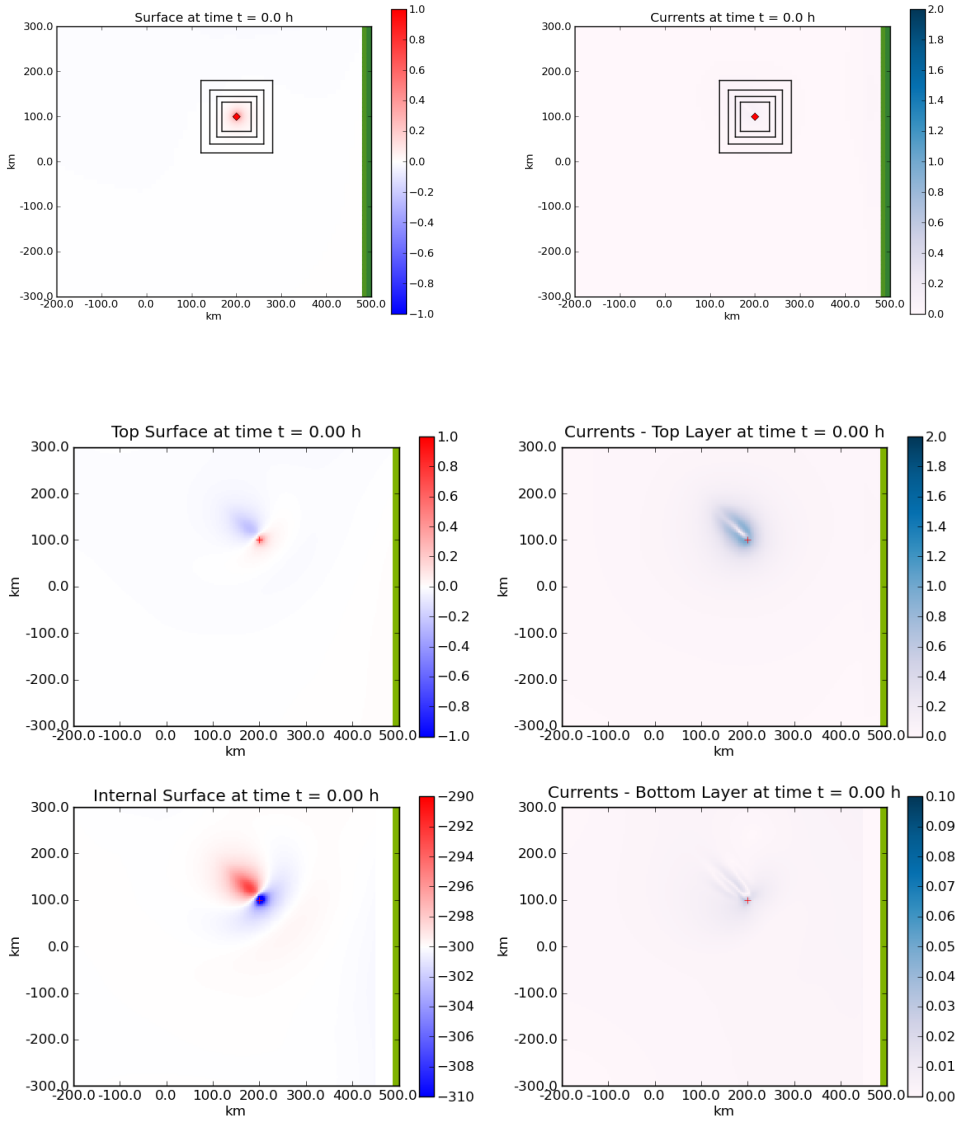

Figure 7.14: Comparison at $t = 0$ of single and two-layer simulations with a hurricane moving at a $-45°$ angle to the shelf at 5 m/s. The top two figures show the single-layer results of the sea surface on the left and the currents on the right. The bottom two rows are from the two-layer simulation again with the values of the top and internal surfaces on the left and the currents in the top and bottom layers on the right.

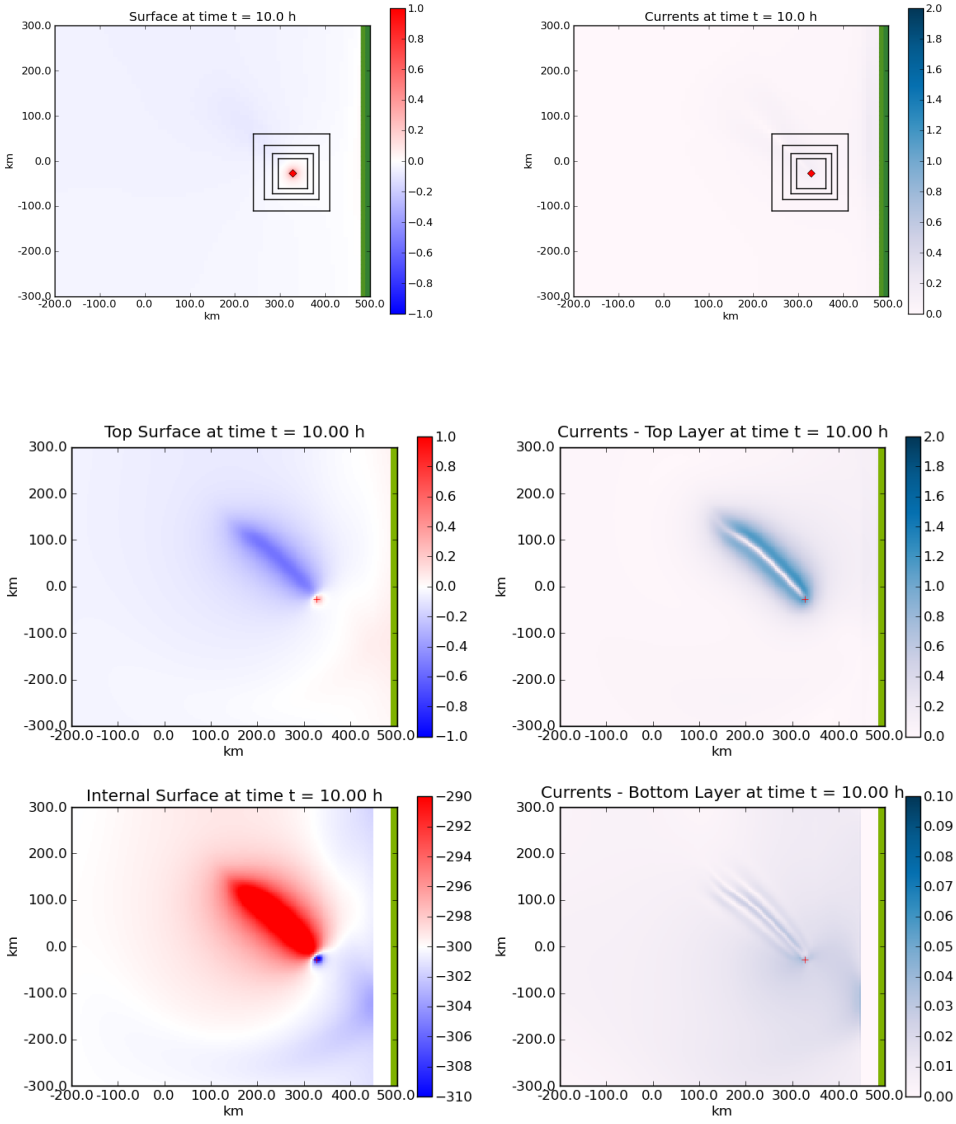

Figure 7.15: Comparison at $t = 10$ hours of single and two-layer simulations with a hurricane moving at a $-45°$ angle to the shelf at 5 m/s. The top two figures show the single-layer results of the sea surface on the left and the currents on the right. The bottom two rows are from the two-layer simulation again with the values of the top and internal surfaces on the left and the currents in the top and bottom layers on the right.

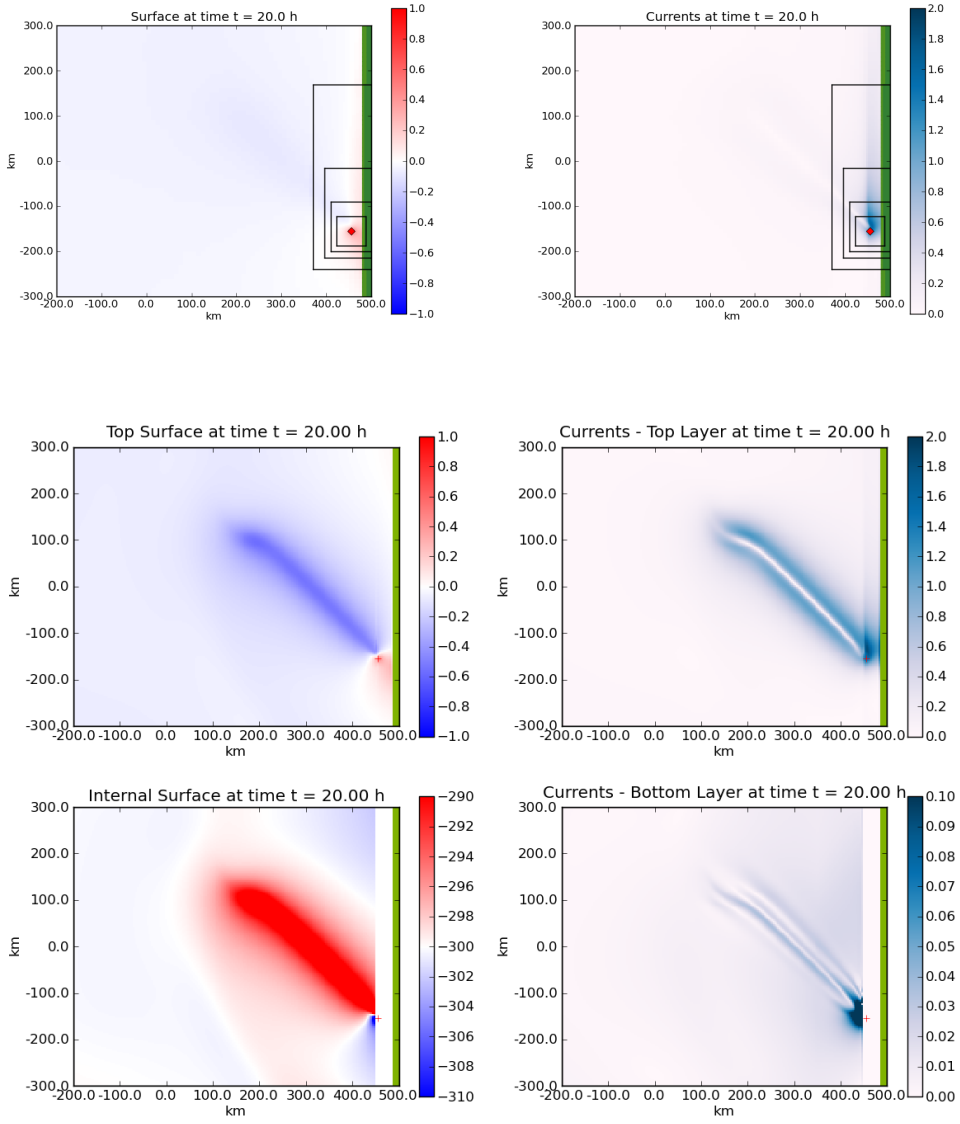

Figure 7.16: Comparison at $t = 20$ hours of single and two-layer simulations with a hurricane moving at a $-45°$ angle to the shelf at 5 m/s. The top two figures show the single-layer results of the sea surface on the left and the currents on the right. The bottom two rows are from the two-layer simulation again with the values of the top and internal surfaces on the left and the currents in the top and bottom layers on the right.

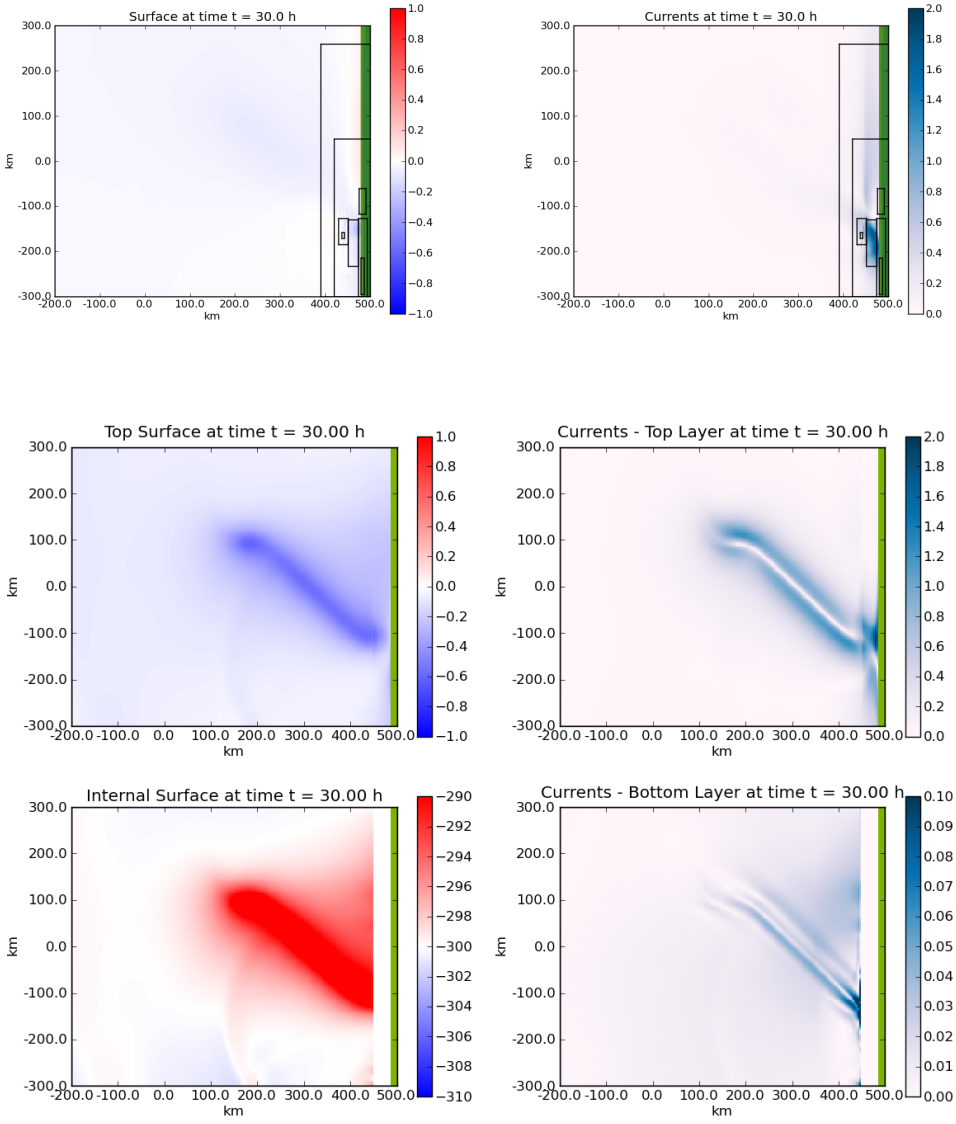

Figure 7.17: Comparison at $t = 30$ hours of single and two-layer simulations with a hurricane moving at a $-45°$ angle to the shelf at 5 m/s. The top two figures show the single-layer results of the sea surface on the left and the currents on the right. The bottom two rows are from the two-layer simulation again with the values of the top and internal surfaces on the left and the currents in the top and bottom layers on the right.

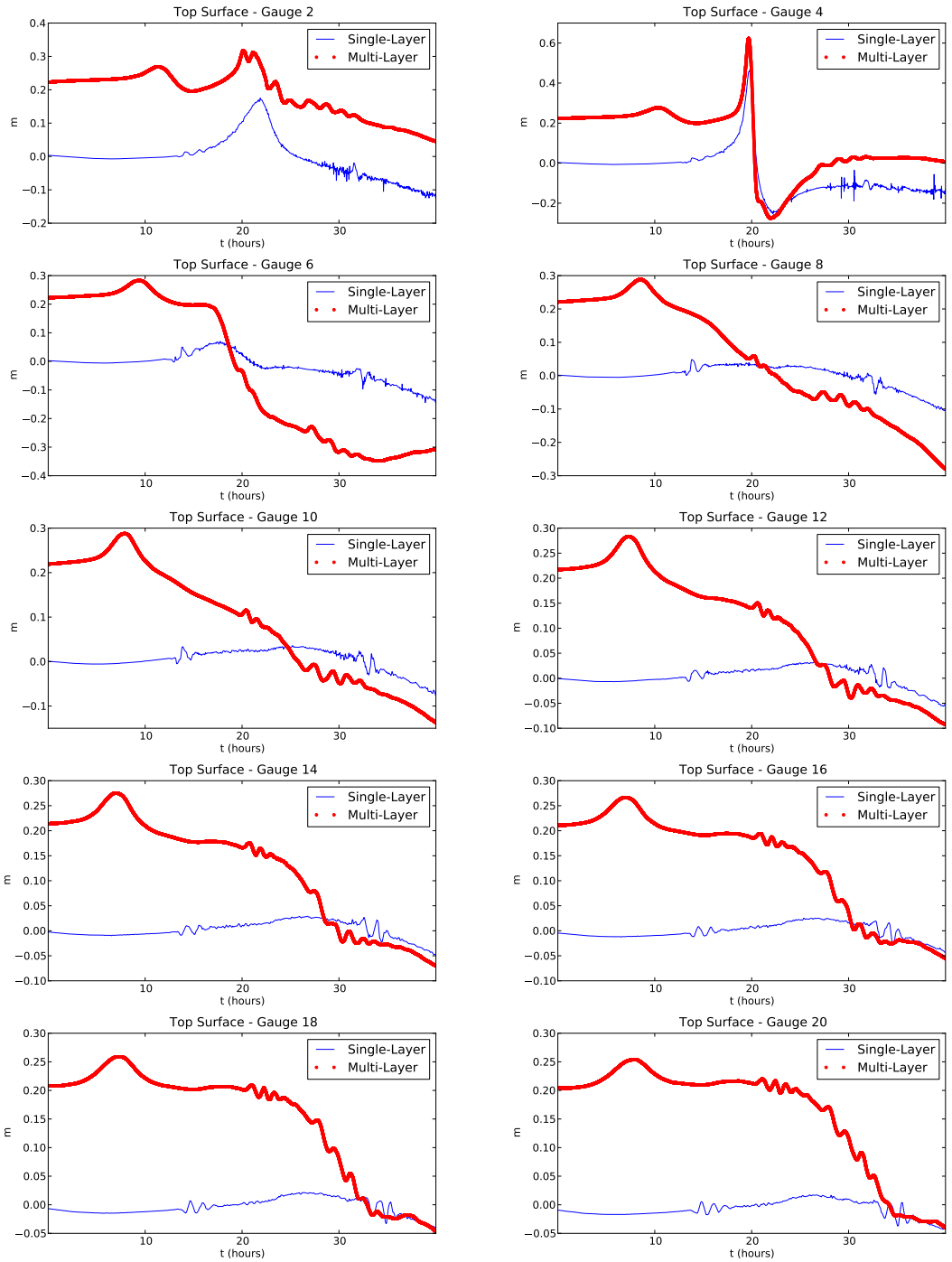

Figure 7.18: Simulated tide gauge data for both the single and two-layer simulations with a hurricane moving at a $-45°$ angle to the shelf at 5 m/s. The blue line represents the single-layer and the red line the two-layer results.

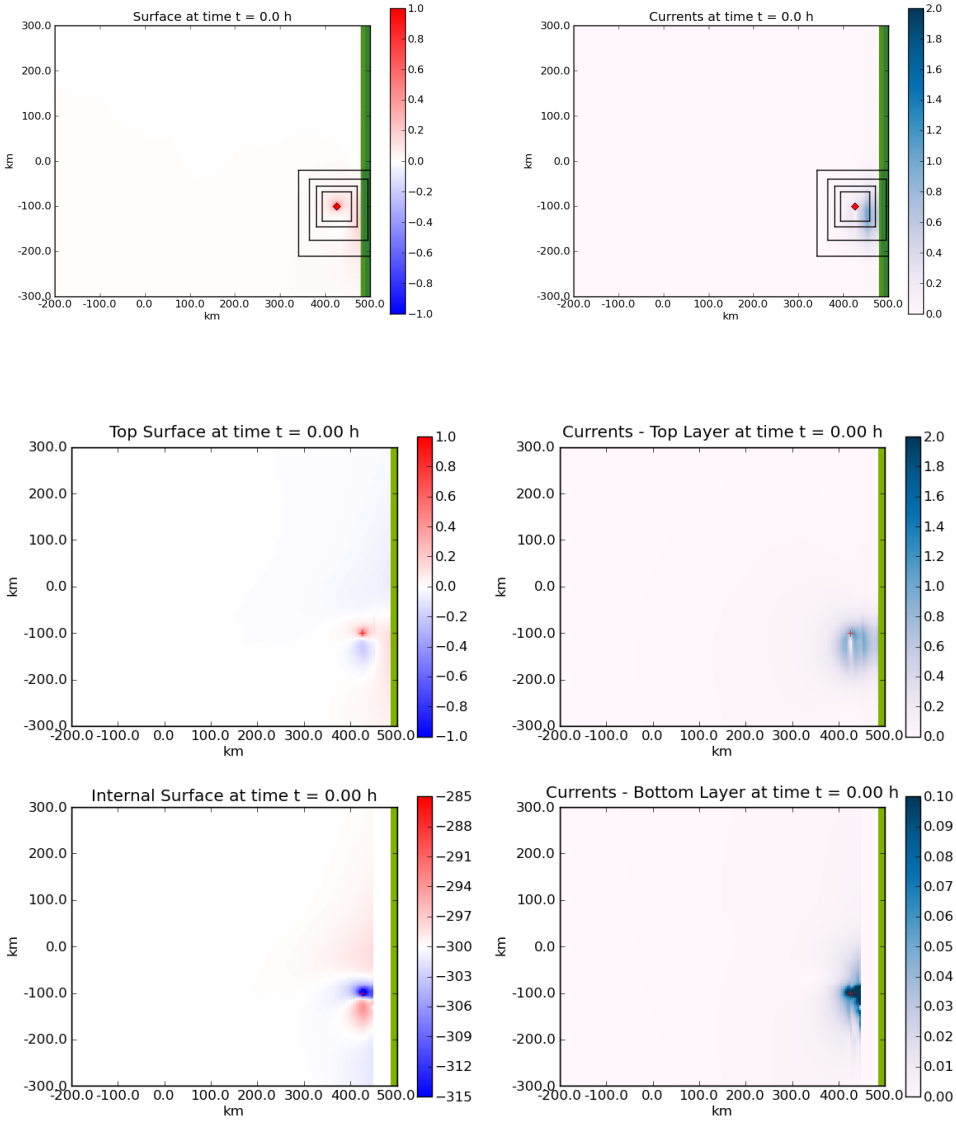

Figure 7.19: Comparison at $t = 0$ of single and two-layer simulations with a hurricane moving parallel in a northerly direction to the shelf at 5 m/s. The top two figures show the single-layer results of the sea surface on the left and the currents on the right. The bottom two rows are from the two-layer simulation again with the values of the top and internal surfaces on the left and the currents in the top and bottom layers on the right.

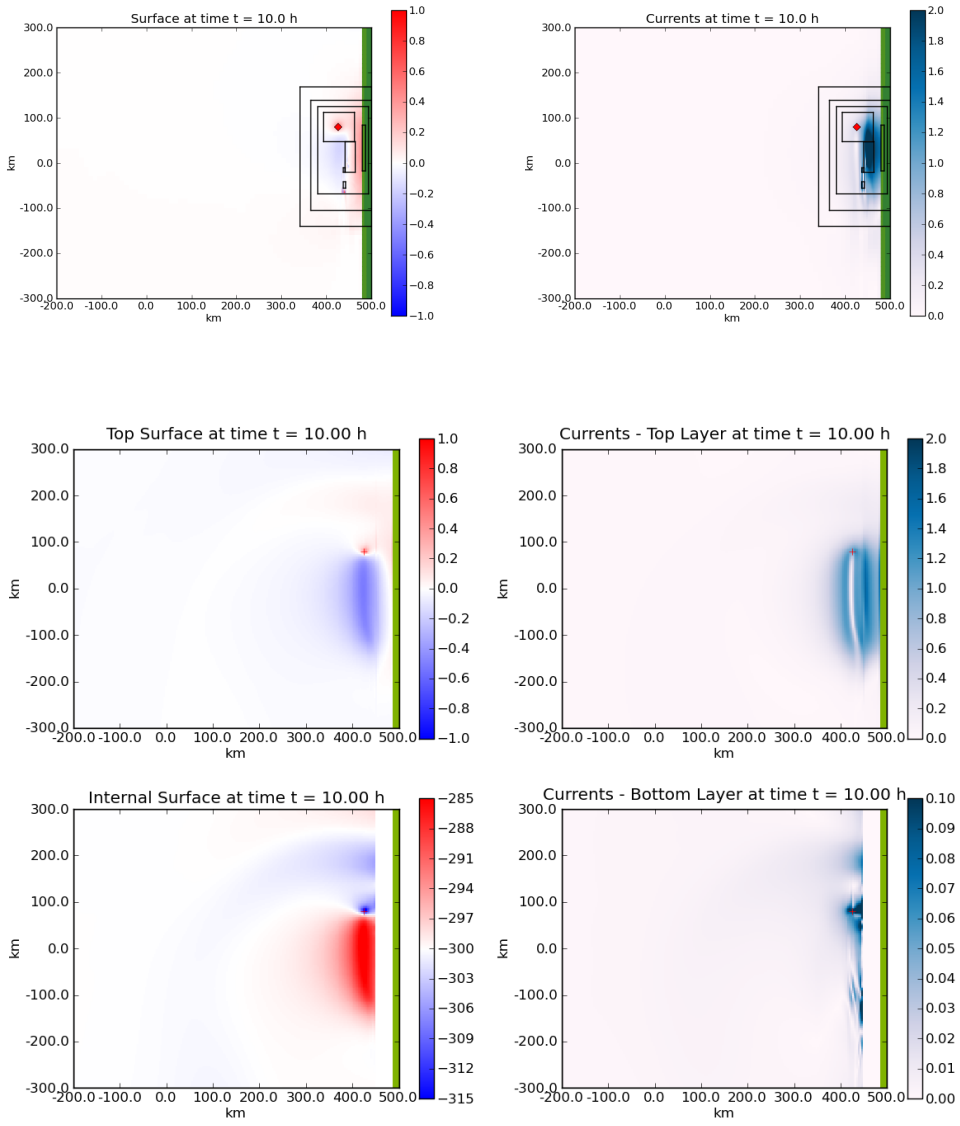

Figure 7.20: Comparison at $t = 10$ hours of single and two-layer simulations with a hurricane moving parallel in a northerly direction to the shelf at 5 m/s. The top two figures show the single-layer results of the sea surface on the left and the currents on the right. The bottom two rows are from the two-layer simulation again with the values of the top and internal surfaces on the left and the currents in the top and bottom layers on the right.

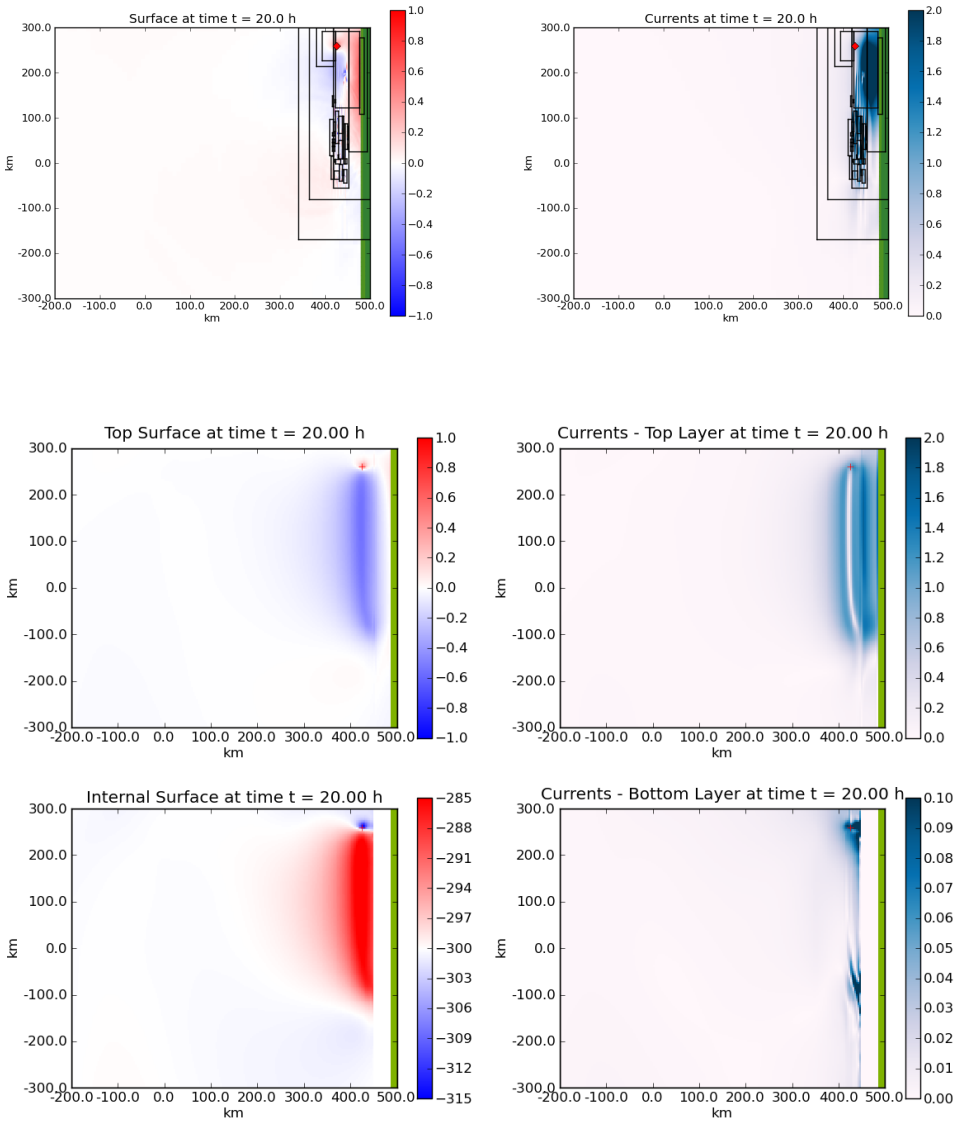

Figure 7.21: Comparison at $t = 20$ hours of single and two-layer simulations with a hurricane moving parallel in a northerly direction to the shelf at 5 m/s. The top two figures show the single-layer results of the sea surface on the left and the currents on the right. The bottom two rows are from the two-layer simulation again with the values of the top and internal surfaces on the left and the currents in the top and bottom layers on the right. Note that at this point the single-layer simulation has become unstable.

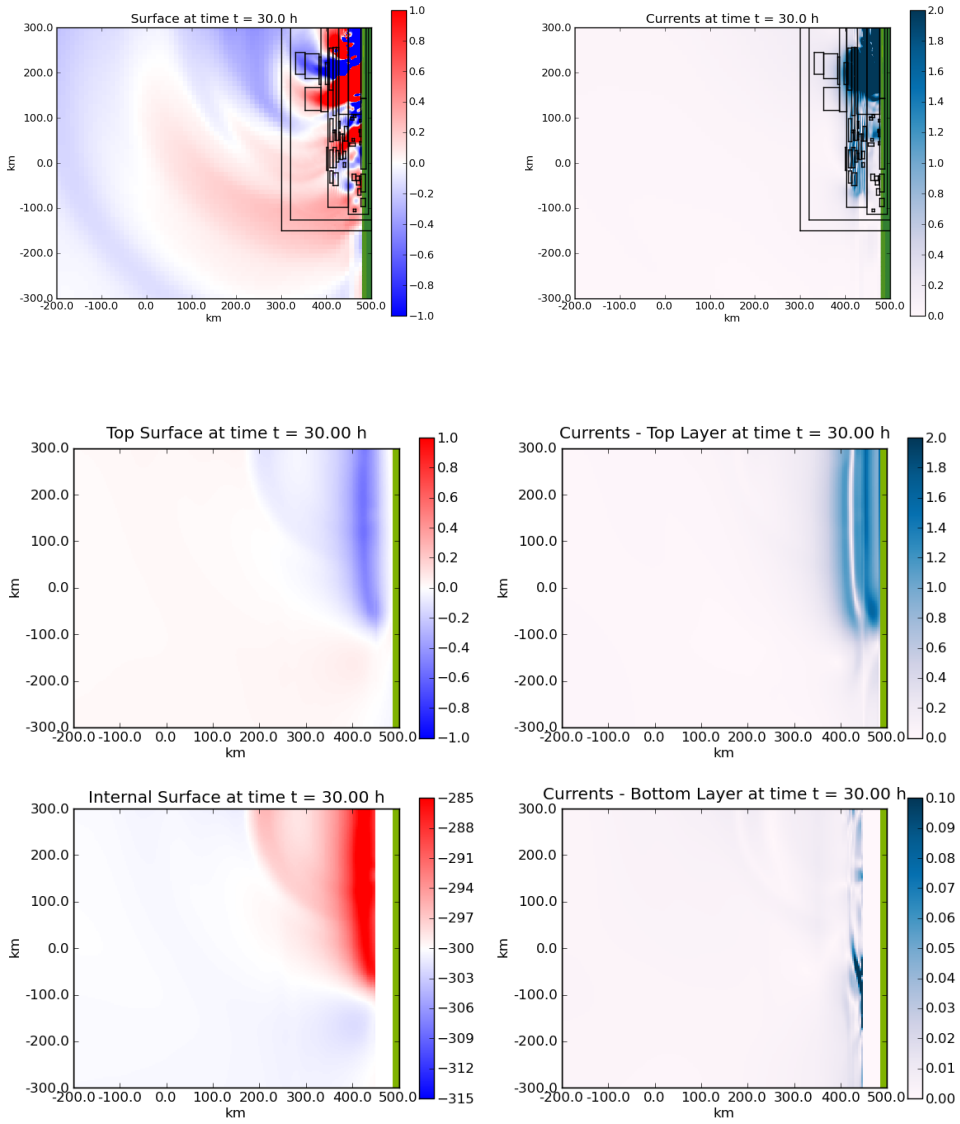

Figure 7.22: Comparison at $t = 30$ hours of single and two-layer simulations with a hurricane moving parallel in a northerly direction to the shelf at 5 m/s. The top two figures show the single-layer results of the sea surface on the left and the currents on the right. The bottom two rows are from the two-layer simulation again with the values of the top and internal surfaces on the left and the currents in the top and bottom layers on the right. Note that at this point the single-layer simulation has become unstable.

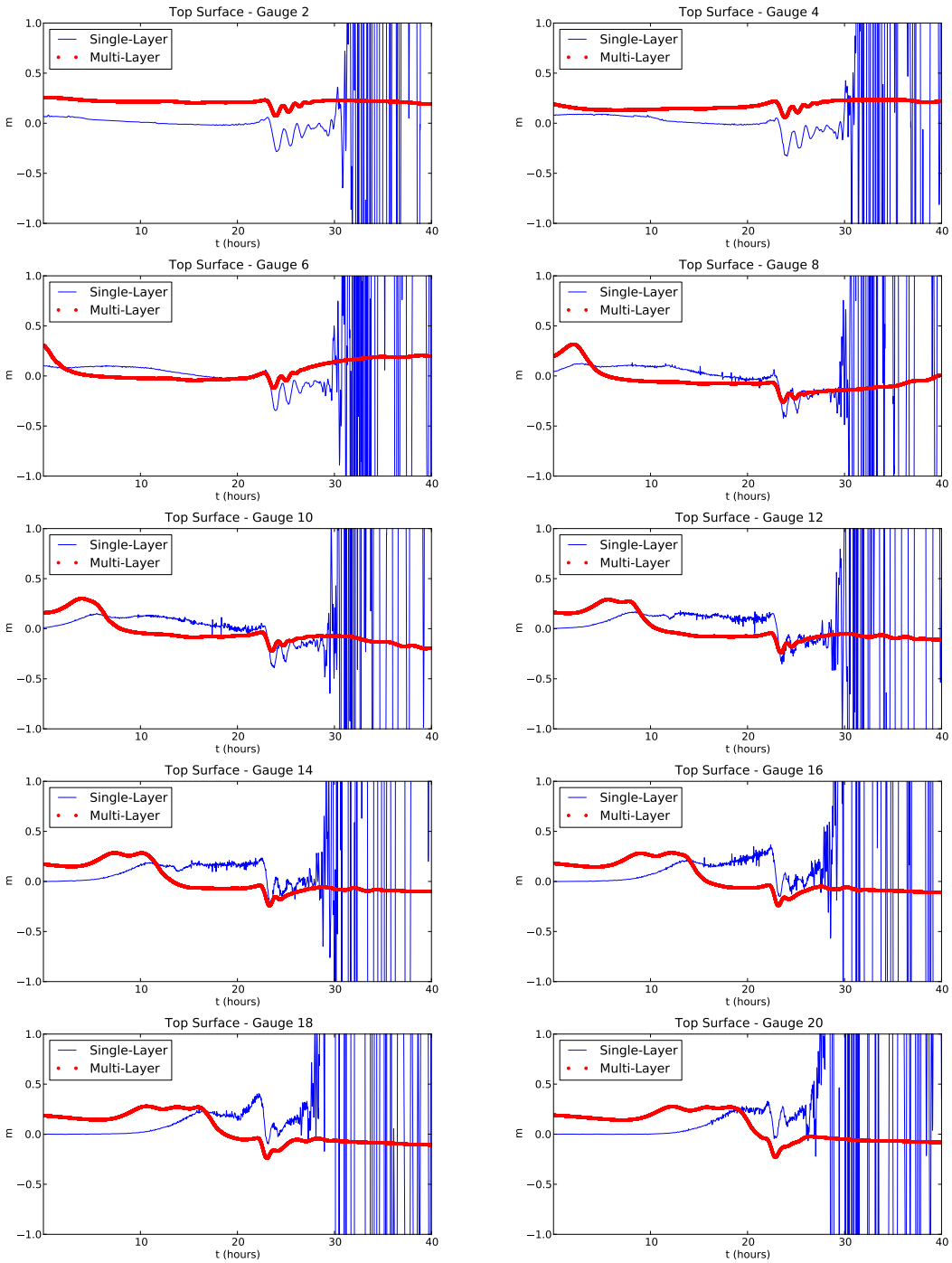

Figure 7.23: Simulated tide gauge data for both the single and two-layer simulations with a hurricane moving parallel in a northerly direction to the shelf at 5 m/s. The blue line represents the single-layer and the red line the two-layer results.

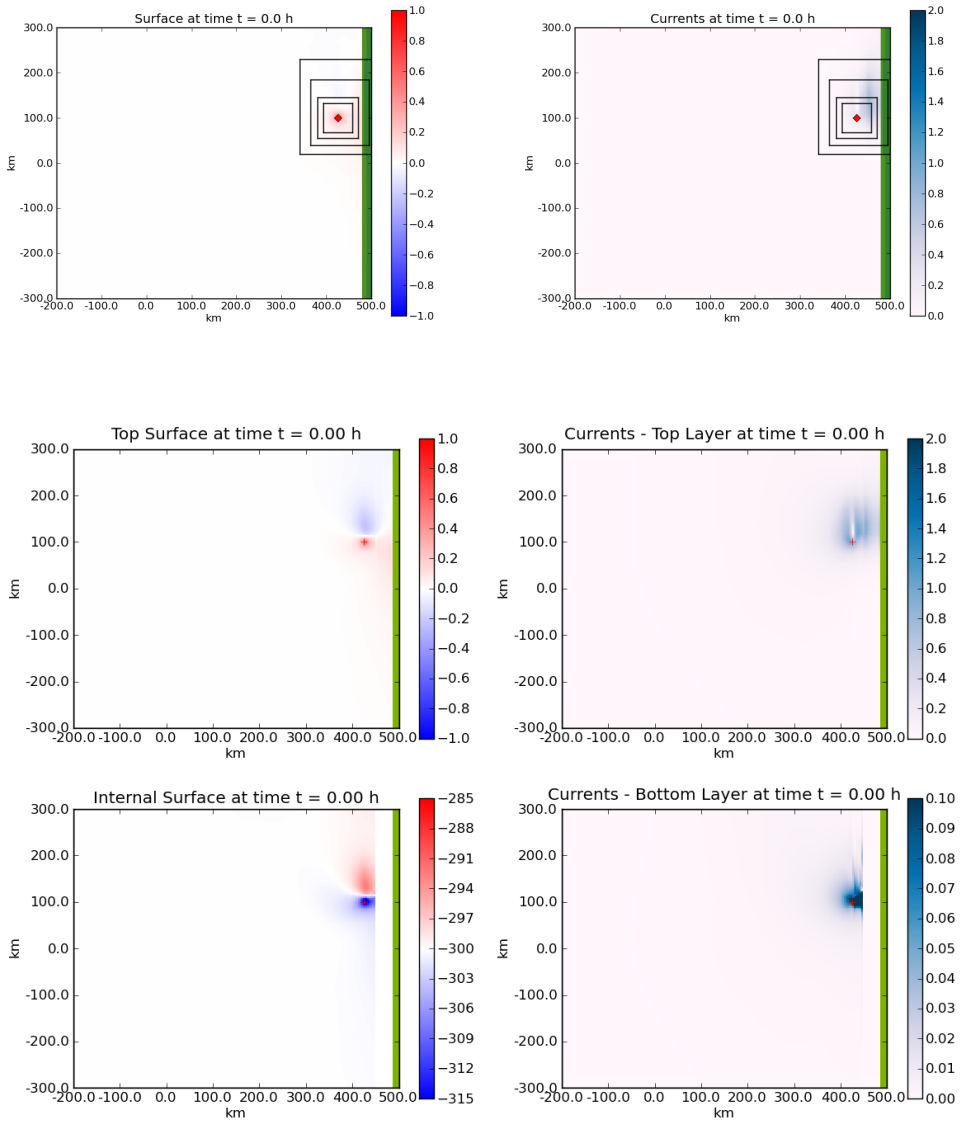

Figure 7.24: Comparison at $t = 0$ of single and two-layer simulations with a hurricane moving parallel in a southernly direction to the shelf at 5 m/s. The top two figures show the single-layer results of the sea surface on the left and the currents on the right. The bottom two rows are from the two-layer simulation again with the values of the top and internal surfaces on the left and the currents in the top and bottom layers on the right.

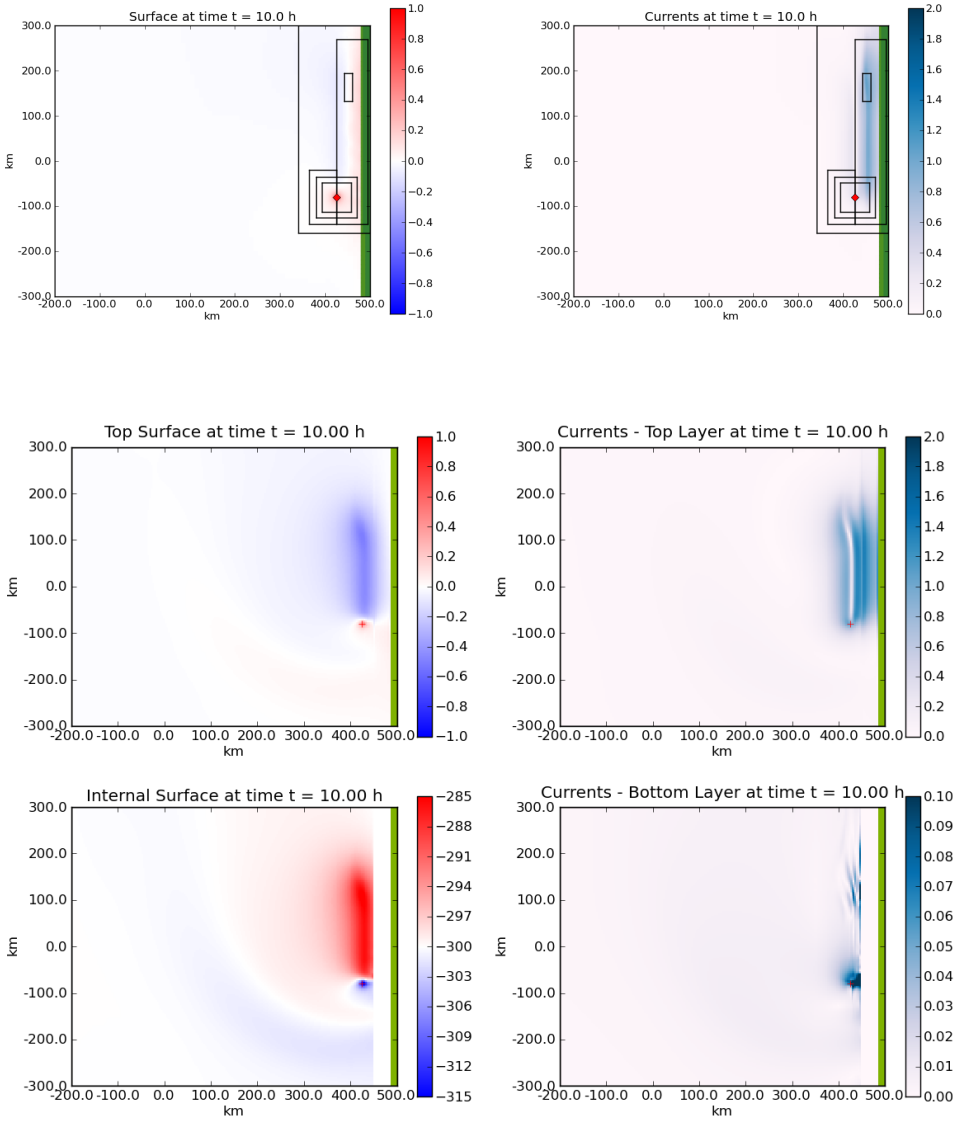

Figure 7.25: Comparison at $t = 10$ hours of single and two-layer simulations with a hurricane moving parallel in a southernly direction to the shelf at 5 m/s. The top two figures show the single-layer results of the sea surface on the left and the currents on the right. The bottom two rows are from the two-layer simulation again with the values of the top and internal surfaces on the left and the currents in the top and bottom layers on the right.

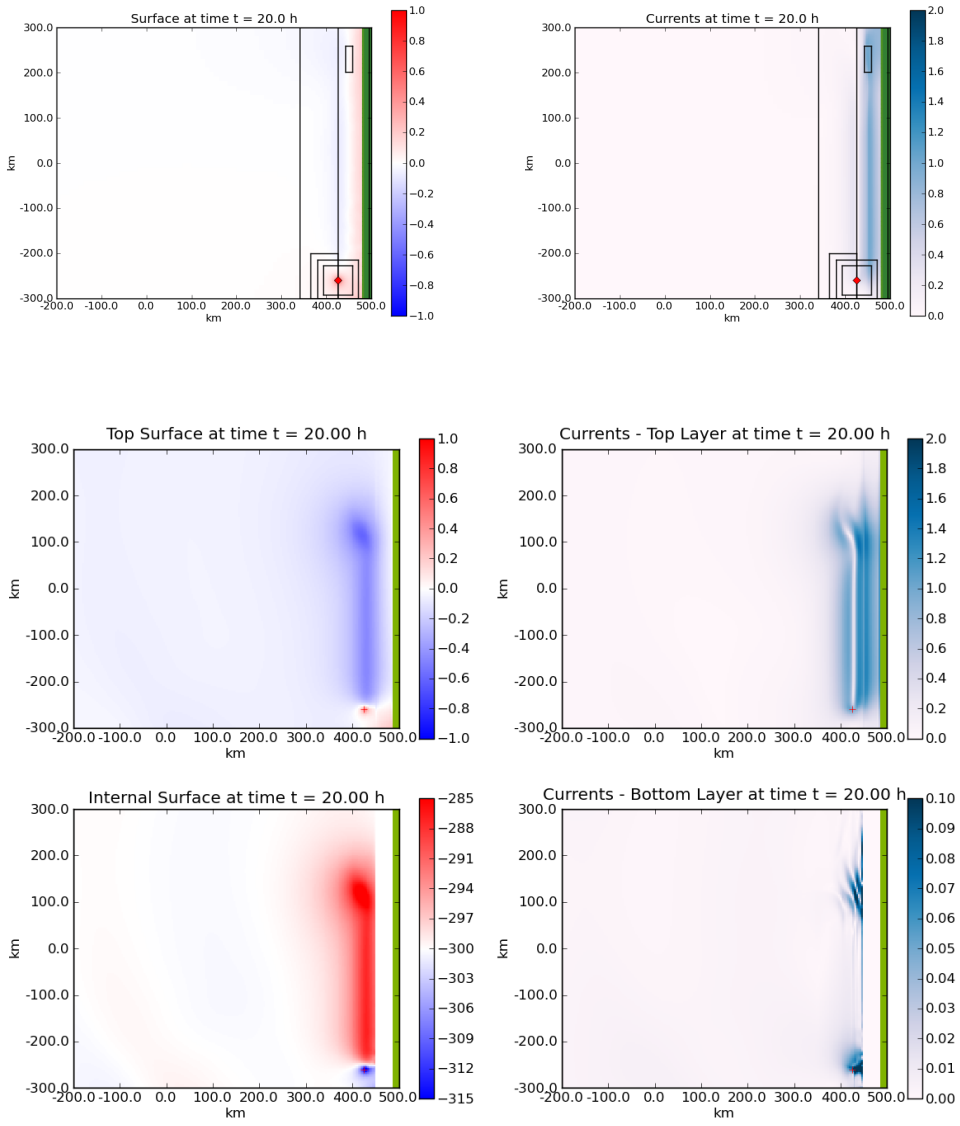

Figure 7.26: Comparison at $t = 20$ hours of single and two-layer simulations with a hurricane moving parallel in a southernly direction to the shelf at 5 m/s. The top two figures show the single-layer results of the sea surface on the left and the currents on the right. The bottom two rows are from the two-layer simulation again with the values of the top and internal surfaces on the left and the currents in the top and bottom layers on the right.

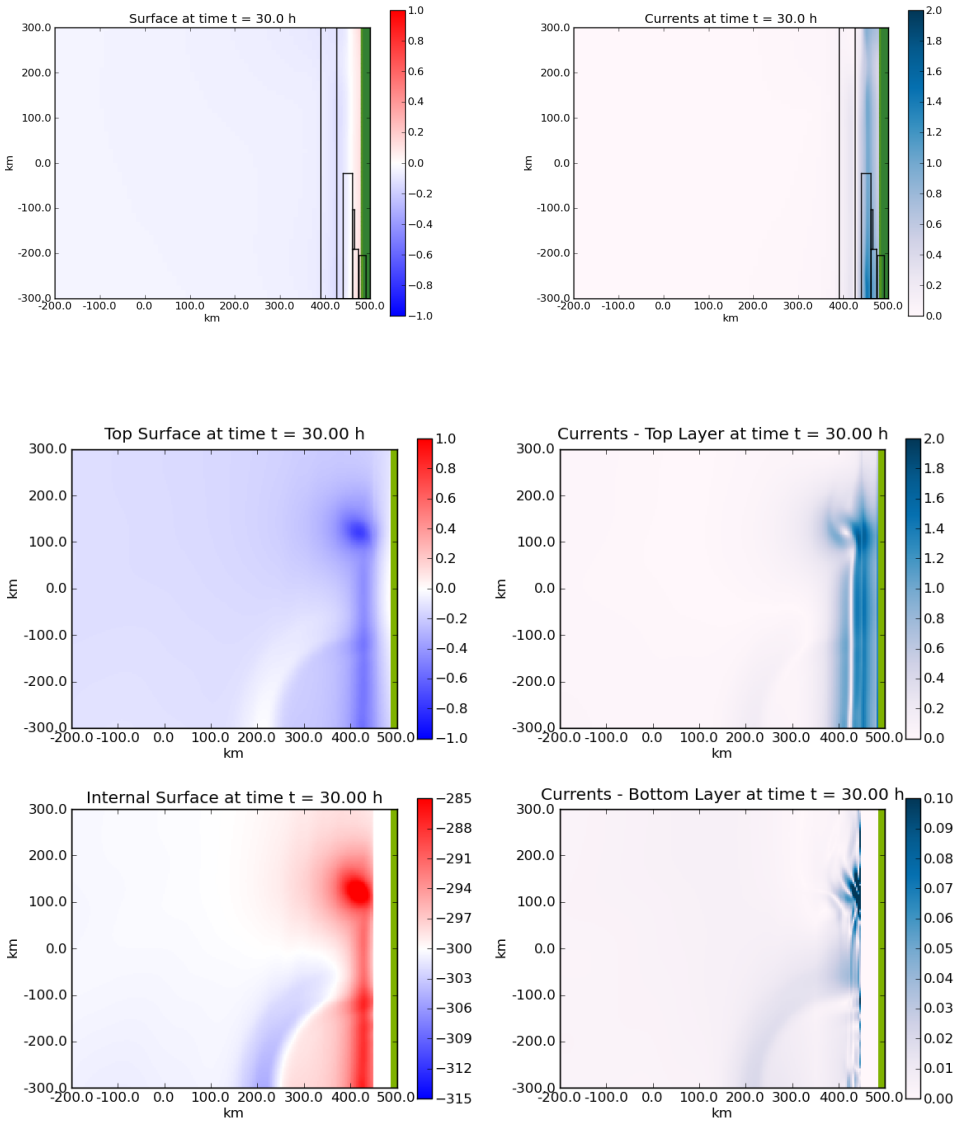

Figure 7.27: Comparison at $t = 30$ hours of single and two-layer simulations with a hurricane moving parallel in a southernly direction to the shelf at 5 m/s. The top two figures show the single-layer results of the sea surface on the left and the currents on the right. The bottom two rows are from the two-layer simulation again with the values of the top and internal surfaces on the left and the currents in the top and bottom layers on the right.

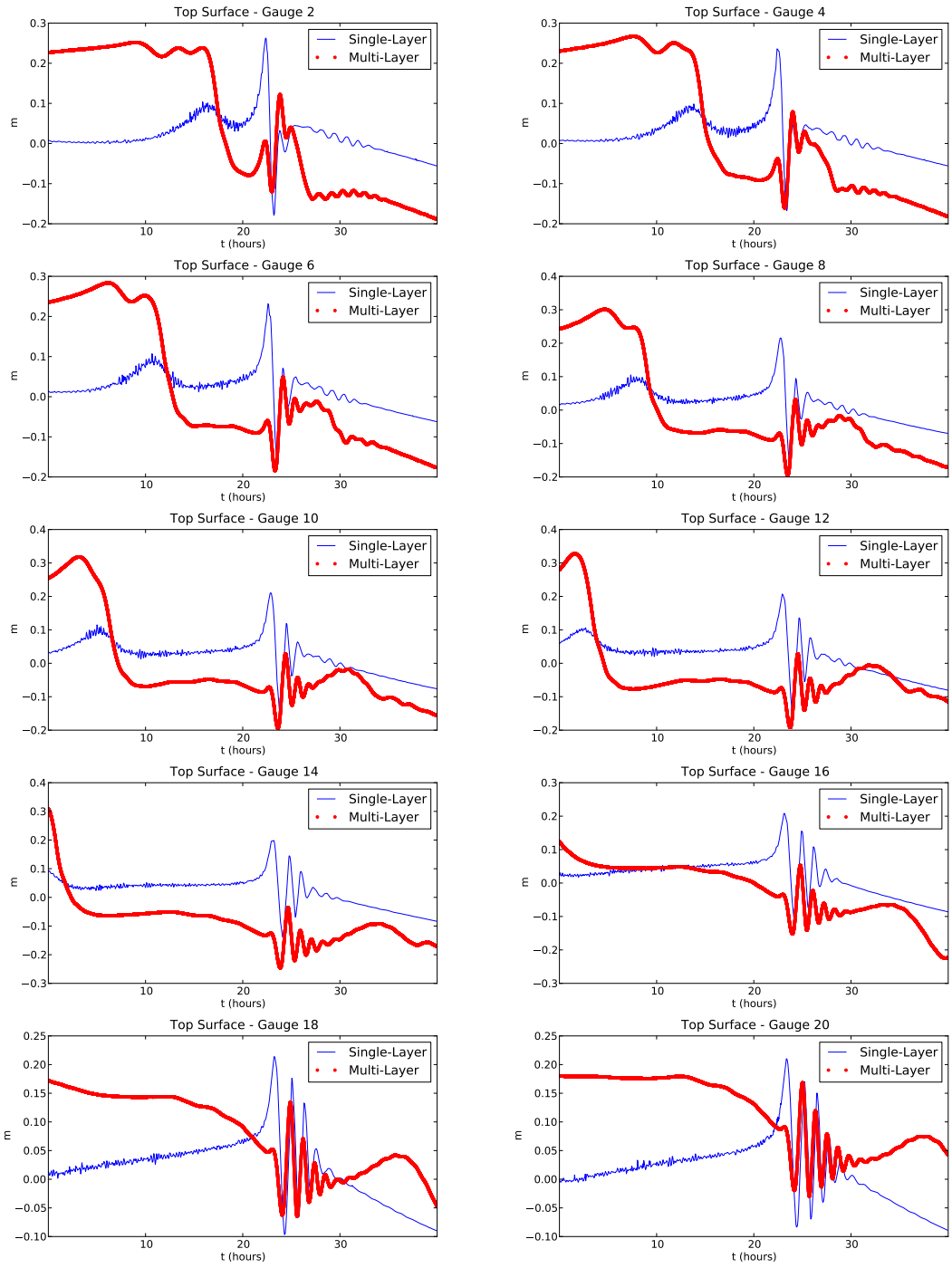

Figure 7.28: Simulated tide gauge data for both the single and two-layer simulations with a hurricane moving parallel in a southernly direction to the shelf at 5 m/s. The blue line represents the single-layer and the red line the two-layer results.

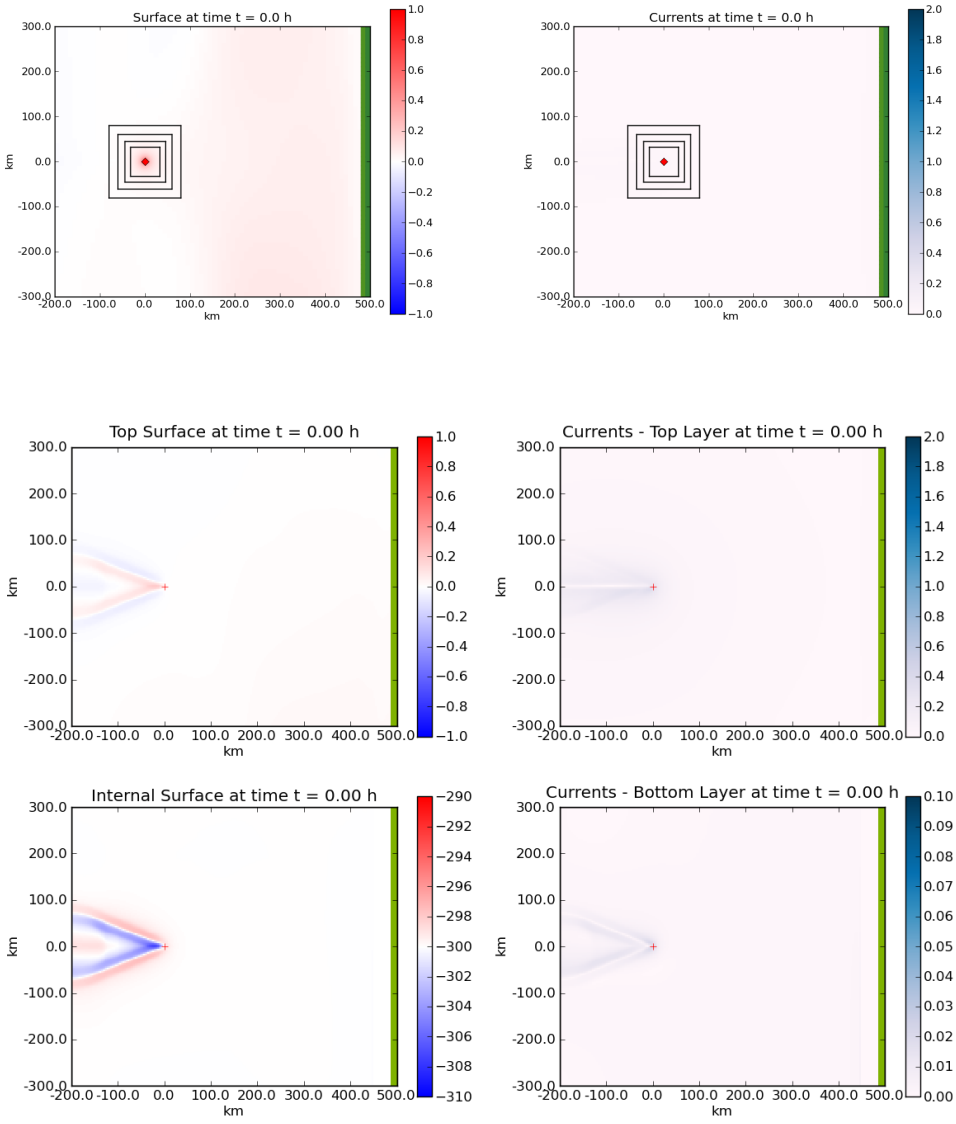

Figure 7.29: Comparison at $t = 0$ of single and two-layer simulations with a hurricane moving perpendicular to the shelf at 25 m/s. The top two figures show the single-layer results of the sea surface on the left and the currents on the right. The bottom two rows are from the two-layer simulation again with the values of the top and internal surfaces on the left and the currents in the top and bottom layers on the right.

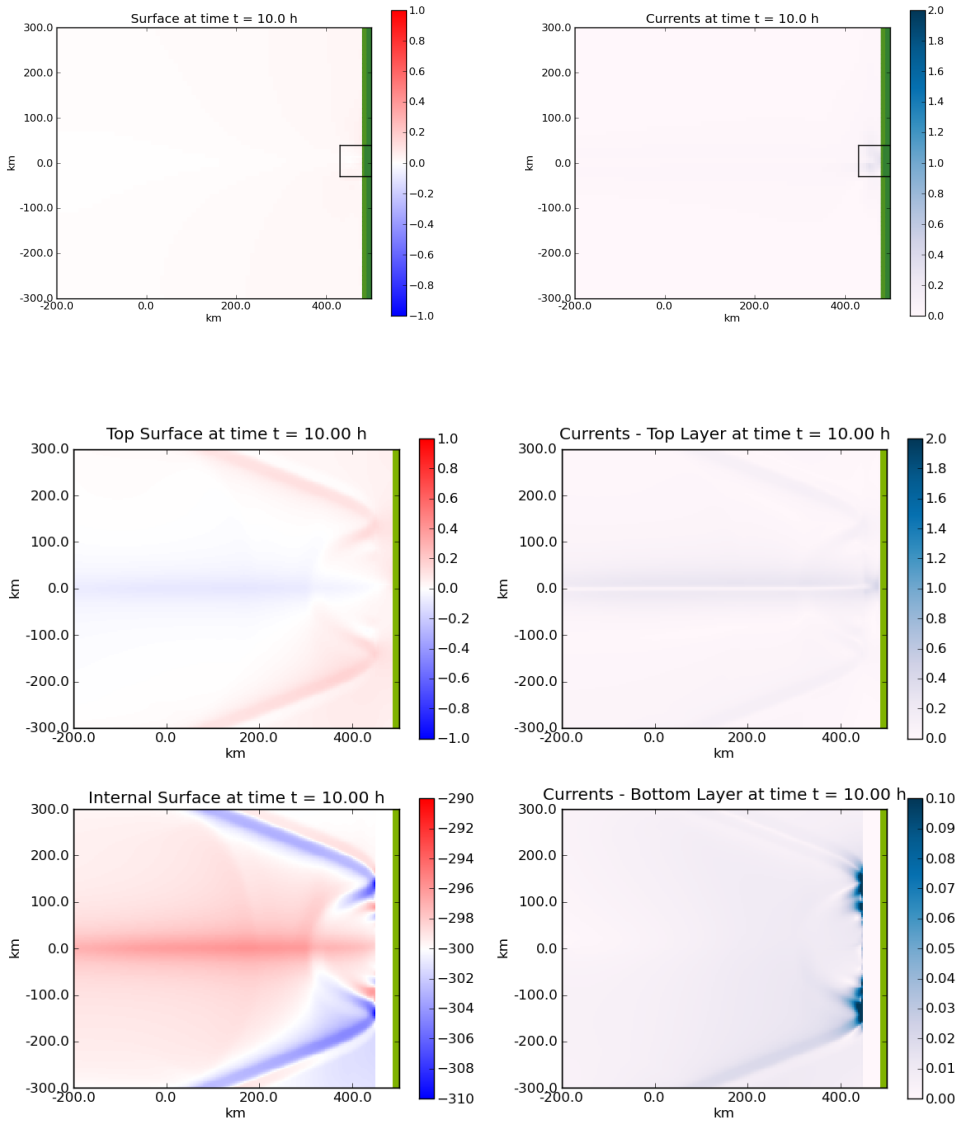

Figure 7.30: Comparison at $t = 10$ hours of single and two-layer simulations with a hurricane moving perpendicular to the shelf at 25 m/s. The top two figures show the single-layer results of the sea surface on the left and the currents on the right. The bottom two rows are from the two-layer simulation again with the values of the top and internal surfaces on the left and the currents in the top and bottom layers on the right.

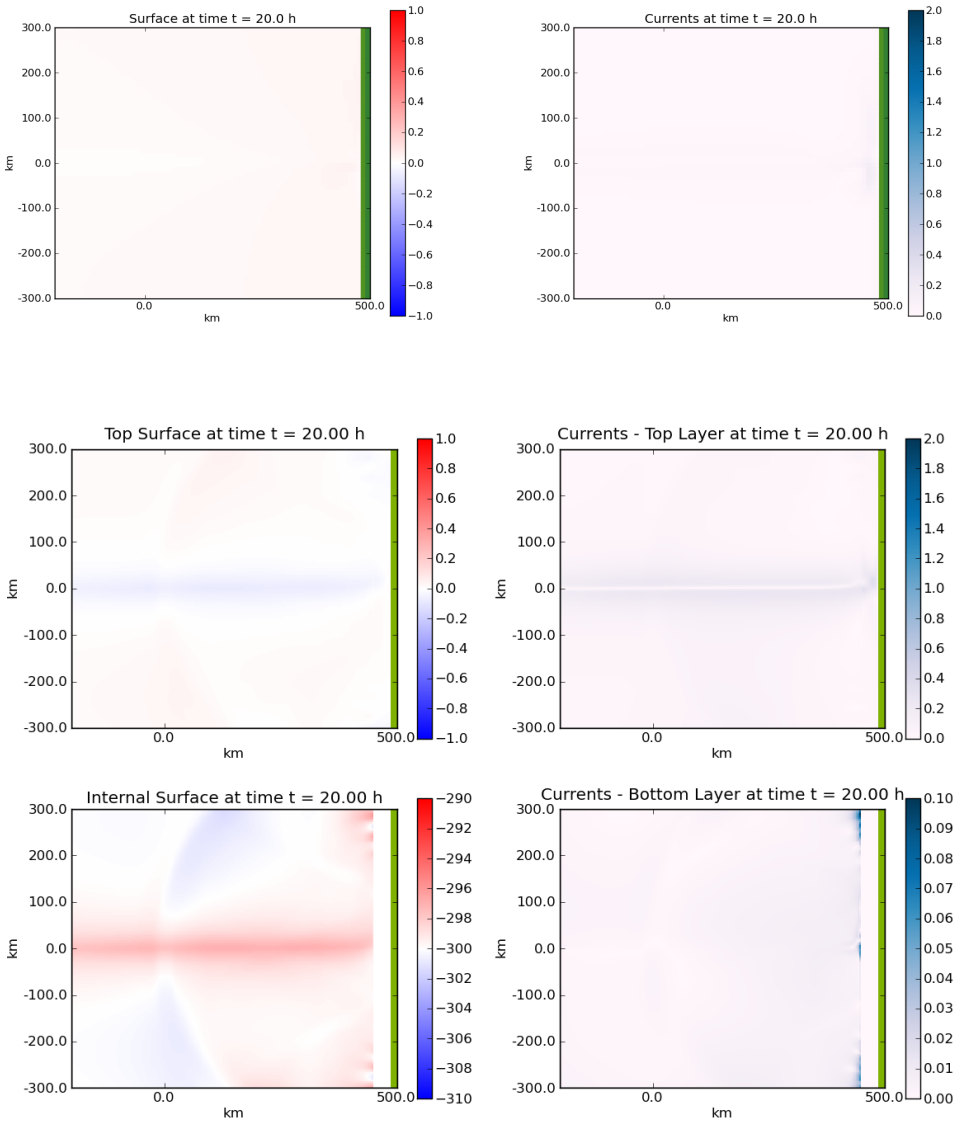

Figure 7.31: Comparison at $t = 20$ hours of single and two-layer simulations with a hurricane moving perpendicular to the shelf at 25 m/s. The top two figures show the single-layer results of the sea surface on the left and the currents on the right. The bottom two rows are from the two-layer simulation again with the values of the top and internal surfaces on the left and the currents in the top and bottom layers on the right.

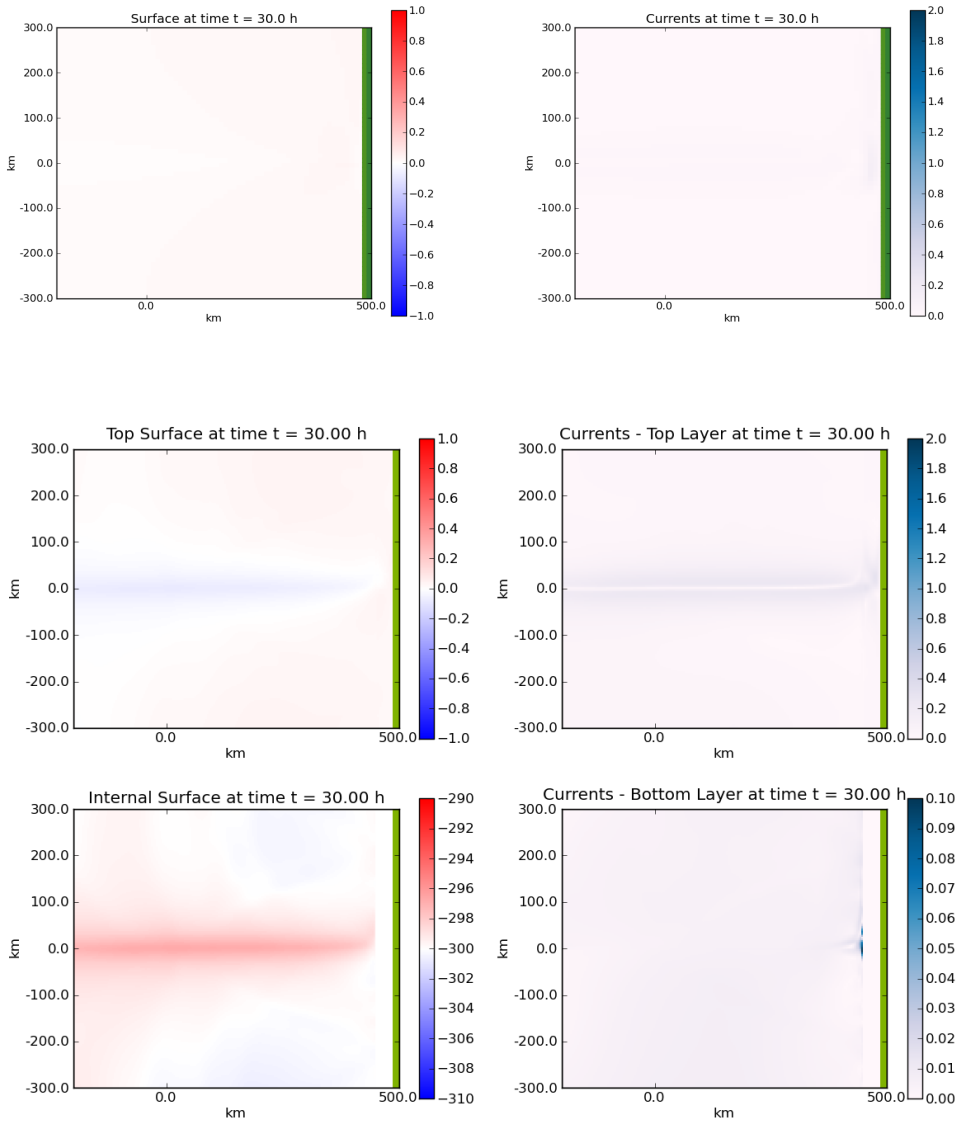

Figure 7.32: Comparison at $t = 30$ hours of single and two-layer simulations with a hurricane moving perpendicular to the shelf at 25 m/s. The top two figures show the single-layer results of the sea surface on the left and the currents on the right. The bottom two rows are from the two-layer simulation again with the values of the top and internal surfaces on the left and the currents in the top and bottom layers on the right.

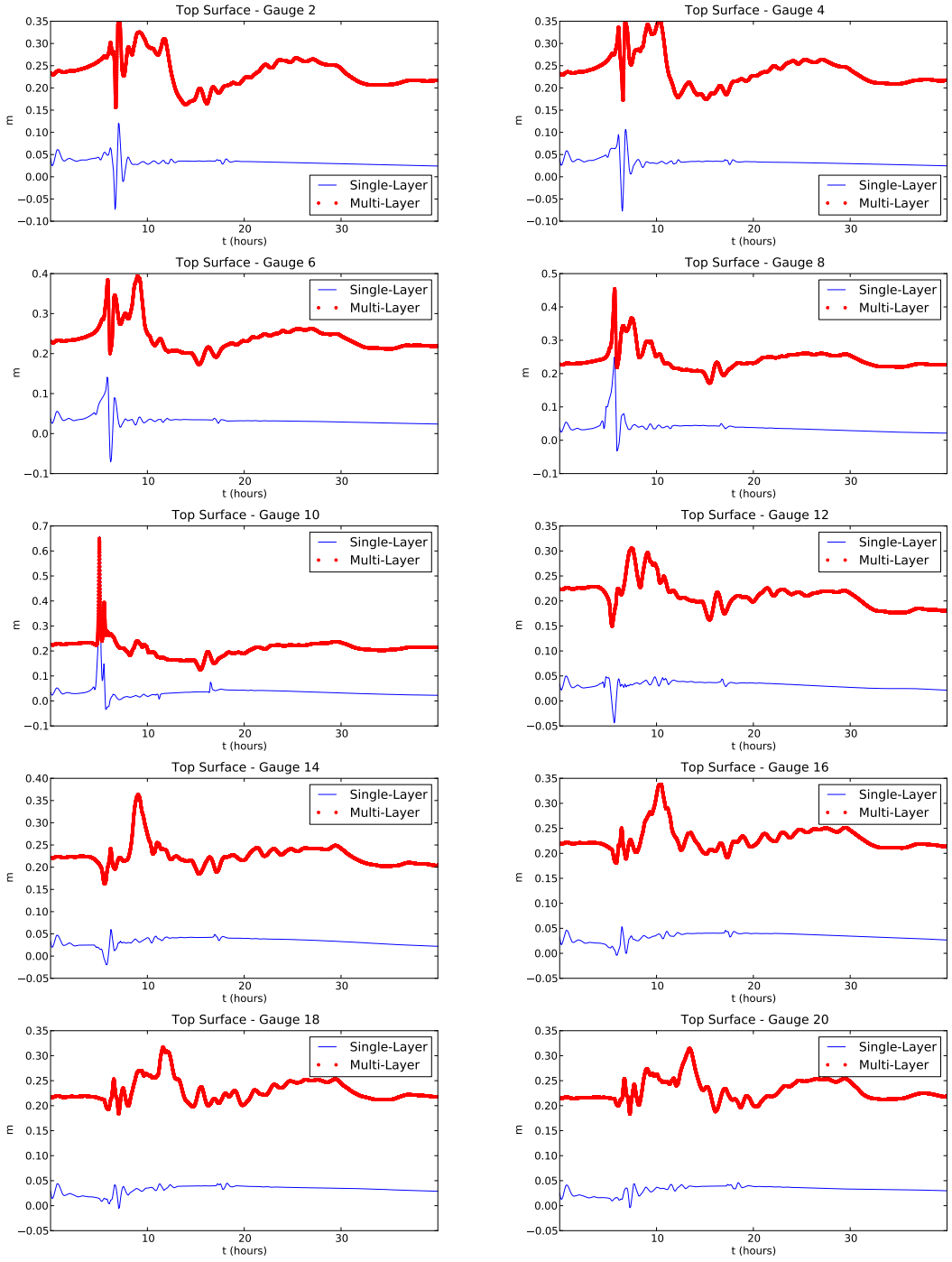

Figure 7.33: Simulated tide gauge data for both the single and two-layer simulations with a hurricane moving perpendicular to the shelf at 25 m/s. The blue line represents the single-layer and the red line the two-layer results.

Chapter 8

CONCLUSIONS AND FUTURE DIRECTIONS

The central goals of this thesis were to develop a numerical method for the multi-layer shallow water equations and to study whether this approach could provide a more suitable model for storm surge inundation relative to the more widely used single-layer shallow water equations or a three dimensional simulation. To this end, analysis was carried out on the essential properties of the multi-layer equations and a family of numerical methods was developed to solve these problems. The storm surge problem itself also required development of numerical approaches for including the unique terms that arise from storm forcing. In this last chapter a summary of the development of the methods and some final remarks on whether the multi-layer shallow water equations may be a more suitable choice for storm surge inundation is given along with directions for future work in this area.

8.1 Multi-Layer Analysis and Numerical Methods

In chapters 5 and 6 an understanding of the multi-layer shallow water equations was developed and a numerical method for their solution was introduced and tested. First the derivation of the one-dimensional two-layer equations was presented and the appropriate approximations demonstrated. The primary goal of the rest of chapter 5 was to either compute the analytic solution to the Riemann problem or find some suitable set of approximations that could be used in the numerical method. The eigenvalue problem was explored and an explicit solution is possible but was found too unwieldy to use directly in further analysis. Approximations to the eigenvalues were therefore introduced and their properties were explored. The solution to the general Riemann problem was then discussed and a system of non-linear equations derived that determines the intermediate states of the Riemann solution and the type of waves in each family. Finally the dry-state wall and inundation problems were considered and solved using the approximations found earlier for the eigenvalues.

A finite volume F-wave propagation method was constructed and tested in chapter 6. Since the goal at the outset was to construct a solver that would be robust and efficient, the approximate eigensolvers were evaluated for accuracy and speed in the regimes of interest. Particular care was taken to capture and preserve dry states in both the wall and inundation cases. This primarily involved careful evaluation of the flux and source functions and insuring that steady-states were preserved. A two-dimensional un-split solver was also introduced and all of the properties of the

solver enforced from the one-dimensional case. Finally a number of tests were used to demonstrate the robustness and efficacy of the solvers. All of this was carried out in the GeoClaw framework so that the bathymetry handling, inundation algorithms, and adaptive mesh refinement capabilities could be utilized. In the case of the top layer becoming dry, the solver already implemented and tested in GeoClaw could be used.

The goal at the outset of this thesis was to construct and evaluate a multi-layer shallow water solver for storm surges. This requires the handling of complex bathymetry, inundation at the coastline, the resolution of multiple scales, fast and efficient solvers for ensemble prediction capabilities, and the correct representation of storm surge physics. Incorporating the solvers developed in this work into the GeoClaw framework has allowed me to leverage GeoClaw's ability to handle complex bathymetry and inundation. Multiple scale resolution will be handled by utilizing adaptive mesh refinement built into the GeoClaw framework, but was not used in the simulations presented due to incompatibilities currently in GeoClaw (see section 8.3 for further discussion). The speed and efficiency have not been explored extensively but preliminary results suggest that two-layer simulations are approximately 30% slower than the single-layer case. This is much faster than a comparable three dimensional solver with similar horizontal resolution. The representation of storm surge physics primarily involves the implementation of each of the primary forcing mechanisms. For both the single and two-layer cases, this was discussed in chapter 7. The final question of the suitability of the two-layer versus one-layer models is addressed in the next section.

8.2 Suitability of Multi-Layer Storm Surge Models

In order to judge the efficacy of each model's representation of a storm surge, a series of idealized simulations were carried varying the hurricane's track. The primary advantage the two-layer equations have over the single-layer representation is its increased vertical representation of the water column. The evidence given in chapter 7 shows that the single and two-layer simulations are consistently different and the two-layer simulations predict higher surge levels. This alone would suggest that pursuing two-layer simulations further is worth while. Moreover, from ocean observations we also expect that the two-layer model is a better representation of the ocean, especially with strong wind forcing at the top of the water column. The decrease in computational speed over the single-layer case is small compared to the speed of a three dimensional solver, which would be too slow for the ensemble simulations that are required for operational storm surge prediction. It is clear that the multi-layer equations provide a possible avenue for increased physics while not appreciably increasing the computational overhead. The next step in evaluating the multi-layer equations will be to take the numerical methods presented and attempt to model realistic storm

surge and compare the single-layer, multi-layer and three dimensional equations and determine whether the multi-layer shallow water equations provide a good balance between model efficiency and a more robust physical representation of the system.

8.3 Future Directions

There are multiple future directions in which this work can be taken. The most immediate need is to correct the incompatibilities in the GeoClaw framework with respect to the adaptive mesh refinement algorithms. This incompatibility is a result of incorrect assumptions in the interpolation and extrapolation routines used to both refine and coarsen grids. An extension has already been formulated and needs to be implemented and tested.

Another avenue of future work is the further study of the inundation dry state problem, in particular the entropy violation that is present in the method presented in this thesis. Solutions may involve modifying the fluxes appropriately to allow a higher flux through the point of inundation.

The eigenvalue problem presented was addressed by the use of an approximation to the original eigensystem. Although comparing the eigenvalues of the linearized method to the LAPACK solver reveals little difference, there are multiple ways to increase the accuracy of both of these solvers via an iterative approach.

In order to truly model the mixed layer underneath a storm storm such as a hurricane or typhoon, vertical mixing must be taken into account. In the method presented this mixing is not allowed. This mixing takes two forms, one is density mixing and the other is momentum mixing or transfer. Multiple methods for transferring density and momentum between layers exist and the most appropriate one needs to be implemented and evaluated in the context presented. In particular, the loss of hyperbolicity would be less of a concern if momentum is allowed to transfer between layers.

Finally, as mentioned in section 8.2, running more realistic storm surge simulations with more complex bathymetry and hurricanes will be necessary to make the final evaluation on the suitability of these equations for modeling storm surge. Comparisons between three dimensional ocean models and the multi-layer shallow water equations will also be needed, and careful comparisons of the speed of each approach will be required.

BIBLIOGRAPHY

[1] Contribution of Working Group I to the Fourth Assessment Report of the Intergovernmental Panel on Climate Change, 2007. Technical report.

[2] UN Atlas of the Oceans. `http://www.oceansatlas.org/servlet/CDSServlet?status=ND0xODc3JjY9ZW4mMzM9KiYzNz1rb3M~`.

[3] R. Abgrall and S. Karni. Two-Layer Shallow Water Systems: A Relaxation Approach. *SIAM Journal of Scientific Computing*, 31(3):1603–1627, Feb. 2009.

[4] E. Anderson, Z. Bai, C. Bischof, S. Blackford, J. Demmel, J. Dongarra, J. Du Croz, A. Greenbaum, S. Hammarling, A. McKenney, and D. Sorensen. *LAPACK Users' Guide*. Society for Industrial and Applied Mathematics, 3 edition, May 1999.

[5] D. S. Bale, R. LeVeque, S. Mitran, and J. A. Rossmanith. A Wave Propagation Method for Conservation Laws and Balance Laws with Spatially Varying Flux Functions. *SIAM Journal of Scientific Computing*, 24(3):955–978, 2002.

[6] M. J. Berger, D. L. George, R. LeVeque, and K. Mandli. The GeoClaw software for depth-averaged flows with adaptive refinement. *arXiv*, physics.geo-ph, Aug. 2010. 18 pages, 11 figures, Animations and source code for some examples at http://www.clawpack.org/links/awr10.

[7] M. J. Berger and R. J. LeVeque. Adaptive Mesh Refinement using Wave-Propagation Algorithms for Hyperbolic Systems. *SIAM Journal on Numerical Analysis*, 35:2298–2316, 1998.

[8] M. J. Berger and J. Oliger. Adaptive mesh refinement for hyperbolic partial differential equations. *Journal of Computational Physics*, 52:484–512, 1984.

[9] E. A. Blackburn, L. Wilson, and R. S. J. Sparks. Mechanisms and dynamics of strombolian activity. *Journal of the Geological Society*, 132(4):429–440, 1976.

[10] E. S. Blake, E. N. Rappaport, and C. W. Landsea. The Deadliest, Costliest, and Most Intense United States Tropical Cyclones from 1851 to 2006. Technical report, NHC Miami, NHC Miami, Apr. 7.

[11] F. Bouchut and T. Morales de Luna. An entropy satisfying scheme for two-layer shallow water equations with uncoupled treatment. *ESAIM: M2AN*, 42(4):683–698, June 2008.

[12] F. Bouchut and M. Westdickenberg. Gravity Driven Shallow Water Models for Arbitrary Topography. *Communication in Mathematical Sciences*, 2(3):359–389, 2004.

[13] F. Bouchut and V. Zeitlin. A robust well-balanced scheme for multi-layer shallow water equations. *Discrete and Continuous Dynamical Systems-Series B*, pages 739–758, 2010.

[14] M. J. Castro, J. A. García-Rodríguez, J. González-Vida, J. Macías, and C. Parés. Improved FVM for two-layer shallow-water models: Application to the Strait of Gibraltar. *Advances in Engineering Software*, 38:386–398, 2007.

[15] M. J. Castro-Díaz, E. D. Fernández-Nieto, J. M. González-Vida, and C. Parés-Madrñal. Numerical Treatment of the Loss of Hyperbolicity of the Two-Layer Shallow-Water System. *Journal of Scientific Computing*, Oct. 2010.

[16] L. Chumakova, F. E. Menzaque, P. A. Milewski, R. R. Rosales, E. G. Tabak, and C. V. Turner. Shear instability for stratified hydrostatic flows. *Communications on Pure and Applied Mathematics*, 62(2):183–197, 2009. Sheared continuously stratified hydrostatic flows contain Howard-Miles criterion of instability coinciding with hyperbolicity loss.

[17] L. Chumakova and E. G. Tabak. Simple waves do not avoid eigenvalue crossings.

[18] B. Cushman-Roisin and J.-M. Beckers. *Introduction to Geophysical Fluid Dynamics*. Physical and Numerical Aspects. Academic Press, June 2010.

[19] C. Dawson, E. J. Kubatko, J. J. Westerink, C. Trahan, C. Mirabito, C. Michoski, and N. Panda. Discontinuous Galerkin methods for modeling Hurricane storm surge. *ADVANCES IN WATER RESOURCES*, 2010.

[20] D. R. Durran. *Numerical Methods for Fluid Dynamics With Applications to Geophysics*. Texts in Applied Mathematics. Springer, 2 edition, May 2010.

[21] B. Einfeldt. On Godunov-Type Methods for Gas Dynamics. *SIAM Journal on Numerical Analysis*, 25(2):294–318, Apr. 1988.

[22] E. Fernández-Nieto, M. C. Díaz, and C. Parés. A Computationally Fast and Precise solver for the two-layer shallow-water system. 2010.

[23] F. G. Friedlander and M. Joshi. *Introduction to the Theory of Distributions*. Cambridge University Press, 2 edition, Jan. 1999.

[24] D. L. George. *Finite Volume Methods and Adaptive Refinement for Tsunami Propagation and Inundation*. PhD thesis, University of Washington, 2006.

[25] D. L. George. Augmented Riemann solvers for the shallow water equations over variable topography with steady states and inundation. *Journal of Computational Physics*, 227(6):3089–3113, Mar. 2008.

[26] D. L. George. Adaptive finite volume methods with well-balanced Riemann solvers for modeling floods in rugged terrain: Application to the Malpasset dam-break flood (France, 1959). *International Journal for Numerical Methods in Fluids*, 2010.

[27] S. K. Godunov. A difference method for numerical calculation of discontinuous solutions of the equations of hydrodynamics. *Matematicheskii Sbornik*, 47(89):271–306, 1959.

[28] A. Harten, P. D. Lax, and B. Van Leer. On Upstream Differencing and Godunov-type Schemes for Hyperbolic Conservation Laws. *SIAM Review*, 25, Jan. 1983.

[29] G. J. Holland. An Analytic Model of the Wind and Pressure Profiles in Hurricanes. *Monthly Weather Review*, 108:1212–1218, 1980.

[30] C. P. Jelesnianski, J. Chen, and W. A. Shaffer. SLOSH: Sea, Lake and Overland Surges from Hurricanes. Technical report, NOAA, NOAA, 1992.

[31] J. Le Sommer, S. Medvedev, R. Plougonven, and V. Zeitlin. Singularity formation during relaxation of jets and fronts toward the state of geostrophic equilibrium. *Nonlinear Sciences and Numerical SImulation*, pages 415–442, 2003. Shows that the criteria of hyperbolicity loss and of Kelvin-Helmholtz instability coincide in two-layer shallow water with a rigid lid.

[32] R. LeVeque. *Finite Volume Methods for Hyperbolic Problems*. Cambridge Texts in Applied Mathematics. Cambridge University Press, Cambridge, UK, 2002.

[33] R. LeVeque and M. Pelanti. A Class of Approximate Riemann Solvers and Their Relation to Relaxation Schemes. *Journal of Computational Physics*, 172:572–591, 2001.

[34] R. J. LeVeque, D. L. George, and M. J. Berger. Tsunami Propagation and inundation with adaptively refined finite volume methods. *Acta Numerica*, pages 211–289, 2011.

[35] P. Milewski, E. Tabak, C. Turner, R. Rosales, and F. Menzaque. Nonlinear Stability of Two-Layer Flows. *Communication in Mathematical Sciences*, 2(3):427–442, 2004.

[36] NOAA and COMET Program. Storm Surge Diagram. `http://www.nhc.noaa.gov/ssurge/images/stormsurgevsstormtide.jpg`.

[37] C. Parés and M. L. Muñoz-Ruiz. On Some Difficulties of the Numerical Approximation of Nonconservative Hyperbolic Systems. *Bol. Soc. Esp. Mat. Apl.*, (47):19–48, 2009.

[38] M. Pelanti and R. LeVeque. High-Resolution Finite Volume Methods for Dusty Gas Jets and Plumes. *SIAM Journal of Scientific Computing*, 28(4):1335–1360, 2006.

[39] D. T. Resio and J. J. Westerink. Modeling the Physics of Storm Surges. *Physics Today*, pages 33–38, 2008.

[40] P. L. Roe. Approximate Riemann Solvers, Parameter Vectors, and Difference Schemes. *Journal of Computational Physics*, 43(2):357–372, Oct. 1981.

[41] H. Schlichting and K. Gersten. Boundary-layer theory. *Springer*, page 799, 2000.

[42] E. F. Toro. *Riemann solvers and numerical methods for fluid dynamics*. Springer Verlag, 2 edition, 1999.

[43] C. Vreugdenhil. *Numerical Methods for Shallow-Water Flow*, volume 13. 1994.

[44] R. H. Weisberg and L. Zheng. Hurricane Storm Surge Simulations for Tampa Bay. *Estuaries and Coasts*, 29(6A):899–913, Dec. 2006.

[45] J. J. Westerink, R. A. Luettich, J. C. Feyen, J. H. Atkinson, C. Dawson, H. J. Roberts, M. D. Powell, J. P. Dunion, E. J. Kubatko, and H. Pourtaheri. A Basin- to Channel-Scale Unstructured Grid Hurricane Storm Surge Model Applied to Southern Louisiana. *Monthly Weather Review*, page 833, 2008.

Appendix A

DERIVATION OF SINGLE LAYER DEPTH AVERAGED MODELS

In this appendix I will discuss the process and assumptions that produce a depth averaged model and discuss if these approximations are valid in the cases of interest. The hydrostatic assumption is of particular interest here as it is often unclear as to its validity in many contexts of interest. If the hydrostatic assumption is not not valid I will also show some extensions that may increase their range of applicability.

In order to simplify the discussion, a simplified version of the Navier-Stokes equations (4.1) will be considered, namely the two dimensional version of the same equations with simplified boundary conditions written as

$$\begin{aligned} &u_x + w_z = 0, \\ &u_t + (u^2)_x + (uw)_z = -\frac{1}{\rho}P_x, \quad \text{and} \\ &w_t + (uw)_x + (w^2)_z = -\frac{1}{\rho}P_z - g. \end{aligned} \tag{A.1}$$

The full three dimensional derivation is discussed in section 4.1.

A.0.1 Non-Dimensionalization and Scaling

We first define a set of non-dimensional parameters based on the characteristic length scales of the problem, namely the horizontal length scale λ and the vertical length scale a. We also define a set of non-dimensional quantities

$$\frac{x}{\lambda} = \tilde{x} \qquad \frac{z}{a} = \tilde{z} \qquad \frac{t}{T} = \tilde{t}$$

as well as the physical quantities

$$\frac{u}{U} = \tilde{u} \qquad \frac{w}{W} = \tilde{w} \qquad \frac{P}{P_0} = \tilde{P}.$$

With these in hand, we now define a set of scaling parameters whose meaning we will interpret as they come into the equations:

$$\epsilon = \frac{a}{\lambda} \qquad U = \sqrt{ga} \qquad W = \epsilon U \qquad T = \frac{\lambda}{U}.$$

The quantity ϵ is the traditional definition for the shallow water scaling parameter and its magnitude will be the primary determining factor on which our approximations will rest. Note also that the scalings for the velocities and time are based on the surface gravity wave speeds determined by the characteristic depth.

Applying these scalings to the incompressibility condition (4.2) leads to

$$\begin{aligned} & u_x + w_z = 0 \Rightarrow \\ & \frac{U}{\lambda}\tilde{u}_{\tilde{x}} + \frac{W}{a}\tilde{w}_{\tilde{z}} = 0 \Rightarrow \\ & \tilde{u}_{\tilde{x}} + \frac{\epsilon U \lambda}{aU}\tilde{w}_{\tilde{z}} = 0 \Rightarrow \\ & \tilde{u}_{\tilde{x}} + \tilde{w}_{\tilde{z}} = 0 \end{aligned} \tag{A.2}$$

The fact that all of these terms are of the same order is purposeful as they were partially chosen so as to keep all the terms in the incompressibility condition of the same order. Applying the scalings to the horizontal velocity component of the momentum from (A.1) we obtain

$$\begin{aligned} & u_t + (u^2)_x + (uw)_z = -\frac{1}{\rho}P_x \Rightarrow \\ & \frac{U}{T}\tilde{u}_{\tilde{t}} + \frac{U^2}{\lambda}(\tilde{u}^2)_{\tilde{x}} + \frac{UW}{a}(\tilde{u}\tilde{w})_{\tilde{z}} = -\frac{P_0}{\rho\lambda}\tilde{P}_{\tilde{x}} \Rightarrow \\ & \tilde{u}_{\tilde{t}} + \frac{UT}{\lambda}(\tilde{u}^2)_{\tilde{x}} + \frac{TW}{a}(\tilde{u}\tilde{w})_{\tilde{z}} = -\frac{TP_0}{\rho\lambda U}\tilde{P}_{\tilde{x}} \Rightarrow \\ & \tilde{u}_{\tilde{t}} + (\tilde{u}^2)_{\tilde{x}} + (\tilde{u}\tilde{w})_{\tilde{z}} = -\frac{P_0}{\rho U^2}\tilde{P}_{\tilde{x}} \end{aligned}$$

By assuming again that all terms in these equations are of the same order, we are forced to choose P_0 such that $\frac{P_0}{\rho U^2} = 1$ and the equation becomes

$$\tilde{u}_{\tilde{t}} + (\tilde{u}^2)_{\tilde{x}} + (\tilde{u}\tilde{w})_{\tilde{z}} = -\tilde{P}_{\tilde{x}} \tag{A.3}$$

Finally, inserting the scalings into the vertical momentum equation from (A.1)

leads to

$$
\begin{aligned}
&w_t + (uw)_x + (w^2)_z = -\frac{1}{\rho}P_z - g \Rightarrow \\
&\frac{W}{T}\tilde{w}_{\tilde{t}} + \frac{UW}{\lambda}(\tilde{u}\tilde{w})_{\tilde{x}} + \frac{W^2}{a}(\tilde{w}^2)_{\tilde{z}} = -\frac{P_0}{\rho a}\tilde{P}_{\tilde{z}} - g \Rightarrow \\
&\tilde{w}_{\tilde{t}} + \frac{UT}{\lambda}(\tilde{u}\tilde{w})_{\tilde{x}} + \frac{WT}{a}(\tilde{w}^2)_{\tilde{z}} = -\frac{T}{W}\left(\frac{P_0}{\rho a}\tilde{P}_{\tilde{z}} + g\right) \Rightarrow \\
&\tilde{w}_{\tilde{t}} + (\tilde{u}\tilde{w})_{\tilde{x}} + (\tilde{w}^2)_{\tilde{z}} = -\frac{\lambda}{\epsilon U^2}\left(\frac{P_0}{\rho a}\tilde{P}_{\tilde{z}} + g\right) \Rightarrow \\
&\tilde{w}_{\tilde{t}} + (\tilde{u}\tilde{w})_{\tilde{x}} + (\tilde{w}^2)_{\tilde{z}} = -\frac{1}{g\epsilon^2}\left(g\tilde{P}_{\tilde{z}} + g\right) \Rightarrow \\
&\epsilon^2\left(\tilde{w}_{\tilde{t}} + (\tilde{u}\tilde{w})_{\tilde{x}} + (\tilde{w}^2)_{\tilde{z}}\right) = -\tilde{P}_{\tilde{z}} - g
\end{aligned}
\tag{A.4}
$$

Performing the same operations on the boundary conditions requires the introduction of two additional non-dimensional quantities, $\eta/a = \tilde{\eta}$ and $b/a = \tilde{b}$. Inserting these into the boundary conditions leads us to the conclusion that all terms in the boundary conditions are of the same order and leads to a mirrored non-dimensional version of the original boundary conditions.

The final, non-dimensionalized system is

$$
\begin{aligned}
&u_x + w_z = 0 \\
&u_t + (u^2)_x + (uw)_z = -P_x \\
&\epsilon^2\left(w_t + (uw)_x + (w^2)_z\right) = -P_z - 1
\end{aligned}
$$

with boundary conditions in the simplest case

$$
\begin{aligned}
&\epsilon\frac{\lambda}{\delta}w = \eta_t + u\eta_x \qquad && P = P'_a \qquad && z = \eta \\
&\epsilon\frac{\lambda}{\beta}w = ub_x && && z = b
\end{aligned}
$$

where P'_a it the appropriately scaled atmospheric pressure condition and we have dropped the $\tilde{\cdot}$ notation.

A.0.2 Depth Integration

We now turn to the primary operation required to reduce the dimensionality of the original system, integrating from the surface η to the bottom b. First integrating the

scaled incompressibility equation (A.2) leads to

$$\begin{aligned}
&\int_b^\eta (u_x + w_z)\, dz = 0 \Rightarrow \\
&\frac{\partial}{\partial x}\int_b^\eta u dz - u\eta_x|_{z=\eta} + ub_x|_{z=b} + w|_{z=\eta} - w|_{z=b} = 0 \Rightarrow \\
&\frac{\partial}{\partial x}\int_b^\eta u dz + [w - u\eta_x]_{z=\eta} + [ub_x - w]_{z=b} = 0 \Rightarrow \\
&\frac{\partial}{\partial x}\int_b^\eta u dz + \eta_t = 0 \Rightarrow \\
&h_t + \frac{\partial}{\partial x}\int_b^\eta u dz = 0.
\end{aligned}$$

In order to simplify the discussion of the non-hydrostatic pressure, we will introduce a form of the pressure that explicitly takes account of the hydrostatic contribution to the pressure along with the boundary condition

$$P(x,z,t) = P_A(x,t) + (\eta(x,t) - z) + p(x,z,t), \tag{A.5}$$

where now $p(x,z,t)$ represents the non-hydrostatic contribution to the pressure. This form assumes that the density does not vary with depth as well.

Now integrating the scaled horizontal momentum equation (A.3) leads to

$$\begin{aligned}
&\int_b^\eta \left(u_t + (u^2)_x + (uw)_z\right) dz = -\int_b^\eta (P_a + (\eta - z) + p)_x dz \Rightarrow \\
&\frac{\partial}{\partial t}\int_b^\eta u dz - \eta_t u|_{z=\eta} + \frac{\partial}{\partial x}\int_b^\eta u^2 dz - \eta_x u^2|_{z=\eta} + b_x u^2|_{z=b} + uw|_{z=\eta} - uw|_{z=b} = -\int_b^\eta (\eta + p)_x dz \Rightarrow \\
&\frac{\partial}{\partial t}\int_b^\eta u dz + \frac{\partial}{\partial x}\int_b^\eta u^2 dz - [u(\eta_t + \eta_x u - w)]_{z=\eta} + [u(b_x u - w)]_{z=b} \\
&\qquad = -\frac{\partial}{\partial x}\int_b^\eta (\eta + p) dz + \eta_x \eta - b_x(\eta + p|_{z=b}) \Rightarrow \\
&\frac{\partial}{\partial t}\int_b^\eta u dz + \frac{\partial}{\partial x}\int_b^\eta u^2 dz = \frac{\partial}{\partial x}\left[-\eta h - \int_b^\eta p dz + \frac{1}{2}\eta^2\right] - b_x(\eta + p|_{z=b}) \Rightarrow \\
&\frac{\partial}{\partial t}\int_b^\eta u dz + \frac{\partial}{\partial x}\int_b^\eta u^2 dz = \frac{\partial}{\partial x}\left[-\int_b^\eta p dz - h^2 + hb + \frac{1}{2}(h^2 + 2hb + b^2)\right] - b_x(h + b + p|_{z=b}) \Rightarrow \\
&\frac{\partial}{\partial t}\int_b^\eta u dz + \frac{\partial}{\partial x}\int_b^\eta u^2 dz = \frac{\partial}{\partial x}\left[-\int_b^\eta p dz - \frac{1}{2}h^2\right] - b_x(h + p|_{z=b}) \Rightarrow \\
&\frac{\partial}{\partial t}\int_b^\eta u dz + \frac{\partial}{\partial x}\left(\int_b^\eta u^2 dz + \int_b^\eta p dz + \frac{1}{2}h^2\right) = -b_x(h + p|_{z=b}).
\end{aligned}$$

Doing the same for the scaled vertical momentum equation (A.4) gives

$$\epsilon^2 \int_b^\eta \left(w_t + (uw)_x + (w^2)_z\right) dz = -\int_b^\eta \left(P_a + (\eta - z) + p\right)_z + 1) \, dz \Rightarrow$$
$$\epsilon^2 \left(\frac{\partial}{\partial t}\int_b^\eta w dz - \eta_t w|_{z=\eta} + \frac{\partial}{\partial x}\int_b^\eta uw dz - \eta_x uw|_{z=\eta} + b_x uw|_{z=b} + w^2|_{z=\eta} - w^2|_{z=b}\right)$$
$$= -\int_b^\eta (-1 + p_z + 1) \, dz \Rightarrow$$
$$\epsilon^2 \left(\frac{\partial}{\partial t}\int_b^\eta w dz + \frac{\partial}{\partial x}\int_b^\eta uw dz - \left[w(\eta_t + u\eta_x - w)\right]_{z=\eta} + \left[w(ub_x - w)\right]_{z=b}\right) = p|_{z=b} \Rightarrow$$
$$\epsilon^2 \left(\frac{\partial}{\partial t}\int_b^\eta w dz + \frac{\partial}{\partial x}\int_b^\eta uw dz\right) = p|_{z=b}.$$

The depth averaged equations we now have are

$$h_t + \frac{\partial}{\partial x}\int_b^\eta u dz = 0$$
$$\frac{\partial}{\partial t}\int_b^\eta u dz + \frac{\partial}{\partial x}\left(\int_b^\eta u^2 dz + \int_b^\eta p dz + \frac{1}{2}h^2\right) = -b_x(h + p|_{z=b})$$
$$\epsilon^2 \left(\frac{\partial}{\partial t}\int_b^\eta w dz + \frac{\partial}{\partial x}\int_b^\eta uw dz\right) = p|_{z=b}.$$

Note that we have come to these by utilizing the boundary conditions which were also scaled, so the resulting equations are dependent on those scalings. Last, we can simplify notation by defining

$$\overline{u} = \frac{1}{h}\int_b^\eta u dz, \qquad \overline{w} = \frac{1}{h}\int_b^\eta w dz,$$
$$\overline{u^2} = \frac{1}{h}\int_b^\eta u^2 dz, \qquad \overline{w^2} = \frac{1}{h}\int_b^\eta w^2 dz,$$
$$\overline{p} = \frac{1}{h}\int_b^\eta p dx, \qquad \text{and} \qquad \overline{uw} = \frac{1}{h}\int_b^\eta uw dz$$

as the depth averages of the specified quantities. This leads to the final one dimen-

sional, depth averaged equations as

$$\frac{\partial}{\partial t}h + \frac{\partial}{\partial x}(h\overline{u}) = 0 \tag{A.6}$$

$$\frac{\partial}{\partial t}(h\overline{u}) + \frac{\partial}{\partial x}\left(h\overline{u^2} + h\overline{p} + \frac{1}{2}h^2\right) = -(h+p|_{z=b})\frac{\partial b}{\partial x} \tag{A.7}$$

$$\epsilon^2\left(\frac{\partial}{\partial t}(h\overline{w}) + \frac{\partial}{\partial x}(\overline{uw})\right) = p|_{z=b}. \tag{A.8}$$

One last equation for the pressure will be useful as it will provide a means to calculate $\overline{p}$ depending on the approximations we will make in the next section. Consider again (A.4) and integrate from η to a vertical level $b+\alpha h$ where $\alpha \in [0,1]$. Then we can write

$$\begin{aligned}
&\epsilon^2\int_{b+\alpha h}^{\eta}\left(w_t + (uw)_x + (w^2)_z\right)dz = -\int_{b+\alpha h}^{\eta} p_z dz \Rightarrow \\
&\epsilon^2\left\{\frac{\partial}{\partial t}\int_{b+\alpha h}^{\eta} w dz - w\eta_t|_{z=\eta} + w\alpha\eta_t|_{z=b+\alpha h} + \frac{\partial}{\partial x}\int_{b+\alpha h}^{\eta} uw dz - uw\eta_x|_{z=\eta}\right. \\
&\qquad\left. + uw(b+\alpha h)_x|_{z=b+\alpha h} + w^2|_{z=\eta} - w^2|_{z=b+\alpha h}\right\} = p|_{z=b+\alpha h} \Rightarrow \\
&\epsilon^2\left\{\frac{\partial}{\partial t}\int_{b+\alpha h}^{\eta} w dz + \frac{\partial}{\partial x}\int_{b+\alpha h}^{\eta} uw dz - \left[w(\eta_t + u\eta_x - w)\right]_{z=\eta} + \left[w(\alpha\eta_t + u(b+\alpha h)_x - w)\right]_{z=b+\alpha h}\right\} \\
&\qquad = p|_{z=b+\alpha h} \Rightarrow \\
&\epsilon^2\left\{\frac{\partial}{\partial t}\int_{b+\alpha h}^{\eta} w dz + \frac{\partial}{\partial x}\int_{b+\alpha h}^{\eta} uw dz + \left\{w[\alpha(\eta_t + u\eta_x) + (1+\alpha)ub_x - w]\right\}|_{z=b+\alpha h}\right\} = p|_{z=b+\alpha h}.
\end{aligned}$$

In order to find the expression for $\overline{p}$ we then need to take the integral over $\alpha \in [0,1]$,

$$\begin{aligned}
\overline{p} &= \frac{\epsilon^2}{h}\int_0^1\left\{\frac{\partial}{\partial t}\int_{b+\alpha h}^{\eta} w dz + \frac{\partial}{\partial x}\int_{b+\alpha h}^{\eta} uw dz + \left\{w[\alpha(\eta_t + u\eta_x) + (1+\alpha)ub_x - w]\right\}|_{z=b+\alpha h}\right\} d\alpha \\
&= \frac{\epsilon^2}{h}\left\{\frac{\partial}{\partial t}\int_0^1\int_{b+\alpha h}^{\eta} w dz d\alpha + \frac{\partial}{\partial x}\int_0^1\int_{b+\alpha h}^{\eta} uw dz d\alpha\right. \\
&\qquad\left. + \int_0^1 \left\{w[\alpha(\eta_t + u\eta_x) + (1+\alpha)ub_x - w]\right\}|_{z=b+\alpha h}\, d\alpha\right\}.
\end{aligned} \tag{A.9}$$

A.0.3 Approximations

No Vertical Variation

If it is assumed that neither u or w vary in the depth, the consequence is that all the average quantities $\bar{\cdot}$ become identical to the functions they represent. First we must

evaluate $\overline{p}$ as

$$\begin{aligned}\overline{p} &= \frac{\epsilon^2}{h}\left\{\frac{\partial}{\partial t}\left(w\int_0^1\int_{b+\alpha h}^{\eta} dzd\alpha\right) + \frac{\partial}{\partial x}\left(uw\int_0^1\int_{b+\alpha h}^{\eta} dzd\alpha\right)\right\}\\ &= \frac{\epsilon^2}{2h}\left\{(hw)_t + (huw)_x\right\}\\ &= \frac{1}{2h}p|_{z=b}.\end{aligned}$$

The governing equations then become

$$\begin{aligned}&h_t + (hu)_x = 0\\ &(hu)_t + \left(hu^2 + \frac{1}{2}p + \frac{1}{2}h^2\right)_x = -(h+p)b_x\\ &\epsilon^2\left((hw)_t + (huw)_x\right) = p,\end{aligned}$$

where we have now dropped the evaluation notation on p.

Shallow Water Equations

The shallow water equations are now easily obtained by assuming $\epsilon \ll 1$, thereby decoupling any affects the vertical acceleration may have on the bulk flow and the non-hydrostatic pressure is consequently negligible. These are then

$$\begin{aligned}&h_t + (hu)_x = 0, \quad \text{and}\\ &(hu)_t + \left(hu^2 + \frac{1}{2}h^2\right)_x = -hb_x.\end{aligned} \tag{A.10}$$

Non-Hydrostatic Modified Equations

If it is not assumed that $\epsilon \ll 1$ then we are left with a system of three equations with p appearing in the horizontal momentum flux and the source terms. A modified version of the equations isolates the pressure and produces a balance law involving the pressure so that it can be used directly

$$\begin{aligned}&h_t + (hu)_x = 0,\\ &(hu)_t + \left(hu^2 + \frac{1}{2}p + \frac{1}{2}h^2\right)_x = -(h+p)b_x, \quad \text{and}\\ &\epsilon^2\left((p)_t + (up)_x\right) = \varphi.\end{aligned}$$

If we can evolve the third equation effectively with φ being modeled correctly, a Riemann solver can be constructed that evolves the system. The problem then turns

to how to calculate φ as a source term for non-hydrostatic pressure.

Linear Vertical Variation in the Vertical Velocity

Assume now that w varies in the vertical direction linearly. Via (A.2) we know $w_z = -u_x$ which allows us to make the following ansatz for the form of w,

$$w = w(x,t) - u_x z.$$

Integrating the quantities in the average pressure equation (A.9) we find

$$\begin{aligned}
\int_0^1 \int_{b+\alpha h}^{\eta} w dz d\alpha &= \int_0^1 \int_{b+\alpha h}^{\eta} (w - u_x z) dz d\alpha = \int_0^1 \left[wz - \frac{1}{2} u_x z^2 \right]_{b+\alpha h}^{\eta} d\alpha \\
&= \int_0^1 \left[(wh + u_x hb)(1-\alpha) + \frac{1}{2} u_x h^2 (1 - \alpha^2) \right] d\alpha \\
&= \int_0^1 \left[hw + u_x hb + \frac{1}{2} u_x h^2 - (wh + u_x hb)\alpha - \frac{1}{2} u_x h^2 \alpha^2 \right] d\alpha \\
&= \left[(hw + u_x hb + \frac{1}{2} u_x h^2)\alpha - \frac{1}{2}(wh + u_x hb)\alpha^2 - \frac{1}{6} u_x h^2 \alpha^3 \right]_0^1 \\
&= \frac{1}{2} hw + \frac{1}{2} u_x hb + \frac{1}{3} u_x h^2
\end{aligned}$$

and

$$\int_0^1 \int_{b+\alpha h}^{\eta} uw dz d\alpha = u \int_0^1 \int_{b+\alpha h}^{\eta} (w - u_x z) dz d\alpha = \frac{1}{2} huw + \frac{1}{4} (u^2)_x hb + \frac{1}{6} (u^2)_x h^2$$

for the integrals involving w and u directly. For the boundary terms, we have the expression

$$\begin{aligned}
\int_0^1 \left[w(\alpha(\eta_t + u\eta_x) + (1+\alpha)ub_x - w)\right]_{z=b+\alpha h} d\alpha &= \int_0^1 \Big[(-w^2 + uwb_x + 2wu_xb - (u_x)^2b^2 - \frac{1}{2}((ub)^2)_x \\
&\quad + \alpha(-w^2 + 3u_xwh + 2wbu_x + wub_x - 2hb(u_x)^2 - \frac{1}{2}((ub)^2)_x - (bu_x)^2 - hb(u_x)^2 - \frac{1}{2}h(u^2)_x \\
&\quad + \alpha^2(u_xhw - 2(u_xh)^2 - u_xh(ub)_x)\Big]\, d\alpha \\
= (-w^2 + uwb_x + 2wu_xb - (u_x)^2b^2 - \frac{1}{2}((ub)^2)_x) & \\
&\quad + \frac{1}{2}(-w^2 + 3u_xwh + 2wbu_x + wub_x - 2hb(u_x)^2 - \frac{1}{2}((ub)^2)_x - (bu_x)^2 - hb(u_x)^2 - \frac{1}{2}h(u^2)_x \\
&\quad + \frac{1}{3}(u_xhw - 2(u_xh)^2 - u_xh(ub)_x) \\
= -\frac{3}{2}w^2 + \frac{3}{2}uwb_x + 3bwu_x - \frac{3}{2}b^2(u_x)^2 - \frac{3}{4}((ub)^2)_x + \frac{11}{6}hwu_x - \frac{3}{2}hb(u_x)^2 - \frac{1}{4}h(bu^2)_x & \\
\quad - \frac{2}{3}(hu_x)^2 - \frac{1}{3}hb_x(u_x)^2. &
\end{aligned}$$

Now turning back to the expression for the depth integrated pressure (A.9), we have

$$\begin{aligned}
\overline{p} = \frac{\epsilon^2}{h}\Big\{ \frac{\partial}{\partial t}\int_0^1\int_{b+\alpha h}^{\eta} w dz d\alpha + \frac{\partial}{\partial x}\int_0^1\int_{b+\alpha h}^{\eta} uw dz d\alpha + \int_0^1 \{w[\alpha(\eta_t + u\eta_x) + (1+\alpha)ub_x - w]\}|_{z=b+\alpha} & \\
= \frac{\epsilon^2}{h}\Big\{ \frac{\partial}{\partial t}\left(\frac{1}{2}hw + \frac{1}{2}u_xhb + \frac{1}{3}u_xh^2\right) + \frac{\partial}{\partial x}\left(\frac{1}{2}huw + \frac{1}{4}(u^2)_xhb + \frac{1}{6}(u^2)_xh^2\right) & \\
\quad - \frac{3}{2}w^2 + \frac{3}{2}uwb_x + 3bwu_x - \frac{3}{2}b^2(u_x)^2 - \frac{3}{4}((ub)^2)_x + \frac{11}{6}hwu_x & \\
\quad - \frac{3}{2}hb(u_x)^2 - \frac{1}{4}h(bu^2)_x - \frac{2}{3}(hu_x)^2 - \frac{1}{3}hb_x(u_x)^2\Big\}. &
\end{aligned}$$

Turning back to the equations at hand, we must calculate the depth averaged quantities,

$$\begin{aligned}
\overline{w} = \frac{1}{h}\int_b^{\eta} w(x,t) - u(x,t)_x z dz = \frac{1}{h}\left[wz - \frac{1}{2}u_xz^2\right]_b^{\eta} = \frac{1}{h}\left[wz - \frac{1}{2}u_xz^2\right]_b^{\eta} & \\
= \frac{1}{h}\left[wh - \frac{1}{2}u_x(h^2 + 2hb)\right] = w - u_x\left(\frac{1}{2}h + b\right). &
\end{aligned}$$

We can then finally write down the governing equations in this case as

$$
\begin{aligned}
&h_t + (hu)_x = 0, \\
&(hu)_t + \left(hu^2 + \frac{1}{2}h^2 + h\overline{p} \right)_x = -b_x(h + p|_{z=b}), \text{ and} \\
&(hw)_t + (huw)_x - \left[\left(hu_x \left(\frac{1}{2}h + b \right) \right)_t + \left(huu_x \left(\frac{1}{2}h + b \right) \right)_x \right] = p|_{z=b},
\end{aligned}
$$

where we have omitted the expression calculated for $\overline{p}$ for clarity.

VITA

Kyle T. Mandli was born in Madison, Wisconsin on the 10th of December, 1981. He earned his Bachelors degrees in applied mathematics, engineering and physics at the University of Wisconsin, Madison. He then received an M.S. and Ph.D. in applied mathematics at the University of Washington, Seattle in 2005 and 2011 respectively.